

TECTONIC HISTORY AND COALBED GAS GENESIS

GUEST EDITORS: QUANLIN HOU, YIWEN JU, JONATHAN AITCHISON, HONGYUAN ZHANG,
AND YUDONG WU





Tectonic History and Coalbed Gas Genesis

Journal of Geological Research

Tectonic History and Coalbed Gas Genesis

Guest Editors: Quanlin Hou, Yiwen Ju, Jonathan Aitchison,
Hongyuan Zhang, and Yudong Wu



Copyright © 2012 Hindawi Publishing Corporation. All rights reserved.

This is a special issue published in “Journal of Geological Research.” All articles are open access articles distributed under the Creative Commons Attribution License, which permits unrestricted use, distribution, and reproduction in any medium, provided the original work is properly cited.

Editorial Board

William Austin, UK
Zsolt Berner, Germany
Ognjen Bonacci, Croatia
Marco Bonini, Italy
Christophe Colin, France
Nathalie C. Nebout, France
Antonio Costa, Italy
Antonio Delgado Huertas, Spain
M. H. Engel, USA
Christophe Falgueres, France
Michel Faure, France
Martin Feely, Ireland
Paulo Fonseca, Portugal
Steven L. Forman, USA
Salvatore Gambino, Italy
Michael O. Garcia, USA
Helena Granja, Portugal

Michel Grégoire, France
Agust Gudmundsson, UK
Keiko Hattori, Canada
Gunnar Jacks, Sweden
Ryszard Kryza, Poland
Saro Lee, Korea
Spencer Lucas, USA
Valter Maggi, Italy
Jesus Martinez-Frias, Spain
Leszek Marynowski, Poland
Giuseppe Mastronuzzi, Italy
Teresa Moreno, Spain
Roberto Moretti, Italy
Karoly Nemeth, New Zealand
Atle Nesje, Norway
Josep Pares, Spain
Petr Pruner, Czech Republic

Uwe Ring, Sweden
Idoia Rosales, Spain
Joaquin Ruiz, USA
Satish Sangode, India
Young Kwan Sohn, Korea
Sheng-Rong Song, Taiwan
David T. A. Symons, Canada
Umberta Tinivella, Italy
Emanuele Tondi, Italy
Luigi Tosi, Italy
Alan Trenhaile, Canada
Sergio Vinciguerra, Italy
Lixin Wu, China
Bernd Wuennemann, Germany
Seong-Taek Yun, Republic of Korea
Lifei Zhang, China
Hong-Fei Zhang, China

Contents

Tectonic History and Coalbed Gas Genesis, Quanlin Hou, Yiwen Ju, Jonathan Aitchison, Hongyuan Zhang, and Yudong Wu

Volume 2012, Article ID 282789, 1 page

The Dabie Extensional Tectonic System: Structural Framework, Quanlin Hou, Hongyuan Zhang, Qing Liu, Jun Li, and Yudong Wu

Volume 2012, Article ID 369513, 8 pages

Structural Characteristics and Physical Properties of Tectonically Deformed Coals, Yiwen Ju, Zhifeng Yan, Xiaoshi Li, Quanlin Hou, Wenjing Zhang, Lizhi Fang, Liye Yu, and Mingming Wei

Volume 2012, Article ID 852945, 14 pages

Applications of Vitrinite Anisotropy in the Tectonics: A Case Study of Huaibei Coalfield, Southern North China, Yudong Wu, Quanlin Hou, Yiwen Ju, Daiyong Cao, Junjia Fan, and Wei Wei

Volume 2012, Article ID 526016, 16 pages

Geochronology and Tectonic Evolution of the Lincang Batholith in Southwestern Yunnan, China, Hongyuan Zhang, Junlai Liu, and Wenbin Wu

Volume 2012, Article ID 287962, 11 pages

The Structural Framework of the Erlangping Group in North Qinling, Central China, Hongyuan Zhang, Chunqiang Zhao, Fanglei Xu, and Yanlong Dong

Volume 2012, Article ID 850282, 7 pages

The Mesozoic Tectonic Dynamics and Chronology in the Eastern North China Block, Quanlin Hou, Qing Liu, Hongyuan Zhang, Xiaohui Zhang, and Jun Li

Volume 2012, Article ID 291467, 11 pages

Pan-African Paleostresses and Reactivation of the Eburnean Basement Complex in Southeast Ghana (West Africa), Mahaman Sani Tairou, Pascal Affaton, Solomon Anum, and Thomas Jules Fleury

Volume 2012, Article ID 938927, 15 pages

Different Origins of the Fractionation of Platinum-Group Elements in Raobazhai and Bixiling Mafic-Ultramafic Rocks from the Dabie Orogen, Central China, Qing Liu, Quanlin Hou, Liewen Xie, Hui Li, Shanqin Ni, and Yudong Wu

Volume 2012, Article ID 631426, 11 pages

FTIR and Raman Spectral Research on Metamorphism and Deformation of Coal, Xiaoshi Li, Yiwen Ju, Quanlin Hou, Zhuo Li, and Junjia Fan

Volume 2012, Article ID 590857, 8 pages

Characterization of Coal Reservoirs in Two Major Coal Fields in Northern China: Implications for Coalbed Methane Development, Junjia Fan, Yiwen Ju, Quanlin Hou, Yudong Wu, and Xiaoshi Li

Volume 2012, Article ID 701306, 10 pages

Total Scanning Fluorescence Characteristics of Coals and Implication to Coal Rank Evaluation, Junjia Fan, Keyu Liu, Yiwen Ju, Shaobo Liu, and Lili Gui

Volume 2012, Article ID 692865, 6 pages

Editorial

Tectonic History and Coalbed Gas Genesis

Quanlin Hou,¹ Yiwen Ju,¹ Jonathan Aitchison,² Hongyuan Zhang,³ and Yudong Wu⁴

¹ Key Laboratory of Computational Geodynamics of Chinese Academy of Sciences, College of Earth Science, University of Chinese Academy of Sciences, Beijing 100049, China

² School of Geosciences, University of Sydney, NSW 2006, Australia

³ School of the Earth Sciences and Resources, China University of Geosciences in Beijing, No. 29 Xueyuan Road, Haidian, Beijing 100083, China

⁴ Institute of Mineral Resources, Chinese Academy of Geological Sciences, No. 26 Baiwanzhuang Street, Xicheng, Beijing 100037, China

Correspondence should be addressed to Quanlin Hou, quhou@ucas.ac.cn

Received 22 November 2012; Accepted 22 November 2012

Copyright © 2012 Quanlin Hou et al. This is an open access article distributed under the Creative Commons Attribution License, which permits unrestricted use, distribution, and reproduction in any medium, provided the original work is properly cited.

General review of tectonic history and further careful research on deformed coal rocks form the basic way to clarify problems of coalbed gas genesis.

In China, one increasing attention should be the Mesozoic tectonic history of North China and its surrounding areas, and also the related coalbed gas genesis study in this most important coalbed gas product area of China.

Geometry, kinematics, and geochronology data from outcrops of the China Central Orogen and the North China offered excellent clues of extension event for understanding the tectonic conditions of coalbed gas. Q. Hou et al. studied the Mesozoic Tectonic Dynamics and Chronology in the Eastern North China Block.

Central Orogen of China, related to Tethys Closure and mainly formed during the Triassic Period, includes both the Qinling Orogen in the west and the Dabie Mountains in the east. H. Zhang et al. separately concluded the Mesozoic tectonic evolution of the Lincang Batholith, during palaeo-Tethys collision, and reviewed the structural framework of the Erlangping Group in North Qinling. Q. Hou clarified the framework of the Dabie Extensional Tectonic System. Furthermore, Q. Liu made out the different origins of the fractionation of Platinum-Group elements in Raobazhai and Bixiling Mafic-Ultramafic Rocks from the Dabie Orogen.

Several achievements of coal field research in Northern China showed us the characteristics, developments, and genesis of coalbed gas. Y. Ju et al. gave us general properties of tectonically deformed coal rocks. J. Fan et al. studied the characterization of coal reservoirs in two major coal fields of China. Y. Wu et al. showed a case study of vitrinite anisotropy from Huaibei Coalfield from southern North China.

Some kinds of techniques on brittle, brittle-ductile, and ductile deformation zones are very important for future research. M. S. Tairó et al. studied the “*Pan-African paleostresses and reactivation of the eburnean basement complex in Southeast Ghana (West Africa)*”. X. Li et al. took use of the Fourier transform infrared and Raman Spectral to study the metamorphism and deformation of coal. J. Fan et al. gave us one new coal rank evaluation method by total scanning fluorescence characteristics.

In general, the eleven papers here constitute a significant contribution to our knowledge by reporting the tectonic settings, characteristics, and research methods of coalbed gas genesis. The papers also laid a research system for further work of coal geology.

Quanlin Hou
Yiwen Ju
Jonathan Aitchison
Hongyuan Zhang
Yudong Wu

Research Article

The Dabie Extensional Tectonic System: Structural Framework

Quanlin Hou,¹ Hongyuan Zhang,² Qing Liu,¹ Jun Li,³ and Yudong Wu⁴

¹ Graduate University of the Chinese Academy of Sciences, Beijing 100049, China

² School of Earth Sciences and Resources, China University of Geosciences, Beijing 100083, China

³ Institute of Geology and Geophysics, The Chinese Academy of Sciences, Beijing 100029, China

⁴ MLR Key Laboratory of Metallogeny and Mineral Assessment, Institute of Mineral Resources, CAGS, Beijing 100037, China

Correspondence should be addressed to Quanlin Hou, quhou@gucas.ac.cn

Received 10 May 2012; Revised 31 July 2012; Accepted 22 August 2012

Academic Editor: Yi-Wen Ju

Copyright © 2012 Quanlin Hou et al. This is an open access article distributed under the Creative Commons Attribution License, which permits unrestricted use, distribution, and reproduction in any medium, provided the original work is properly cited.

A previous study of the Dabie area has been supposed that a strong extensional event happened between the Yangtze and North China blocks. The entire extensional system is divided into the Northern Dabie metamorphic complex belt and the south extensional tectonic System according to geological and geochemical characteristics in our study. The Xiaotian-Mozitan shear zone in the north boundary of the north system is a thrust detachment, showing upper block sliding to the NNE, with a displacement of more than 56 km. However, in the south system, the shearing direction along the Shuihou-Wuhe and Taihu-Mamiao shear zones is tending towards SSE, whereas that along the Susong-Qingshuihe shear zone tending towards SW, with a displacement of about 12 km. Flinn index results of both the north and south extensional systems indicate that there is a shear mechanism transition from pure to simple, implying that the extensional event in the south tectonic system could be related to a magma intrusion in the Northern Dabie metamorphic complex belt. Two ⁴⁰Ar-³⁹Ar ages of mylonite rocks in the above mentioned shear zones yielded, separately, ~190 Ma and ~124 Ma, referring to a cooling age of ultrahigh-pressure rocks and an extensional era later.

1. Introduction

Dabie area is well known of owning one largest area of ultrahigh-pressure metamorphic belt (UHPB) in the world, located, as a tectonic zone, between the North China Block and Yangtze Block (Figure 1).

The Dabie area experienced a complicated tectonic evolution during the Mesozoic and resulted in thrust-nappe, extensional detachment, and strike-slip structures [1, 2]. Much attention has been paid to the tectonic evolution of the Dabie Mountains, with most tectonic models proposing although compressional tectonism for the formation of the orogen. However, Mesozoic extensional structures in the Dabie Mountains are also obvious and important for understanding the Mesozoic tectonic regime inversion from compression to extension occurred throughout the Dabie Mountains and even in the eastern North China Block [3].

The purpose of this paper is to figure out the structural framework of the Dabie Late Mesozoic extensional detachment system by analyzing deformation, tectonic styles, and

physical conditions, to constrain the time of the extensional tectonics, and finally to discuss the tectonic implications.

2. Tectonic Background

The general geology of the Dabie area has been described in multiple publications [5–13]. Briefly, from north to south, the Dabie Mountains can be divided into four major tectonic units: (1) the North Huaiyang Flysch belt (NHMB) mainly composed of the Foziling Group (Pt₂); (2) the Northern Dabie metamorphic complex belt (NDMCB), composed dominantly of granitic gneisses of TTG composition, with the Xiaotian-Mozitan and the Shuihou-Wuhe shear zones defining the northern and southern boundaries, respectively; (3) the ultrahigh-pressure metamorphic belt (UHPB) refers to the Central Dabie ultrahigh pressure metamorphic complex and is bounded in the south by the Taihu-Mamiao shear zone; (4) the high-pressure belt (HPB) refers to the Southern Dabie high-pressure blueschist/greenschist terrane [10],

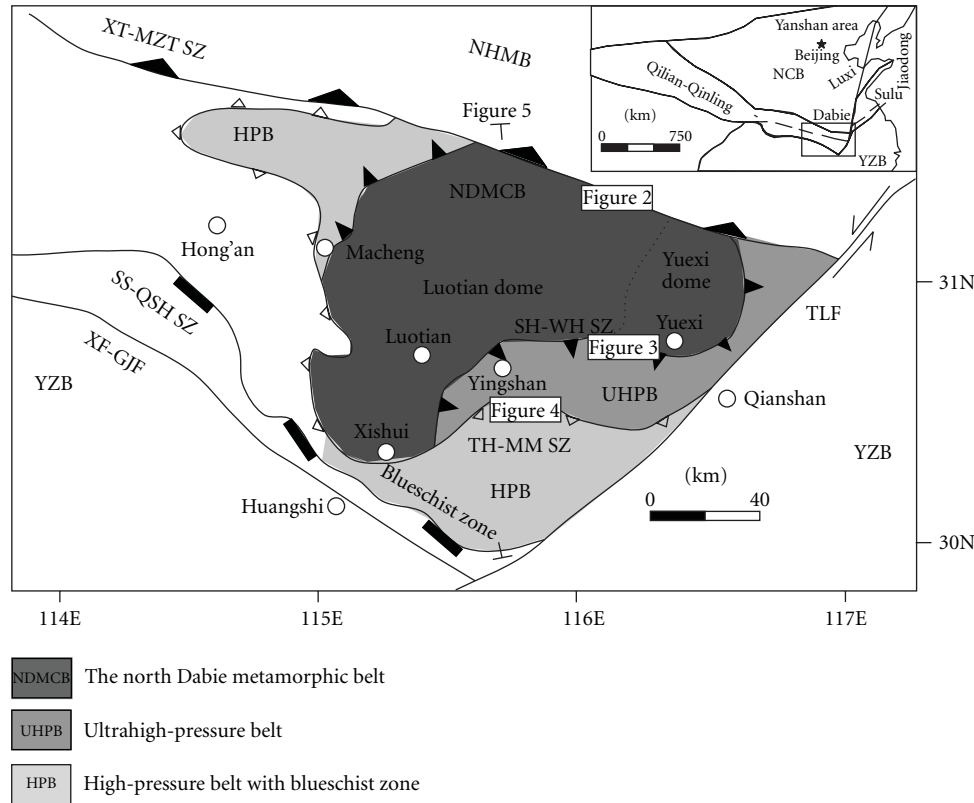


FIGURE 1: Simplified map of late Mesozoic main shear zones in eastern Dabie Mountain, Central China (after Suo et al., 2000 [4]). NCC: Northern China Block; YZC: Yangzi Block; NHMB: North Huaiyang metamorphic belt; NDMCD: North Dabie metamorphic complex belt; UHPB: Ultrahigh-pressure metamorphic belt; HPB: high-pressure metamorphic belt; SH-WH SZ: Shuihou-Wuhe shear zone; TH-MM SZ: Taihu-Mamiao shear zone; SS-QSH SZ: Susong-Qingshuihe shear zone; XT-MZT SZ: Xiaotian-Mozitan shear zone; TLF: Tancheng-Lujiang Fault (Tanlu Fault); XF-GJF: Xiangfan-Guangji Fault.

whose southern margin is defined by the Susong-Qingshuihe shear zone (Figure 1).

Several contrasting tectonic models have been proposed for the Dabie orogenic belt. Suo et al. [4, 14] identified extensional tectonism in the Dabie orogen during the middle-late Mesozoic. Song [15] defined extensional structures in metamorphic rocks with different ages that formed prior to the continental collision that produced the Qinling-Dabie orogen. Based on geochemical analyses of the Wangmuguan pluton in Xinxian, Zhang et al. [16] proposed that the pluton formed within extensional conditions after the formation of the orogen and was related to lithosphere detachment. A two-stage extension model proposed by Jin et al. [17] describes extension during the early Caledonian period, which resulted in the local sea and the beginnings of the Dabie-Qinling metamorphic core complex; extension during the Yanshan period coincided with the formation of the core complex and the intrusion of granite. Wang and Yang [18] investigated the extensional domes in the Dabie Mountains. Li [19] studied the late Mesozoic extension in the eastern part of the Dabie Mountains. Among these studies, there is a hot debate about the timing of the onset of extension, its direction, and tectonic styles. In this paper, we describe the results of our field observations and geochemical analysis, which provide some

new insights into understanding the evolution of the late Mesozoic extensional detachment zones in the Dabie area.

3. Deformation History of Extensional Detachment Zones

The NDMCB is the crystalline core of the late Mesozoic extensional structures. These features can be divided into two tectonic systems, the north extensional tectonic system and the south extensional tectonic system (Figure 1).

3.1. The North Extensional Tectonic System. The principal detachment shear zone is the XT-MZT SZ, which is located between the NHMB and the NDMCB. To the east (i.e., along the Huoshan-Zhujiapu Road), the brittle-ductile extensional shear zone dips to the NE (60°) at an angle of 30° – 40° to the horizontal. To the west (i.e., in the Jinzhai-Qingshan area), the shear zone dips towards the NNE-NE (30° – 50°). From south to the north, the dip angle changes from steep (about 70°) to gentle. Hence, it is shaped like a shovel and is locally sinuate (orientation 220° and dip 20°). The displacement orientation on the shear zone is to the NE or NNE. Noticeably, the extensional shear zone locally in the

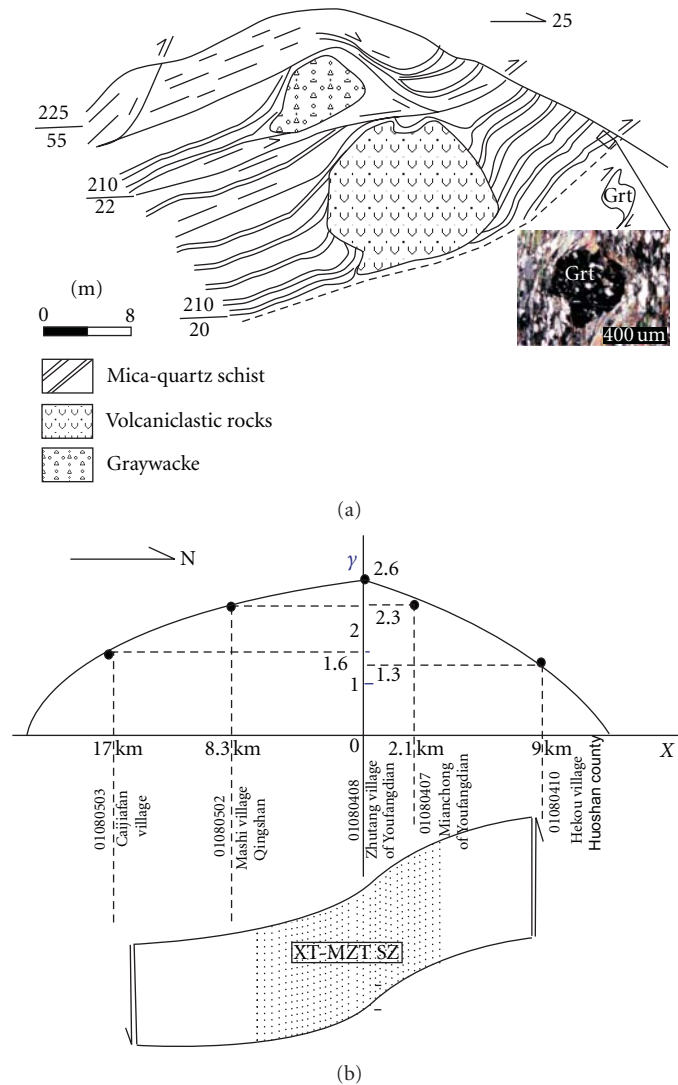


FIGURE 2: (a) The north extensional detachment zone suggests extension shearing after late Jurassic from the XT-MZT SZ. Late Jurassic volcaniclastic tectonite blocks are hosted by mica-quartz schist (Pt_2). The photo right below shows snow ball structure observed by microscopy. (b) The shear length of the XT-MZT SZ is more than 56 km.

NHMB has developed into an inconsecutive extensional crenulation cleavage (C' , the same as S_3 in some places) with NE-dip. The extensional crenulation cleavage is an important character of the north extensional tectonic system. The foliations (S_1 or S_2) dipping SW in quartz schist (Pt_2) may represent earlier overshear deformation in the NHMB. Asymmetric augen in amphibole gneiss in the Huoshan area indicates shearing towards the NE. Using the optical microscope, garnet in quartz schist has a “snowball” texture and also confirms that NE-directed shearing (Figure 2(a)).

According to a systematical strain-measurement analysis of the snowball textures in garnet and deformed quartz grains, the shear strain (γ) in the central part of the north detachment zone is up to 2.6 and gradually decreases outward. Measurements of a rock finite strain in the detachment zone indicated that the shear displacement is at least 56 km.

3.2. The South Extensional Tectonic System. The south extensional tectonic system is composed mainly of one deep ductile shear zone and two brittle-ductile shear zones.

3.2.1. One Deep Ductile Shear Zone (Shuihou-Wuhe). The Shuihou-Wuhe ductile shear zone (SH-WH SZ) consists of feldspar mylonite and formed under lower crustal conditions; the shear zone was named the “first southern detachment zone” by Zhong et al. [20]. The shear zone dips towards the S, SSW, and SSE at an angle of 40–60°. The S-C shear fabrics, sheath folds, and shear folds in the shear zone consistently dip towards the south (Figures 3(a) and 3(b)). Much of these extensional shear deformations superpose on earlier thrust-shearing deformation and strike-slip deformation. The shear strain (γ) in the zone is up to 5, such as observations in the north of Yingshan (Figure 3(a)).

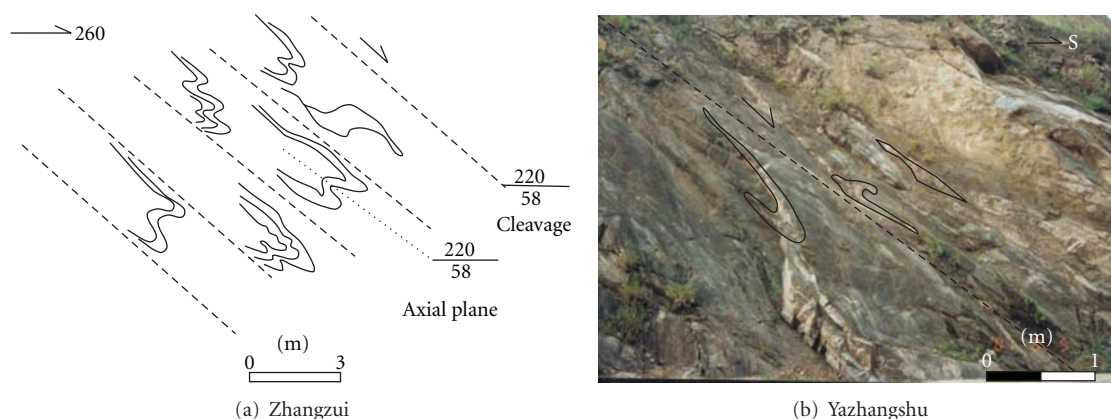


FIGURE 3: Quartz bands in gneiss in the Shuihou-Wuhe shear zone, the shear zone dips SSW; (a) and (b) are, respectively, from places the Zhangzui village and the Yazhangshu primary school of the Yingshan County.

Based on strain-measurement analysis, the strain ellipsoid of the shear zone displays the Flinn parameter (K) range of 0.01–0.1, corresponding with pancake-shape flattening and reflecting intense compression and pure shear deformation.

According to the fabric analysis of deformed quartz, the small-circle belt at the east segment of the SH-WH SZ reflects high-temperature deformations conditions ($>700^{\circ}\text{C}$) and relatively slow strain-rate velocity (10^{-7}s^{-1}). The middle segment was asymmetric with point belonging to a rhomb slide system, which reflects middle-high-temperature deformational conditions ($650\text{--}700^{\circ}\text{C}$). The quartz fabric analysis also shows that the principal stress direction was oriented NE-SW, which is consistent with the principal stress direction determined from the preferred orientation of amphibole long axes. The paleodifferential stress was calculated at about 92 Mpa based on quartz dislocation density.

3.2.2. Two Brittle-Ductile Shear Zones (Taihu-Mamiao, Susong-Qingshuihe)

(a) *The Taihu-Mamiao Shear Zone.* The Taihu-Mamiao shear zone (TH-MM SZ) lies to the south of the SH-WH SZ and is bounded by the southern Dabie and Susong metamorphic zones in the north and south, respectively (Figure 1). The TH-MM SZ dips mainly towards the S or SSE; the dip angle changes from steep to gentle with increasing depth. A series of recumbent folds, S-C shear fabrics, asymmetric augen, extensional lineations in some profiles indicate that extension was to the SSE (Figures 4(a) and 4(b)). Based on strain-measurement analysis, the Flinn parameter for the shear zone is about 1, indicating a planar strain.

(b) *The Susong-Qingshuihe Shear Zone.* The Susong-Qingshuihe shear zone (SS-QSH SZ) lies to the south of the TH-MM SZ and to the north of the Xiangfan-Guangji fault (XF-GJ F.). The SS-QSH SZ marks the interface between high-pressure eclogite and blueschist units (Figure 1). The stretch lineation of monzogranitic mylonite in Qingshuihe plunges towards the SSW. According to strain-measurement analysis,

the Flinn parameter of the shear zone is more than 7, which suggests cigar-shaped, extensional deformation. The shear displacement along the detachment zone is more than 12 km based on strain measurement analysis. Deformed quartz displays asymmetric point coarctation, belonging to a rhomb slide system, and suggesting middle-to-high temperatures during deformation. Based on the dislocation density of quartz, we calculated the paleodifferential stress 70–84 Mpa, which is smaller than that of the SH-WH SZ.

Based on the structural analysis above, the three shear zones in the south extensional tectonic system probably represent deeper, middle, and upper detachment systems, ranging from north to south, respectively. Deformation temperatures and differential stresses decrease from the northern Dabie complex to the south. Remarkably, strain changes from north to south; from flattened (i.e., $K \ll 1$) in the northern the SH-WH SZ, to planar (i.e., $K \approx 1$), and then to extensional strain (i.e., $K \gg 1$) in the southern SS-QSH SZ. This transition of strain reflects the influence of magmatic intrusion during the extensional detachment.

4. Chronological Constraints on the Extensional Detachment

$^{40}\text{Ar}/^{39}\text{Ar}$ dating of biotite and hornblende from the four extensional detachment zones in Dabie area are shown in Table 1. The data can be divided into two groups, ca. 124 Ma and ca. 190 Ma, respectively. The north extensional tectonic system and the SS-QSH SZ were active at ca. 124 Ma, representing the time of extensional detachment to this period. In contrast, the SH-WH and TH-MM SZs, on the north and south sides of ultrahigh-pressure metamorphic zone, respectively, have ages of ca. 190 Ma, representing the time of exhumation of ultrahigh-pressure metamorphic rocks.

5. Discussion

The north extensional detachment zone hosts a shear zone that cuts the Late Proterozoic Xinyang Group (Pt_2n) mica-quartz schist. The shear zone contains allochthonous blocks

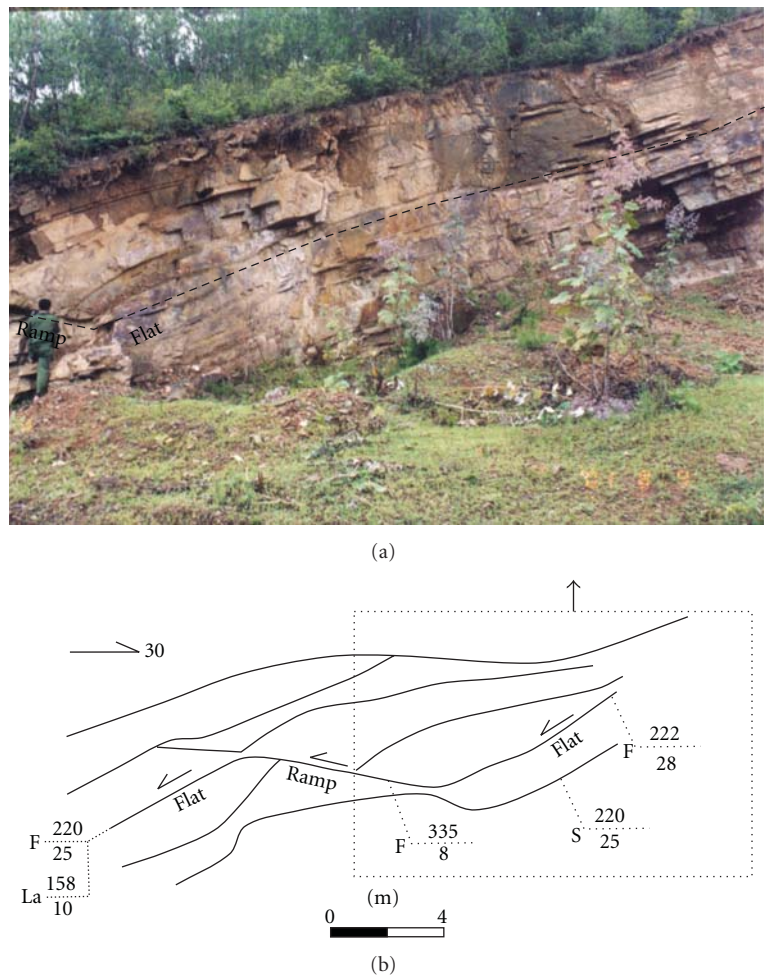


FIGURE 4: Extensional flat-ramp structure in the Taihu-Mamiao shear zone, indicating S-extension (near Luoxi village along the road between Liuyang and Hualiangting in the Taihu County). The occurrences of gneiss cleavage, flat and ramp, and extensional lineation are marked.

TABLE 1: Summary of mineral ^{40}Ar - ^{39}Ar data in the main shear zone of eastern Dabie Mountains.

Shear zone	Sample locations	Mineral	Weighted mean plateau age (Ma)
XT-MZT SZ	Qingshan town	Biotite	124.17 ± 0.25
	Zhangchong village	Biotite	126.91 ± 0.30
SH-WH SZ	Shuihou village	Biotite	190.59 ± 0.42
TH-MM SZ	Luoxi village	Hornblende	197.41 ± 0.46
	Luoxi village	Biotite	189.42 ± 0.29
SS-QSH SZ	Qingshuihe village	Biotite	124.87 ± 0.21
	Chenhan village	White mica	194.01 ± 0.36
	Qingshuihe village	Biotite	127.96 ± 0.30

of Late Jurassic volcanoclastic rocks and tuff that are up to several meters in size (Figure 2).

Large-scale, harmonic, recumbent folds also occur in the Late Jurassic volcanoclastic rocks and the Late Proterozoic mica schist. In the south extensional detachment system, the Hong'an Group (Pt) and Yanshanian granite (J_3 — K_1) experienced extensional shear deformation at the same time. These features suggest that the extensional detachment of

both the south and north detachment systems took place after the Late Jurassic.

The age group ~ 200 Ma is coincide with the U-Pb ages, Sm-Nd ages, and Rb-Sr ages of UHP rocks [22–26], which reflect protracted cooling or partial resetting by Jurassic or Cretaceous magmatism.

In addition, massive granitic intrusions and numerous ultrabasic plutons were emplaced in the NDMCB during

TABLE 2: The comparison of deformation ages from southern Dabie belt of China.

Age groups	Data of XT-MZT SZ [21]		Our data from other shear zones
~200 Ma			229.8 ± 70.97
			219.52 ± 1.57
150~190 Ma			197.41 ± 0.46
			194.01 ± 0.36
	156.7 ± 1.5		190.59 ± 0.42
			189.42 ± 0.29
			156.5 ± 7.15
145~110 Ma	136.5 ± 1.3	132.0 ± 0.8	
	129.8 ± 0.6	141.9 ± 1.2	
	129.2 ± 1.0	127.1 ± 0.7	127.96 ± 0.30
	133.1 ± 0.9	128.3 ± 0.9	124.87 ± 0.21
	134.1 ± 0.9	127.0 ± 0.8	124.56 ± 2.4
	136.8 ± 1.1	122.5 ± 0.6	
	130.7 ± 1.0	120.7 ± 0.7	

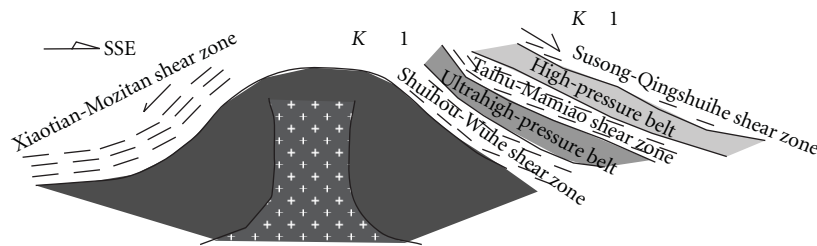


FIGURE 5: Extensional detachment model for the late Mesozoic in the Dabie Mountains.

the extensional phase at about 120 Ma. The Ar-Ar and Rb-Sr isotopic analyses of rocks in the Dabie group also record this time at about 110–145 Ma (Table 2). All these lines of evidence suggest that they were closely related to extensional detachment. The Cretaceous lacustrine, fluvial, and piedmont facies (several kilometers thick in the Hefei basin) also reflect a regional extensional setting and intense mountain-basin movement. Therefore, voluminous magmatic emplacement and lithosphere delamination during the early Cretaceous induced the rapid uprising of the North Dabie central area, with extensional detachment on both sides. The intense denudation resulted in the thick sediment deposits in the Hefei basin. The high- and ultrahigh-pressure eclogites were probably emplaced during this event (Figure 5). Large-scale extension in the Dabie Mountains during the late Mesozoic is representative of the tectonic regime inversion that affects the eastern North China Block.

Lastly, the deposition of platinum group elements (PGEs) in ultramafic and/or mafic rocks with two ages, ca. 120 Ma and ca. 230 Ma, in the North Dabie complex core suggests that their source region was the upper mantle. The PGE data indicate that the late Mesozoic upper mantle (ca. 120 Ma) enriched in PGE, whereas depleted PGE before 120 Ma. The late Mesozoic upper mantle with PGE enrichment in the Dabie region is contaminated with about 8% Earth core materials, as the PGE contents in the Earth's core are much higher than in the upper mantle [27, 28]. If this is correct,

then the PGE mantle enrichment must be related to the late Mesozoic extensional detachment in the Dabie area.

6. Conclusions

(1) The main shear zones in the Dabie area are characterized by extensional detachment during late Mesozoic era. The XT-MZT SZ is detached to the NNE, the SH-WH SZ, and the TH-MM SZ are displaced to the SSE, while the SS-QSH SZ is displaced to the SW.

(2) The shear length of the XT-MZT SZ is more than 56 km and that of the SS-QSH SZ is more than 12 km. The Flinn parameter of the Shuihou-Wuhe shear zone is much smaller than 1 (i.e., 0.01–0.1), which suggests that the shear zone was flattened when it formed. The Flinn parameter of the Taihu-Mamiao shear zone is about 1 (i.e., 1.1), whereas the Susong-Qingshuihe shear zone is much more than 1 (i.e., 7.6), which suggests that they were formed during extension. From north to south in the south extensional tectonic system, these Flinn parameter values display the transition from pure shear to simple shear, possibly reflecting the active intrusion of magma during the extensional detachment.

(3) Two deformation ages, ~190 Ma and ~124 Ma based on mineral ^{40}Ar - ^{39}Ar data, are concluded from the main shear zones in the Dabie area. The early age (~190 Ma) could be related to the UHP cooling and reversion during orogenesis, whereas the later one (~124 Ma) could represent

the extensional detachment age after the formation of the orogeny.

(4) The strain analysis, chronology, and the mantle enrichment in platinum group elements suggests that magmatic intrusion in the north Dabie complex core is the main cause for extensional detachment structures during the late Mesozoic.

Acknowledgments

The authors thank Professors Jiliang Li, Wenjiao Xiao, Mingguo Zhai, and Zhihong Wang from the Institute of Geology and Geophysics, Chinese Academy of Sciences, and Tianshan Gao from the University of Science and Technology of China for the excellent field and inner laboratory discussions; they also thank Dr. Paul Duuring from The University of British Columbia, Canada for much help. This work is supported by the National Natural Science Foundation of China (Grant no. 41030422), the Major Project of Chinese Academy of Sciences (Grants KZCX1-07), and the Key project of the National Natural Science Foundation of China (Grant no. 40234050).

References

- [1] S. Li, T. M. Kusky, X. Liu et al., "Two-stage collision-related extrusion of the western Dabie HP-UHP metamorphic terranes, central China: evidence from quartz c-axis fabrics and structures," *Gondwana Research*, vol. 16, no. 2, pp. 294–309, 2009.
- [2] S. Z. Li, X. Liu, Y. H. Suo et al., "Triassic folding and thrusting in the Eastern Block of the North China Craton and the Dabie-Sulu orogen and its geodynamics," *Acta Petrologica Sinica*, vol. 25, pp. 2031–2049, 2009.
- [3] S. Z. Li, T. M. Kusky, G. Zhao et al., "Mesozoic tectonics in the Eastern Block of the North China Craton: implications for subduction of the Pacific plate beneath the Eurasian plate," *Geological Society Special Publication*, no. 280, pp. 171–188, 2007.
- [4] S. Suo, Z. Zhong, and Z. You, "Extensional deformation of post ultrahigh-pressure metamorphism and exhumation process of ultrahigh-pressure metamorphic rocks in the Dabie massif, China," *Science in China, Series D*, vol. 43, no. 3, pp. 225–236, 2000.
- [5] E. Eide, "A model for the tectonic history of HP and UHPM regions in east central China," in *Ultrahigh-Pressure Metamorphism*, R. G. Coleman and X. M. Wang, Eds., pp. 391–426, Cambridge Press, 1995.
- [6] X. M. Wang, R. Y. Zhang, and J. G. Liou, "UHPM terrane in east central China," in *Ultrahigh Pressure Metamorphism*, R. G. Coleman and X. M. Wang, Eds., pp. 356–390, Cambridge University Press, Cambridge, UK, 1995.
- [7] B. L. Cong, *Ultrahigh-Pressure Metamorphic Rocks in the Dabieshan-Sulu Region of China*, Kluwer Academic Publishers, Science Press Beijing, 1996.
- [8] B. R. Hacker, X. Wang, E. A. Eide, and L. Ratschbacher, "The qinling-dabie ultrahigh-pressure collisional orogen," in *The Tectonic Evolution of Asia*, A. Yin and T. M. Harrison, Eds., pp. 345–370, Cambridge University Press, Cambridge, UK, 1996.
- [9] J. G. Liou, R. Y. Zhang, X. M. Wang, E. A. Eide, W. G. Ernst, and S. Maruyama, "Metamorphism and tectonics of highpressure and ultrahigh-pressure belts in the Dabie-Su-Lu region, China," in *The Tectonic Evolution of Asia*, A. Yin and T. M. Harrison, Eds., pp. 300–344, Cambridge University Press, Cambridge, UK, 1996.
- [10] B. M. Jahn, F. Wu, C. H. Lo, and C. H. Tsai, "Crust-mantle interaction induced by deep subduction of the continental crust: geochemical and Sr-Nd isotopic evidence from post-collisional mafic-ultramafic intrusions of the northern Dabie complex, central China," *Chemical Geology*, vol. 157, no. 1–2, pp. 119–146, 1999.
- [11] S. Li, T. M. Kusky, G. Zhao et al., "Two-stage Triassic exhumation of HP-UHP terranes in the western Dabie orogen of China: constraints from structural geology," *Tectonophysics*, vol. 490, no. 3–4, pp. 267–293, 2010.
- [12] S. Z. Li, G. C. Zhao, G. W. Zhang et al., "Not all folds and thrusts in the Yangtze foreland thrust belt are related to the Dabie Orogen: insights from Mesozoic deformation south of the Yangtze River," *Geological Journal*, vol. 45, no. 5–6, pp. 650–663, 2010.
- [13] S. Li, T. M. Kusky, G. Zhao et al., "Thermochronological constraints on two-stage extrusion of HP/UHP terranes in the Dabie-Sulu orogen, east-central China," *Tectonophysics*, vol. 504, no. 1–4, pp. 25–42, 2011.
- [14] S. Suo, L. Sang, Y. Han et al., *The Petrology and Tectonics in Dabie Precambrian Metamorphic Terranes, Central China*, China University of Geosciences Press, Wuhan, China, 1993.
- [15] H. L. Song, "Early extensional tectonics in Qinglin-Dabie orogen," in *Extensional Tectonics Research*, X. L. Qian, Ed., pp. 12–21, Geology Press, Beijing, China, 1994.
- [16] Q. Zhang, W. P. Ma, J. W. Jin et al., "Geochemistry and tectonic significance of post-tectonic gabbro from Wangmuguan of Xinxian county, Henan province," *Chinese Journal of Geochemistry*, vol. 24, 4, pp. 341–350, 1995.
- [17] W. Jin, H. Song, and W. Ma, "Extensional tectonics in tongbai-west Dabie mountain," *Scientia Geologica Sinica*, vol. 32, no. 2, pp. 156–164, 1997.
- [18] G. C. Wang and W. R. Yang, "Uplift evolution during Mesozoic-Cenozoic of the Dabie orogenic belt: evidence from the tectono-chronology," *Earth Science—Journal of China University of Geosciences*, vol. 23, no. 5, pp. 461–467, 1998.
- [19] J. Li, *The Dabie Shan main shear zone of Late Mesozoic and extension structure [M.S. thesis]*, Institute of Geology and Geophysics, Chinese Academy of Sciences, 2003.
- [20] Z. Q. Zhong, S. Suo, and Z. D. You, "Extensional tectonic framework of post high and ultrahigh pressure metamorphism in Dabieshan, China," *Earth Science—Journal of China University of Geosciences*, vol. 23, no. 3, pp. 225–229, 1998.
- [21] Y. S. Wang, B. W. Xiang, G. Zhu et al., "⁴⁰Ar-³⁹Ar geochronology records for post-orogenic extension of the Xiaotian-Mozitan fault," *Geochimica*, vol. 38, pp. 458–471, 2009.
- [22] L. E. Webb, L. Ratschbacher, B. R. Hacker et al., "Kinematics of exhumation of high-and ultrahigh-pressure rocks in the Hong'an and Tongbai Shan of the Qinling-Dabie collisional orogen, eastern China," *GSA Memoirs*, vol. 194, pp. 231–245, 2001.
- [23] J. C. Grimmer, L. Ratschbacher, M. McWilliams et al., "When did the ultrahigh-pressure rocks reach the surface? A 207Pb/206Pb zircon, ⁴⁰Ar-³⁹Ar white mica, Si-in-white mica, single-grain provenance study of Dabie Shan synorogenic foreland sediments," *Chemical Geology*, vol. 197, no. 1–4, pp. 87–110, 2003.

- [24] B. R. Hacker, S. R. Wallis, L. Ratschbacher, M. Grove, and G. Gehrels, "High-temperature geochronology constraints on the tectonic history and architecture of the ultrahigh-pressure Dabie-Sulu orogen," *Tectonics*, vol. 25, no. 5, Article ID TC5006, 2006.
- [25] B. R. Hacker, S. R. Wallis, M. O. McWilliams, and P. B. Gans, " ^{40}Ar - ^{39}Ar constraints on the tectonic history and architecture of the ultrahigh-pressure Sulu orogen," *Journal of Metamorphic Geology*, vol. 27, no. 9, pp. 827–844, 2009.
- [26] B. R. Hacker, L. Ratschbacher, and J. G. Liou, "Subduction, collision and exhumation in the ultrahigh-pressure Qinling-Dabie orogen," *Geological Society Special Publication*, no. 226, pp. 157–175, 2004.
- [27] Q. Liu, *Study on the distribution of Platinum group elements in Dabie (ultra-) mafic rocks and Fuxin volcanic rocks [Ph.D. thesis]*, Graduate University of the Chinese Academy of Sciences, 2005.
- [28] Q. Liu, Q. L. Hou, X. H. Zhou, and L. W. Xie, "The distribution of platinum-group elements in gabbros from Zhujiapu, Dabie orogen," *Acta Petrologica Sinica*, vol. 21, no. 1, pp. 227–239, 2005.

Research Article

Structural Characteristics and Physical Properties of Tectonically Deformed Coals

Yiwen Ju, Zhifeng Yan, Xiaoshi Li, Quanlin Hou, Wenjing Zhang, Lizhi Fang, Liye Yu, and Mingming Wei

Key Laboratory of Computational Geodynamics, College of Earth Science, Graduate University of Chinese Academy of Sciences, Beijing 100049, China

Correspondence should be addressed to Yiwen Ju, juyw03@163.com

Received 13 February 2012; Accepted 28 March 2012

Academic Editor: Yu-Dong Wu

Copyright © 2012 Yiwen Ju et al. This is an open access article distributed under the Creative Commons Attribution License, which permits unrestricted use, distribution, and reproduction in any medium, provided the original work is properly cited.

Different mechanisms of deformation could make different influence on inner structure and physical properties of tectonically deformed coal (TDC) reservoirs. This paper discusses the relationship between macromolecular structure and physical properties of the Huaibei-Huainan coal mine areas in southern North China. The macromolecular structure and pore characteristics are systematically investigated by using techniques such as X-ray diffraction (XRD), high-resolution transmission electron microscopy (HRTEM), electron paramagnetic resonance (EPR), nuclear magnetic resonance (NMR), and low-temperature nitrogen adsorption method. The results suggest that under the directional stress, basic structural units (BSU) arrangement is closer, and the orientation becomes stronger from brittle deformed coal to ductile deformed coal. Structural deformation directly influences the macromolecular structure of coal, which results in changes of pore structure. The nanoscale pores of the cataclastic coal structure caused by the brittle deformation are mainly mesopores, and the proportion of mesopores volume in ductile deformed coal diminishes rapidly. So the exploration and development potential of coalbed gas are good in reservoirs such as schistose structure coal, mortar structure coal and cataclastic structure coal. It also holds promise for a certain degree of brittle deformation and wrinkle structure coal of low ductile deformation or later superimposed by brittle deformation.

1. Introduction

Tectonically deformed coal (TDC) is a kind of coal in which, under mono- or multiphase tectonic stress fields, its primary texture and structure is significantly destroyed. Tectonic deformation could influence coal macromolecular or deform structure and enhance coalification to a certain degree [1–6]. Through structural shearing, graphitization can be facilitated [7, 8]. In fact, tectonic deformation can not only further alter coal's molecular structure at different degrees but also change the physical properties of reservoirs (such as porosity and permeability). Based on measurement of mercury intrusion, researchers compared micropore features of TDCs collected from different coalfields [9–12]. These experiments have indicated that the pore structure of TDCs showed greater medium pores and mesopore volumes than normal undeformed coals, but there was rare

difference in micropores between primary structure coals and TDCs. This indicated that structural deformation did not obviously influence micropore structure (less than 10 nm in diameter). Meanwhile, the nanoscale pore structure of TDCs is the main adsorption space for coalbed gas, and the macromolecular structure is an important factor for restricting the adsorption capacity in coal. Therefore, the problem of macromolecular structure and nanoscale pores in TDCs are worthy research topics [13–15], and the behavior of gas adsorption/desorption and permeability of micropore in coal have strong relationship with the occurrence and distribution of coalbed gas [16–24].

The deformation of coals causes changes of structure and chemical composition of coal because of differences in the property, mode, and intensity of stress and the deformation environment. Moreover, the physical properties of TDCs also vary significantly [5, 22]. Therefore, comprehensive studies

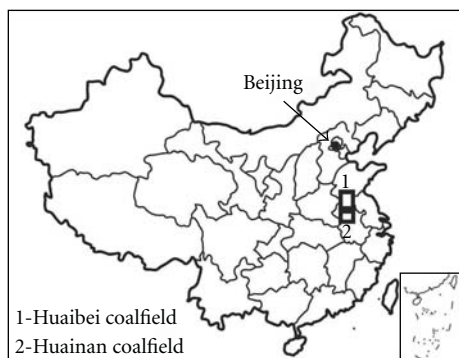


FIGURE 1: Huaibei-Huainan coalfield in the southern North China.

on stress action, strain environment, physical and chemical structures of TDCs, and physical properties of deformed coals will provide the theoretical basis for exploration and evaluation of coalbed gas resources and aid in understanding the prevention and control of coal and gas outbursts. These studies will also provide insight into gas emission, which is studied in the coalbed gas research field. In this study, the author would like to reveal the structures and the physical properties of tectonically deformed and metamorphic coals.

2. Geologic Background and Coal Structure in Huainan and Huaibei Mine Areas

The Paleozoic coal-bearing basins, especially in eastern China, underwent complexly multiphase structural evolution by compressing, shearing, and extending. This resulted in structural reworking of the primary structure of coal at different degrees, forming the different types of TDCs. The existing data from China have shown that tectonic deformation is an important factor in restricting the exploration and development of coalbed gas; it is also a direct cause of gas outbursts of coal mines.

In the Huaibei and Huainan coalfields, situated in the southern North China (Figure 1), coal measurement revealed Permo-Carboniferous systems which were formed in the Paleozoic and structurally influenced in the Mesozoic. The main coal-bearing areas were found in fault depression basins, especially in the syncline. The upwelling areas between depression basins have undergone destruction and denudation at different degrees. The different types of faults and folds in the distribution area of coal have given rise to obvious breakages and deformations in the coal seams, leading to changes of the coal structure. At the end of this process, different types of TDCs, such as cataclastic structure coal, mortar structure coal, schistose structure coal, mealy structure coal, and even wrinkle structure coal and mylonitic structure coal, were formed [5].

3. The Sample and Methods

The research areas possess six mine wells of the Suzhou mine area and the Linhuan mine area in the Huaibei coal mine region. Three of them are contained by the Xinji mine region,

Zhangji mine region and Panji mine region, which represent different tectonic units. The sample sets were collected from the Huaibei and Huainan coalfields (Figure 1). These samples belong to different kinds of TDCs, suffering from multiphase tectonic deformation and magmatic events.

In this study, two significant aspects were taken into account in the selection of the samples. The first aspect is the evolutionary degree of coal, namely, reflectance ($R_{o,max}$) of samples ranging from 0.76% to 3.59%, including low, middle, and high metamorphic coal. The second aspect is the characteristics of TDCs formed by different mechanisms. The samples of brittle deformation series, ductile deformation series, and brittle-ductile series were selected separately.

Because of different sedimentation and tectonic environments, coal often contains different maceral compositions and various kinds of mineral components, which greatly affect the results of coal structural testing. Therefore, coal samples must be prepared before testing and analysis to extract vitrinite components and take off inorganic (mineral) components.

On the basis of in situ investigation, detailed microstructural observations of these samples using optical and scanning electron microscopy (SEM) were described elsewhere. $R_{o,max}$ measurements were carried out on polished sections under halogen lamp and oil immersion conditions by using a Leitz Orthoplan/MPV-SP microscope photometer.

Using X-ray diffraction (XRD), high-resolution transmission electron microscopy (HRTEM), electron paramagnetic resonance (EPR), and nuclear magnetic resonance (NMR), systematic research has been conducted on the characteristics of macromolecular structure and chemical structure of different kinds of TDCs.

The instrument of X-ray diffraction testing is a D/Max-IIIB X-ray diffractometer which is made by Rigaku Inc. Of Japan; the instrument of the HRTEM is a JEM-2010 HRTEM made in Japan by JEOL Inc.; the instrument of EPR testing is the E-109 electron paramagnetic resonance spectrometer made by Varian Inc. of America; the instrument of NMR testing is the Infinity 400 nuclear magnetic resonance spectrometer made by Varian Inc. of America. The experimental conditions of different instruments are discussed in detail by Ju et al. [5, 6].

The pore characteristics of TDCs have been determined by use of the low-temperature nitrogen adsorption method and scan electron microscopy (SEM). The permeability has been analyzed through experiments of in-lab permeability measurements of large diameter, in-site samples from TDCs.

The instrument used for low-temperature liquid nitrogen adsorption experiments is the ASAP-2010 made in America by Micromeritics Instrument Inc. This instrument is used for measuring the micropore specific surface area and distribution of pore diameter. In the gas-water phase permeability experiment, the whole core flow system, made by Terra Tek company, was utilized as the main instrument. This system was primarily used to simulate crustal pressure and rock permeability under natural oil reservoir pressure. The highest simulated confined pressure and fluid pressure were 70 MPa and 65 MPa, respectively. The measurement system was composed of the pressure system, the constant

temperature system, the control system, the core clumper and separator equipment.

4. Results

4.1. Forming Environments and Structure-Genetic

Classification of Tectonically Deformed Coals

4.1.1. Forming Environments of Tectonically Deformed Coals.

The Huaibei and Huainan coal mine areas underwent complexly multiphase structural and magma-thermal activities. Thus, under different metamorphic and deformed environments, various kinds of TDCs were formed in these mine areas [11, 20–22]. By combining deformational characteristics of macrocosms and microcosms of different kinds of TDCs, we recognized three kinds of metamorphic and deformed environments where TDCs were formed in the Huaibei and Huainan coal mine areas. The first type is the metamorphic and deformed environment of the low-rank coals ($R_{o,max}$ lower than 1.30%), which is based on the plutonic metamorphism; the second type is the metamorphic and deformed environments of the middle-rank coals ($R_{o,max}$ from 1.30 to 2.00%), which resulted from plutonic metamorphism and a superimposed magmatic thermal and dynamic metamorphism. The third type of metamorphic and deformed environment of the high-rank coals ($R_{o,max}$ greater than 2.00%) resulted from plutonic metamorphism and a superimposed, stronger magmatic thermal and dynamic metamorphism.

4.1.2. Structural-Genetic Classification of Tectonically Deformed Coals.

Based on the results of the in situ measurement of coal mines and microstructural observation, a structural-genetic classification system has been proposed that can be applied not only to the exploitation of coalbed gas but also to the prevention and control of coal and gas outbursts. In terms of the scale of hand specimens or samples of coal core from boreholes, TDCs formed by different deformational mechanisms have been divided into three deformation series and ten classes (Table 1). The brittle deformation series includes cataclastic structure coal, mortar structure coal, granulitic structure coal, mealy structure coal, schistose structure coal, and thin-layer structure coal. The ductile deformation series includes wrinkle structure coal, mylonitic structure coal, and ductile structure coal. The brittle-ductile series includes scaly structure coal. Compared to the previous classifications [17, 19, 25, 26] of brittle deformational coals, schistose structure coal and thin-layer structure coal have been added into this series. This is because these coals are quite different from the cataclastic structure coals in structural and physical properties. Similarly, ductile structure coal has been divided into the ductile deformation series. For ductile deformational coals, wrinkle structure coal was considered to be formed in a compressing and shearing process, mylonitic structure coal is formed by strong ductile shearing, while ductile structure coal is formed during the creeping process of higher temperatures. Moreover, a brittle-ductile transition

type of coal has been proposed; this may include scaly structure coal.

4.2. Structural Evolution and Deformational Mechanisms of Tectonically Deformed Coals. Temperature is the main factor that causes the change of coal chemical structure; it also facilitates metamorphism and improves coal rank [27, 28]. The temperature and stress together lead to change in coal macromolecular structure and its chemical components [4, 5]. Under thermal and stress conditions, how does the structural evolution of a deformational mechanism, over different kinds of TDCs, take place?

Thermal action and directional stress are the important factors in changing coal macromolecular structures and destroying bond forces. The vitrinite reflectance anisotropy (VRA) characteristic of deformed coals was well known and was interpreted from the ordering degree promoted by the stress [5, 29, 30]. Meanwhile, $R_{o,max}$ optical characteristics are shown in different kinds of TDCs (Table 2). Because of thermal values and stress, the value of $R_{o,max}$, the size of stacking (L_c) and extension (L_a) of basic structural units (BSU), carbon aromaticity (f_a) and radical density (N_g) increase. Accordingly, layers of the microcrystal (N) and the number of benzene rings of each layer also increase, whereas the spacing among monolayers of aromatics (d_{002}), L_a/L_c and the aliphatic spacing (d_r) continually decrease. In addition, the values of L_a/L_c (formed under the condition of stress) are obviously lower than those formed under conditions of thermal action. Therefore, the whole coalification process is the course of condensation of aromatic rings in which pores change continually [31]. Furthermore, when the structural deformation enhances, the faint orientation and bad ordering domain of schistose structure coal formed by brittle deformation extend to a local orientation, a strong orientation, and an integer orientation orderliness (Table 2 and Figure 2). It is obvious that stress has affected the chemical structure of coal. However, in the past, researchers had not convinced that the effect of tectonic stress is not the same for different kinds of ductile deformation coals. The macromolecular structure of wrinkle structure coal shows smaller changes, while the macromolecular structures of mylonitic structure coal and ductile structure coal change significantly.

4.3. Physical Properties of Tectonically Deformed Coals and Their Relation with Structure

4.3.1. Porosity of Tectonically Deformed Coals. Coal contains a large numbers of pores [10, 13, 15], even more in TDCs. The nanoscale pore diameters of different kinds of TDCs have been grouped into four types: mesopores (15 ~ 100 nm), micropores (5 ~ 15 nm), submicropores (2.5 ~ 5 nm), and ultramicropores (<2.5 nm) [22]. This was done according to the average pore diameter of the natural distribution at three points: 15 nm, 5 nm, and 2.5 nm, and through combining the adsorbed gas and diffused features.

In this study, the parameters of pore structure were tested and the experimental results were shown in Table 3.

TABLE 1: The structural-genetic classification of TDCs.

Deformation series	Type of tectonically deformed coals	Texture and structure	Structural fracture and wrinkle	Breaking degree	Micro characteristics	Deformational mechanism and environment
Brittle deformation series	Cataclastic structure coal	Band texture could be seen; layer structure was preserved	Multidirectional fracture cuts; no obvious displacement	More hardness; crumbing is difficult	Tensile fracture, shear fracture, and compressional fracture	Multi directional compression and extension; extension was the predominant role
	Mortar structure coal	Little band texture was seen; lentoid structure was formed	Multidirectional fracture cuts; obvious displacement in the mortar	Broken into detritus from 1 to 5 cm; angular shape		
	Granulitic structure coal	Primary structure not present; disorder of layers	Multi directional cross fracture; particles were rotated	Broken into detritus, 1 cm		
	Mealy structure coal	Primary structure not present; powdered particles formed	No obvious directions for the particles	Be pinched into powered particles		Strong compressional fracture zone or scaly structure coal be reconstructed later
	Schistose structure coal	Band texture could be seen; layer structure was preserved	Single directional fracture; little displacement on the surface	Broken into detritus from 1 to 5 cm, shard shape		Single directional compression and extension or shearing strain environment
	Thin-layer structure coal	Little band texture was seen; layer structure was not obvious	Single directional fracture; obvious displacement on the surface	Broken into detritus, 1 cm		
Brittle-ductile series	Scaly structure coal	Primary structure not present; scaly structure was formed	Multi directional cross-fracture; coal was cut and wrinkled; the particles could be rotated	Broken into detritus, 0.5 cm; shard shape	Shear fracture, cleavages	Strong shearing or cleaving strain environment
Ductile deformation series	Wrinkle structure coal	Primary structure not present; wrinkle structure was formed	Coal was wrinkled	Broken into detritus, 0.5 cm, shard shape	Wrinkle, foliated coal, S-C structure, eyed structure, optical anisotropy structure and wavy extinction	Strong shearing or long and low stress deformation
	Mylonitic structure coal	Primary structure not present; mylonitic structure was formed	The particles had directional arrangement; flow structure was formed	Was pinched into powered particles		
	Ductile structure coal	Primary structure not present; lump and lentoid structures were formed	No obvious physical deformation	More hardness; crumbing was difficult		Long and low stress creep; ductile flow at high temperatures

Research was performed on the nanoscale pore structure in metamorphic-deformed environment of low-rank coal and the different deformational series of structural coal. Our results have demonstrated that the volume of mesopores reduces rapidly while the volume of micropores and pores whose diameters are lower than micropores increase in the metamorphic deformed environment of low-rank coal. Also, submicropores and ultramicropores can be found, the specific surface area of mesopores reduces greatly while and

submicropores increase rapidly. The change of pore parameters in nonhomogeneous coal structure is similar to the weak brittle deformation coal. For different types of tectonic coals formed in metamorphic-deformed environments of middle- and high-rank coal, pore parameter change is basically consistent with the metamorphic-deformed environment of low-rank coal. But, there are differences in the changes among different kinds of tectonic coals. To sum up, the conditions of temperature and confining pressure can play

TABLE 2: The characteristics of structural parameter of tectonically deformed coals.

Type of tectonically deformed coals	Coal sample's number	$R_{0,max}$ $R_{0,max}$	$R_{0,max}$ $R_{0,max}$	$R_{0,bi}$ $R_{0,bi}$	NMR f_a^* (%)	EPR $N_g \times 10^{18}$ spins/g	d_{002}	L_c (nm)	L_a (nm)	d_r	N	n	L_a/L_c	HRTEM lattice images
Cataclastic structure coal	QN03	1.23	0.33			75.0365	0.3667	1.3755	1.8575	0.568	3.75	51.9	1.35	
Mortar structure coal	TY02	1.51	0.32			44.8972	0.3662	1.4903	1.8546	0.535	4.07	51.8	1.24	
Mortar structure coal	XY02	1.99	0.44			45.5163	0.3699	1.2997	1.8444	0.561	3.51	51.2	1.42	
Granulitic structure coal	XY01	1.26	0.31			33.8709	0.3665	1.4379	1.9163	0.540	3.92	55.3	1.33	
Mealy structure coal	ZXZ06	1.33	0.28			65.7937	0.3561	1.5138	2.0003	0.528	4.25	60.3	1.32	Dispersedly isolated points, with weak orientation
Schistose structure coal	ZJ01	0.95	0.23		0.791	52.4347	0.3828	0.9011	1.7254	0.613	2.35	44.8	1.91	
Thin-layer structure coal	XJ03	1.01	0.23			44.1508	0.3716	0.928	1.8524	0.592	2.50	51.7	2.00	
Scaly structure coal	LL01	1.45	0.43		0.795	64.0869	0.3659	1.3645	1.8997	0.535	3.73	54.3	1.39	
Wrinkle structure coal	BJ05	1.08	0.24		0.778	36.1217	0.3716	1.0827	1.7684	0.57	2.91	47.1	1.63	Gracile worm shape, with local orientation
Mylonitic structure coal	QN09	0.96	0.27			46.3902	0.3665	1.3782	1.8187	0.536	3.76	49.8	1.32	
Mylonitic structure coal	ZXZ04	1.82	0.41		0.809	136.9129	0.3684	1.4733	1.9754	0.558	4.00	53.0	1.27	
Ductile structure coal	XY06	2.21	0.53			77.4869	0.3601	1.6195	2.1802	0.528	4.50	71.6	1.35	
Schistose structure coal	LH05	1.75	0.38		0.802	61.2011	0.3617	1.5694	2.0895	0.538	4.34	65.8	1.33	
Schistose structure coal	TT10	1.94	0.40			41.9478	0.3619	1.566	1.9791	0.534	4.33	59	1.26	
Cataclastic structure coal	HZ01	2.97	0.58		0.873	107.7825	0.3537	2.0291	2.4107	0.485	5.73	87.5	1.19	Striations patch group, with strong orientation
Mylonitic structure coal	HZ07	3.59	0.71		0.925	84.3871	0.3497	2.5172	2.4489	0.467	7.20	90.3	0.97	

* f_a : carbon aromaticity; N : layers of the microcrystal; n : numbers of benzene rings; L_c : size of stacking of basic structural units; L_a : extension of basic structural units; d_{002} : the spacing among monolayers of aromatics; d_r : the aliphatic spacing; N_g : radical density. Broad horizontal lines in the table distinguish TDCs formed in different metamorphic and deformational environments; narrow horizontal lines distinguish tectonically deformed coals of different deformational series. Parts of Table 3 are the same.

TABLE 3: The characteristics of pore structural parameter of TDCs.

Type of tectonically deformed coals	Coal sample's number	V_t (cm ³ /g)	Pore volume			V_7/V_t	V_6/V_t	V_5/V_t	Pore specific surface				S_7/S_t		S_6/S_t	S_5/S_t		S_4/S_t		S_3/S_t		S_2/S_t		S_1/S_t		S_0/S_t		S_{total}/S_t		N_2 adsorption volume (cm ³ /g)	
			V_4/V_t	V_3/V_t	V_2/V_t				S_4/S_t	S_3/S_t	S_2/S_t	S_1/S_t	S_0/S_t																		
Cataclastic structure coal	QN03	0.00046	95.652	4.348					83.33	16.667																					0.3105
Mortar structure coal	TY02	0.00079	78.481	11.392					30.357	21.429																					0.9606
Mortar structure coal	XY02	0.00055	92.727	5.455					59.722	16.667																					0.3566
Granulitic structure coal	XY01	0.00229	81.223	13.100					43.789	28.31																					1.9401
Schistose structure coal	ZJ01	0.00066	86.364	7.576					46.341	15.447																					3.762
Thin-layer structure coal	XJ03	0.00491	70.061	18.534					25.853	28.467																					3.7620
Scaly structure coal	LL01	0.00215	82.791	10.698					41.164	22.845																					1.9104
Wrinkle structure coal	BJ05	0.00407	76.167	17.700					37.401	33.929																					3.1771
Mylonitic structure coal	QN09	0.00930	67.229	19.277					24.772	28.376																					6.1405
Mylonitic structure coal	ZXZ04	0.01871	74.025	19.401					33.880	34.972																					12.9174
Ductile structure coal	XY06	0.00078	85.900	5.128					35.443	11.392																					0.5320
Schistose structure coal	LH05	0.00093	94.624	4.301					72.277	12.871																					0.6216
Schistose structure coal	TT10	0.00090	96.667	3.333					85.185	13.580																					0.5834
Cataclastic structure coal	HZ01	0.00049	81.663	8.163					43.810	10.476																					0.4836
Mylonitic structure coal	HZ07	0.00882	28.458	14.286					5.027	10.008																					6.9903

V_4 : 15 ~ 100 nm; V_5 : 5 ~ 15 nm; V_6 : 2.5 ~ 5 nm; V_7 : <2.5 nm; V_t : Total pore volume; S_4 : 15 ~ 100 nm; S_5 : 5 ~ 15 nm; S_6 : 2.5 ~ 5 nm; S_7 : <2.5 nm; S_t : Total specific surface area.

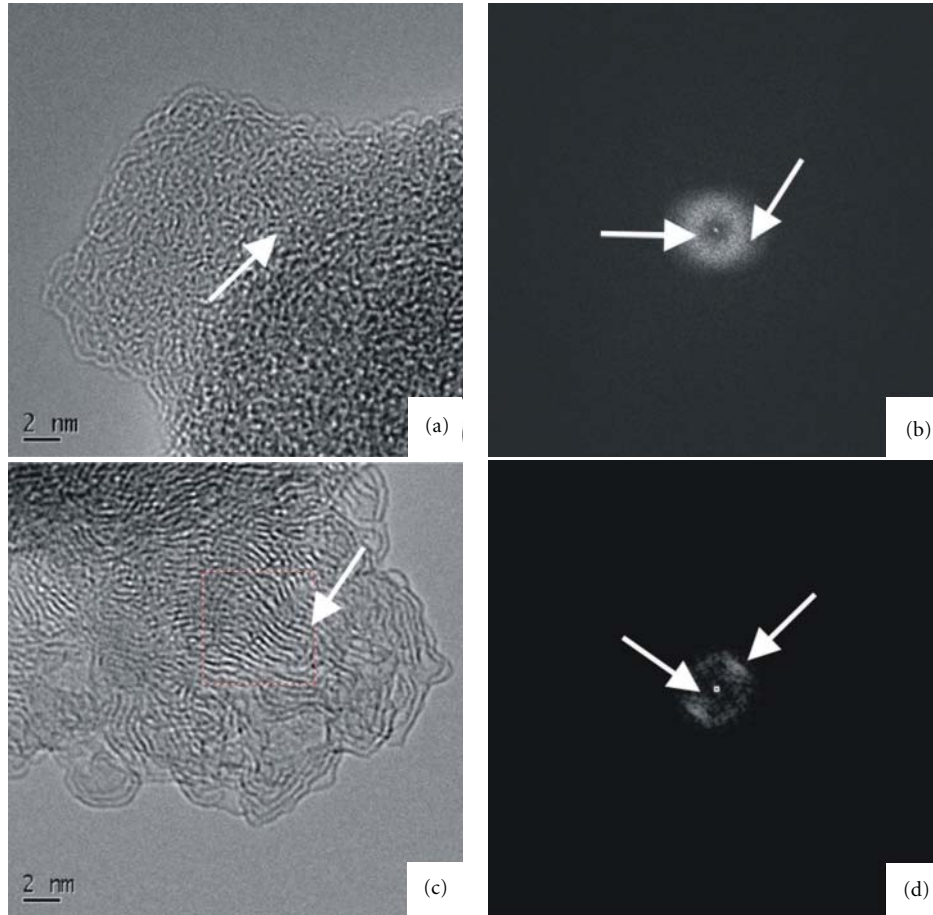


FIGURE 2: HRTEM images of TDCs. (a) Sample ZJ01 of schistose structure coal, in the lattice image; BSU is dispersive and isolated, its diameter is smaller, and BSU has weak orientation, Zhangji Coal Mine, Huainan Coalfield; (b) Sample ZJ01 of schistose structure coal, (002) the (inner ring) diffraction ring lightness is stronger, (101) outer ring looms, Zhangji Coal Mine, Huainan Coalfield; (c) Sample HZ07 of mylonitic structure coal, in the image; BSU is striation group shape, its diameter is large, and BSU has stronger orientation, HRTEM, Haizi Coal Mine, Huaibei Coalfield; (d) Sample HZ07 of mylonitic structure coal, (002) diffraction ring lightness is dispersive, (101) can be seen clearly, and symmetry light spot appears, HRTEM, Haizi Coal Mine, Huaibei Coalfield.

an important role in the evolution of nanoscale pore characteristics, but structural stress is the predominant factor influencing the formation of the characteristics of nanoscale pores.

4.3.2. Permeability of Tectonically Deformed Coals. Often, the TDCs are believed to be low-permeability coals without much value for exploitation [32–34]. In fact, this is not always true. The porosity and permeability of TDCs vary according to changes in their tectonic deformation [19, 22, 35]. In this study, the parameters of permeability in different types of TDCs were tested and the experimental results were shown in Table 4. Those samples were drilled in the coal mine samples collected from the Huaibei and Huainan coalfields. The gas-water phase permeability of TDCs is mainly determined by their type and their sample drilling style. It can be seen clearly from Table 4 that the gas-water phase permeability of brittle deformation increases sequentially. The increase begins with cataclastic structure coal and moves to mortar structure coal, then to schistose

structure coal, which is perpendicular to the fracture, and, finally, to the schistose structure coal, which is parallel to the fracture.

On the other hand, the value of gas-water phase permeability of coal in ductile deformation is less than that in brittle deformation. Moreover, the permeability of TDCs in which ductile deformation is superimposed by later brittle deformation has been significantly increased. Thus, TDCs suffering from certain degrees of deformation have a higher permeability than those of primitive structure coals or very weak TDCs [36].

5. Discussion

5.1. Structural Evolution and Deformational Mechanisms of Tectonically Deformed Coals

5.1.1. Main Geological Factors Affecting Deformation and Metamorphism of Coals.

The relationship between coal

TABLE 4: The experiment results of gas-water phase permeability for TDCs.

Deformation series	Type of tectonically deformed coal	Coal sample's number*	Apparent fracture porosity (%)	K_0^{**} of CH_4 ($10^{-3} \mu\text{m}^2$)	K_0 of He ($10^{-3} \mu\text{m}^2$)	K_w ($10^{-3} \mu\text{m}^2$)
Brittle deformation	Cataclastic structure coal	HZ01	4.1	0.162	0.180	0.099
	Cataclastic structure coal	QN03	1.5	0.019	0.020	0.017
	Cataclastic structure coal	TY10	2.4	0.178	0.205	0.075
	Mortar structure coal	TY02	2.6	0.183	0.211	0.087
	Mortar structure coal	XY02	3.1	0.471	0.495	0.138
	Schistose structure coal	ZJ01 (vertical sampling)	2.9	0.534	0.535	0.155
	Schistose structure coal	ZJ01 (lateral sampling)	2.9	1.630	2.120	0.359
Ductile deformation	Wrinkle structure coal	BJ05	2.7	0.362	0.378	0.124
	Ductile structural coal	XY06	2.0	0.089	0.098	0.056

* The direction and degree of fractures affect the drilling coal samples. We made vertical drilling in samples when there is the cross of two sets of fractures (e.g., schistose structure coal, mortar structure coal). And lateral drilling when there is only one set of fracture (Cataclastic structure coal).

** K_0 : absolute permeability; K_w : water phase permeability.

structure and metamorphism has been discussed over a century [37]. It is thought that temperature, pressure, and time are the general geologic factors that control coalification. Pressure factors of coalification include static pressure (confining pressure) and dynamic pressure (tectonic stress). Previous studies focused on the influence of temperature and confining pressure on coal structure. As a result, the existed studies have indicated that temperature is the main factor causing the changes in the chemical structure of coal, facilitating metamorphism and improving coal rank [37, 38]; confining pressure benefits physical coalification but suppresses chemical coalification. Tectonic stress has seldom involved the metamorphism of coals [37, 38]. From BSU testing and the extraction of dissoluble organic molecules of tectonic coals, Cao et al. [4, 39] and Cao et al. [40] concluded that temperature and stress lead to changes in coal macromolecular structure and chemical components. The changes in coal macromolecular structure parameters are mainly caused by compression or shearing. Both brittle and ductile deformation can affect the macromolecular structure of the coal, which leads to dynamic metamorphism and elevation in the coal rank, to a certain degree. The influence of macromolecular structure in ductile deformation coals is stronger than that in brittle deformation coals. The reason is that carbon aromaticity and the degree of ring condensation have been obviously increased in the former. In this research, by using the XRD, HRTEM, EPR, and NMR, L_c , L_a , f_a , and N_g increase, while L_a/L_c , d_{002} , and d_r decrease. The results showed that the cracking and removal of straight and side-chain compounds of organic matter in coal caused reduction in molecular weights and directly changed the chemical composition of macromolecules in coal, especially in low and medium coalification stages. This shows "dynamic hydrocarbon generation". The change of structural parameters promotes the BSU rearrangement, as well as ordering enlargement and orientation growth. The result is an increase of the aromatic condensed ring system. The stress polycondensation is usually represented by VRA increasing. Therefore, structural stress promotes physical coalification and chemical coalification.

5.1.2. The Types of Tectonic Stress Affecting Deformation and Metamorphism of Coals. There has been speculation as to how stress affects the optical properties of coal and whether deformed coal changes chemically when its physical structure changes. Based on the present studies, the influence model of the tectonic stress on the dynamic evolution of organic matter can be concluded as the followings: friction heat view, strain energy view, and mechanochemistry chemical view.

Stone and Cook [41] suggested that anisotropic stress may influent coalification by strain being imparted to vitrinite during coalification. Teichmüller and Teichmüller [42], Bustin [43] and Suchy et al. [44] suggested that local increases in coal rank and local graphitization resulted from frictional heating. Levine and Davis [45] assumed that the applied stress field caused increased bireflectance by the preferred nucleation and growth of favorably oriented lamellae. Based on XRD, TEM, and micro-Raman spectroscopy evaluations, Ju et al. [5, 6] concluded that the coal structure generated under shearing was changed through elongation and contraction of pores between the aromatic lamellae, thus enhancing growth of aromatic stacks. Observation of increased reflectance or local coalification can be classified either by a thermal mechanism [42–44] or mechanical strain mechanism [41].

In the brittle deformational coals, structural influence of different TDCs is not the same. As the deformation becomes stronger, coal macromolecular structures change from a cataclastic structure coal, mortar structure coal, or granulitic structure coal to mealy structure coal. It is similar when going from schistose structure coal to thin-layer structure coal. Under the effect of stress, the structural fractures quickly spread along weak belts of bond forces in coal; the coal body breaks, and the blocks and particles glide, rotate, and displace; friction heat is then produced, which promotes local coal metamorphism. From the observation of XRD, HRTEM and the highest bireflectance in shear zones, stress-chemistry and frictional heating of shearing strain areas might play a more important role in increasing brittle deformation which is because the rate of strain is high enough to destroy bond forces on the stress direction,

generate thermal heat, and locally alter coal structure under stress.

Levine and Davis [45] postulated a mechanical-chemical mechanism in which stress reoriented the lamellae and facilitated growth. Bustin et al. [8] and Ross and Bustin [46], on the other hand, thought strain energy transformation played an significant role in graphitization from coal under the shear stress regime. A previous study of ductile deformation showed that the size of aromatic stacks and reflectance increase in deformed coals [4, 6, 30]. It is obvious that for distinct kinds of ductile deformation coals, the effect of tectonic stress is not the same. There are three main types of changes in macromolecular structures for TDCs: dislocation glide between the aromatic layers of coal cores, shear glide of the aromatic cores, and destruction/recombination of the coal molecular structure bonding energy. The changes of macromolecular structure in ductile deformation become greater than that in brittle deformation. Superimposition of these types of deformations in coal macromolecular structure is, therefore, the basic process of coal structure shearing and also the essential process of strong ductile deformation of coal. These findings are consistent with the hypothesis of aromatic lamellae growing and reorientating proposed by Levine and Davis [45] and the strain energy transformation presented by Bustin et al. [8] and Ross and Bustin [46]. Since deformation was the result of strain effects in coal, the chemical coalification derived from deformation should be attributable to the strain. During deformation of the coal seam, strain might play significant roles which depend upon the strain rate and the geological setting. In strong ductile shearing, reorientation of aromatic lamellae responsible for higher bireflectance or biaxial vitrinite reflectance indicatrices may occur without brittle failure under lower strain rates. In this case, coal would deform ductilely and the aromatic lamellae would become oriented with the new stress regime [4, 5]. A progressive strain may tend to flatten porosity and shorten the distance between lamellae. If the rearrangement of lamellae was slow enough, all of the chemical structural units might conform to the new stress setting with no chemical change. If the coal was pulverized to a fine grain size by ductile shearing, grain flow would parallel the stress direction. During grain flow, strain would be translated to particle surface thus causing thin areas of strain. Changes in the physical and chemical structures of coal might occur on the particle surface, where local changes in coalification might be produced. Strain rearrangement of aromatic lamellae on the particle surface would lead to local coalification [4]. The degree to which strain rearrangement translates to the particle interior may have a profound influence on the gross change in coal structure. Greater strain on the particle surface not only causes reorientation of aromatic lamellae but also may result in some chemical change.

The fact that the highest bireflectance occurs in shear zones, similar to strain area, has been observed from the anthracite specimens deformed at high temperature and pressure [8]. Thus, it may be supposed that strain energy might play a more important role than frictional heating in increasing coal deformation and metamorphism because the

rate of strain is insufficient to generate temperatures high enough to thermally alter coal.

5.2. *Physical Properties of Tectonically Deformed Coals and Their Relation with Structure*

5.2.1. Porosity of Tectonically Deformed Coals and Their Relation with Structure. Coal is one of the few highly porous media found in nature. Porosity, pore diameter distribution, and pore specific surface area are the main physical properties of coals. These physical properties are important in coalbed methane exploitation and evaluation of coal and gas outburst tendency [4, 16–22, 47]. The pore volumes and specific surface areas of coals have been widely studied [9, 13, 15, 48–56]. Under a scanning electron microscope and high-resolution transmission electron microscopy, pore shape, pore diameter, the molecular structure and relationship of these features with thermal deformation mechanisms have been identified and discussed [31, 57–59]. Duber and Rouzaud [31] found that the pore structure change determined the carbon microcosmic structure and the bireflectance of coal. The size and shape of the pores depended on the processes of coalification, temperature, and tectonic stress. Coal was considered to be formed with different size and shape of pores and aromatic clusters around the pore wall. Coalification was considered to be a process of aromatic ring concentration with pores changing size and shape. Studies of pore structure are therefore scientifically significant.

Tectonic deformation can not only alter coal's macromolecular structure to distinct degrees but can also change pore structure. Based on measurements of mercury intrusion, researchers compared micropore features of TDCs collected from different coalfields [9–11]. These experiments showed that TDCs possessed with greater medium pore volume than normal coal. No difference in mesopores and micropores was found, however. This suggested that tectonic deformation did not significantly influence micropore structure (less than 10 nm in diameter). Ju et al. [5, 6] suggested that tectonic deformation can not only change the micropore structure (>10 nm) of coal but also influence coal's nanoscale pore structure (<10 nm), which is the main adsorption space for coalbed methane.

From the results listed in Tables 3 and 4, the parameters of pore structure, such as pore diameter structure, pore volume and specific surface area, are seriously influenced by changes in thermal conditions. In contrast, the structural deformation of coal results from variability in pore porosity. Brittle and ductile deformation might change the structural parameters of coal pores, but the structural parameters of different kinds of TDC pores are distinct. It can be seen that the volume and specific surface area of nanoscale pores (<10 nm) in TDCs are more than those in normal coals. This finding indicates that TDCs have a higher potential of gas accumulating and pooling. On the other hand, Zhang et al. [10] and Ju et al. [23] have showed that the volumes and specific surface areas of macro- and medium pores of TDCs

have a similar variation. The macro- and medium pores of TDCs reveal stronger laminar flow.

Thermal and stress action can facilitate coalification and change the macromolecular structure and nanoscale pore structure of TDCs [28, 39], but manner and degree of changes are different. Under thermal conditions, the meso- and micromolecules can be arranged to recomposition and condensation by means of physical resultant force. The increase of ordering degree is not quite obvious in orientation, leading to the aromatic layers remaining thin. This commonly enhances the thermal stability of the aromatic structure. Because the aromatic layers are disordered, a more concentrated arrangement results in the formation of mesopores and micropores, forming one or several channels that are connected by pores. Under stressful conditions, the amount of coal macromolecules increases continuously. Additionally, the bordering aromatic rings continue to polymerize and form superpositions. For the local directional and surrounding nondirectional aromatic layers to assemble together, the dislocation of the aromatic cores and slippage of aromatic layers must occur. The larger pores are produced between the aromatic cores and aromatic layers. The pore of TDCs are mainly micropores and submicropores, while ultramicropores are also developed with worse connection. In the local direction process of aromatic structure units, special thin neck, bottle-shaped pores have developed. These are mainly built up by pores between the directional and undirectional structure units.

5.2.2. Permeability of Tectonically Deformed Coals and Their Role in CBM Exploitation. This experimental result shows that the gas-water phase permeability of TDCs is mainly determined by type. The permeability of TDCs could be very high. The permeability increases sequentially, beginning with cataclastic structure coal, to mortar structure coal, to schistose structure coal, which is vertical to the fracture, and, finally, to the schistose structure coal that is parallel to the fracture. TDC with early low ductile deformation superposed by brittle deformation, gas-water phase permeability in the range of $0.1\text{--}5.0 \times 10^{-3} \mu\text{m}^2$, which is in the middle or higher than the primary structure coals and TDCs with weak deformation (Table 4, Figure 3). If the structural fractures are filled with calcite veins or the other mineral matter (Figure 3), gas-water phase permeability would decrease. This means that traditional theory, which states that the permeability in the area where TDCs are common is low, is inaccurate. The permeability of TDCs obtained from the experiment of samples with in situ large diameter in the indoor test can be an important parameter that reflects the real permeability of the coalbed.

When we study the in situ permeability of the coalbed, we should get representative samples of each type of coal in order to obtain integrative permeability. Because of the heterogenous characteristics of the coal seams, especially in the area developing TDCs, we may predict a permeability change of the TDCs according to the types present and the coal gas mining style in different places and seams.

As the stress increases, the coals are further crushed into cataclastic-angular and/or cataclastic-granular pieces. Original cleats [60, 61] that are completely covered with deformation may wrench and tightly compress the fractures, even grinding the coals. Locally intensive deformation may wrench and tightly compress the fractures, even grinding coal into powder, which may plug sheared fractures. However, a combination of the original cleats and tectonic-induced fractures with deformation style (brittle or ductile), size, continuity, and connectivity of the sheared fractures contribute significantly to the overall permeability and are likely to play a major role in the flow of methane through structurally deformed coal in both diffusion at the micropore level and laminar flow at the cleat level [35].

In general, structurally deformed coals are formed through a brittle deformation mechanism and are called cataclastic coals and schistose coals. In such coals which have a hierarchy of open, continuous, and connecting fractures and cleats, the effective block size is not defined at present by the cleat spacing [60, 61], but somewhere between cleats and microfractures. A large number of brittle fractures in structurally deformed coals will make methane migration faster than that in normal coals. This tendency is extremely important for the development of CBM projects and may not only preserve significant gases but also increase the inherent permeability.

Nevertheless, not all structurally deformed coal possesses the properties of fast desorption and laminar flow. Ductile deformation coals, such as mylonitic coals, which are locally and ductilely generated in an intensively compressive and shearing environment, always display tightly compressed and broken fractures to be pushed into one another with worse connectivity for methane migration.

The various types of TDCs formed by the structural deformation of coal seams, especially the coals such as schistose, mortar and cataclastic structure coals subjected to a certain degree of brittle fractures, have good exploration and development potential for coalbed gas. Low ductile deformation superimposed by later brittle deformation also has this potential. On the other hand, changes in coal seam thickness from structural stress and destruction of coal structures caused by the rheology of coal seams are the major factor resulting in the gas outbursts of the coal mines [62, 63]. Therefore, according to the intensity, type and distribution of the rheology of coal seams, the zone of pooling coalbed gas and gas outbursts could be predicted. TDCs of strong brittle-ductile and ductile deformation, such as scale structure coal and mylonitic structure coal, are the main problems in preventing and controlling coal and gas outbursts and gas emissions. These problems need to be resolved urgently.

6. Conclusions

Taking Huaibei and Huainan as typical examples of coal mine areas in the southern North China, the structural characteristics and the physical properties of TDCs have

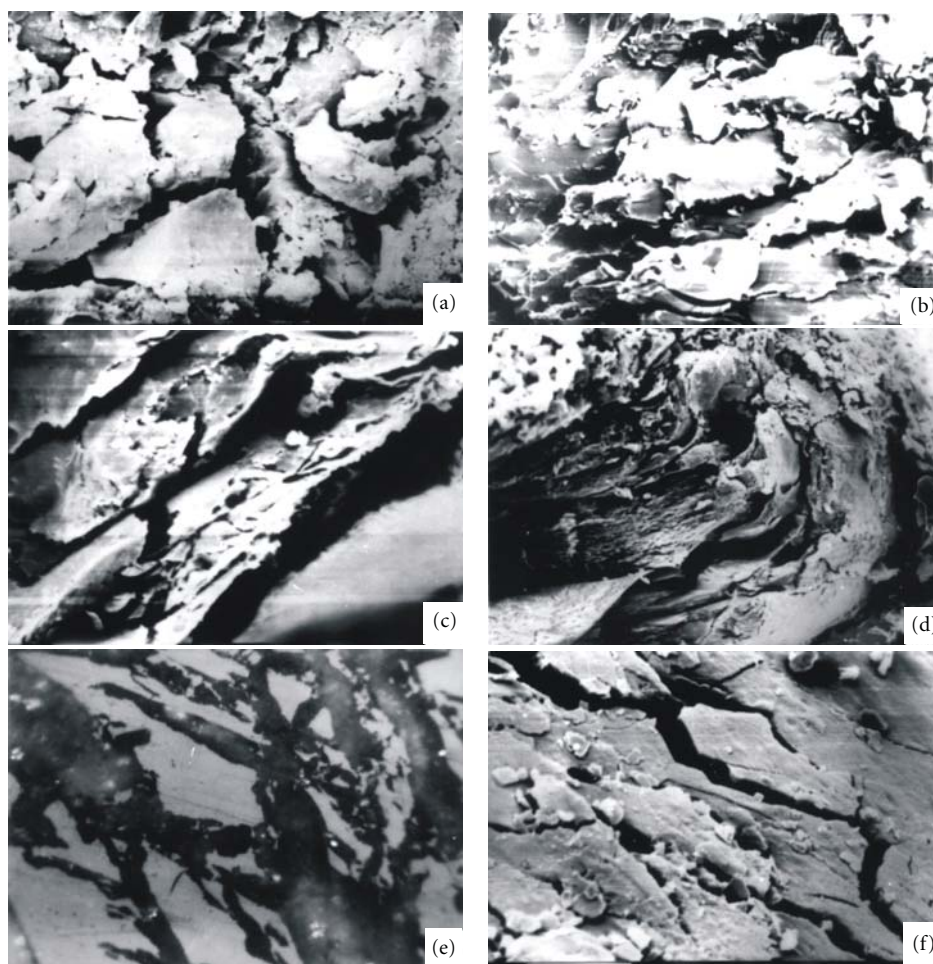


FIGURE 3: SEM and optical microscopy images of TDCs (a) cataclastic structure coal, multidirectional fracture cutting, and no obvious displacement in the blocks, SEM; (b) mortar structure coal, multidirectional fracture cutting, and obvious displacement in the blocks, SEM; (c) schistose structure coal, single directional fracture, and little displacement on its surface, SEM; (d) wrinkle structure coal; coal was wrinkled, and later superimposed by brittle fractures, SEM; (e) cataclastic structure coal with the structural fractures filled with calcite veins, optical microscopy; (f) cataclastic structure coal with the structural fractures expanded the cleats, SEM.

been studied by the authors. Some conclusions are drawn as follows.

(1) Tectonically deformed coals (TDCs) formed by different deformational mechanisms have been divided into three deformation series and ten classes. In the metamorphic-deformed environments, from brittle deformed coal to ductile deformed coal, the changes in characteristics of the macromolecular structures and chemical compositions are that as the increase in structural deformation becomes stronger, from the brittle deformation coal to ductile deformation coal, the ratio of width at the half height of the aromatic carbon and aliphatic carbon peaks (H_{fa}/H_{fal}) was increased. As carbon aromaticity is raised further, carbon aliphaticity reduced obviously and different compositions of macromolecular structure appeared as a jump and wave pattern except that in wrinkle structure coal. Under the directional stress, BSU arrangement is closer, and the orientation becomes stronger from brittle deformed coal to ductile deformed coal. Under the effect of oriented stress, the

orientation of the macromolecular structure becomes locally stronger, and the ordering degree of the arrangement of the BSU is dramatically enhanced.

(2) The characteristics of structural evolution of different kinds of tectonically deformed coals have been further investigated. Structural deformation directly influences the macromolecular structure of coal, which results in dynamic metamorphism. In the brittle deformational coals, frictional heating and stress chemistry of shearing strain areas might play a more important role in increasing brittle deformation because the rate of strain is big enough to generate high temperature, locally altering coal structure under stress. In ductile deformation coals, it may be assumed that strain areas might play a more significant role than frictional heating in increasing coal deformation and metamorphism because the rate of strain is insufficient to generate temperatures high enough to thermally alter coal.

(3) In comparison with the previous results, the characteristics of macromolecular structures and micro- and

nanoscale pore structures of different kinds of TDCs have been analyzed in detail. In particular, advanced research on the formation mechanism of TDCs has been carried out. The nanoscale pore of the cataclastic structure coals caused by the brittle deformation is mainly mesopores; the rest are micropores and submicropores. As the action of tectonic deformation increases, the volume of micropores and the pores whose diameters are even smaller, increases dramatically, and submicropores and ultramicropores can be found. In coals that have experienced ductile deformation, the proportion of mesopores volume in wrinkle structure coal diminishes rapidly, and an increase in the proportion of micropores and submicropores is observed. The proportion of mesopores volume of mylonitic structure coal decreases continually as tectonic stress increases, while the volume of micropores and submicropores increases rapidly, and ultramicropores can also be found. Ductile structure coal has a characteristic similar with the weak brittle deformation coals, but submicropores and ultramicropores are present. The main factor that produces a change in pore structure is strongly tectonic deformation. It is proposed that brittle and ductile deformation can change the pore distribution, which then change spacing and chemical structure.

(4) The permeability of different kinds of TDCs has been investigated which could be very high. The permeability increases sequentially, beginning with cataclastic structure coal, to mortar structure coal, to schistose structure coal, which is perpendicular to the fracture, and, finally, to the schistose structure coal, which is parallel to the fracture. The permeability of TDCs where weak ductile deformation was superimposed by later brittle deformation is better than primary structural coal. According to the results of the coalbed gas testing well, the permeability of TDCs obtained from the experiment of in situ major diameter samples in the indoor test can be an important parameter that reflects the real permeability of the coalbed.

Acknowledgments

This study was financially supported by the National Basic Research Program of China (also called 973 Program) (Grant no. 2009CB219601), the National Natural Science Foundation of China (Grant no. 40772135; 41030422; 40972131; 40172058), and Strategic Priority Research Program of the Chinese Academy of Sciences (Grant no. XDA05030100).

References

- [1] M. Teichmüller, "Organic material and very low-grade metamorphism," in *Temperature Metamorphism*, M. Frey, Ed., pp. 114–161, Blackie Academic & Son, London, UK, 1987.
- [2] M. Nishioka, "The associated molecular nature of bituminous coal," *Fuel*, vol. 71, no. 8, pp. 941–948, 1992.
- [3] P. Fowler and R. A. Gayer, "The association between tectonic deformation, inorganic composition and coal rank in the bituminous coals from the South Wales coalfield, United Kingdom," *International Journal of Coal Geology*, vol. 42, no. 1, pp. 1–31, 1999.
- [4] Y. X. Cao, G. D. Mitchell, A. Davis et al., "Deformation metamorphism of bituminous and anthracite coals from China," *International Journal of Coal Geology*, vol. 43, no. 1–4, pp. 227–242, 2000.
- [5] Y. W. Ju, B. Jiang, Q. L. Hou, and G. L. Wang, "Relationship between nano-scale deformation of coal structure and metamorphic-deformed environments," *Chinese Science Bulletin*, vol. 50, no. 16, pp. 1784–1795, 2005.
- [6] Y. W. Ju, B. Jiang, Q. L. Hou et al., "¹³C NMR spectra of tectonic coals and the effects of stress on structural components," *Science in China, Series D*, vol. 48, no. 9, pp. 1418–1437, 2005.
- [7] K. R. Wilks, M. Mastalerz, R. M. Bustin et al., "The role of shear strain in the graphitization of a high-volatile bituminous and an anthracitic coal," *International Journal of Coal Geology*, vol. 22, no. 3–4, pp. 247–277, 1993.
- [8] R. M. Bustin, J. V. Ross, and J. N. Rouzaud, "Mechanisms of graphite formation from kerogen: experimental evidence," *International Journal of Coal Geology*, vol. 28, no. 1, pp. 1–36, 1995.
- [9] Y. A. Wang and S. J. Yang, "Some characteristics of coal seam with hazard of outburst," *Journal of China Coal Society*, vol. 1, pp. 47–53, 1980 (Chinese).
- [10] J. Zhang, B. Yu, and J. X. Tang, "Study on pore structures of coal seam Blowing out gas," *Coal Geology of China*, vol. 8, no. 2, pp. 71–74, 1996 (Chinese).
- [11] D. X. Yao and J. Lu, "Study on porosity of coal from the First Mine, Xiejiaji, Huainan," *Coal Geology of China*, vol. 8, no. 6, pp. 31–33, 1996 (Chinese).
- [12] T. Wang and W. T. Huang, "Porous structure, characteristics of a coal seam's soft slice in Xinhua coal mine, Jiangxi," *Coal Geology of China*, vol. 6, no. 4, pp. 57–59, 1994 (Chinese).
- [13] H. Gan, S. P. Nandi, and P. L. Walker, "Nature of the porosity in American coals," *Fuel*, vol. 51, no. 4, pp. 272–277, 1972.
- [14] S. J. Gregg and K. S. W. Sing, *Adsorption Surface Area and Porosity*, Academic Press, London, UK, 2nd edition, 1982.
- [15] G. Gürdal and M. N. Yalçın, "Pore volume and surface area of the carboniferous coal from the Zonguldak basin (NW Turkey) and their variations with rank and maceral composition," *International Journal of Coal Geology*, vol. 48, no. 1–2, pp. 133–144, 2001.
- [16] H. Evans and K. M. Brown, "Coal structures in outbursts of coal and firedamp conditions," *Mining Engineering*, no. 148, pp. 171–179, 1973.
- [17] C. F. Yuan, "Tectonically deformed coal and coal and gas outbursts," *Gas Geology Started*, pp. 45–52, 1985 (Chinese).
- [18] Y. X. Cao, *Tectonically deformed coal: its physicochemical properties and mining hazards*, Ph.D. thesis, Peking University, Beijing, China, 1999.
- [19] H. Y. Li, "Major and minor structural features of a bedding shear zone along a coal seam and related gas outburst, Pingdingshan coalfield, Northern China," *International Journal of Coal Geology*, vol. 47, no. 2, pp. 101–113, 2001.
- [20] B. Jiang, Y. Qin, B. H. Fan et al., "Physical property of coal reservoir and exploration prospects for coal bed methane in Huaibei area," *Journal of China University of Mining and Technology*, vol. 30, no. 5, pp. 433–437, 2001 (Chinese).
- [21] Y. W. Ju and G. L. Wang, "Rheology of coal seams and their relation with gas outbursts: a case study of the Haizi coal mine, Huaibei coalfield," *Geological Review*, vol. 48, no. 1, pp. 96–105, 2002 (Chinese).
- [22] Y. W. Ju, *Characteristics of structural evolution and physical properties of reservoirs of tectonically deformed coals and theirs*

- action mechanism, Ph.D. thesis, China University of Mining and Technology, Xuzhou, China, 2003.
- [23] Y. W. Ju, G. L. Wang, B. Jiang, and Q. L. Hou, "Microcosmic analysis of ductile shearing zones of coal seams of brittle deformation domain in superficial lithosphere," *Science in China, Series D*, vol. 47, no. 5, pp. 393–404, 2004.
 - [24] L. J. Xu, C. L. Liu, and X. F. Xian, *Fractal Structure and Properties of Coal in Outburst Zone*, Chongqing University Press, Chongqing, China, 2004.
 - [25] S. Q. Chen, "Characteristics of tectonic deformation Permian coal in Hubei, Hunan, Guangdong and Guangxi provinces and analysis of its origin," *Journal of China Coal Society*, vol. 4, pp. 1–9, 1989 (Chinese).
 - [26] D. Y. Cao, S. R. Zhang, and D. Y. Ren, "The influence of structural deformation on coalification: a case study of carboniferous coal measures in the northern foothills of the Dabie orogenic belt," *Geological Review*, vol. 48, no. 3, pp. 313–317, 2002 (Chinese).
 - [27] E. Stach, M.-T. Mackowsky, and M. Teichmüller, *Stach's Textbook of Coal Petrology*, Gebrüder Borntraeger, Berlin, Germany, 3rd edition, 1982.
 - [28] Y. Qin, *Micropetrology and Structural Evolution of High-Rank Coals in P. R. China*, China University of Mining & Technology Press, Xuzhou, China, 1994.
 - [29] A. Oberlin and G. Terriere, "Graphitization studies of anthracites by high resolution electron microscopy," *Carbon*, vol. 13, no. 5, pp. 367–376, 1975.
 - [30] B. Jiang and Y. Qin, *Evolution Mechanism of Structures of Deformed Coal and Its Geological Significance*, China of University of Mining and Technology Press, Xuzhou, China, 1998.
 - [31] S. Duber and J. N. Rouzaud, "Calculation of reflectance values for two models of texture of carbon materials," *International Journal of Coal Geology*, vol. 38, no. 3–4, pp. 333–348, 1999.
 - [32] M. Y. Sun, L. W. Yang, and X. W. Lu, "Geology possibility and technology feasibility to develop coal bed methane resources in China," *Coal Science and Technology of China*, vol. 29, no. 1, pp. 45–46, 2001.
 - [33] L. W. Yang and M. Y. Sun, "Peculiarities of China CBM reservoirs and their dictation on CBM production technology," *Natural Gas Industry*, vol. 21, no. 6, pp. 17–19, 2001 (Chinese).
 - [34] C. L. Lei and C. Y. Liu, "Reformed pattern of coal reservoirs in reformed coal basins and effect on favorable blocks of coalbed gas in the North China craton," *Coal Geology and Exploration*, vol. 32, no. 2, pp. 20–23, 2004 (Chinese).
 - [35] H. Y. Li, Y. Ogawa, and S. Shimada, "Mechanism of methane flow through sheared coals and its role on methane recovery," *Fuel*, vol. 82, no. 10, pp. 1271–1279, 2003.
 - [36] X. H. Fu, Y. Qin, B. Jiang, W. F. Wang, and S. N. Zhou, "Research on permeability of multiphase medium of middle to high-rank coals," *Journal of China University of Mining and Technology*, vol. 13, no. 1, pp. 11–15, 2003.
 - [37] J. C. Hower, "Observations on the role of the Bernice coal field (Sullivan County, Pennsylvania) anthracites in the development of coalification theories in the Appalachians," *International Journal of Coal Geology*, vol. 33, no. 2, pp. 95–102, 1997.
 - [38] G. H. Taylor, M. Teichmüller, A. Davis et al., *Organic Petrology*, Gebrüder Borntraeger, Berlin, Germany, 1998.
 - [39] Y. X. Cao, A. Davis, R. X. Li et al., "The influence of tectonic deformation on some geochemical properties of coals—a possible indicator of outburst potential," *International Journal of Coal Geology*, vol. 53, no. 2, pp. 69–79, 2003.
 - [40] D. Y. Cao, X. M. Li, and S. R. Zhang, "Influence of tectonic stress on coalification: stress degradation mechanism and stress polycondensation mechanism," *Science in China, Series D*, vol. 50, no. 1, pp. 43–54, 2007.
 - [41] I. J. Stone and A. C. Cook, "The influence of some tectonic structures upon vitrinite reflectance," *Journal of Geology*, vol. 87, no. 5, pp. 479–508, 1979.
 - [42] M. Teichmüller and R. Teichmüller, "Geological causes of coalification," *Coal Science*, vol. 55, pp. 133–155, 1966.
 - [43] R. M. Bustin, "Heating during thrust faulting in the rocky mountains: friction or fiction?" *Tectonophysics*, vol. 95, no. 3–4, pp. 309–328, 1983.
 - [44] V. Suchy, M. Frey, and M. Wolf, "Vitrinite reflectance and shear-induced graphitization in orogenic belts: a case study from the Kandersteg area, Helvetic Alps, Switzerland," *International Journal of Coal Geology*, vol. 34, no. 1–2, pp. 1–20, 1997.
 - [45] J. R. Levine and A. Davis, "The relationship of coal optical fabrics to Alleghanian tectonic deformation in the central Appalachian fold-and-thrust belt, Pennsylvania," *Geological Society of America Bulletin*, vol. 101, no. 10, pp. 1333–1347, 1989.
 - [46] J. V. Ross and R. M. Bustin, "The role of strain energy in creep graphitization of anthracite," *Nature*, vol. 343, no. 6253, pp. 58–60, 1990.
 - [47] B. B. Beamish and P. J. Crosdale, "Instantaneous outbursts in underground coal mines: an overview and association with coal type," *International Journal of Coal Geology*, vol. 35, no. 1–4, pp. 27–55, 1998.
 - [48] R. A. Meyers, *Coal Structure*, Academic Press, New York, NY, USA, 1982.
 - [49] S. Parkash and S. K. Chakrabarty, "Porosity of coal from Alberta planes," *International Journal of Coal Geology*, vol. 6, pp. 55–70, 1986.
 - [50] P. L. Walker, S. K. Verma, J. Rivera-Utrilla et al., "Densities, porosities and surface areas of coal macerals as measured by their interaction with gases, vapours and liquids," *Fuel*, vol. 67, no. 12, pp. 1615–1623, 1988.
 - [51] Z. F. Lu, X. M. Zhang, L. W. Zhong et al., "The pore features of lump coal and its influence factors," *Journal of China University of Mining & Technology*, vol. 20, no. 3, pp. 45–50, 1991 (Chinese).
 - [52] J. Wu, "Studies on characteristics of micropore and its relation with the migration and concentration of oil and gas," *Science in China, Series B*, vol. 23, no. 7, pp. 77–84, 1993 (Chinese).
 - [53] Y. Qin, Z. W. Xu, and J. Zhang, "Natural classification of the high-rank coal pore structure and its application," *Journal of China Coal Society*, vol. 20, no. 3, pp. 265–271, 1995 (Chinese).
 - [54] C. R. Clarkson and R. M. Bustin, "Effect of pore structure and gas pressure upon the transport properties of coal: a laboratory and modeling study. 1. Isotherms and pore volume distributions," *Fuel*, vol. 78, no. 11, pp. 1333–1344, 1999.
 - [55] K. Bratek, W. Bratek, I. Gerus-Piasecka et al., "Properties and structure of different rank anthracites," *Fuel*, vol. 81, no. 1, pp. 97–108, 2002.
 - [56] A. M. Raichur and S. P. Vijayalakshmi, "The effect of nature of raw coal on the adhesion of bacteria to coal surface," *Fuel*, vol. 82, no. 2, pp. 225–231, 2003.
 - [57] Q. Hao, "On morphological character and origin of micropores in coal," *Journal of China Coal Society*, vol. 4, pp. 52–54, 1987 (Chinese).
 - [58] J. N. Rouzaud and A. Oberlin, "The characterization of coals and cokes by transmission electron microscopy," in *Advanced Methodologies in Coal Characterization*, *Coal Science*

- and Technology*, C. Henri, Ed., vol. 15, pp. 311–355, Elsevier, New York, NY, USA, 1990.
- [59] F. H. Zhao and D. Y. Ren, “The application of high-resolution transmission electron microscopy to study the structures of coal macerals,” *Geological Review*, vol. 41, no. 6, pp. 564–570, 1995 (Chinese).
- [60] C. Ö. Karacan and E. Okandan, “Fracture/cleat analysis of coals from Zonguldak Basin (northwestern Turkey) relative to the potential of coalbed methane production,” *International Journal of Coal Geology*, vol. 44, no. 2, pp. 109–125, 2000.
- [61] X. B. Su, Y. L. Feng, J. F. Chen et al., “The characteristics and origins of cleat in coal from Western North China,” *International Journal of Coal Geology*, vol. 47, no. 1, pp. 51–62, 2001.
- [62] J. H. Hao, C. F. Yan, and Z. X. Zhang, “The tectonic coal and its effects on coal gas outburst,” *Journal of Jiaozho Institute of Technology*, vol. 19, no. 6, pp. 403–406, 2000 (Chinese).
- [63] M. B. Díaz Aguado and C. González Nicieza, “Control and prevention of gas outbursts in coal mines, Riosa-Olloniego coalfield, Spain,” *International Journal of Coal Geology*, vol. 69, no. 4, pp. 253–266, 2007.

Research Article

Applications of Vitrinite Anisotropy in the Tectonics: A Case Study of Huaibei Coalfield, Southern North China

Yudong Wu,^{1,2} Quanlin Hou,² Yiwen Ju,² Daiyong Cao,³ Junjia Fan,⁴ and Wei Wei²

¹ MLR Key Laboratory of Metallogeny and Mineral Assessment, Institute of Mineral Resources, CAGS, Beijing 100037, China

² Key Lab of Computational Geodynamics of Chinese Academy of Sciences and College of Earth Science, Graduate University of the Chinese Academy of Sciences, Beijing 100049, China

³ Key Laboratory of Coal Resources, China University of Mining and Technology, Beijing 100083, China

⁴ Key laboratory of Basin Structure and Petroleum Accumulation, CNPC and PetroChina Research Institute of Petroleum Exploration and Development, Beijing 100083, China

Correspondence should be addressed to Quanlin Hou, quhou@gucas.ac.cn

Received 28 February 2012; Accepted 6 April 2012

Academic Editor: Hongyuan Zhang

Copyright © 2012 Yudong Wu et al. This is an open access article distributed under the Creative Commons Attribution License, which permits unrestricted use, distribution, and reproduction in any medium, provided the original work is properly cited.

29 oriented and 10 nonoriented coal samples are collected in the study from three different regions of the Huaibei coalfield, eastern China, and their vitrinite reflectance indicating surface (RIS) parameters are systematically calculated and analyzed. Using the available methods, Kilby's transformations and RIS triaxial orientations are obtained. The magnitudes and orientations of the RIS axes of the three regions were respectively projected on the horizontal planes and vertical sections. The results show that the samples in high deformed region have significant anisotropy magnitudes (higher B_w/R_{\max} and R_{am} values) with a biaxial negative style, whereas the samples in the slightly deformed area have unimpressive anisotropy magnitudes with a biaxial negative style. Thermal metamorphism superposed might enhance the complication and variation of RIS style. RIS projection analysis deduced that the RIS orientation is mainly controlled by regional tectonic stress, and likely influenced by deformation mechanisms of coal.

1. Introduction

During the coalification, tectonic-thermal events could influence the vitrinite reflectance of coal [1, 2]. Effects of temperature and stress on modifying vitrinite reflectance anisotropy (VRA) were proved by high temperature-pressure experiments on bituminous anthracite [3–13]. Patterns of VRA [14, 15] in coal are usually represented by a three-dimensional graphical form resembling an ellipsoid and termed as RIS (reflectance indicating surface).

The investigation of the RIS for vitrinite in coals is performed by means of sections cut from oriented samples, and the magnitudes and orientations of the ellipsoid parameters are obtained by calculating the data measured from three mutually perpendicular surfaces. This method has been reported [14] and verified by high temperature-pressure experiments [16] and tectonic stress field analysis [11, 15, 17–20]. The anisotropy of RIS in this method is quantified

by a function of rank [15], including in terms of bireflectance ratio [21], anisotropy ratio [17] and bireflectance [22].

The RIS styles may also be obtained by nonoriented sections from crushed coal samples. The method requires measurement of the maximum and minimum apparent reflectance from a series of randomly oriented vitrinite particles, and the magnitudes of RIS principal reflectance axes were estimated by using the reflectance crossplots [23, 24]. A series of parameters named as Kilby's transformations in the method are proposed more effectively to estimate the anisotropy magnitude and shape of RIS ellipsoid, including RIS style (R_{st}), anisotropy magnitude (R_{am}), and reflectance of equivalent volume isotropic RIS (R_{ev}). Compared with Levine's method, basing on the application of vitrinite maximum reflectance versus vitrinite random reflectance [25], less time consuming is found during Kilby's data processing [13, 23, 26–30]. In the nonoriented sections,

however, the orientations of three principal reflectance axes are missing.

Previous works suggested that the anisotropic strains developed by lithostatic pressure, especially by tectonic strains, including oriented pressures and shears. High rank coals and anthracites show evidence of the presence of biaxial negative materials [15, 19, 23, 31, 32]. As the result of tectonic dislocations, in many cases associated with fractures in the plane normal to the coal bedding, it is possible to find microtextures responsible for the biaxial positive character [29, 30]. It is found that minimum reflectance develops incrementally parallel to the direction of maximum compressive stress (σ_1) during coalification, and maximum reflectance develops incrementally parallel to the direction of minimum compressive stress (σ_3) [1, 14]. These viewpoints are verified by simple shear experiments in high temperature-pressure environment [28, 33, 34]. On this basis, the RIS may approximate to finite strain ellipsoid [35], and the orientations and magnitudes of RIS principal reflectance axes may correspondingly have further usages in the tectonic stress field analysis.

The Huaibei Coalfield in Anhui Province of China has abundant coal resources. Thermal model research showed that the coal experienced low temperature (<230°C) after being buried during the coalification process [36] and, therefore, thermal function was limited in the coalification history. Although the coalification process was influenced by other geological agencies such as tectonic stress, the RIS parameters may provide semiquantitative information about the magnitudes and orientations of tectonic deformation.

In this paper, 29 oriented coal samples from the working face of the underground mines and 10 nonoriented coal samples from the core drilling were collected. In order to estimate the magnitudes and orientations of the three principal reflectance axes, the RIS was built on the oriented coal sample blocks. The orientation of RIS was obtained by calculating the data measured from three mutually perpendicular surfaces. Meanwhile, the anisotropy magnitude and shape were analyzed with the parameters such as bireflectance ratio, Flinn's diagram, and Kilby's transformations. The effects of tectonic stress and thermal evolution on coal are therefore expected to be evaluated.

2. Geology of the Study Area

The Huaibei Coalfield in the southeast area of North China Craton was influenced by the Tancheng–Lujiang sinistral strike-slip fault in Mesozoic [39–42] and a related arcuate thrust system [37]. Many researchers believed that the arcuate thrust system was a west-thrust imbricate fan with the arc-top near to Huaibei City [37, 43]. A syncline formed in the margin of the thrust system had a certain influence on the burial depth of coal seams and the level of coal rank [44]. Coal-bearing strata mainly occur in Permo-Carboniferous age.

The Huaibei Coalfield is divided into three regions representing different stress-thermal environments. Vitrinite

reflectance of coal samples collected from these regions was measured and sampling locations are shown in Figure 1(a).

- (1) Region A, including the coal mines of Taoyuan (label 3), Qinan (label 4), Qidong (label 5), and Xutuan (label 9). The strata were likely influenced less by magmatism and tectonic agency and more by burial metamorphism.
- (2) Region B, including the coal mines of Haizi (label 6), Linhuan (label 7), Tongting (label 8) and Baishan (label 10). Both Mesozoic deformation and magmatism affected deeply the strata and likely impacted on the samples collected in the region.
- (3) Region C, including the coal mines of Luling (label 1), Zhuxianzhuang (label 2), Shitai (label 11) and Yangzhuang (label 12). The strata in the region strongly deformed, and samples are probably highly influenced by effects of tectonic deformation and thermal-shearing.
- (4) The lithostratigraphic sequence of the study area is shown in Figure 1(b). The major coal seams occur in the lower Permian system (P_1) and minor coal seams locally occur in the upper Permian System (P_2). Southward marine regression during early Permian time led to deposition in an island-lagoon environment and followed by terrestrial delta-plain deposits that contained extensive and minable coal seams [44]. The deltaic environment became unstable in early Late Permian, and coal seams became thinned, discontinuous and unminable. The alluvial deposits in Late Permian marked the end of coal accumulation in the Huaibei coalfield [44]. All the oriented samples collected from the working face in coal seams of 3rd, 7th, 8th and 10th and the nonoriented samples collected from the well-drills belonging to the Permian strata.

3. Experimental Section

Coal macerals of samples were determined by spot checks before the reflectance measurement, and the reflectance was measured by means of the method described in GB/T 8899-1998 (equated with ISO7404/3 standard). At least 500 points for each sample were measured on the same polished specimen. The contents of vitrinite, inertinite, liptinite, and mineral matter were obtained and are shown in Table 1. Coal lithotype in the Huaibei coalfield is dominated by clarain, with secondary durian and vitrain, and coal maceral is dominated by vitrinite (40.6~92.5%), which is followed by inertinite and liptinite (Table 1).

3.1. Sample Preparation. The 29 oriented samples were prepared following the rules described in GB/T 16773-2008 (equated with ISO7404/2 standard) and cut into cubes with approximately 3-4 cm in dimensions (Figure 2). One pair of planes are paralleling to the horizontal plane and the other two mutually perpendicular pairs normal to the horizontal one. Each sample, therefore, has three pairs of mutually

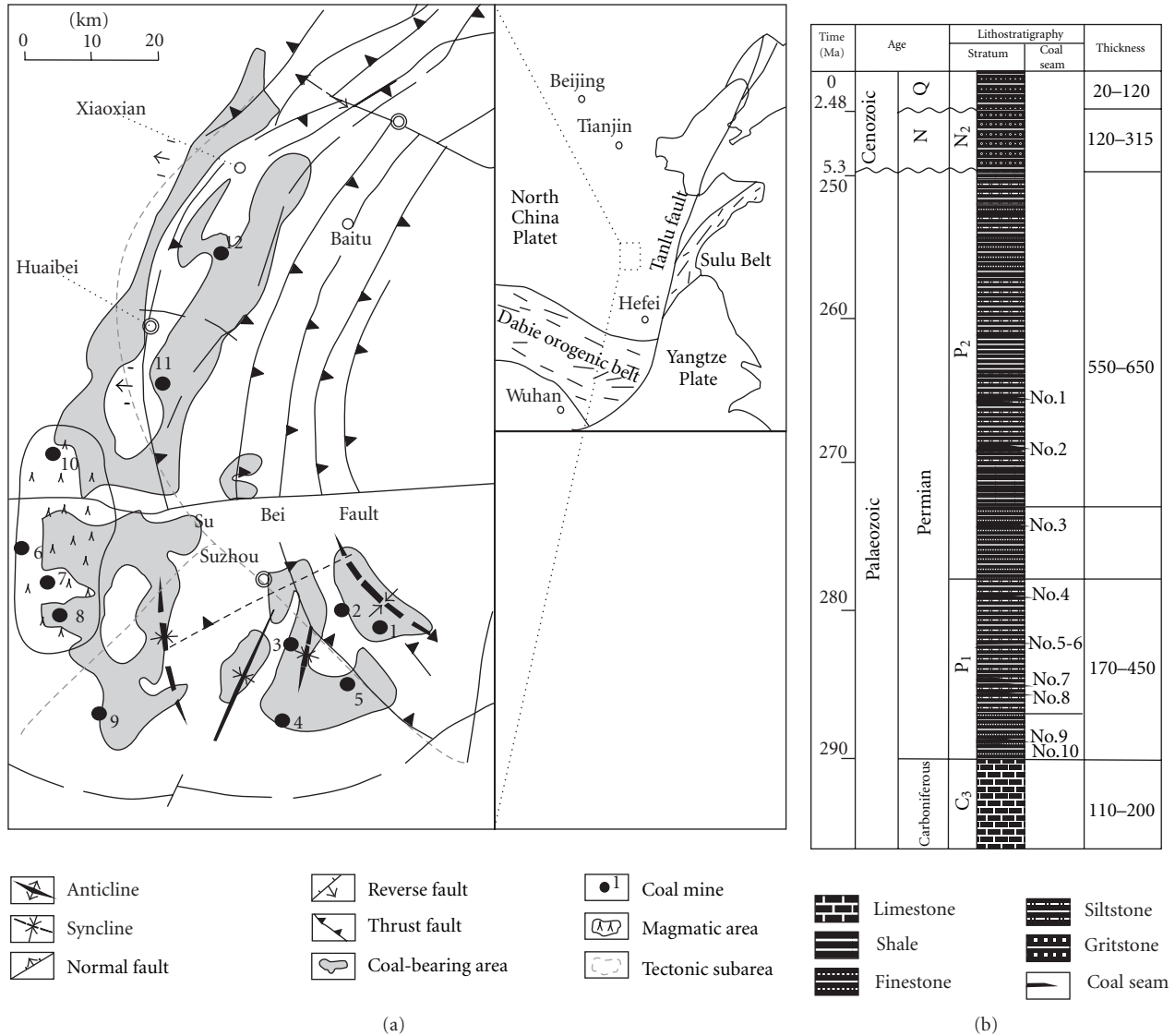


FIGURE 1: Simplified geologic map with late Paleozoic stratigraphic column of the Huaibei Coalfield. Coal mine label: (1) Luling mine, (2) Zhuxianzhuang mine, (3) Taoyuan mine, (4) Qinan mine, (5) Qidong mine, (6) Haizi mine, (7) Linhuan mine, (8) Tongting mine, (9) Xutuan mine, (10) Baishan mine, (11) Yangzhuang mine, (12) Shitai mine. The location is shown in the inset of Figure 1(a): Areas in gray where Upper Permian coal bearing strata are preserved in the Huaibei coalfield. Oriented coal samples were gathered from the Luling (LL), Taoyuan (TY), Haizi (HZ), Linhuan (LH), Xutuan (XT), Shitai (ST), and Yangzhuang (YZ) mines. The nonoriented coal samples were collected from bore holes in TY, XT, LH and Qidong (QD) coal mines. As shown in Figure 1(b), the Mesozoic and lower Cenozoic strata were suffered from erosion and missed. The Permian strata mainly consist of sandy mudstone and fine sandstone with 10 major coal seams (Nos. 1~10). Geological data are compiled based on [37, 38] the stratigraphic column is modified from China National Administration of coal Geology (1996).

perpendicular surfaces (a/a' , b/b' , and c/c' as shown in Figure 2) under the process of polishing surface.

The 11 nonoriented samples were prepared by a modified procedure of GB/T 16773-2008 (equated with ISO 7404/02 standard). These samples were also used in our previous work for thermal simulation of maturation for coal [36].

3.2. Optical Microscopic Measurements. The measurements were performed for each oriented sample using an MPV-3

Combi (Leitz) microscope, reflected light, and oil immersion objectives. The maximum and minimum apparent reflectance (R_{\max} and R_{\min}) on each polished surface were measured in polarized light ($\lambda = 546\mu$) and by rotating the microscope stage through 360° and following the analytical method described in GB/T 6948-2008 (equated with ISO7404/5 standard). at least 20 points on each surface of each sample were measured to obtain the mean statistical values and azimuths of R_{\max} and R_{\min} .

TABLE 1: Maceral composition of coal samples studied.

Sample number	V (%)	I (%)	E (%)	MM (%)
TYM03	40.6	22.5	36.7	0.2
TY02	66.4	18.4	14.4	0.8
XTM08	89.2	9.2	0.8	0.8
LHM03	67.4	31.7	x	0.9
LHM02	81.9	17.4	x	0.7
LHM10	76.8	22.8	x	0.4
HZM03	92.5	7.0	x	0.5
LLM05	58.2	24.2	15.2	2.4
LLM08	65.0	17.9	16.3	0.8
LLM01	67.8	18.3	12.4	1.5
YZM12	67.3	32.6	x	0.1
STM05	67.7	30.8	x	1.5

See Figure 1 for sample location. Abbreviations: V → vitrinite content (vol.%); I → inertinite content (vol.%); E → Exinite content (vol.%); MM → mineral matter content (vol.%). x = content < 0.1%.

As for nonoriented samples, at least 20 points were measured with the same analytical method, and the mean statistical values of R_{\max} and R_{\min} were obtained.

3.3. Data Processing. On the basis of measured mean values, the values and occurrences of maximum reflectance (R_{\max}), intermediate reflectance (R_{int}), and minimum reflectance (R_{\min}) axes may be obtained by solving ellipsoid equation in analytic geometry of space [35], which is the magnitudes and orientations of RIS. The computing method is in Figure 3 as follows:

$$\lambda'_x x^2 + \lambda'_y y^2 + \lambda'_z z^2 - 2\gamma'_{xy} xy - 2\gamma'_{yz} yz - 2\gamma'_{zx} zx = 1, \quad (1)$$

where

$$\lambda'_x = \frac{1}{\lambda_x}, \quad \lambda'_y = \frac{1}{\lambda_y}, \quad \lambda'_z = \frac{1}{\lambda_z}, \quad \gamma' = \frac{\gamma}{\lambda} = \gamma\lambda',$$

$$\lambda'_x = \frac{\cos^2 \bar{\theta}_x}{(\bar{R}_{\max})_{xy}^2} + \frac{\sin^2 \bar{\theta}_x}{(\bar{R}_{\min})_{xy}^2},$$

$$\lambda'_y = \frac{\sin^2 \bar{\theta}_x}{(\bar{R}_{\max})_{xy}^2} + \frac{\cos^2 \bar{\theta}_x}{(\bar{R}_{\min})_{xy}^2},$$

$$\gamma'_{xy} = \left[\frac{1}{(\bar{R}_{\max})_{xy}^2} - \frac{1}{(\bar{R}_{\min})_{xy}^2} \right] * \sin \bar{\theta}_x * \cos \bar{\theta}_x,$$

$$\lambda'_y = \frac{\cos^2 \bar{\theta}_y}{(\bar{R}_{\max})_{yz}^2} + \frac{\sin^2 \bar{\theta}_y}{(\bar{R}_{\min})_{yz}^2},$$

$$\lambda'_z = \frac{\sin^2 \bar{\theta}_y}{(\bar{R}_{\max})_{yz}^2} + \frac{\cos^2 \bar{\theta}_y}{(\bar{R}_{\min})_{yz}^2},$$

$$\gamma'_{yz} = \left[\frac{1}{(\bar{R}_{\max})_{yz}^2} - \frac{1}{(\bar{R}_{\min})_{yz}^2} \right] * \sin \bar{\theta}_y * \cos \bar{\theta}_y,$$

$$\lambda'_z = \frac{\cos^2 \bar{\theta}_z}{(\bar{R}_{\max})_{zx}^2} + \frac{\sin^2 \bar{\theta}_z}{(\bar{R}_{\min})_{zx}^2},$$

$$\lambda'_x = \frac{\sin^2 \bar{\theta}_z}{(\bar{R}_{\max})_{zx}^2} + \frac{\cos^2 \bar{\theta}_z}{(\bar{R}_{\min})_{zx}^2},$$

$$\gamma'_{zx} = \left[\frac{1}{(\bar{R}_{\max})_{zx}^2} - \frac{1}{(\bar{R}_{\min})_{zx}^2} \right] * \sin \bar{\theta}_z * \cos \bar{\theta}_z.$$

(2)

This ellipsoid equation has three eigenvalues, corresponding with the values of three RIS ellipsoid axes ($R_{\max} > R_{\text{int}} > R_{\min}$):

$$1 + e_i = \sqrt{\lambda_i}; \quad i = 1, 2, 3. \quad (3)$$

The occurrence of three RIS ellipsoid axis is calculated according to the formula

$$A_i = \frac{\arctan M_i}{L_i}, \quad B_i = \arccos N_i, \quad i = 1, 2, 3, \quad (4)$$

where A_i and B_i represent the direction and dip angle of the axis in the coordinate system, respectively

$$L_i = \cos R_{ix} = \frac{X_i}{\sqrt{\lambda_i}}; \quad M_i = \cos R_{iy} = \frac{Y_i}{\sqrt{\lambda_i}},$$

$$N_i = \cos R_{iz} = \frac{Z_i}{\sqrt{\lambda_i}}, \quad i = 1, 2, 3,$$

$$X_i + Y_i + Z_i = \lambda_i,$$

$$\frac{X_i}{\lambda'_y \lambda'_z - \lambda'_i \lambda'_y - \lambda'_i \lambda'_z + \lambda_i'^2 - \gamma_{yz}'^2} \quad (5)$$

$$= \frac{-Y_i}{-\gamma'_{xy} \lambda'_z + \gamma'_{xy} \lambda'_i - \gamma'_{zx} \gamma'_{yz}}$$

$$= \frac{-Z_i}{\gamma'_{xy} \gamma'_{yz} + \gamma'_{zx} \lambda'_y - \gamma'_{zx} \lambda'_i}.$$

The geological occurrence of RIS ellipsoid axis ($\text{Dir}_i \angle \text{Dip}_i$), however, needs a data conversion as follows:

$$\begin{aligned} \text{if } B_i \geq 0, \quad \text{Dir}_i &= C_i - A_i \pm 360^\circ, \quad \text{Dip}_i = B_i, \\ \text{if } B_i < 0, \quad \text{Dir}_i &= C_i - A_i \pm 180^\circ, \quad \text{Dip}_i = -B_i, \end{aligned} \quad (6)$$

where $0 < \text{Dir}_i < 360^\circ$, $0 < \text{Dip}_i < 90^\circ$; where C_i represents the geological direction of arrowhead in Figure 2.

Therefore, the reflectance anisotropy (bireflectance B_w and R_{am} coefficient values) and RIS shapes (such as R_{ev} , R_{st} coefficient value, Flinn's parameters, etc.) can be determined. The details of the parameters are given as follows.

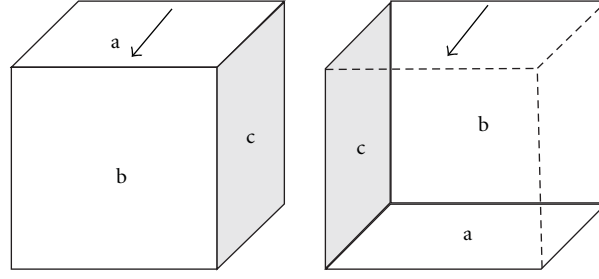


FIGURE 2: Diagram of three sections cut from oriented blocks. Arrowhead on the top surface of the block shows the spatial orientation. Surfaces marked with a/a' , b/b' , c/c' were mutually perpendicular with the surfaces a and a' horizontal and c and c' vertical and parallel to the arrowhead.

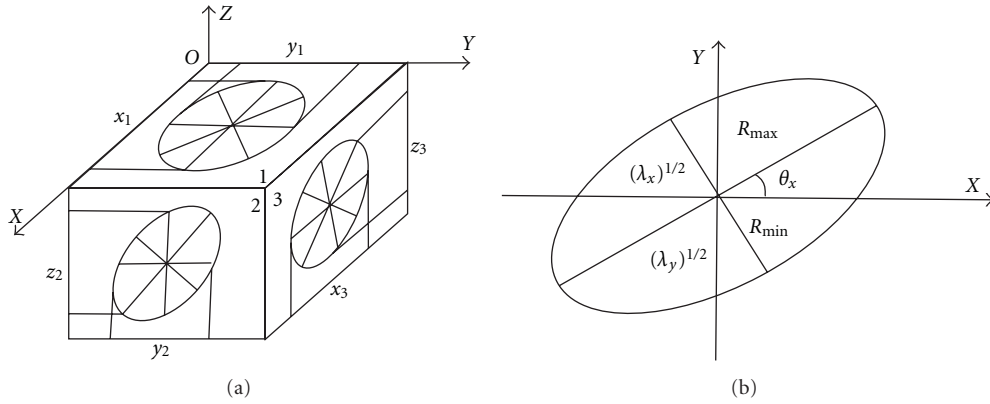


FIGURE 3: Coordinates and coal brick VR ellipses [11]. A coal sample brick was demonstrated in Figure 3(a), the measuring result were quantitatively represented in the YXZ coordinate system. The value and orientation of R_{\max}/R_{\min} on each polished surface were shown on three mutually perpendicular cube face, represented by the long/minor axis of ellipse. For example, as shown in Figure 3(b), the measured value ($R_{XOY \cdot \max}$ and $R_{XOY \cdot \min}$) and their orientations (θ_x) are expressed as their coordinates and the RIS ellipsoid equation can be built.

- (1) B_w coefficient value [22], representing bireflectance value, is calculated according to the formula.

$$B_w = R_{\max} - R_{\min}. \quad (7)$$

B_w/R_{\max} [21] represents the bireflectance ratio.

- (2) Flinn's parameter was firstly proposed for examining the geometry of three-dimensional homogeneous strain [35, 45]. Formula of Ramsay was chosen here

$$K = \frac{\varepsilon_1 - \varepsilon_2}{\varepsilon_2 - \varepsilon_3}, \quad (8)$$

where

$$\varepsilon_1 = \ln(R_{\max}), \quad \varepsilon_2 = \ln(R_{\text{int}}), \quad \varepsilon_3 = \ln(R_{\min}). \quad (9)$$

- (3) R_{am} coefficient value [23, 24], representing the RIS anisotropy magnitude, is calculated according to the formula

$$R_{\text{am}} = (x^2 - y^2)^{1/2}, \quad (10)$$

where

$$x = \frac{R_{\text{int}}}{R_{\max} + R_{\text{int}} + R_{\min}} + \left[y + \frac{1}{3} \cos 30^\circ \right] \tan 30^\circ - \frac{1}{2},$$

$$y = \left[\frac{R_{\max}}{(R_{\max} + R_{\text{int}} + R_{\min})} - \frac{1}{3} \right] \cos 30^\circ. \quad (11)$$

This value is the distance between the plotted position of RIS and the position of an isotropic RIS, a single measure of anisotropy for all styles of RIS [23]. Isotropic constituent of coal is characterized by $R_{\text{am}} = 0$. The higher coefficient value is, the stronger optical anisotropy will be. Typical R_{am} values for raw vitrinites are from 0.03 to 0.05 and the value of 0.1 represents strong anisotropy of a constituent.

- (4) R_{st} coefficient value [23, 24], representing RIS style, is calculated according to the formula

$$R_{\text{st}} = 30 - \arctan \left(\frac{x}{y} \right), \quad (12)$$

where x and y are determined in the same way as shown above. R_{st} values range from (-30) to $(+30)$ and the RIS shape is described as

$R_{st} = (-30)$: uniaxial negative; $R_{st} = (+30)$: uniaxial positive; $-30 < R_{st} < 0$: biaxial negative; $0 < R_{st} < +30$: biaxial positive; $R_{st} = 0$: biaxial neutral.

- (5) R_{ev} coefficient value [23, 24], representing the reflectance of equivalent volume of isotropic RIS, is calculated according to the formula

$$R_{ev} = (R_{max} \times R_{int} \times R_{min})^{1/3}. \quad (13)$$

4. Results

4.1. Anisotropic Properties of Nonoriented Samples. R_{max} and R_{min} of 11 non-oriented samples were measured and the anisotropic properties of the material such as B_w and B_w/R_{max} were calculated as shown in Table 2.

4.2. Magnitude and Orientation of RIS. The magnitudes and orientations of RIS for 29 oriented samples were calculated by measuring the values and azimuths of the R_{max} and R_{min} . Many of the coal samples suffered from tectonic deformation during coalification. The deformation types were identified by the proposed tectonic coals standard [38] and divided into three series: brittle-ductile transition, ductile shear, and brittle crush as shown in Table 3.

4.3. Anisotropic Property of Oriented Samples. Based on magnitudes and orientations of RIS, Levine's rank and Kilby's transformations are obtained as shown in Table 4.

5. Discussion

5.1. Major Facts Affecting VRA. Both temperature and stress have influences on modifying VRA. It is therefore necessary to estimate roughly the thermal effects during coalification before analyzing RIS.

In previous works, the mean random vitrinite reflectance ($R_m\%$) shows a strong correlation ($r^2 = 0.7$, $n > 600$) with maximum burial temperature (T_{max} in $^{\circ}\text{C}$). These data are modeled by the linear regression equation [46]:

$$\ln(R_m) = 0.0078T_{max} - 1.2. \quad (14)$$

The conversion between R_{max} and R_m is following the analytical method described in GB/T 6948-2008 (equated with ISO7404/5 standard). On the basis of correlation given above, the maximum temperatures sustained during burial are estimated.

As shown in Table 5, the measured reflectance values range from 0.74% to 3.01, indicating conversion of medium-volatile bituminous coal to anthracite coal. Most of the studied samples experienced a maximum temperature between 120~20 $^{\circ}\text{C}$, less than 290 $^{\circ}\text{C}$. The available high temperature-pressure experiments on bituminous anthracite show that there is little change in vitrinite reflectance anisotropy under the temperature less than 400 $^{\circ}\text{C}$ [47, 48]. It is reasonable to believe that the vitrinite reflectance anisotropy here was mainly caused by the tectonic differential stress.

TABLE 2: The vitrinite reflectance anisotropy of non-oriented samples, Huaibei coalfield.

Coal mine	Sample number	Coal seam	R_{max}	R_{min}	B_w	B_w/R_{max}	R_{max}/R_{min}
Linhuan	LH10	9	1.37	1.24	0.13	0.09	1.10
Shitai	ST04	3	1.44	1.29	0.15	0.10	1.12
Taoyuan	TY01	7	1.02	0.9	0.12	0.12	1.13
Taoyuan	TY02	10	1.00	0.91	0.09	0.09	1.10
Taoyuan	TY03	10	1.14	1.02	0.12	0.11	1.12
Taoyuan	TY04	7	1.06	0.95	0.11	0.10	1.12
Taoyuan	TY05	3	0.87	0.79	0.08	0.09	1.10
Qidong	QD01	9	1.09	0.97	0.12	0.11	1.12
Qidong	QD02	7	0.94	0.87	0.07	0.07	1.08
Qidong	QD03	9	0.89	0.77	0.12	0.13	1.16
Qidong	QD04	10	0.98	0.88	0.10	0.10	1.11

Abbreviations: R_{max} : maximum reflectance; R_{int} : intermediate reflectance; R_{min} : minimum reflectance; B_w : bireflectance, $R_{max} - R_{min}$.

5.2. Magnitudes of RIS. The three sampling regions represent different stress-thermal environments and, therefore, the corresponding coal samples experienced different effects of deformation and metamorphism. The parameters of reflectance anisotropy (bireflectance B_w and R_{am} coefficient values) and RIS shapes (such as R_{ev} and R_{st} coefficient values, Flinn's parameters) are analyzed as follows.

5.2.1. Bireflectance. The bireflectance increases progressively with upgrading of coal rank under the heat treatment without differential stress involved. In that case, the bireflectance for the coal ranking from medium-volatile bituminous to anthracite coal should be at the same level and the B_w/R_{max} coefficient, representing bireflectance ratio, should be suitable for the bireflectance analysis among various coal ranks.

Relationships between R_{max} and B_w/R_{max} are shown in Figure 4. The range of R_{max} value is 0.81~1.21% in Region A (Taoyuan mine, Qidong mine, and Xutuan mine) and 1.21~3.13% in Region B (Linhuan mine and Haizi mine). This obvious difference above indicates that samples from Region B was dominated by the magmatic thermal activity. However, compared with Region A (Luling mine, Shitai mine, and Yangzhuang mine), samples in Region C where experienced extra effects of tectonic deformation and shearing heat, are manifested by the various R_{max} ranges of 0.83~1.72%.

In contrast to Region B, the B_w/R_{max} value in Region C and Region A simultaneously increased with the R_{max} and indicates that the reflectance in the two regions is dominated by the tectonic deformation and shearing heat.

The 95% confidence intervals of B_w/R_{max} value are 0.13 ± 0.0195 in Region A and 0.23 ± 0.0333 in Region C. The difference between two regions represents the effects of tectonic stress. The same indicator in Region B is 0.17 ± 0.0326 . The coal samples in the region were partly influenced by Mesozoic magmatism, and represent polarization of

TABLE 3: Magnitude and orientation of RIS, Huaibei coalfield.

Region	Coal number	Coal seam	DT	R_{\max} axes			R_{int} axes			R_{\min} axes		
				Value	Strike	Dip	Value	Strike	Dip	Value	Strike	Dip
Region A	TYM03	8	BD	1.01	41°	81°	0.95	177°	21°	0.77	266°	6°
	TYM04	8	BC	1.00	323°	69°	0.90	153°	55°	0.81	37°	44°
	TYM06	10	BC	0.87	234°	89°	0.85	28°	49°	0.74	160°	16°
	TYM07	10	BC	0.79	164°	4°	0.75	291°	72°	0.72	82°	89°
	XTM01	7	BC	1.11	151°	69°	0.99	239°	36°	0.89	37°	63°
	XTM02	7	BD	1.11	106°	87°	1.01	157°	1°	0.97	248°	77°
	XTM06	7	DS	1.13	248°	85°	1.07	107°	40°	0.98	25°	63°
	XTM07	7	BC	1.11	242°	64°	1.05	126°	4°	0.98	60°	45°
Region B	LHM02	7	DS	1.31	339°	87°	1.26	250°	67°	1.14	139°	86°
	LHM03	7	DS	1.55	300°	88°	1.25	108°	6°	1.17	196°	54°
	LHM04	9	BD	1.46	256°	54°	1.40	344°	22°	1.29	82°	67°
	LHM05	9	BD	3.09	56°	74°	2.69	310°	54°	2.36	222°	49°
	LHM09	9	BD	1.44	295°	56°	1.31	174°	36°	1.15	25°	82°
	LHM12	10	BD	1.24	62°	85°	1.15	196°	5°	1.10	272°	82°
	LHM14	10	BD	1.50	344°	15°	1.36	205°	72°	1.18	73°	55°
	LHC01*	—	—	1.37	337°	41°	1.15	246°	1°	1.13	156°	41°
	HZM03	10	BC	1.92	121°	32°	1.70	47°	89°	1.63	222°	35°
	HZM04	10	BC	2.01	98°	27°	1.98	333°	82°	1.82	186°	89°
	HZM10	8	DS	2.66	332°	33°	2.54	233°	16°	2.51	151°	84°
	HZC02*	—	—	1.46	93°	26°	1.32	345°	31°	1.17	214°	46°
	HZC03*	—	—	1.45	3°	36°	1.26	101°	11°	1.13	205°	51°
	BSC04*	—	—	2.61	24°	1°	2.16	289°	87°	2.08	114°	3°
	BSC05*	—	—	2.54	249°	8°	2.21	343°	26°	1.96	149°	62°
Region C	YZM11	3	BC	1.70	30°	77°	1.59	160°	89°	1.34	215°	63°
	YZM14	3	BC	1.69	132°	88°	1.61	248°	29°	1.38	335°	88°
	YZM16	3	BC	1.82	164°	24°	1.60	3°	65°	1.30	254°	74°
	STM01	3	BD	1.52	128°	84°	1.47	4°	11°	1.21	275°	75°
	STM02	3	BC	1.41	215°	33°	1.36	17°	83°	1.10	97°	42°
	STM03	3	BD	1.72	94°	2°	1.25	209°	64°	1.18	16°	2°
	STC06*	—	—	1.52	186°	22°	1.37	277°	3°	1.19	15°	67°
	LLM03	8	BD	1.06	47°	50°	0.99	261°	38°	0.88	171°	77°
	LLM05	8	DS	0.84	322°	74°	0.76	247°	17°	0.59	118°	63°
	LLM07	10	BC	0.95	156°	45°	0.86	345°	47°	0.74	256°	57°
	LLM08	10	BC	0.83	146°	18°	0.80	357°	79°	0.75	235°	83°
	LLM10	8	DS	1.11	307°	67°	0.92	35°	42°	0.83	168°	68°

* Data compiled from [18].

Abbreviations: DT: deformation type; BD: brittle-ductile transition; DS: ductile shear; BC: brittle crush; R_{\max} : maximum reflectance; R_{int} : intermediate reflectance; R_{\min} : minimum reflectance.

R_0 value. Meanwhile, some strata underwent stronger deformation with increasing B_w/R_{\max} values.

5.2.2. Reflectance of Equivalent Volume Isotropic RIS. RIS parameter R_{ev} , the reflectance of the isotropic RIS of equivalent volume, as a result of the chemical structure

ordering during heating, is suggested to characterize the basic structure unites (BSU) [49].

As shown in Figure 5, positive linear regression relationships between R_{\max} and R_{ev} (r^2) for Regions A, B, and C are 0.956, 0.980, and 0.965, respectively. The correlations between R_{ev} values and the hydrogen contents (H^{daf}) have

TABLE 4: Calculated results of RIS parameters, Huaibei coalfield.

Region	Coal number	Coal seam	DT	R_{st}	R_{am}	R_{ev}	B_w	B_w/R_{max}	R_{max}/R_{int}	Axis ratio R_{int}/R_{min}	R_{max}/R_{min}	K
Region A	TYM03	8	BD	-14.43	0.05	0.90	0.24	0.24	1.07	1.23	1.31	0.33
	TYM04	8	BC	1.06	0.04	0.90	0.19	0.19	1.11	1.11	1.23	0.96
	TYM06	10	BC	-20.43	0.03	0.82	0.13	0.15	1.03	1.15	1.18	0.20
	TYM07	10	BC	-0.05	0.02	0.75	0.07	0.09	1.05	1.05	1.10	0.95
	XTM01	7	BC	2.52	0.04	0.99	0.23	0.20	1.12	1.12	1.26	1.04
	XTM02	7	BD	14.66	0.03	1.03	0.14	0.12	1.10	1.04	1.14	2.49
	XTM06	7	DS	-6.05	0.03	1.06	0.16	0.14	1.06	1.10	1.16	0.64
	XTM07	7	BC	-4.73	0.02	1.05	0.12	0.11	1.05	1.07	1.13	0.71
Region B	LHM02	7	DS	-12.79	0.03	1.23	0.18	0.13	1.04	1.11	1.16	0.41
	LHM03	7	DS	17.42	0.06	1.31	0.38	0.24	1.23	1.07	1.32	2.93
	LHM04	9	BD	-9.73	0.02	1.38	0.17	0.12	1.04	1.08	1.13	0.51
	LHM05	9	BD	2.89	0.05	2.70	0.72	0.23	1.15	1.14	1.31	1.04
	LHM09	9	BD	-3.89	0.04	1.29	0.30	0.21	1.10	1.15	1.26	0.70
	LHM12	10	BD	12.26	0.02	1.16	0.14	0.11	1.08	1.04	1.13	2.08
	LHM14	10	BD	-4.52	0.03	1.34	0.33	0.22	1.10	1.16	1.28	0.67
	LHC01*	—	—	25.69	0.04	1.21	0.24	0.18	1.19	1.02	1.21	9.98
	HZM03	10	BC	15.63	0.03	1.75	0.30	0.15	1.13	1.05	1.18	2.65
	HZM04	10	BC	-21.15	0.02	1.94	0.19	0.09	1.02	1.09	1.10	0.19
	HZM10	8	DS	18.44	0.01	2.57	0.15	0.06	1.05	1.01	1.06	3.63
	HZC02*	—	—	-1.14	0.04	1.31	0.29	0.20	1.11	1.13	1.25	0.84
	HZC03*	—	—	6.18	0.05	1.27	0.32	0.22	1.15	1.12	1.28	1.29
	BSC04*	—	—	21.95	0.05	2.27	0.53	0.20	1.21	1.04	1.25	5.01
	BSC05*	—	—	4.55	0.05	2.22	0.58	0.23	1.15	1.13	1.30	1.16
Region C	LLM03	8	BC	-7.01	0.04	0.98	0.18	0.17	1.07	1.12	1.21	0.59
	LLM05	8	BC	-11.51	0.07	0.72	0.24	0.29	1.10	1.28	1.41	0.40
	LLM07	10	BC	-6.37	0.05	0.85	0.21	0.22	1.10	1.17	1.28	0.60
	LLM08	10	BD	-8.05	0.02	0.79	0.08	0.10	1.04	1.07	1.11	0.58
	LLM10	8	BC	11.71	0.06	0.94	0.27	0.25	1.20	1.11	1.33	1.84
	YZM11	3	BC	-12.87	0.05	1.54	0.37	0.21	1.07	1.19	1.27	0.38
	YZM14	3	BC	-15.35	0.04	1.55	0.32	0.19	1.05	1.17	1.23	0.32
	YZM16	3	BC	-4.68	0.06	1.56	0.53	0.29	1.14	1.23	1.41	0.63
	STM01	3	BD	-21.59	0.05	1.39	0.32	0.21	1.03	1.22	1.26	0.17
	STM02	3	BC	-20.95	0.05	1.28	0.31	0.22	1.04	1.24	1.29	0.18
	STM03	3	BD	23.20	0.08	1.37	0.54	0.31	1.38	1.06	1.46	5.57
	STC06*	—	—	-3.00	0.05	1.35	0.33	0.22	1.11	1.15	1.28	0.74

* Data compiled from [18] except for the coal seam and deformation type of these four samples. Abbreviations: BD: brittle-ductile transition; DS: ductile shear; BC: brittle crush; DT: deformation type; R_{max} : maximum reflectance; R_{int} : intermediate reflectance; R_{min} : minimum reflectance; B_w : bireflectance, $R_{max} - R_{min}$; K: Flinn's parameter, $(\epsilon_1 - \epsilon_2)/(\epsilon_2 - \epsilon_3)$, where $\epsilon_1 = \ln(R_{max})$, $\epsilon_2 = \ln(R_{int})$, $\epsilon_3 = \ln(R_{min})$; R_{am} : RIS anisotropy magnitude, $(x^2 - y^2)^{1/2}$; $R_{st} \rightarrow R_{IS}$ style, 30-arctan (x/y) ; R_{ev} : reflectance of equivalent volume isotropic RIS, $(R_{max} \times R_{int} \times R_{min})^{1/3}$; where $x = R_{int}/(R_{max} + R_{int} + R_{min}) + [y + 1/3 \cos 30^\circ] \times \tan 30^\circ - 1/2$, $y = [R_{max}/(R_{max} + R_{int} + R_{min}) - 1/3] \times \cos 30^\circ$.

TABLE 5: Maximum temperatures sustained during burial, Upper Permian strata, Huaibei coalfield.

Region A			Region B			Region C		
Number	R_{\max}	T_{\max} (°C)	Number	R_{\max}	T_{\max} (°C)	Number	R_{\max}	T_{\max} (°C)
TYM03	1.01	147	LHM02	1.31	180	STM01	1.52	200
TYM04	0.94	138	LHM03	1.52	200	STM02	1.41	190
TYM06	0.88	129	LHM04	1.41	190	STM03	1.72	215
TYM07	0.81	119	LHM05	3.13	283	STC06*	1.52	200
TY01	1.02	148	LHM09	1.34	183	YZM11	1.70	214
TY02	1.00	146	LHM12	1.21	170	YZM14	1.69	213
TY03	1.14	163	LHM14	1.37	186	YZM16	1.82	223
TY04	1.06	153	LHC01*	1.37	186	ST01	1.44	193
TY05	0.87	128	LH01	1.37	186	LLM03	1.11	159
QD01	1.09	157	HZM03	1.82	223	LLM05	0.83	122
QD02	0.94	138	HZM04	1.99	234	LLM07	0.96	141
QD03	0.89	131	HZM10	2.58	261	LLM08	0.88	129
QD04	0.98	143	HZC02*	1.46	194	LLM10	1.04	151
XTM01	1.13	162	HZC03*	1.45	193			
XTM02	1.12	160	BSC04*	2.61	263			
XTM06	1.13	162	BSC05*	2.54	260			
XTM07	1.21	170						

* Data compiled from [18]. During the calculation, R_{\max} is converted into random vitrinite reflectance at first, and then the maximum buried temperature are obtained by the formula given above. Abbreviations: R_{\max} : maximum reflectance; T_{\max} : maximum buried temperature.

been verified that the R_{ev} depends on the chemical composition of anthracites rather than the three-dimensional BSU [30]. Since the chemical composition and structure mainly evolved under the effect of temperature and coincided with the results, the linear- regression slope of Region B seems to be mainly influenced by the thermal effect.

5.2.3. RIS Style and Anisotropy Magnitude. The coefficient values of R_{st} and R_{am} construct polar scatter plots proposed by [23], and the three-dimensional style and anisotropy magnitude of RIS can be analyzed together. As shown in Figure 6(a), samples from Region A and C are characterized by substantial RIS style of biaxial negative (R_{st} ranges between $-30 \sim 15$). The anisotropy magnitude in Region C (R_{am} ranges between $0.04 \sim 0.08$), however, is higher than that in Region A (R_{am} ranges between $0.02 \sim 0.04$), which coincides with the distribution of bireflectance ratio. Conversely, as shown in Figure 6(b), the samples from Region B are characterized by significant biaxial positive character or un conspicuous biaxial negative (R_{st} ranges between $-15 \sim 30$) and the anisotropy magnitude (R_{am}) is various, ranging from 0.02 to 0.06.

5.2.4. RIS-Logarithmic Flinn Diagrams. For a more complete characterization of the optical properties of both raw and carbonized anthracites, the modified Flinn's K parameters [35], related to the anisotropy as well as the optical character, are also calculated and shown in. The samples from Region C and A are characterized by evolvement of RIS style from constriction types to flattening types ($0 < k < 1$ shown in

Figure 7(a)). However, RIS styles of the samples from Region B are complicated and various (as shown in Figure 7(b)), corresponding to plane strain in finite strain analysis.

5.2.5. RIS Anisotropy Evolution Stages . The deformation path of finite strain analyses proposed by Ramsay suggested that the cleavage is developed by the route of “sphere types \rightarrow uniaxial oblate types \rightarrow uniaxial prolate types \rightarrow uniaxial oblate types \rightarrow flattening types”. The anisotropic coal samples may have the same evolution process. A related evolutionary path of RIS style during coalification was reported by Levine [15] and the stages are given as follows.

The first stage was after the deposition. The peat was subjected to mild geothermal process due to broad regional subsidence and burial of overlying rocks. During this period, the ambient geologic stresses were nontectonic and only due to vertical static pressure loading by the overlying strata. Owing to the vertical downward lithostatic pressure, RIS would show the style of uniaxial negative. At the second stage, the anisotropic strain developed by tectonic differential stress (in a lateral direction) and lithostatic pressure (in the vertical direction) and the coal seams would suffer from extrusion in two directions and the anisotropic RIS represents the style of biaxial positive. At the third stage, with the increase of buried depth (more than 1000 m), the pressure on the coal seams from the overlying strata may approximately represent as isotropic hydrostatic pressure (Heim's hypothesis). The tectonic differential stress is upgraded with the enhancement of tectonic agency. All of these factors would make the anisotropic RIS style as biaxial negative.

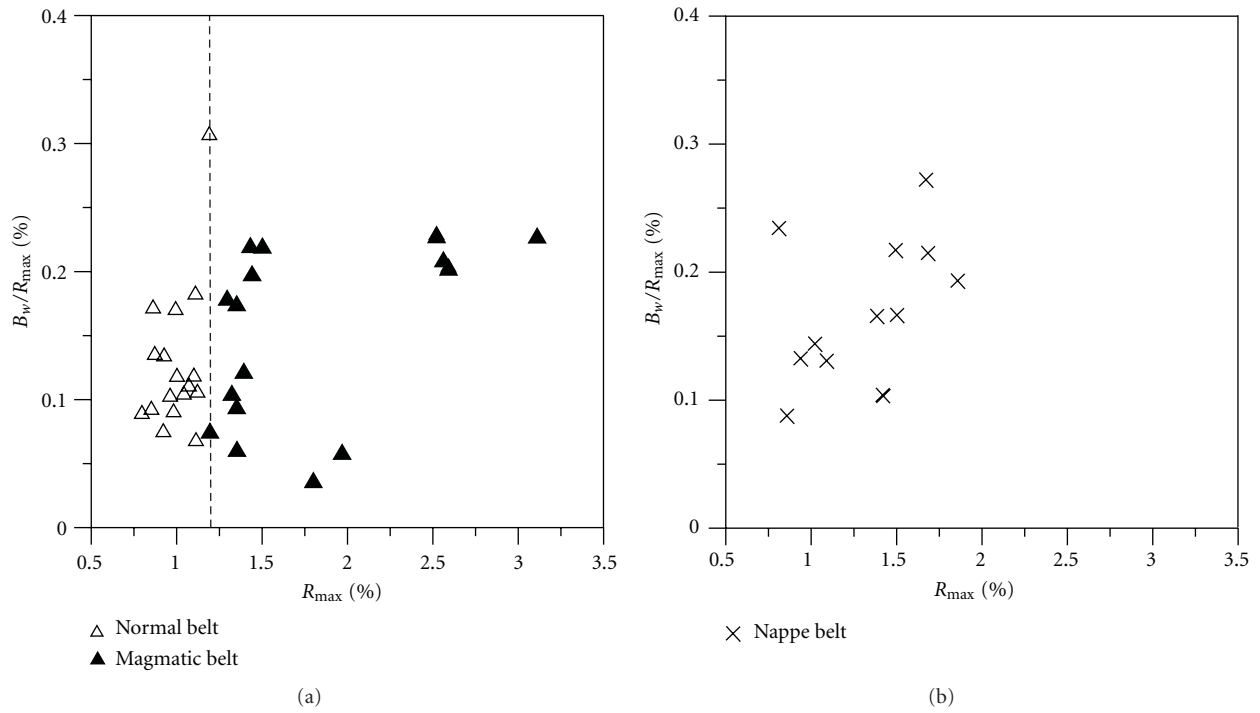


FIGURE 4: Correlations between R_{\max} and B_w/R_{\max} for the anthracites. R_{\max} : maximum reflectance; B_w/R_{\max} : bireflectance ratio.

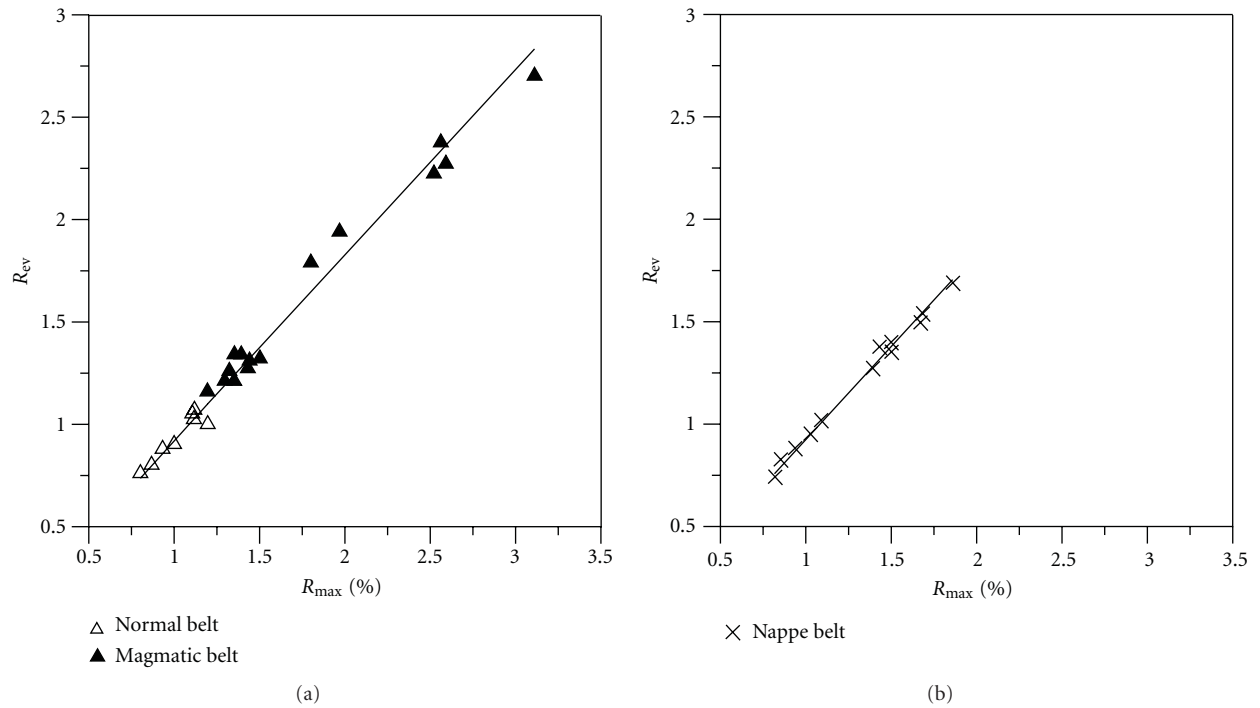


FIGURE 5: Correlation between R_{\max} and R_{ev} for the anthracites. Region A: $y = (0.866 * x) + 0.057$ (coef. of determination, $r^2 = 0.956$); Region B: $y = 0.888x + 0.031$ (coef. of determination, $r^2 = 0.980$); Region C: $y = (0.838 * x) + 0.063$ (coef. of determination, $r^2 = 0.965$); R_{\max} : maximum reflectance; R_{ev} : Reflectance of equivalent volume isotropic RIS, $(R_{\max} \times R_{int} \times R_{min})^{1/3}$.

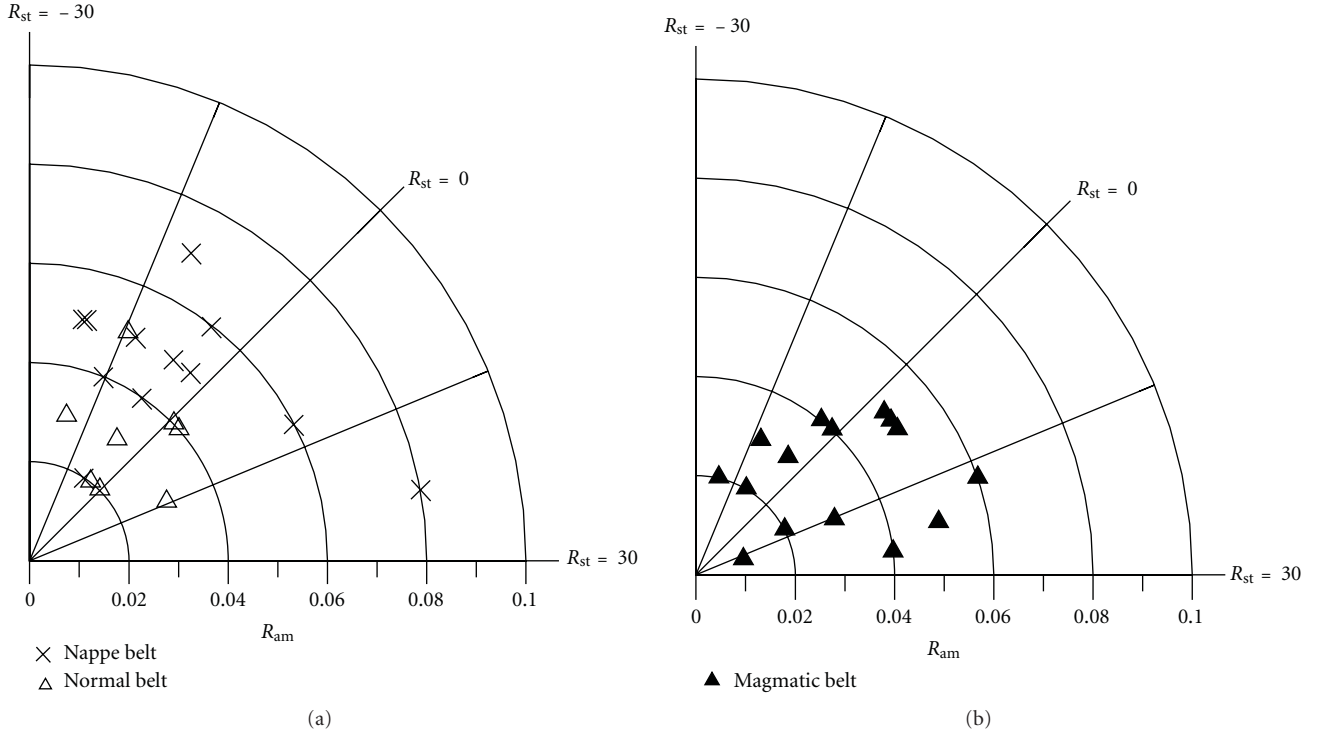


FIGURE 6: R_{st} - R_{am} polar plots of anthracites. R_{am} -RIS anisotropy magnitude, $(x^2 - y^2)^{1/2}$; R_{st} -RIS style, $30\text{-arc tan}(x/y)$ where $x = R_{int}/(R_{max} + R_{int} + R_{min}) + [y + 1/3 \cos 30^\circ] \times \tan 30^\circ - 1/2$, $y = [R_{max}/(R_{max} + R_{int} + R_{min}) - 1/3] \times \cos 30^\circ$; RIS shape described as $-30 < R_{st} < 0$ -biaxial negative; $0 < R_{st} < +30$ -biaxial positive; $R_{st} = (-30)$ uniaxial negative; $R_{st} = (+30)$ uniaxial positive, $R_{st} = 0$ -biaxial neutral.

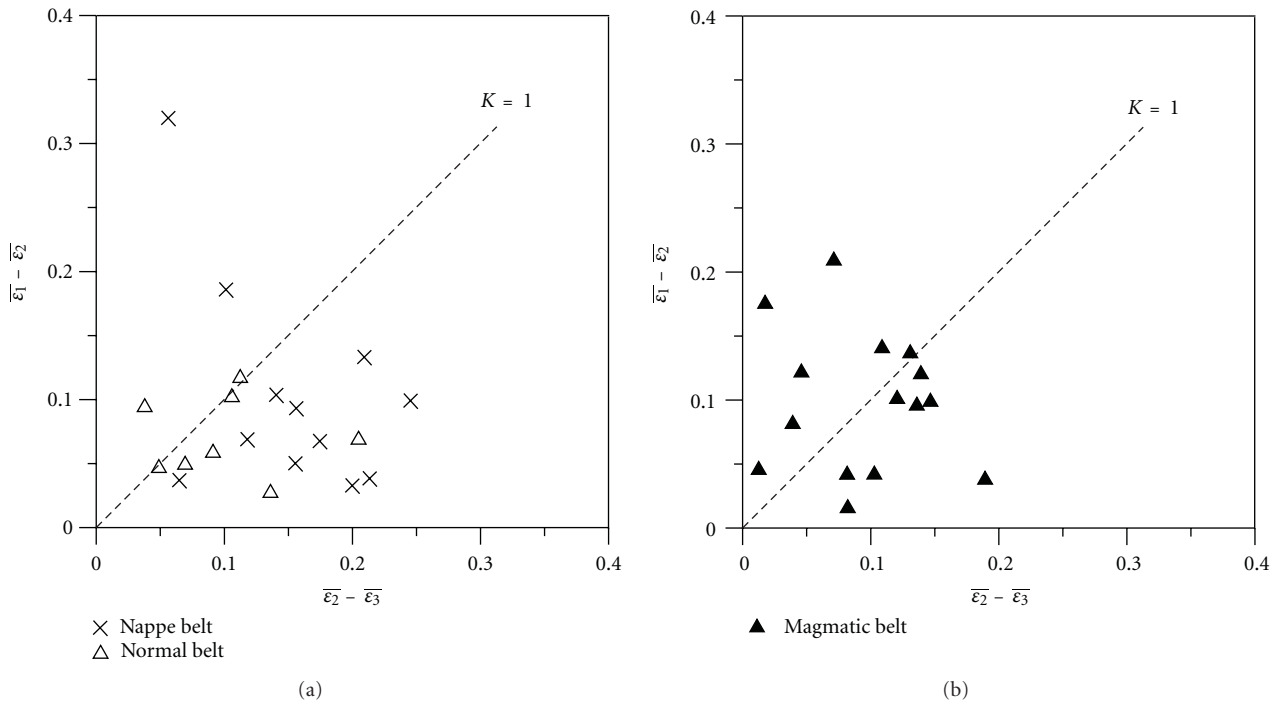


FIGURE 7: RIS-logarithmic Flinn diagrams. The arrowhead directs the evolutionary path of RIS style; K -Flinn's parameter [35], $(\epsilon_1 - \epsilon_2)/(\epsilon_2 - \epsilon_3)$, where $\epsilon_1 = \ln(R_{max})$, $\epsilon_2 = \ln(R_{int})$, $\epsilon_3 = \ln(R_{min})$; $K = \infty$ -uniaxial prolate types; $K = 0$ -uniaxial oblate types; $K = 1$ -plane strain types; $1 < K < \infty$ -constriction types; $0 < K < 1$ -flattening types.

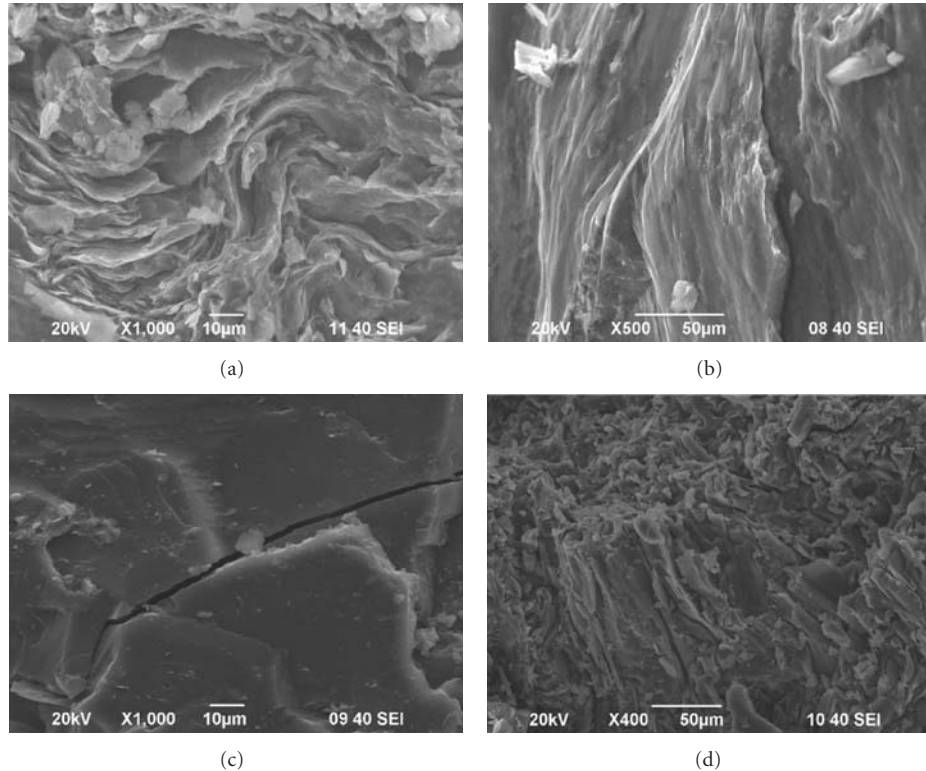


FIGURE 8: SEM photographs showing different types of deformation. (a) YZM16, strongly folded deformation; (b) LHM05, ductile shear deformation; (c) HZM03, slight deformation, brittle fractures; (d) HZM10, strong deformation, locally folded.

As the suggested route given above, the style of uniaxial negative might take place either in the third stage or in the transition between the first and the second stages. More evidence is needed to constrain the actual process of physical deformation and metamorphism. During coalification, the coal samples collected from three regions likely belong to different evolution stages.

- (1) Samples of Region C experienced more effects of tectonic deformation and shearing heat. With significant anisotropy magnitude (higher B_w/R_{\max} and R_{am} value) and biaxial negative style, they have more likely reached into the third stage.
- (2) Samples of Region A experienced more effect of burial metamorphism and less influenced by magmatism and tectonic agency. With unimpressive anisotropy magnitude (lower B_w/R_{\max} and R_{am} value) and biaxial negative style, they more likely belong to the transition between the first to the second stage.
- (3) Samples of Region B influenced by the Mesozoic magmatism, representing polarized anisotropy magnitude (diversified value of R_0 , B_w/R_{\max} and R_{am}). With complicated and various RIS style, they probably belong to the transition between the second and the third stage. Scanning electron microscopic (SEM) photos of coals in the study area indicated that some coal seams have strong deformation (Figure 8). The local stress field was presumably influenced by the

complicated volcanic activity such as granite pegmatite and diorite porphyry during the Yanshanian orogeny [50].

5.3. Implications of RIS-Orientations. As mentioned in Section 1, previous works suggest that minimum reflectance develops incrementally parallel to σ_1 and maximum reflectance develops incrementally parallel to σ_3 during coalification [1, 14]. These viewpoints were verified by simple shear experiments under high temperature-pressure environment [28, 33, 34]. On this basis, the vitrinite reflectance may provide important information about tectonic stress in each period during the coalification, and the σ_1 -direction could be indicated by the minimum reflectance axis.

Eastern North China Craton experienced an important tectonic inversion during Mesozoic. The EW-trending tectonic grain was transformed to NE-NNE-trending and the contractional regime to an extensional regime during Jurassic-Middle Cretaceous [51]. The Huaibei Coalfield lies in the southeastern margin of North China Craton, and influenced by multistage and complicated tectonic events, which could be represented by the triaxial rotation of RIS.

The orientations of RIS axes are respectively projected on the horizontal plane, (Figure 9) and vertical section (Figure 10), and analyzed as follows:

5.3.1. Horizontal Projection. The horizontal projections are based on the stereographic polar method. The radius of base

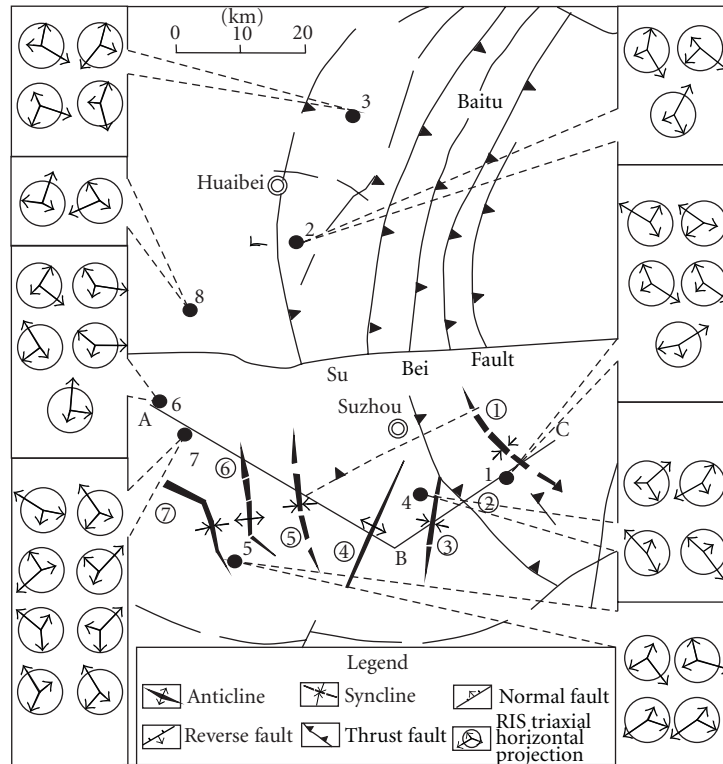


FIGURE 9: RIS-triaxial horizontal Projection. Coal mine label: 1-Luling mine, 2-Yangzhuang mine, 3-Shitai mine, 4-Taoyuan mine, 5-Xutuan mine, 6-Haizi mine, 7-Linhuan mine, 8-Baishan mine. Structure label: (1) Luling syncline; (2) Xisipo fault; (3) Sunan syncline; (4) Sunan anticline; (5) Nanping syncline; (6) Tongting anticline; (7) Wugou syncline. The radius of base circle represents the value of R_{int} ; long (middle and short) arrows represent R_{max} (R_{int} and R_{min}).

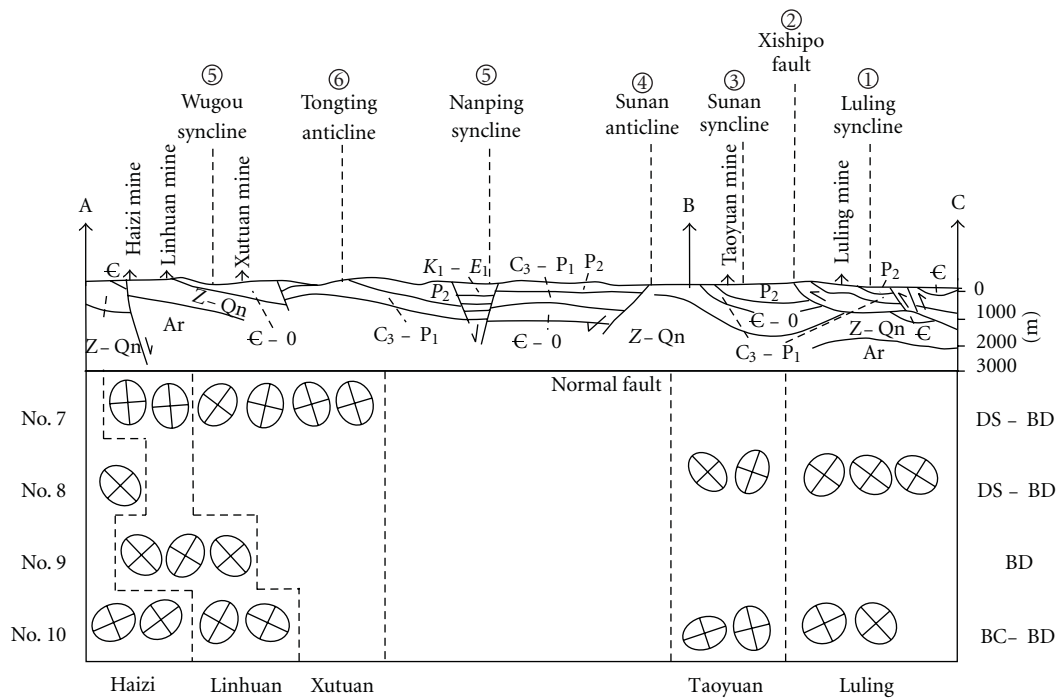


FIGURE 10: RIS-vertical projection. Generally speaking, stronger tectonic agency played the primary role and brought about coal seams to be RIS-orientation basically alike.

circle represents the value of R_{int} . Based on the feature that minimum reflectance develops incrementally parallel to σ_1 [1, 14], the cumulative effect of multistage tectonism on each sample is indicated by the orientation of R_{min} axis.

The samples collected from different working faces have different RIS orientation, even though they are in the same coal mine. The samples of Region C are fan-shaped distributing on the thrust arc, and their R_{min} axial directions are mainly pointing to the center of the circle such as, from north to south in order, NW-SW or NNW-SSE direction in the Luling mine), NEE-SWW direction in Yangzhuang mine, SSE-NNW or NNE-SSW direction in the Shitai mine. In other words, the R_{min} axial direction was parallel to the thrust- direction.

The samples of Region A and B are distributing in the front of the thrust arc and a series of NNW-NE-trending folds. Their R_{min} axial directions are mainly perpendicular to the corresponding fold-hinge as shown in Figure 9. These features suggest that the RIS-orientation in these areas was primarily controlled by the thrust-fold system.

5.3.2. Vertical Projections. The cross-section (A-B-C) is about perpendicular to the hinges of the major folds and its position is shown in Figure 9. The vertical projections on the cross-section are based on RIS-analyses of the samples from five coal mines. Since most of the R_{min} axial directions are located in the cross-section, the projection provides information on RIS-dip angles.

Samples of the Luling mine belong to Region C, and their RIS orientations were following the direction of thrust. Number 8 coal seam has similar RIS dips as Number 10. However, samples of the Taoyuan mine, Xutuan mine, Linhuan mine and Haizi mine seem to be more influenced by the regional tectonic stress, the distinctions between samples of different coal seam are obvious.

Combining with the deformation type of coal samples (as listed in Table 3), No. 7, No. 8, and No. 9 coal seams are mainly characterized as ductile-type or brittle-ductile-type, with lower R_{min} axial dip angles. In contrast, No. 10 coal seam is mainly characterized as brittle-type or brittle-ductile type, and their RIS R_{min} axial dip angles are higher. The contrastive fact indicates that the coal samples in different deformation types have remarkably different RIS orientation, although they belong to the same structural unit.

6. Conclusions

Our results indicate that:

- (1) there are obvious relationships between the anisotropic parameters and tectonic stress action. Based on the tectonic situation, the Huaibei Coalfield is divided into three regions. Samples of each region have special RIS-shape and magnitude. Samples of Region C have significant anisotropy magnitude (higher B_w/R_{max} and R_{am} value) and biaxial negative style. By contrast, samples of the Region A have unimpressive anisotropy magnitude and biaxial negative style. Samples of Region B represent

polarized anisotropy magnitude (diversified value of R_o , B_w/R_{max} and R_{am}) with complicated and various RIS styles,

- (2) orientation of RIS is mainly controlled by regional tectonic stress: either parallel to the direction of thrusting or perpendicular to the hinge of folds. It is likely influenced by deformation mechanisms of coal.

Acknowledgments

These research results are part of a key project carried out in 2006–2011 and financially supported by The national Natural Science Foundation of China (Grant no. 41030422; 40940014; 40772135) and National Basic Research Program of China (Grant no. 2009CB219601). The authors are grateful to Dai Jiming and Ai Tianjie at China University of Mining and Technology (Beijing) for their assistance in the experiments. Many thanks to Zheng Yadong, Wang Guiliang, Jin Weijun and Liu Qinfu, Liu Dameng, and three reviewers for their help with improving the paper.

References

- [1] I. Stone and A. Cook, "The influence of some tectonic structures upon vitrinite reflectance," *The Journal of Geology*, vol. 87, pp. 497–508, 1979.
- [2] E. Stach, M.-T. Mackowsky, M. Techmuller, G. H. Taylor, D. Chandra, and R. Techmuller, *Stach's Textbook of Coal Petrology*, 3rd edition, 1982.
- [3] J. V. Ross, R. M. Bustin, and J. N. Rouzaud, "Graphitization of high rank coals—the role of shear strain: experimental considerations," *Organic Geochemistry*, vol. 17, no. 5, pp. 585–596, 1991.
- [4] R. M. Bustin, J. V. Ross, and J. N. Rouzaud, "Mechanisms of graphite formation from kerogen: experimental evidence," *International Journal of Coal Geology*, vol. 28, no. 1, pp. 1–36, 1995.
- [5] J. Komorek and R. Morga, "Relationship between the maximum and the random reflectance of vitrinite for coal from the Upper Silesian Coal Basin (Poland)," *Fuel*, vol. 81, no. 7, pp. 969–971, 2002.
- [6] S. Pusz, S. Duber, and B. K. Kwiecińska, "The study of textural and structural transformations of carbonized anthracites," *Fuel Processing Technology*, vol. 77–78, pp. 173–180, 2002.
- [7] J. Komorek and R. Morga, "Vitrinite reflectance property change during heating under inert conditions," *International Journal of Coal Geology*, vol. 54, no. 1–2, pp. 125–136, 2003.
- [8] S. Pusz, B. K. Kwiecińska, and S. Duber, "Textural transformation of thermally treated anthracites," *International Journal of Coal Geology*, vol. 54, no. 1–2, pp. 115–123, 2003.
- [9] M. Krzesińska, S. Pusz, and A. Koszorek, "Elastic and optical anisotropy of the single-coal monolithic high-temperature (HT) carbonization products obtained on a laboratory scale," *Energy and Fuels*, vol. 19, no. 5, pp. 1962–1970, 2005.
- [10] D. Y. Cao, X. M. Li, and S. R. Zhang, "Influence of tectonic stress on coalification: stress degradation mechanism and stress polycondensation mechanism," *Science in China, Series D*, vol. 50, no. 1, pp. 43–54, 2007.
- [11] J. P. Jiang, G. Y. Gao, and J. W. Kang, "Tests on vitrinite reflectance of coal and analysis of tectonic stress field," *Chinese*

- Journal of Geophysics (Acta Geophysica Sinica)*, vol. 50, no. 1, pp. 138–145, 2007.
- [12] J. Komorek and R. Morga, "Evolution of optical properties of vitrinite, sporinite and semifusinite in response to heating under inert conditions," *International Journal of Coal Geology*, vol. 71, no. 4, pp. 389–404, 2007.
 - [13] I. Suárez-Ruiz and A. B. García, "Optical parameters as a tool to study the microstructural evolution of carbonized anthracites during high-temperature treatment," *Energy and Fuels*, vol. 21, no. 5, pp. 2935–2941, 2007.
 - [14] J. R. Levine and A. Davis, "Optical anisotropy of coals as an indicator of tectonic deformation, Broad Top Coal Field, Pennsylvania (USA)," *Geological Society of America Bulletin*, vol. 95, no. 1, pp. 100–108, 1984.
 - [15] J. R. Levine and A. Davis, "Reflectance anisotropy of Upper Carboniferous coals in the Appalachian foreland basin, Pennsylvania, U.S.A.," *International Journal of Coal Geology*, vol. 13, no. 1-4, pp. 341–373, 1989.
 - [16] B. Jiang and Y. Qin, "Experimental research on deformation of optical fabric of coal vitrinite reflectance experimental research on deformation of optical fabric of coal vitrinite reflectance," *Coal Geology & Exploration*, vol. 25, pp. 11–15, 1997 (Chinese).
 - [17] J. C. Hower and A. Davis, "Vitrinite reflectance anisotropy as a tectonic fabric element," *Geology*, vol. 9, pp. 165–168, 1981.
 - [18] D. Y. Cao, "The vitrinite reflectance anisotropy in the nappe structure in the Huaibei coalfield, Anhui province," *Geology Review*, vol. 36, pp. 333–340, 1990 (Chinese).
 - [19] W. Langenberg and W. Kalkreuth, "Reflectance anisotropy and syn-deformational coalification of the Jewel seam in the Cadomin area, Alberta, Canada," *International Journal of Coal Geology*, vol. 19, no. 1-4, pp. 303–317, 1991.
 - [20] B. Jiang, F. Y. Xu, Y. Liu, and F. L. Jin, "Vitrinite optical fabric and stress-strain analysis of northern margin of Chaidamu Basin," *Journal of China University of Mining & Technology*, vol. 31, pp. 561–564, 2002.
 - [21] J. Jones and S. Creaney, "Optical character of thermally metamorphosed coals of northern England," *Journal of Microscopy*, vol. 109, pp. 105–118, 1977.
 - [22] G. K. Khorasani, D. G. Murchison, and A. C. Raymond, "Molecular disordering in natural cokes approaching dyke and sill contacts," *Fuel*, vol. 69, no. 8, pp. 1037–1046, 1990.
 - [23] W. E. Kilby, "Recognition of vitrinite with non-uniaxial negative reflectance characteristics," *International Journal of Coal Geology*, vol. 9, no. 3, pp. 267–285, 1988.
 - [24] W. E. Kilby, "Vitrinite reflectance measurement—some technique enhancements and relationships," *International Journal of Coal Geology*, vol. 19, no. 1-4, pp. 201–218, 1991.
 - [25] J. C. Hower, R. F. Rathbone, G. D. Wild, and A. Davis, "Observations on the use of vitrinite maximum reflectance versus vitrinite random reflectance for high volatile bituminous coals," *Journal of Coal Quality*, vol. 13, pp. 71–76, 1994.
 - [26] K. R. Wilks, M. Mastalerz, R. M. Bustin, and J. V. Ross, "The role of shear strain in the graphitization of a high-volatile bituminous and an anthracitic coal," *International Journal of Coal Geology*, vol. 22, no. 3-4, pp. 247–277, 1993.
 - [27] D. W. Houseknecht and C. M. B. Weesner, "Rotational reflectance of dispersed vitrinite from the Arkoma basin," *Organic Geochemistry*, vol. 26, no. 3-4, pp. 191–206, 1997.
 - [28] J. V. Ross and R. M. Bustin, "Vitrinite anisotropy resulting from simple shear experiments at high temperature and high confining pressure," *International Journal of Coal Geology*, vol. 33, no. 2, pp. 153–168, 1997.
 - [29] S. Duber and J. N. Rouzaud, "Calculation of relectance values for two models of texture of carbon materials," *International Journal of Coal Geology*, vol. 38, no. 3-4, pp. 333–348, 1999.
 - [30] S. Duber, S. Pusz, B. K. Kwecińska, and J. N. Rouzaud, "On the optically biaxial character and heterogeneity of anthracites," *International Journal of Coal Geology*, vol. 44, no. 3-4, pp. 227–250, 2000.
 - [31] A. C. Cook, D. G. Murchison, and E. Scott, "Optically biaxial anthracitic vitrinites," *Fuel*, vol. 51, no. 3, pp. 180–184, 1972.
 - [32] F. Ting, "Uniaxial and biaxial vitrinite reflectance models and their relationship to paleotectonics," in *Organic Maturation Studies and Fossil Fuel Exploration*, J. Brooks, Ed., pp. 379–392, Academic Press, London, UK, 1981.
 - [33] R. M. Bustin, J. V. Ross, and I. Moffat, "Vitrinite anisotropy under differential stress and high confining pressure and temperature: preliminary observations," *International Journal of Coal Geology*, vol. 6, no. 4, pp. 343–351, 1986.
 - [34] B. Jiang, F. Jin, Q. Zhou, and W. Wang, "Experimental research on deformation of optical fabric of coal vitrinite reflectance," *Coal Geology & Exploration*, vol. 25, pp. 11–15, 1997 (Chinese).
 - [35] J. G. Ramsay, *Folding and Fracturing of Rocks*, Mc Graw-Hill, New York, NY, USA, 1967.
 - [36] Y. D. Wu, Y. W. Ju, Q. L. Hou, S. Hu, S. Q. Ni, and J. J. Fan, "Characteristics of tectono-thermal modeling and restriction on coalbed-gas generation in Sulin mining area, Huaibei coalfield," *Progress in Natural Science*, vol. 19, pp. 1134–1141, 2009 (Chinese).
 - [37] W. Guiliang, J. Bo, C. Daiyong, Z. Hai, and J. Weijun, "On the Xuzhou-Suzhou arcuate duplex-imbricate fan thrust system," *Acta Geologica Sinica*, vol. 72, no. 3, pp. 235–236, 1998.
 - [38] Y. W. Ju, Q. L. Hou, B. Jiang, G. L. Wang, and A. M. Fang, "Tectonic coals: structure and physical properties of reservoirs," in *Proceedings of the Proceedings of the 6th International Workshop on CBM/CMM in China*, Beijing, China, 2006.
 - [39] G. Zhu, C. Song, D. Wang, G. Liu, and J. Xu, "Studies on $^{40}\text{Ar}/^{39}\text{Ar}$ thermochronology of strike-slip time of the Tan-Lu fault zone and their tectonic implications," *Science in China, Series D*, vol. 44, no. 11, pp. 1002–1009, 2001.
 - [40] G. Zhu, Y. Wang, G. Liu, M. Niu, C. Xie, and C. Li, " $^{40}\text{Ar}/^{39}\text{Ar}$ dating of strike-slip motion on the Tan-Lu fault zone, East China," *Journal of Structural Geology*, vol. 27, no. 8, pp. 1379–1398, 2005.
 - [41] G. Zhu, C. L. Xie, Y. S. Wang, M. L. Niu, and G. S. Liu, "Characteristics of the Tan-Lu high-pressure strike-slip ductile shear zone and its $^{40}\text{Ar}/^{39}\text{Ar}$ dating," *Acta Petrologica Sinica*, vol. 21, no. 6, pp. 1687–1702, 2005.
 - [42] A. Yin and S. Nie, "An indentation model for the north and south China collision and development of the Tan-Lu and Honam fault systems, Eastern Asia," *Tectonics*, vol. 12, pp. 810–813, 1993.
 - [43] G. Zhu, Y. S. Wang, N. M. Lan, G. S. Liu, and C. L. Xie, "Synorogenic movement of the Tan-Lu fault zone," *Earth Science Frontiers*, vol. 11, pp. 169–182, 2004 (Chinese).
 - [44] D. Liu, Y. Yao, D. Tang, S. Tang, Y. Che, and W. Huang, "Coal reservoir characteristics and coalbed methane resource assessment in Huainan and Huaibei coalfields, Southern North China," *International Journal of Coal Geology*, vol. 79, no. 3, pp. 97–112, 2009.
 - [45] D. Flinn, "On folding during three-dimensional progressive deformation," *Quarterly Journal of the Geological Society*, vol. 118, pp. 385–428, 1962.

- [46] C. Barker and M. Pawlewicz, "The correlation of vitrinite reflectance with maximum temperature in humic organic matter," *Lecture Notes in Earth Science*, vol. 5, pp. 79–81, 1986.
- [47] F. Goodarzi and D. G. Murchison, "Optical properties of carbonized vitrinites," *Fuel*, vol. 51, no. 4, pp. 322–328, 1972.
- [48] D. G. Murchison, "Petrographic aspects of coal structure: reactivity of macerals in laboratory and natural environments," *Fuel*, vol. 70, no. 3, pp. 296–315, 1991.
- [49] S. Duber, J. N. Rouzaud, C. Clinard, and S. Pusz, "Microporosity and optical properties of some activated chars," *Fuel Processing Technology*, vol. 77–78, pp. 221–227, 2002.
- [50] G. L. Wang, B. Jiang, D. Y. Cao, H. Zou, and W. J. Jin, "On the Xuzhou-Suzhou arcuate duplex-imbricate fan thrust system," *Acta Geologica Sinica (in Chinese with English summary)*, vol. 72, pp. 228–236, 1998.
- [51] M. Zhai, R. Zhu, J. Liu et al., "Time range of Mesozoic tectonic regime inversion in eastern North China Block," *Science in China, Series D*, vol. 47, no. 2, pp. 151–159, 2004.

Research Article

Geochronology and Tectonic Evolution of the Lincang Batholith in Southwestern Yunnan, China

Hongyuan Zhang,^{1,2} Junlai Liu,^{1,2} and Wenbin Wu²

¹ State Key Laboratory of Geological Processes and Mineral Resources, China University of Geosciences, Beijing 100083, China

² Faculties of Earth Sciences and Resources, China University of Geosciences, Beijing 100083, China

Correspondence should be addressed to Hongyuan Zhang, zhang-hong-yuan@263.net

Received 15 February 2012; Accepted 5 April 2012

Academic Editor: Quan-Lin Hou

Copyright © 2012 Hongyuan Zhang et al. This is an open access article distributed under the Creative Commons Attribution License, which permits unrestricted use, distribution, and reproduction in any medium, provided the original work is properly cited.

Geochronological research of the Lincang Batholith is one key scientific problem to discuss the tectonic evolution of the Tethys. Two granitic specimens were selected from the Mengku-Douge area in the Lincang Batholith to perform the LA-ICPMS Zircon U-Pb dating based on thorough review of petrological, geochemical, and geochronological data by the former scientists. Rock-forming age data of biotite granite specimen from Kunsai is about 220 Ma, the Norian age. However, the west sample from Mengku shows 230 Ma, the Carnian age. The later intrusion in Kunsai area located east to the Mengku area shows directly their uneven phenomena in both space and time and may indirectly reflect the space difference of the contraction-extension transformation period of the deep seated faults. Considering the former $^{40}\text{Ar}/^{39}\text{Ar}$ data and the outcrop in Mengku, the Lincang Batholith should have experienced one tectonic exhumation and regional subsidence cycle. The regional subsidence cycle has close relations to the expansion of the Meso Tethys.

1. Introduction

The Sanjiang-Indochina region is one key area to study the evolution of the Tethys [1–10] (Figure 1). The Changning-Menglian zone was considered as the major faunal break between Gondwanan assemblage to the west and Cathaysian to the east [11, 12]. The subduction-related magmatism occurred along the western edge of the Lanping-Simao-Indochina terrane throughout the Triassic and the closure of Palaeo-Tethys [12, 13]. The Lincang Batholith extends ~370 km from north to south, covering the Chiangrai-Chiang Mai region of Thailand, with an area of more than 10000 km² (Figure 2). It has been shown by many authors that there is great mineral potential [14].

The Lincang Batholith was divided into three lithologic intervals by previous authors, the Xiaojie, Lincang, and Menghai intervals (Figure 2) [15–17]. The major intrusion is porphyritic monzonitic granite, which mainly contains quartz, zonal plagioclase, K-feldspar, and biotite. In addition, geochemical studies have shown that the granite mainly has source features of the crust mixing origin [16, 18].

The Lincang Batholith was proposed to form in a passive continental margin according to geochemical research [19]. The intrusive timing spans from late Permian to late Triassic based on whole-rock Rb-Sr, mineral $^{40}\text{Ar}/^{39}\text{Ar}$, whole-rock $^{87}\text{Sr}/^{86}\text{Sr}$, Rb-Sr, Sm-Nd, and some other methods (Table 1).

But there are also some understanding differences on the crystallization period and evolution time of the Lincang Batholith. Many predecessors discussed mineral diagenesis and tectonic evolution through traditional data [16, 20], although, not from the viewpoint of the plate tectonics. On scientific problems of the Lincang Batholith, some solutions were put forward such as single period of mixed granite [16], quasi-situ metasomatic granite [20], or Neoproterozoic type I granite complex batholith with multiperiod transforming events [19].

Therefore, the formation and evolution of the Lincang Batholith is still the key to discuss the regional tectonic evolution of the Baoshan and Lanping-Simao-Indochina block. In this study, we conducted petrographic analysis of the Lincang Batholith and provide new LA-ICP-MS U-Pb data in order to constrain the tectonic evolution of the

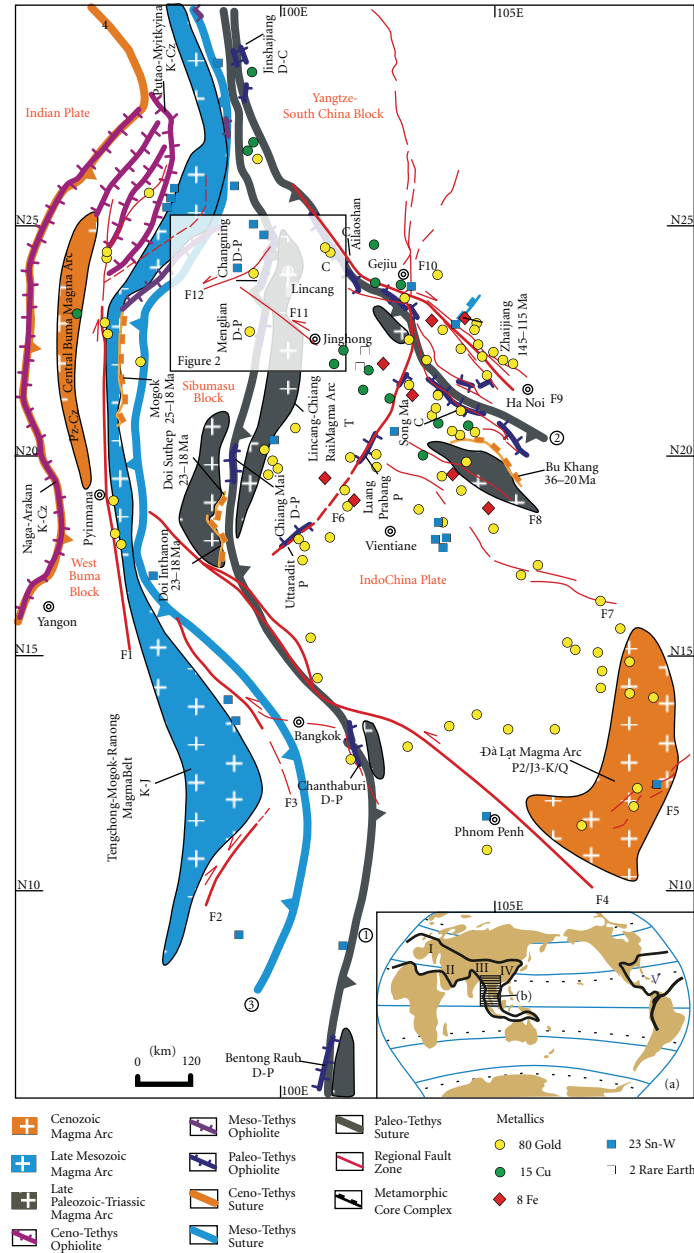


FIGURE 1: Map of plate tectonics and ore-forming metals in the southern Sanjiang and Indochina peninsula. (a) Scope of Tethys and zone divisions; (b) research area and distribution of major metals: (1) Changning-Menglian-Chiangmai Paleotethys Suture (time and space after [1, 21, 22]); (2) Ailaoshan-Song Ma Paleotethys Suture (time and space after [2, 6, 8]); (3) Bangong Co-Nujiang Meso-Tethys Suture (time and space after [5]); (4) Yanlung Tsangpo-Naga-Arakan New-Tethys Suture (time and space after [22, 23]); (F1) Nujiang-Saging Fault Zone; (F2) Ranong Fault Zone; (F3) Three Tower Fault Zone; (F4) Tonle Sap Fault Zone; (F5) Đà Lạt-Bianhe Fault Zone; (F6) Điện Biên Phủ Fault Zone; (F7) Changshan-Da Nang Fault Zone; (F8) Lanjiang Fault Zone; (F9) Ailaoshan-Red River Fault Zone; (F10) Xianshuihe-Xiaojiang Fault Zone; (F11) Lancang-Jinghong Fault Zone.

Batholith. We discuss these results of dating in the context of regional tectonic evolution.

2. Dating Methods, Specimens, and Results

2.1. Dating Methods. The U-Pb zircon age dating of monzonitic granite samples selected from the Mengku-Douge research area in Lincang segment (Figures 2 and 3) was

designed and completed in the Institute of Geology and Geophysics, Chinese Academy of Sciences. Jobs of single zircon grain micro-area U-Pb geochronological analysis were taken through Laser Ablation Inductively Coupled Plasma Mass Spectrometry (LA-ICPMS) of 7500a-type produced by Agilent Co. Ltd., with which the laser beam diameter is $60\ \mu\text{m}$, the erosion frequency is 8 Hz, the energy density is $15\sim 20\ \text{J}\cdot\text{cm}^{-2}$, the erosion time is about 60 s. For detailed

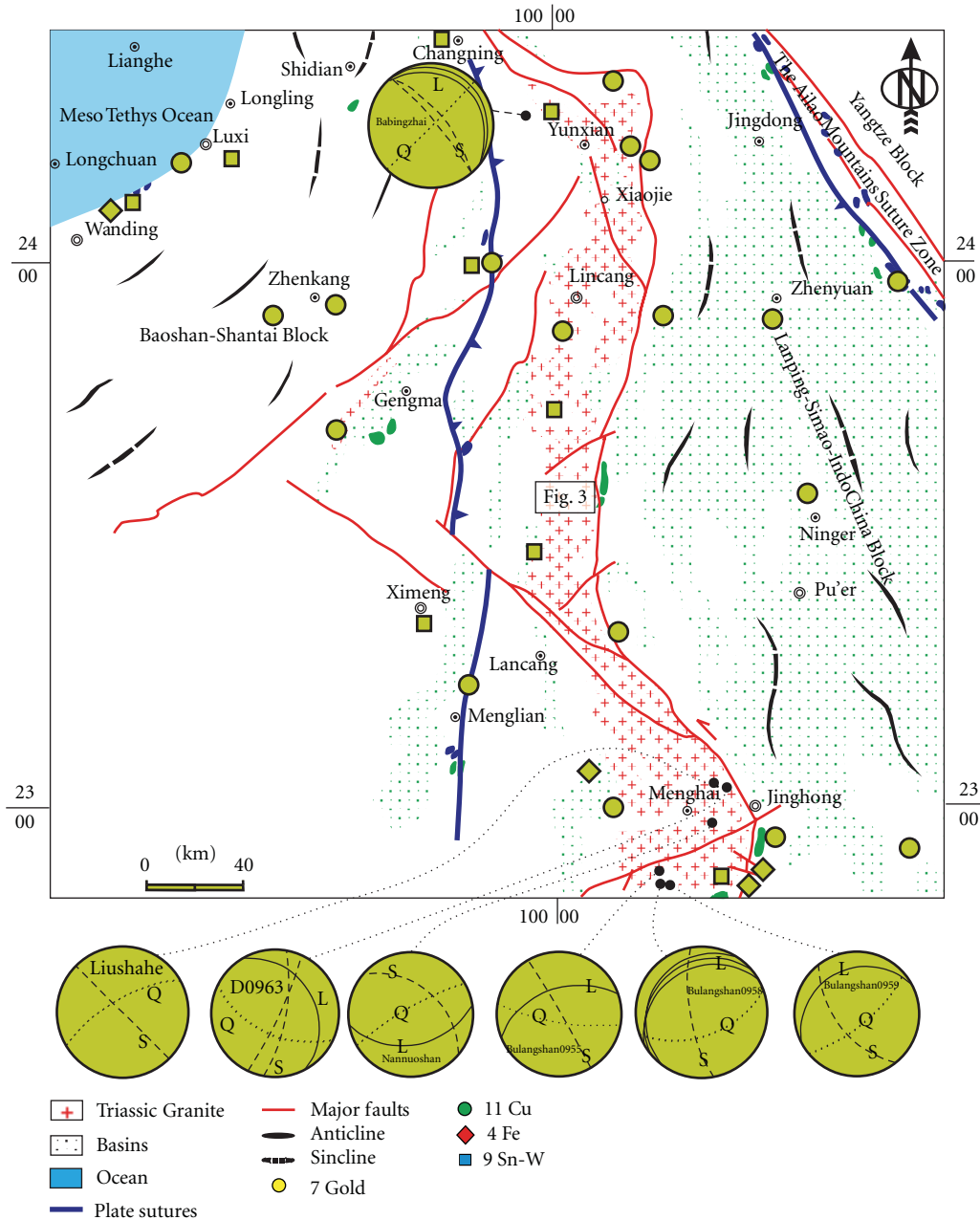


FIGURE 2: Regional map of Indian Period and research locality in western Yunnan. The distribution of metal deposits also indicates that there is an important boundary along the Lincang Granite Batholith. Stereographic maps of lower hemisphere projection indicating the initial occurrence of Lincang granite Batholith are also plotted in the regional map. L, S, Q refer to joints parallel to the initial foliation, parallel to the flow direction but upright to the initial foliation, upright to both the flow direction and initial foliation. Orientation of shear fractures can be generated by local stress system of the Batholith with emplacements [24].

analysis procedures, please see Xu et al. [32]. The Zircon U-Pb isotope and the U, Th data processing are finished by software Glitter4. 0 [33], and computing of U-Pb concordia diagrams, weighted average ages and graphics were completed by software Isoplot3.0 [34].

2.2. Specimens

2.2.1. Specimen from Kunsai Quarries. The biotite monzonitic granite samples were selected from the Kunsai

quarries to the east of Quannei-Douge migmatite rock belt (Figures 3 and 4(a)). The north part of the rock unit is plunged into the Jurassic basin (Figure 3). Field study shows that both the rock unit and the Jurassic basin have experienced a period of ductile transformation events. The microstructure study shows brittle deformed feldspar (Figures 4(b) and 4(c)), dynamically recrystallized quartz (Figure 4(c)), microdeflected biotite (Figure 4(d)), zircon grains with relatively intact crystal, long column, some

TABLE 1: Isotopic age data for the Lincang Batholite in the earlier stage.

Lithologic section	Lithology	Measured objects and methods	Dating results, Ma	Sample positions	Testers and the time
Xiaojie	Granite porphyry	Whole-rock (Rb-Sr)	169 ± 5	Laomaocun	Zhang et al., 2006 [25]
Xiaojie	Monzonitic granite	Whole-rock ($^{87}\text{Sr}/^{86}\text{Sr}$)	279	Yun County	Chen, 1991 [26]
Lincang	Biotite granite	Biotite ($^{40}\text{Ar}/^{39}\text{Ar}$)	201.1 ± 2.7	Near the Lancangjiang River	Dai et al., 1986 [27]
Lincang	Monzonitic granite	Whole-rock (Rb-Sr)	279	Lincang	Chen, 1991 [26]
Lincang	Medium-grained equigranular granodiorite	Whole-rock (Rb-Sr)	263.8	Milestone along Lincang-Mengku road 327–387 km	Zhang et al., 1990 [28]
Lincang	Unequal-sized biotite granite	Whole-rock (Rb-Sr)	193	Shangyun-Xiaotang	Zhang et al., 1990 [28]
Lincang	Monzonitic granite	Whole-rock (Rb-Sr)	275 ± 59	Lincang	Liu et al., 1989 [18]
Menghai	Monzonitic granite	Whole-rock ($^{87}\text{Sr}/^{86}\text{Sr}$)	279	Menghai	Chen, 1991 [26]
Menghai	Monzonitic granite	Biotite (Rb-Sr)	256	Menghai	Wang, 1984 [29]

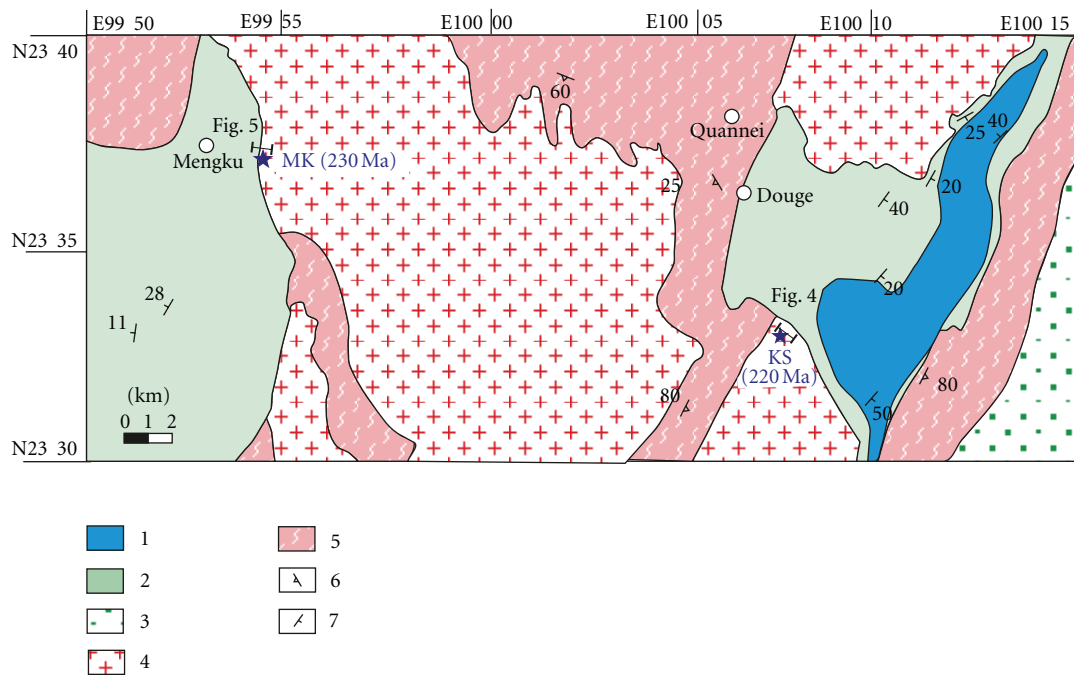


FIGURE 3: Geological sketch map in Mengku-Douge area (revised after [15–17, 30, 31]) (1) Area of ingress ion sea of the Meso-Tethys; (2) Jurassic terrigenous sediments; (3) Early Jurassic volcanic sedimentary rocks; (4) Lincang Triassic granite rock; (5) deep metamorphic wedge with local granodiorite quality migmatization Late Paleozoic; (6) schistosity occurrence; (7) bedding occurrence.

rounded output and a higher degree of porosity which is symbiotic to microcline grains (Figure 4(b)). The cathode luminescence (CL) images show that the typical magmatic zircon characteristics are colorless and transparent here with oscillatory zoning, the length of about $120\ \mu\text{m}$ – $420\ \mu\text{m}$ and the aspect ratio of 1.2 to 4.1 (Figure 4(e)). Totally, for 22 points of 22 zircon grains of sample biotite granodiorite KS-2 from the Kunsai quarries we performed U-Pb isotope analysis in order to statistically gain a feasible dating result (Figure 4(f)). All points were selected on the edge of long- column euhedral grains where the magmatic zircon oscillatory zoning is clear.

2.2.2. Specimens from Mengku Quarries. The monzonitic granite sample MK-4 is selected from the Mengku East Quarry at the eastern side of the Mengku Town in the Shuangjiang County, which separates Jurassic red clastic rocks with one bedding bottom granitic conglomerate by the paleo-weathering crust in between (Figures 5(a), 5(b), and 5(c)). Figure 5(a) shows the position photo of the biotite monzonitic granite sample in the Mengku East Quarry. From the field outcrop, both granitic intrusion (lower left) and its weathering top can be found to be cleaved which had been covered by the upper Jurassic red detrital sediments with terrigenous origin, namely, the Huakaizuo Formation.

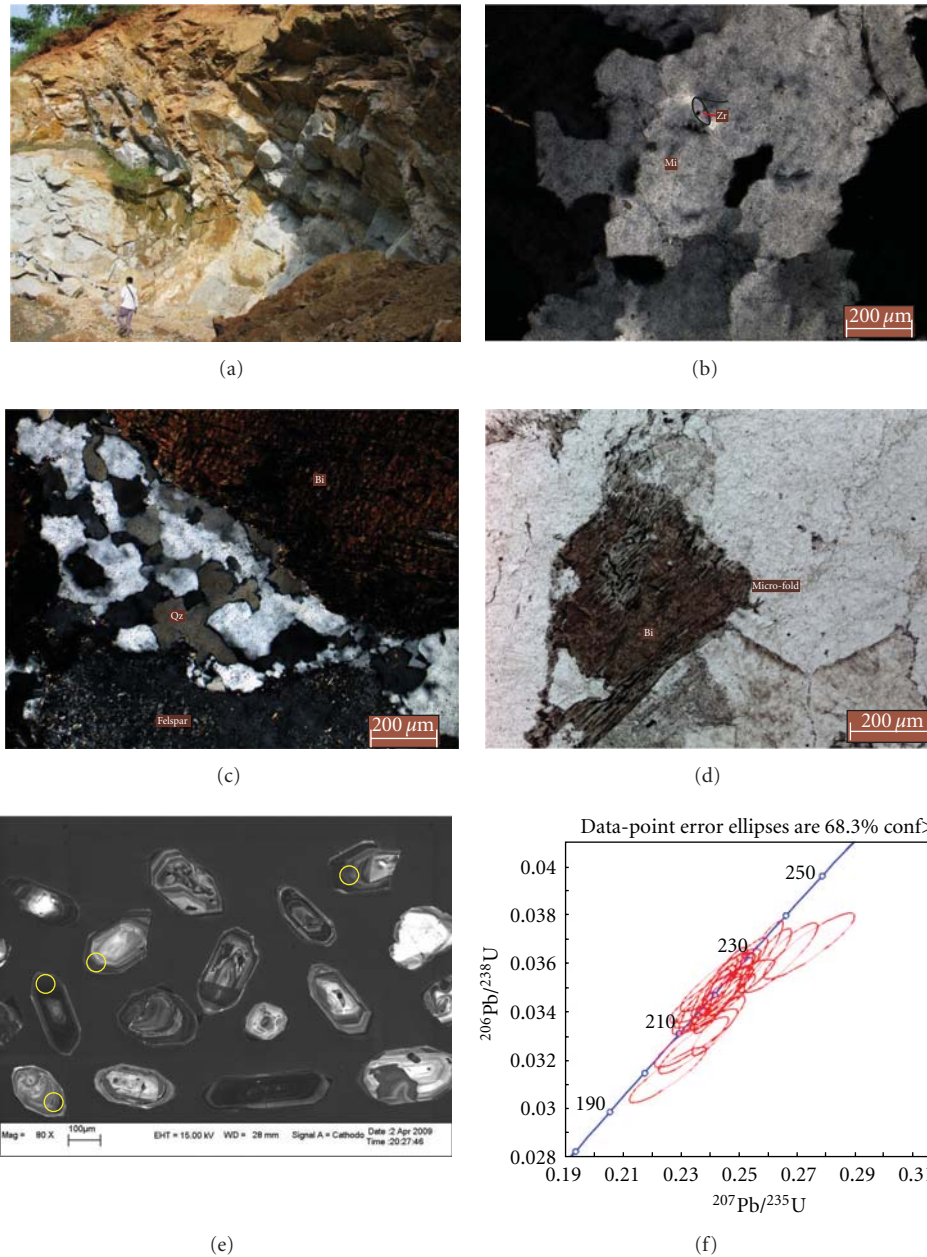


FIGURE 4: Geochronological research of granite sample KS-2. (a) Position photo of the biotite monzonitic granite sample in the field of Kunsai Quarry. (b) The zircon grows together with the microcline CPL. (c) The microstructure of complete recrystallized quartz indicates the rock once experienced high-greenschist facies of deformation, CPL. (d) One biotite crystal is folded, PPL. (e) Magmatic zircon is shown by the SEM cathodoluminescence (CL) image. The circled area is deduced to form during the crystallization of granite and is just the measured area by laser-ICPMS (f) Zircon La-ICPMS U-Pb dating figure, and the average age is about 220 Ma.

The MK-4 zircon grains (Figure 5(d)) change greatly and have different shapes and sizes, such as long column, fan, and irregular granular. However, size of zircon grains is uniform with length between 90 μm and 150 μm and length-width ratio in 1.1:1–1.8:1. Zircon grains develop with quartz, plagioclase in rocks. The rock sample has been affected by weathering, showing retrograde metamorphism (Figure 5(e)). Characteristic oscillatory zoning of typical magmatic zircon is rendered on the cathode CL image. The

idiomorphic degree of zircon is high, but some fragmented. On the sample of MK-4, 18 zircon grains and 18 points were analyzed by ICP-MS. Edge of the long-column idiomorphic or the chipped-hypidiomorphic zircon grains, and the clear zone of magmatic zircon oscillatory were always selected to perform the micro isotope analysis (Figure 5(f)).

2.2.3. Dating Results. As shown in Figure 4(f) and Table 2, the overall harmony values of KS-2 zircon age data range



FIGURE 5: Geochronological research of the granite sample MK-4. (a) Position photo of the biotite monzonitic granite sample in a field Quarry of east Mengku. (b) Granitic intrusion (lower left) and its fossil weathering were cleaved. (c) The red detrital material of terrigenous origin, Huakaizuo Formation in Jurassic, was normal gradational. (d) Granitic intrusions are selected as sample. (e) The micro characteristics of MK-4 and the zircon setting are shown. The zircon grains are associated with quartz and plagioclase and have been degraded by some weathering process, CPL, (f) Magmatic zircon is shown by the SEM cathodoluminescence (CL) image. The circled area is deduced to form during the crystallization of granite and is just the measured area by laser-ICPMS. (g) Zircon La-ICPMS U-Pb dating figure, and the average age is about 245 Ma.

TABLE 2: U-Pb isotopic dating for the single grain Zircon from granite of Kunsai.

No.	$^{207}\text{Pb}/^{206}\text{Pb}$			$^{207}\text{Pb}/^{235}\text{U}$			$^{206}\text{Pb}/^{238}\text{U}$			$^{208}\text{Pb}/^{232}\text{Th}$			$^{207}\text{Pb}/^{206}\text{Pb}$			$^{207}\text{Pb}/^{235}\text{U}$			$^{206}\text{Pb}/^{238}\text{U}$			$^{208}\text{Pb}/^{232}\text{Th}$		
	Ratio	Error (1σ)		Ratio	Error (1σ)		Ratio	Error (1σ)		Ratio	Error (1σ)		Ratio	Error (1σ)		Ratio	Error (1σ)		Ratio	Error (1σ)		Ratio	Error (1σ)	
A77	0.05789	0.00231		0.25961	0.00949		0.03251	0.00089		0.01383	0.00076		526	38		234	8		206	6		278	15	
A78	0.05188	0.00244		0.23562	0.00953		0.03294	0.00079		0.01035	0.00025		280	110		215	8		209	5		208	5	
A79	0.05273	0.00141		0.24329	0.00604		0.03345	0.00081		0.01108	0.00055		317	26		221	5		212	5		223	11	
A80	0.05213	0.00216		0.23471	0.00801		0.03265	0.00077		0.01025	0.00024		291	97		214	7		207	5		206	5	
A81	0.05209	0.00131		0.25938	0.00608		0.0361	0.00086		0.01177	0.00034		289	25		234	5		229	5		237	7	
A82	0.05014	0.00118		0.24192	0.00531		0.03498	0.00082		0.01113	0.00044		201	24		220	4		222	5		224	9	
A83	0.05126	0.00122		0.24287	0.00541		0.03435	0.00081		0.01155	0.0006		253	24		221	4		218	5		232	12	
A84	0.05027	0.00114		0.24534	0.00525		0.03539	0.00083		0.01176	0.00041		207	24		223	4		224	5		236	8	
A89	0.0521	0.00237		0.22575	0.00875		0.03143	0.00075		0.00987	0.00023		290	107		207	7		199	5		199	5	
A90	0.05305	0.00182		0.2649	0.0084		0.03621	0.00094		0.01376	0.00075		331	33		239	7		229	6		276	15	
A91	0.05739	0.00113		0.23972	0.00441		0.03029	0.0007		0.00946	0.00032		507	23		218	4		192	4		190	6	
A92	0.05076	0.00135		0.24604	0.00612		0.03515	0.00085		0.01173	0.00045		230	26		223	5		223	5		236	9	
A93	0.05089	0.00279		0.24455	0.01197		0.03485	0.00086		0.01098	0.00025		236	127		222	10		221	5		221	5	
A94	0.05114	0.00155		0.24377	0.00683		0.03457	0.00087		0.01167	0.00055		247	29		222	6		219	5		235	11	
A95	0.05055	0.00109		0.24175	0.00488		0.03469	0.00081		0.01181	0.00045		220	24		220	4		220	5		237	9	
A96	0.05018	0.00134		0.23857	0.00594		0.03448	0.00084		0.01149	0.00049		203	26		217	5		219	5		231	10	
B02	0.05115	0.00119		0.24774	0.00541		0.03514	0.00084		0.01297	0.00054		248	25		225	4		223	5		260	11	
B03	0.05067	0.00224		0.24165	0.00903		0.03459	0.00082		0.0109	0.00025		226	104		220	7		219	5		219	5	
B04	0.05104	0.00235		0.24163	0.00953		0.03433	0.00082		0.01081	0.00025		243	109		220	8		218	5		217	5	
B05	0.05079	0.00153		0.24968	0.00699		0.03567	0.0009		0.01274	0.00067		231	29		226	6		226	6		256	13	
B06	0.05039	0.00095		0.24525	0.00437		0.03531	0.00082		0.01121	0.00038		213	25		223	4		224	5		225	8	
B07	0.05429	0.00243		0.27463	0.01035		0.03669	0.00089		0.01147	0.00027		383	103		246	8		232	6		230	5	
B08	0.05014	0.00223		0.24399	0.00913		0.0353	0.00085		0.01114	0.00026		201	104		222	7		224	5		224	5	
B09	0.05141	0.00105		0.25807	0.00495		0.03643	0.00086		0.01414	0.00053		259	25		233	4		231	5		284	11	

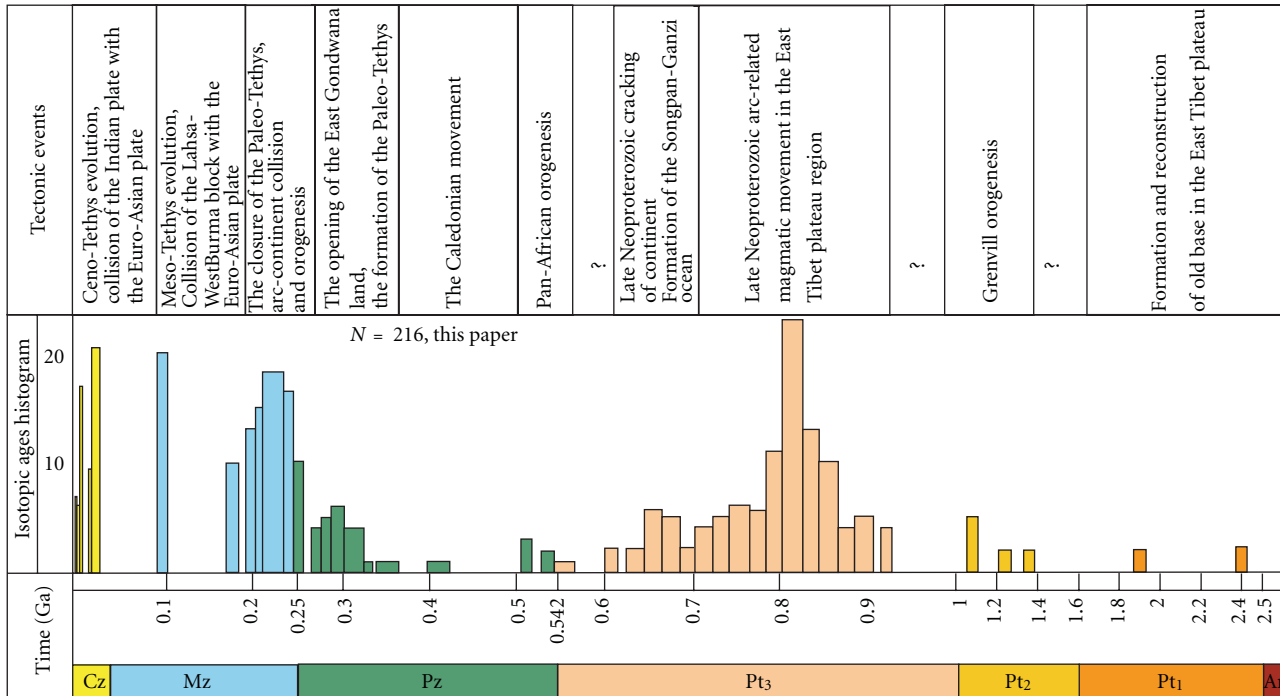


FIGURE 6: Isotopic age histogram showing the major tectonic event in the area east to the Tibet Peateau (after [8]).

from 195 Ma to 245 Ma, but some of them are below the U-Pb harmonic line and deviated from the harmony line. This is probably because the micro region selected is too close to the boundary of the zircon grain. Some zircon grains (Figure 5(f)) also have some cracks in and this may also affect the dating result. From the harmonic visible figure, zircon dating values are focused to a range from 210 Ma to 230 Ma, and the average age is about 220 Ma. This means that the crystallization age of the Kunsai quarries biotite granite is about in the late Triassic Norian period.

As shown in Figure 5(g) and Table 3, the overall harmony values of MK-4 zircon age data range between 190 Ma and 315 Ma. The values are somewhat scattered mainly because the granite of the Mengku quarries has been heavily weathered (Figure 5(d)). During the weathering process, chemical bonds of ZrO_2 in zircon grains of our MK-4 sample would be broken. Therefore, some zircon isotope escaped. The average age of 245 Ma might indicate that the late Permian to early-middle Triassic magmatic event happened in the Mengku Quarries area of the Lincang Batholith.

3. Tectonic Implications

Previous petrological and geochemical studies [18, 26, 28, 35] indicate that the Lincang granite mainly shows two types of granite with an initial strontium isotope ratio ranging from 0.71 to 0.78 and therefore it belongs to S-type granite and once may have been formed in an environment of tectonic collision. Combined with previous chronological data, we propose a three-stage model on the tectonic evolution between late Permian and Jurassic (Figure 6).

(1) *Regional Collision and Contraction before the Formation of the Lincang Batholith.* Before the formation of the Lincang Batholith, the Paleo-Tethys Ocean and many intraoceanic islands distributed between the Baoshan and the Lanping-Simao-Indosinian blocks [36]. In a regional contractional environment of subduction and collision, it is extremely common to find folding, thrusting, and uplifting phenomena (Figure 7(a)).

(2) *Time Heterogeneity of In Situ Hybrid of the Lincang Batholith.* The Lincang Batholith was controlled by one deep-seated fault along the Lancang Jiang River and proposed in situ hybrid origin of the Batholith in the early to middle Triassic collision between the Baoshan-Shantai and Lanping-Simao-Indochina Blocks [16]. Our study shows an ununiform law result in the aspect of mixing time of the Batholith (Figure 7(b)). The intrusion time in the east Qunsai area was later than in the Mengku area, indicating that the regional contraction in Mengku area was weakened or stopped, and triggered magma poured at ~230 Ma, however, the contraction pattern may still remain in the Qunsai area to the east.

(3) *Tectonic Denudation and Regional Exhumation Happened between Late Triassic and Middle Jurassic, Which Is Supported by ~201 Ma Biotite $^{40}\text{Ar}/^{39}\text{Ar}$ Age from the Lincang Batholith [27].* This paper research shows that the upper part of the Lincang Batholith experienced long-term denudation, resulting in the development of the weathering crust (Figure 7(a)). The upper crust is the Jurassic Huakaizuo Formation, characterized by carbonate rocks of shallow sea facies, together with some volcano clastic rocks (Figure 5(b)).

TABLE 3: U-Pb isotopic dating for the single grain Zircon from granite of Mengku.

Analysis no.	$^{207}\text{Pb}/^{206}\text{Pb}$			$^{207}\text{Pb}/^{235}\text{U}$			$^{206}\text{Pb}/^{238}\text{U}$			$^{208}\text{Pb}/^{232}\text{Th}$			$^{207}\text{Pb}/^{206}\text{Pb}$			$^{207}\text{Pb}/^{235}\text{U}$			$^{206}\text{Pb}/^{238}\text{U}$			$^{208}\text{Pb}/^{232}\text{Th}$		
	Ratio	Error (1 σ)		Ratio	Error (1 σ)		Ratio	Error (1 σ)		Ratio	Error (1 σ)		Ratio	Error (1 σ)		Ratio	Error (1 σ)		Ratio	Error (1 σ)		Ratio	Error (1 σ)	
1	0.05174	0.00244		0.32303	0.0139		0.04528	0.00108		0.01152	0.00053		274	56		284	11		285	7		232	11	
2	0.09115	0.00288		2.96352	0.08448		0.23585	0.0053		0.08061	0.00287		1450	25		1398	22		1365	28		1567	54	
3	0.11509	0.00332		0.50952	0.01225		0.03212	0.00066		0.02102	0.00068		1881	19		418	8		204	4		420	13	
4	0.04837	0.00265		0.22077	0.01108		0.03312	0.00085		0.01153	0.00063		117	69		203	9		210	5		232	13	
5	0.04837	0.0022		0.27295	0.01145		0.04095	0.00092		0.01223	0.0006		117	57		245	9		259	6		246	12	
6	0.05351	0.00279		0.29775	0.01415		0.04038	0.00104		0.01371	0.00078		350	62		265	11		255	6		275	16	
7	0.0806	0.00218		2.27431	0.05585		0.2048	0.00394		0.05968	0.00155		1212	22		1204	17		1201	21		1172	30	
8	0.0802	0.00341		2.36577	0.09085		0.2141	0.00577		0.05352	0.00277		1202	37		1232	27		1251	31		1054	53	
9	0.05928	0.00248		0.29959	0.01132		0.03668	0.00082		0.00966	0.00046		577	45		266	9		232	5		194	9	
10	0.04989	0.00375		0.23793	0.0163		0.03461	0.00119		0.00907	0.00072		190	96		217	13		219	7		182	14	
11	0.07866	0.00333		0.34683	0.01279		0.032	0.00079		0.01233	0.00063		1164	37		302	10		203	5		248	13	
12	0.0406	0.00217		0.22437	0.01119		0.04011	0.00095		0.01052	0.00055		-255	72		206	9		254	6		212	11	
13	0.0639	0.00299		0.31538	0.01317		0.03582	0.00089		0.01126	0.00067		738	48		278	10		227	6		226	13	
14	0.07481	0.00441		0.3517	0.01817		0.03412	0.00108		0.01178	0.00078		1063	56		306	14		216	7		237	16	
15	0.06821	0.00263		0.97745	0.03376		0.10399	0.00236		0.03233	0.00106		875	37		692	17		638	14		643	21	
16	0.05116	0.00255		0.26673	0.01227		0.03784	0.00088		0.01057	0.00052		248	64		240	10		239	5		213	10	
17	0.05025	0.00304		0.25181	0.01395		0.03636	0.00102		0.01037	0.00064		207	77		228	11		230	6		209	13	
18	0.05379	0.003		0.27018	0.01369		0.03645	0.00098		0.00965	0.0006		362	67		243	11		231	6		194	12	
19	0.05083	0.00373		0.26778	0.01802		0.03823	0.00125		0.00987	0.00055		233	96		241	14		242	8		199	11	
20	0.06022	0.00487		0.2998	0.0217		0.03612	0.00142		0.01137	0.00113		611	90		266	17		229	9		229	23	
21	0.0473	0.00214		0.20932	0.0087		0.0321	0.0007		0.00892	0.00038		64	55		193	7		204	4		179	8	
22	0.05405	0.00334		0.28442	0.01602		0.03817	0.00111		0.00858	0.0006		373	75		254	13		241	7		173	12	
23	0.05907	0.0024		0.66212	0.02439		0.08128	0.00181		0.03438	0.00121		570	43		516	15		504	11		683	24	
24	0.05064	0.00245		0.21459	0.00944		0.03072	0.00072		0.00797	0.00046		224	59		197	8		195	5		160	9	
25	0.05594	0.00261		0.26352	0.01113		0.03415	0.0008		0.00964	0.00045		450	53		237	9		216	5		194	9	
26	0.06769	0.00524		0.32217	0.02212		0.0345	0.00134		0.01049	0.0009		859	80		284	17		219	8		211	18	
27	0.06354	0.00206		0.75553	0.02205		0.08618	0.00166		0.02056	0.00084		726	32		571	13		533	10		411	17	
28	0.05014	0.00296		0.33191	0.01801		0.04797	0.00129		0.02068	0.0011		201	77		291	14		302	8		414	22	
29	0.23782	0.00377		6.55914	0.08439		0.19984	0.00325		0.01824	0.00075		3105	12		2054	11		1174	17		365	15	

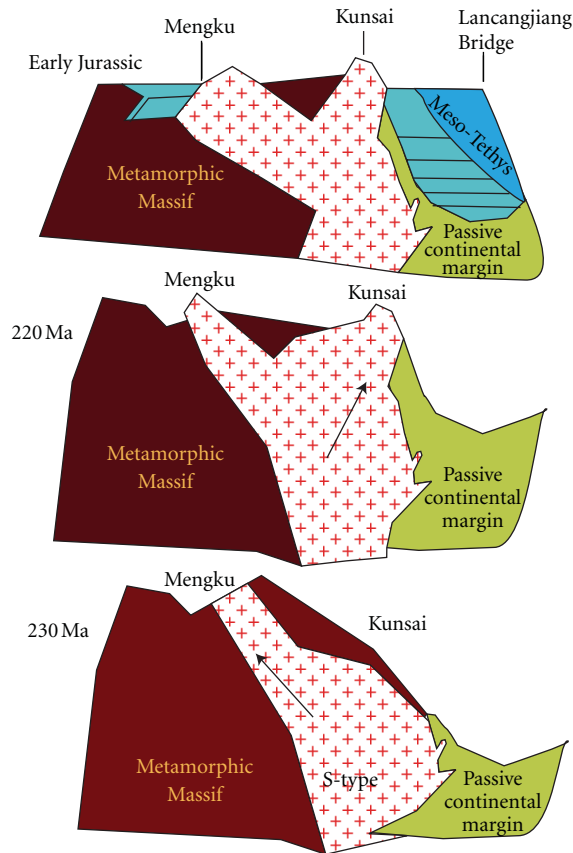


FIGURE 7: Formation and tectonic evolution model for the Lincang Batholith.

Unconformity relationship is shown between the Batholith and the Huakaizuo Formation (Figures 3, 5(a), 5(b), 5(c), and 7(c)). Apparently, the Meso-Tethys expansion also happened in this era and left some effect in the Lincang Area.

Acknowledgments

The authors appreciate sincerely both the field research and inner discussion together with Professor Yong-Qing Chen from China University of Geosciences (Beijing), Research Fellow Ying-Xiang Lu from Yunnan Bureau of Geology and Mineral Resources, and Research Fellow Fang-Cheng Lin from Chengdu Institute of Geology and Mineral Resources. The authors thank Dr. Pengfei Li from University of Queensland for his perfect academic revision of the paper. The research was supported by the China Geology Survey (no. 200811008, no. 1212011121188), the Ministry of Science and Technology (no. 2006BAB01A03-3), the Chinese National Natural Foundation (no. 90814006) of the People's Republic, and the China University of Geosciences in Beijing (no. 2-9-2001-280).

References

[1] J. Q. Huang and B. W. Chen, *The Evolution of the Tethys in China and Adjacent Regions*, Geological Publishing House, Beijing, China, 1987.

[2] P. Jian, D. Liu, A. Kröner et al., "Devonian to Permian plate tectonic cycle of the Paleo-Tethys Orogen in southwest China (II): insights from zircon ages of ophiolites, arc/back-arc assemblages and within-plate igneous rocks and generation of the Emeishan CFB province," *Lithos*, vol. 113, no. 3-4, pp. 767–784, 2009.

[3] H. D. Klemme and G. F. Ulmishe, "Effective petroleum source rocks of the world: stratigraphic distribution and controlling depositional factors," *AAPG Bulletin*, vol. 75, no. 12, pp. 1809–1851, 1991.

[4] G. T. Pan, Z. L. Chen, and X. Z. Li, *Geological Structure Formation and Evolution of East Tethys*, Geological Publishing House, Beijing, China, 1997.

[5] G. T. Pan, H. X. Zheng, Y. R. Xu et al., "A preliminary study on Bangong Co-Nujiang Suture," in *Editing Committee of Geological Memoirs of Qinghai-Xizang Plateau(12)-Geological Tectonics of "Sanjiang"*, pp. 229–242, Geological Publishing House, Beijing, China, 1983.

[6] X. Wang, I. Metcalfe, P. Jian, L. He, and C. Wang, "The Jinshajiang-Ailaoshan Suture Zone, China: tectonostratigraphy, age and evolution," *Journal of Asian Earth Sciences*, vol. 18, no. 6, pp. 675–690, 2000.

[7] A. M. C. Sengor and U. J. Botum, "The Tethys orogenic system: an introduction," in *Tectonic Evolution of the Tethyan Region*, A. M. C. Sengor, Ed., pp. 1–22, Kluwer Academic, Boston, Mass, USA, 1989.

[8] Q. Yan, Z. Wang, S. Liu et al., "Opening of the Tethys in southwest China and its significance to the breakup of East Gondwanaland in late Paleozoic: evidence from SHRIMP U-Pb zircon analyses for the Garze ophiolite block," *Chinese Science Bulletin*, vol. 50, no. 3, pp. 256–264, 2005.

[9] P. A. Ziegler, *Evolution of Laurussia: A Study in Late Palaeozoic Plate Tectonics*, Kluwer Academic, Dordrecht, The Netherlands, 1989.

[10] B. P. Liu, Q. L. Feng, C. Chonglakmani et al., "Framework of paleotethyan archipelago ocean of western Yunnan and its elongation towards north and south," *Earth Science Frontiers*, vol. 9, no. 3, pp. 161–171, 2002.

[11] C. S. Hutchison, *Geological Evolution of Southeast Asia*, vol. 13 of *Oxford Monographs on Geology and Geophysics*, Clarendon Press, Oxford, UK, 1989.

[12] H. R. Wu, C. A. Boulter, B. Ke et al., "The Changning-Menglian suture zone: a segment of the major Cathaysian-Gondwana divide in Southeast Asia," *Tectonophysics*, vol. 242, no. 3, pp. 267–280, 1995.

[13] H. Y. Zhang and J. L. Liu, "Plate tectonics and mineralization of the Tethyan ophiolite in the southern Sanjiang and Indo-China peninsular area," *Earth Science, Journal of China University of Geosciences*, vol. 36, no. 2, pp. 262–276, 2011 (Chinese).

[14] P. F. Fan, "Accreted terranes and mineral deposits of Indochina," *Journal of Asian Earth Sciences*, vol. 18, no. 3, pp. 343–350, 2000.

[15] M. J. Lin, "The volcanic rock sequence and its geological age along the bank of Lancang Jiang, West Yunnan" (Chinese), See: *Geology Papers of Qinghai-Tibet Plateau (13)-Rocks in Sanjiang Area*, pp. 151–158, 1983.

[16] J. Y. Xiong, Y. M. Lin, and S. R. Qin, "A preliminary study on the genesis and the basic characteristics of the Lincang magmatic complex" (Chinese), See: *Geology Papers of Qinghai-Tibet Plateau (13)-Rocks in Sanjiang Area*, pp. 1–19, 1983.

- [17] S. Y. Yu, K. Q. Li, Y. P. Shi, and H. H. Zhang, "A study on the granodiorite in the middle part of Lincang granite batholiths," *Yunnan Geology*, vol. 22, no. 4, pp. 426–442, 2003.
- [18] C. S. Liu, J. C. Zhu, X. S. Xu, X. J. Chu, D. K. Cai, and P. Yang, "Study on the characteristics of Lincang Composite Granite Batholith in West Yunnan," *Yunnan Geology*, vol. 8, no. 3–4, pp. 189–212, 1989 (Chinese).
- [19] X. L. Li, "Basic characteristics and formation structural environment of Lincang Composite granite batholiths," *Yunnan Geology*, vol. 15, no. 1, pp. 1–18, 1996 (Chinese).
- [20] J. C. Chen, "Discussion on the age division and the selects of isotopic age determination for granitic rock in Western Yunnan," *Yunnan Geology*, vol. 6, no. 2, pp. 101–113, 1987 (Chinese).
- [21] X. X. Mo, S. Y. Shen, Q. W. Zhu et al., *Volcanic-Ophiolite and Mineralization of Middle-Southern Part in Sanjiang Area of Southwestern China*, Geological Publishing House, Beijing, China, 1998.
- [22] D. L. Zhong, *Paleo-Tethys Orogenic Zone in Western Yunnan and Western Sichuan*, Science Press, Beijing, China, 1998.
- [23] A. Socquet and M. Pubellier, "Cenozoic deformation in western Yunnan (China-Myanmar border)," *Journal of Asian Earth Sciences*, vol. 24, no. 4, pp. 495–515, 2005.
- [24] R. G. Park, *Foundations of Structural Geology*, Chapman & Hall, New York, NY, USA, 2nd edition, 1989.
- [25] C. H. Zhang, J. S. Liu, D. L. Liu, and S. Yang, "Geological, geochemical characteristics, age and tectonic setting of Lao-maocun small rockbody in South Lancangjiang Zone," *ACTA Mineralogica Sinica*, vol. 26, no. 3, pp. 317–324, 2006.
- [26] J. C. Chen, "Characteristics of Pb, Sr isotopic compositions in west Yunnan granites: discussion on the age and nature of the basement in west Yunnan," *Scientia Geologica Sinica*, vol. 2, pp. 174–183, 1991.
- [27] T. M. Dai, B. Q. Zhu, Y. Q. Zhang, Z. P. Pu, Q. F. Zhang, and A. S. Hong, "Collision and thermal history of Indian-Sandaland-Eurasian Plates as implicated by $^{40}\text{Ar}/^{39}\text{Ar}$ age spectra of granodiorites," *Geochimica*, vol. 15, no. 2, pp. 97–107, 1986.
- [28] Y. Q. Zhang, Y. W. Xie, and J. W. Wang, "Rb and Sr isotopic studies of granitoids in Tri-river region," *Geochimica*, vol. 19, no. 4, pp. 318–326, 1990 (Chinese).
- [29] W. Y. Wang, "Rb-Sr isotopic Data," *Yunnan Geology*, vol. 3, no. 1, pp. 79–96, 1984 (Chinese).
- [30] Yunnan Bureau of Geology and Mineral Resources (YBGM), *Geological Map of the Jinggu Sheet at a Scale of 1:200,000*, Ministry of Geology and Mineral Resources, Beijing, China, 1983.
- [31] Yunnan Bureau of Geology and Mineral Resources (YBGM), *Geological Map of the Gengma Sheet at a Scale of 1:200,000*, Ministry of Geology and Mineral Resources, Beijing, China, 1985.
- [32] P. Xu, F. Wu, L. Xie, and Y. Yang, "Hf isotopic compositions of the standard zircons for U-Pb dating," *Chinese Science Bulletin*, vol. 49, no. 15, pp. 1642–1648, 2004.
- [33] S. E. Jackson, N. J. Pearson, W. L. Griffin, and E. A. Belousova, "The application of laser ablation-inductively coupled plasma-mass spectrometry to in situ U-Pb zircon geochronology," *Chemical Geology*, vol. 211, no. 1–2, pp. 47–69, 2004.
- [34] K. Ludwig, *Isoplot/Ex version 2.0: A Geochronological Tool Kit for Microsoft Excel*, Geochronology Center Berkeley, Special Publication, 1999.
- [35] B. W. Chappell and A. J. R. White, "I- and S-type granites in the lachlan fold belt, Southeast Australia," in *Geology of Granites and their Metallogenic Relations*, X. Keqin and T. Guangchi, Eds., pp. 72–78, Science Press, Beijing, China, 1982.
- [36] B. P. Liu, Q. L. Feng, N. Q. Fang et al., "Tectonic evolution of Paleo-Tethys Poly-island-ocean in Changning-Menglian and Lancangjiang Belts, south-western Yunnan, China," *Earth Science, Journal of China University of Geosciences*, vol. 18, no. 5, pp. 529–539, 1993 (Chinese).

Review Article

The Structural Framework of the Erlangping Group in North Qinling, Central China

Hongyuan Zhang,^{1,2} Chunqiang Zhao,^{1,2} Fanglei Xu,^{1,2} and Yanlong Dong^{1,2}

¹ School of the Earth Sciences and Resources, China University of Geosciences, Beijing 100083, China

² State Key Laboratory of Geological Processes and Mineral Resources, China University of Geosciences, Beijing 100083, China

Correspondence should be addressed to Hongyuan Zhang, zhang-hong-yuan@263.net

Received 30 March 2012; Accepted 4 May 2012

Academic Editor: Yu-Dong Wu

Copyright © 2012 Hongyuan Zhang et al. This is an open access article distributed under the Creative Commons Attribution License, which permits unrestricted use, distribution, and reproduction in any medium, provided the original work is properly cited.

As one major unit of the North Qinling tectonic belt, and being located in the north side of the UHP belt between the Yangtze block and the North China block, the Erlangping Group has become one hot research spot because it still keeps records of both plate and inner-continent evolution histories. Three aspects of the Erlangping Group are reviewed. (1) Research history are concluded into three stages, including the determination of rock assemblages before the late 1980s, the regional metamorphism laws solution in the 1990s, and the formation time and tectonic background discussion in the 2000s. (2) Five major controversies and frontier scientific problems have been offered, such as, the deformation ages determination, the Cretaceous tectonic event definition, the determination of the deformation mechanisms and conditions, the kinematic and dynamic nature of the Zhuyanguan-Xianguan shear zone, and the reconstruction of the evolution and exhumation history. (3) Structural framework of the Erlangping Group is divided into five parts according to our field and laboratory study, including the Erjingou slab, the Damiao-Wantan shear zone, the Huoshenmiao slab, the Xiaozhai-Erlangping shear zone, and the Baoshuping slab. Only the Xiaozhai-Erlangping shear zone has clear kinematic marks of left lateral slip.

1. Introduction

The Erlangping Group, neighbouring the Qinling Group to the south by the Zhuyanguan-Xianguan boundary shear zone along where ultra high pressure metamorphic rocks were found near the Guanpo Town, and connecting with the Kuanping Group by the Waxuezi-Qiaoduan shear zone (Figure 1). In recent years, with continuously enriched inner and regional related research achievements [1–20], the Erlangping Group is gradually becoming a hot research area.

2. Research History

Conclusions of research records of the Erlangping Group indicate one obvious tendency, that is, from the qualitative research of internal combination before 1980s, role of regional metamorphism and thermochronology in the 1990s, and to the time limit research of the construction and comprehensive study in the 21st century.

2.1. The Determination of the Rock Assemblage before the Late 1980s. The cross-section from south to north of the Erlangping Group contains the Zimugou Formation, the Baoshuping Formation, the Xiaozhai Formation, the Huoshenmiao Formation, the Damiao Formation, and the Erjingou Formation. And it is a set of construction of a spilite keratophyre-sedimentary clastic flysch [21, 22]. During this period, the Erlangping Group was generally considered to be formed in the early Paleozoic according to Radiolarian fossils with the pre-Devonian *Liospheridae gen. indet*, *Stylosphoeridae gen. indet* in siliceous rock of the Erlangping Group and 391–467 Ma of K-Ar data of metavolcanic rocks below the flysch layer (formerly called the Waitoushan Formation) [14]. Zonation characteristics of metamorphism within the Erlangping Group were concluded by Liu [23]. Xu et al. [14] determine that sinistral movement occurred at places between Shang county and Guanpo town in the west section of the Zhuyanguan-Xianguan, but they did not perform any deep research according to that book.

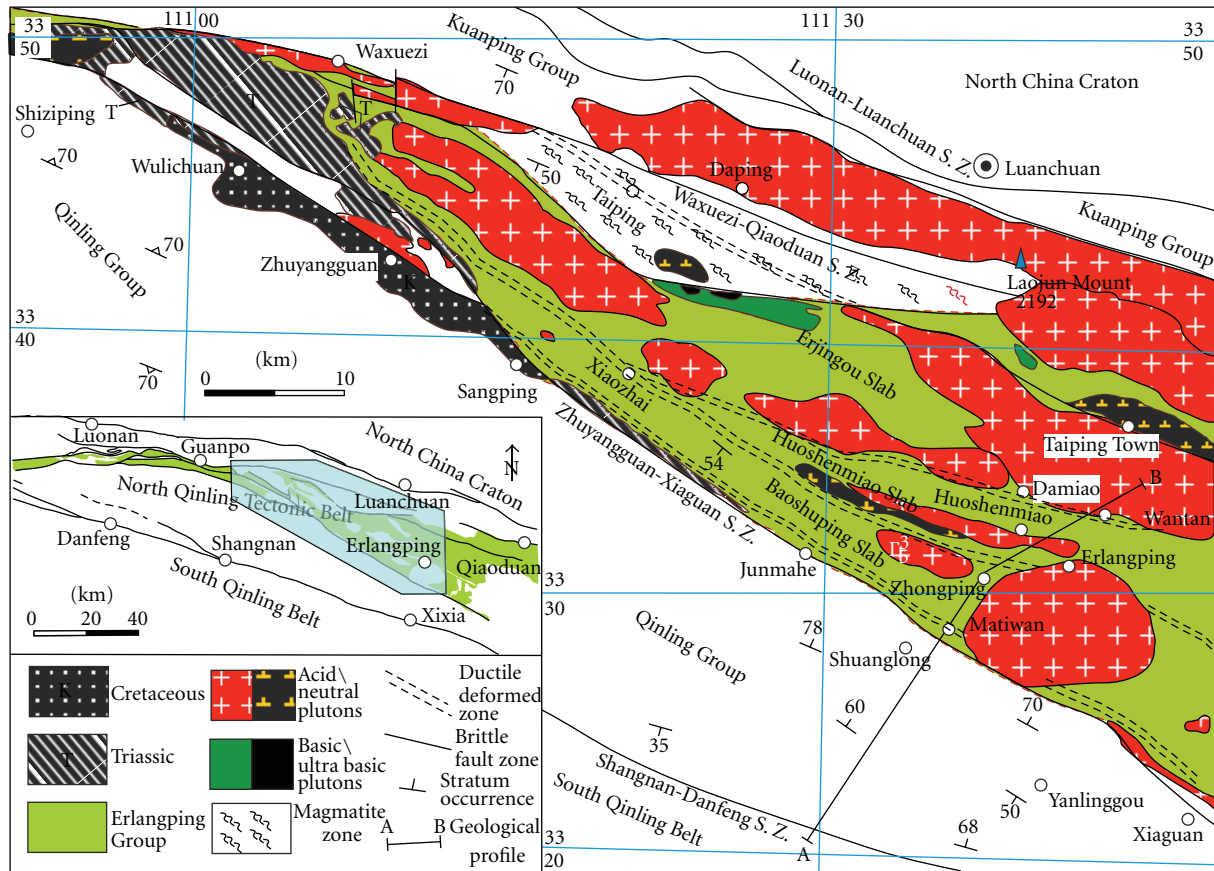


FIGURE 1: Tectonic position of the Erlangping Group in the North Qinling tectonic belt (after [38, 41]).

2.2. The Solution of Regional Metamorphism Laws in the 1990s. During this period, some scholars still hold that the Erlangping Group was formed in the early Paleozoic [24]. However, Pei et al. [25] believed that the Erlangping Group should be formed in the late Paleozoic according to fossils they found. Liu et al. [26] reviewed the metamorphism of the Erlangping Group and found that the wall experienced meso to senior degree of metamorphism with zonation. Regional metamorphism was active in a period ranging from 121.5 to 111.2 Ma according to the metamorphic mineral $^{40}\text{Ar}/^{39}\text{Ar}$ research by Zhao et al. [27], possibly indicating that during the Cretaceous era the whole Qinling orogen are still in its tectonic movement time. As a boundary shear zone of both the Qinling Group and the Erlangping Group, the Zhuyangguan-Xiaguan shear zone was initially emphasized and studied by Suo et al. [28] and Zhong et al. [29], but not much work were carried out inside the Erlangping Group until the late 1990s. Sun et al. [30] reported some zircon U-Pb geochronological data indicating an early Ordovician intrusion event from the Xizhuanghe and Baihuling plutons inside the Erlangping Group. Li et al. [31, 32] considered the Erlangping hedge-type thrust and nappe structure eastern to Guanpo as the records of “bidirectional subduction” with meaning of one to the north subduction downward to the Kuanping ancient continent and another to the south downward to the Qinling ancient

island arc. However, Wang et al. [33] believed that the total structure framework is like “a composite overturned fold system.” The model presented by Wang et al. [33] addresses that the Taiping town principal anticline belt is the central core and that the system is flanked by the Damiao overturned syncline and Zhangjiadazhuang overturned syncline on the south and the Shihuiyao overturned syncline and Penglaojia overturned syncline on the north.

2.3. The Argument on Formation Time and Tectonic Background in the 2000s. Since the 21st century, with the development of traditional paleontology and application of new dating technology, focus has been put on determining the formation age and background of the Erlangping Group, and some new academic clues have been obtained through synthesis research of tectonic-magmatic-regional metamorphism.

In general, we believe that the Erlangping Group was constructed in an era ranging from the late-early Paleozoic to the beginning of the late Paleozoic, possibly in Devonian. At the beginning, Zhang et al. [34] summarizes the formation age as ranging from the Late Paleozoic to the Indosinian epoch which could be proved by some Devonian fossils found near Wantan village [35]. However, a small-scale back-arc spreading basin in the Early Paleozoic is also one possible

explanation to the origination of the Erlangping Group by some scholars [36].

In the aspect of structural geology research, definition of the southern boundary of Erlangping Group, however, obviously there are certain contradiction or disagreement with strike-slip structures found in Shangzhou City, Zhuyangguan-Xiaguan, and other places [14, 31, 32]. Zhang et al. [34] considered that the characteristics of the strike-slip structure in the whole Qinling orogenic belt is inconsecutive, penetrability, and small-scale distribution, and addressed a long-term active thrust system which extended from the north to the south as the southern boundary of the Erlangping Group.

Extensive research jobs have been performed on geochronology in subsequent years and are mostly focused on the intrusive rock bodies, which gradually deepened our understanding on the process of deformation and metamorphism within the Erlangping Group. According to results of Tian and Wei [9], at least two major intrusive bodies in the area of the Erlangping Group, including the Banshanping and the Zhangjiazhuang, have been proved to be formed during the period from the Lower Silurian to the early-middle Devonian. The time of the island-arc accretion system in North Qinling appeared has been proven to be existed in the period from the Ordovician to the Carboniferous [5, 6, 37]. Some Paleozoic granite bodies were concluded to be occurred at the North Qinling by thorough analysis on the granite and magma time-space framework model [13]. Several stages, including plate subduction, collision, flower shape extrusion, and dextral strike-slip have been involved into the evolution of the Zhuyangguan-Xiaguan shear zone [13]. Biotite obtained from mylonite rocks near Matiwan village has $^{40}\text{Ar}/^{39}\text{Ar}$ dating results of 106 Ma [38]. Together with the $^{40}\text{Ar}/^{39}\text{Ar}$ data from the Xiaozhai village obtained by Zhao et al. [27], it is reasonable to think of the early Cretaceous event as an exhumation process.

3. Major Controversies and Problems

3.1. To Determine Deformation Ages. Although time problems of construction and transformation have been partly resolved by modern isotopic geochronology methods during the past two decades [7, 16, 27, 39–41], it is still extremely difficult to explain chronological data of those geologic bodies that undergone deformation and metamorphism with multistages. To increase the data scale of the several dating methods has become more and more difficult to give an effective resolution of time problems of deformation and metamorphism. To clarify structural stages of deformation rocks is also seriously required before other chronological jobs.

3.2. To Define the Cretaceous Tectonic Event. There is still a problem on how to explain the Cretaceous Ar-Ar chronological data obtained from the Erlangping Group. In our opinion, regional geologic characters and even some Cretaceous structures behaviors in eastern China should benefit to the solution of the problem.

Intracontinental deformation dynamics in central eastern China is a complex process in Cretaceous. Although thrust and nappe structures are very popular crust deformation styles in the region of the Qinling Mountains [34], more obvious strike-slip structures are found to the northeast side of the Qinling Mountains and especially in the Taihang Mountains and Xuhuai region, for example, the Tancheng-Lujiang fault [42, 43]. Much differently, to the eastern part of north China, the Liaodong Peninsula of northeast China or the southeast coastal area of China, both macroscale of local reduction of lithosphere [44–46] and regional extensional tectonics [47–52] occurred in Cretaceous.

Two major groups of geochronological data in the eastern Liaodong peninsula are concluded into two groups, about 180 Ma and about 125 Ma separately [53, 54] indicating quite different background, which coincide with the tectonic events of Yanshanian and Sichuanian separately. And similarly, two stages of events were concluded in the Dabie orogenic belt [55]. However, a little different appears in the area of the Erlangping Group, where the Ar-Ar data indicate only the Cretaceous event, seldom Jurassic ones [27, 38, 56]. There are also Cretaceous but seldom Jurassic data in the Qilian-Altin tectonic belt to the west side of the Qinling Mountains [57].

3.3. To Determine Deformation Mechanisms and Conditions. Predecessors concluded some models, including the synclinorium model [33] and the subduction model [31, 32] from the internal framework and the boundary shear zones of the Erlangping Group. How to make the problem clear? According to thoughts of analytical tectonics [58], to study parameter characteristics from aspects including geological geometry, kinematics, dynamics, and rheology and to perform comprehensive quantitative research on the whole tectonic block are essential to figure out the regional structural framework synthetically.

Since the 21st century, microtectonic methods become much popular [59–61]. More and more microscopic quantitative achievements make it possible to study flow mechanics and conditions of tectonites. Some quantitative techniques, including deformation thermometer, deformation stages, deformation dating within a micro area, kinematics of petrofabrics, and rheology have been achieving rapid development in recent years.

Deformation thermometer is a special technique used for deformational temperature testing of ductility deformation rocks. The major types include the crystal shape thermometer, for example, the recrystalline particles size thermometer [62], and the crystallography thermometer, for example, quartz C axial fabric, and chemistry migratory thermometer, for example, TitaniQ thermometer [63, 64]. Fluid inclusions can also be used to define some conditions of deformation [65–67]. Methods of microchronological dating of deformed rocks have been applied into the orogenic belt [68, 69]. Petrofabrics and some flow laws (e.g., vorticity and strain rate) [70] of deformation belts can now be conveniently realized by EBSD (the electron backscattered diffraction) methods together with other traditional methods [71–74].

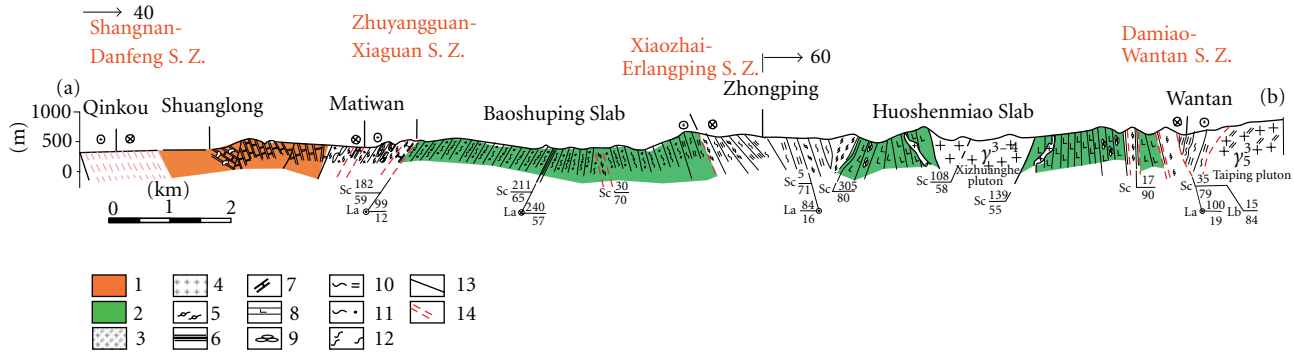


FIGURE 2: Geological section across the Baoshuping and the Huoshenmiao slabs in the Erlangping Group. 1: the Qinling Group; 2: the Erlangping Group; 3: monzonitic granite; 4: granite; 5: mylonite; 6: siliceous rocks; 7: marble; 8: spilite; 9: pillow-like basalt; 10: two mica schists; 11: biotite schist; 12: high-grade metamorphic rocks; 13: brittle fault zone; 14: ductile shear zone.

3.4. To Define the Nature of the Zhuyangguan-Xiaguan Shear Zone. Has the Zhuyangguan-Xiaguan shear zone experienced pure thrust [34], left-lateral slip [14], right-lateral slip [13], or multistage activities [31, 32, 38]? If it is a type of multistage, then whether it belongs to the same process of progressive deformation expression at different part or has experienced progressive overprinting at the same region.

3.5. To Reconstruct Evolution and Exhumation History. Predecessors once hold that there is a central core of anticline in the Taiping town area which transformed the Erlangping Group [33]. But unfortunately, it is just located in the highest level in the mountains. Geologically, there are the Taipingzhen and the Laojunshan acidic intrusive plutons. If exhumation event happened several hundred million years ago, then the outcrop must be in a low valley at present time. Therefore, it is required to get information (e.g., fission track data and Ar-Ar data) from the surface of the earth, which is responding to the exhumation process.

4. Preliminary Research and Clues

Interior metamorphism and deformation zonation have been studied [23, 38], reflecting macroscopic phenomena transformed by derived structure systems formed by different stages in activities of boundary shear zones of the Erlangping Group. The features of each slab and deformation zone are described from north to south as follows (Figures 1 and 2).

4.1. The North Weak Deformed Field (the Erjingou Slab). Located between the Waxuezi-Qiaorui shear zone and the Damiao-Wantan shear zone, the overall rocks show features of senior metamorphic series and commonly expose migmatitic biotite plagioclase amphibolites gneiss and migmatitic amphibolite remained mass. The original rocks are mainly mafic and neutral types of volcanic rocks. Larger rock masses have been mapped out, such as the Caledonian Zhangjiazhuang (ZJZ), Yanshanian Tangping-Changtanhe (TPCT), Taipingzhen-Manziying (TPMZ), and Yanzhen (YZ).

4.2. The North Strong Deformed Zone (the Damiao-Wantan Shear Zone). The Damiao-Wantan shear zone ranges from NWW280°-SEE100° strike to the east of Xiaozhai village, trends along the southern margin of the Yanzhen mass and the Tangping-Changtanhe mass, and goes to the Damiao-Wantan area finally. In the west side of the Xiaozhai village, the shear zone comes together with the Xiaozhai-Erlangping shear zone, another inner strong deformation zone inside the Erlangping Group, which possibly lead to that the Huoshenmiao slab wedged out westward.

Fossil spores of the early-middle Devonian are located in Wantan area [35], with several hundred meters distance south to the Damiao-Wantan shear zone, which is representing the formation state of the Erlangping Group.

Our initial study shows that it experienced at least two stages of transformation. In the traditional Damiao Group, there are mainly phyllonite rocks transformed by movements of the shear zone. The microstructure research from Wantan phyllonite shows significantly fine grained and foliation structures. Inside the foliation domain, the new sericite crystals are popularly born. We preliminarily presumed that the sericite foliation is a mark of rock suffered right-lateral strike-slip shear and is developed earlier than the macroscale duplex structure. In the Wantan area, the diamond blocks and high-angle south-dipped shear foliations are quite clear regionally, showing regional duplex structures with brittle-ductile deformation.

4.3. The Middle Weak Deformed Field (the Huoshenmiao Slab). The Huoshenmiao slab is located between the Damiao-Wantan shear zone and the Xiaozhai-Erlangping shear zone. The main and widest part of it is the Wantan-Erlangping area in the Xixia County of Henan Province. The slab shows an overall wedge geometry and wedges out to west of the Xiaozhai village. The exposed rocks consist of metamorphic mafic volcanic rocks and neutral volcanic rocks (spilite keratophyre). In some areas, primary structures such as pillow basalt, siliceous rocks, and clastic rocks were clearly identified. Gao et al. [35] reported the middle Devonian terrestrial plants Spores, a few suspected *Acritarchs* and very few *Chitinozoa* fossils. The slab was also intruded by

the Caledonian neutral and acidic magmatic rocks, such as the Baihuling diorite mass (BHL) and the Xizhuanghe pale tonalite mass (XZH).

4.4. The South Strong Deformed Zone (the Xiaozhai-Erlangping Shear Zone). The Xiaozhai Formation inside the Erlangping Group was transformed strongly by movement along the Xiaozhai-Erlangping shear zone. Some intrusion relationship marks between the Xiaozhai-Erlangping shear zone and the Erlangping coarse grain granite mass have been recorded according to regional geological survey [21], and our initial study indicated that the rock body has a similar development time to the exhumation of the surrounding slabs. In the shear zone, tectonites were named as sericite schists or two mica schists and observed with left-lateral ductile shear marks. Microscale foliations with biotite enrichment (C) were observed intersecting new muscovite-rich foliations (C') at a very low angle, and coming together into a type of C-C' stretching structure. Occurrence of shear foliations is almost upright, indicating a character of stretch left-lateral strike-slip movement. New muscovite crystals mainly developed in the mica mineral crenulation cleavages, which is possibly caused by local shear heat and related fluid flows.

4.5. The South Weak Deformed Field (the Baoshuping Slab). The Baoshuping slab is located between the Xiaozhai-Erlangping and the Zhuyangguan-Xiaguan shear zones. The slab has been geologically transformed by low-pressure and middle-temperature metamorphism [8, 75]. Generally, exposed rocks of the slab can be titled as biotite schists mingled with some amphibolite stripes. But near boundary shear zones of the slab, two mica schists appear more with muscovite content increasing toward outer the slab and especially to the south direction, the Zhuyangguan-Xiaguan shear zone. Protolith of the Baoshuping slab probably includes alkali and tholiitic basaltic series, which possibly experienced two periods of regional metamorphism [8, 75]. The Yanshanian acid magmatism develops well inside the Baoshuping slab, such as the Gutouya (GTY) and Erlangping (ELP) monzonitic granite masses.

5. Conclusions

According to reviews of literatures about North Qinling Erlangping Group and combining our preliminary jobs, some scientific problems, which will be very important to our correct understanding of the Erlangping thermal evolution and even contribute to the regional tectonic evolution, have been concluded as follows:

- (1) Composition, banded structure and relationships between the cell structures of the Erlangping Group.
- (2) Growth rules of both boundary and internal faults of the Erlangping Group, and their genetic relationship with tectonic evolution of the Erlangping Group.
- (3) Magmatic activity within the Erlangping Group and its relationship with regional tectonic evolution.

- (4) Thermal-dynamic evolution and exhumation history of the Erlangping Group.

Acknowledgments

The authors sincerely thank Professor Jun-Lai Liu from China University of Geosciences (in Beijing) for his rectification of the paper. The first author thanks Professor Zong-Qi Wang and Professor Quan-Ren Yan from the Chinese Academy of Geological Sciences because they gave the first author a lot of professional guidance between 2003 and 2006. The research was supported by "the Fundamental Research Funds for the Central Universities (no. 2-9-2001-280)" and the Chinese National Natural Foundation (no. 90814006 and no. 41030422) of China.

References

- [1] Q. R. Meng and G. W. Zhang, "Geologic framework and tectonic evolution of the Qinling orogen, Central China," *Tectonophysics*, vol. 323, no. 3-4, pp. 183-196, 2000.
- [2] W. Sun, S. Li, Y. Sun, G. Zhang, and Q. Li, "Mid-paleozoic collision in the North Qinling: Sm-Nd, Rb-Sr and $^{40}\text{Ar}/^{39}\text{Ar}$ ages and their tectonic implications," *Journal of Asian Earth Sciences*, vol. 21, no. 1, pp. 69-76, 2002.
- [3] J. S. Yang, Z. Q. Xu, X. Z. Pei et al., "Discovery of diamonds North Qinling: evidence for a giant UHPM belt across Central China and recognition of Paleozoic and mesozoic dual deep subduction between the North China and Yangtze plates," *Acta Geologica Sinica*, vol. 76, no. 4, pp. 484-495, 2002.
- [4] J. S. Yang, Z. Q. Xu, L. F. Dobrzhenetskaya et al., "Discovery of metamorphic diamonds in Central China: an indication of a > 4000-km-long zone of deep subduction resulting from multiple continental collisions," *Terra Nova*, vol. 15, no. 6, pp. 370-379, 2003.
- [5] Z. Q. Wang, T. Wang, Z. Yan, and Q. R. Yan, "Late Paleozoic forearc accretionary piggyback type basin system in the South Qinling, Central China," *Geological Bulletin of China*, vol. 21, no. 8-9, pp. 456-464, 2002.
- [6] Z. Q. Wang, Q. R. Yan, Z. Yan et al., "New division of the main tectonic units of the Qinling orogenic belt, Central China," *Acta Geologica Sinica*, vol. 83, no. 11, pp. 1527-1546, 2009.
- [7] L. Ratschbacher, B. R. Hacker, A. Calvert et al., "Tectonics of the Qinling (Central China): tectonostratigraphy, geochronology, and deformation history," *Tectonophysics*, vol. 366, no. 1-2, pp. 1-53, 2003.
- [8] A. L. Zhang, C. J. Wei, W. Tian et al., "Low-pressure metamorphism of Erlangping Group in North Qinling Mountains," *Acta Petrologica et Mineralogica*, vol. 23, no. 1, pp. 26-36, 2004.
- [9] W. Tian and C. J. Wei, "The Caledonian low Al-TTD series from the Northern Qinling orogenic belt: rock properties, genetic simulation and geological implication," *Science in China, Series D*, vol. 48, no. 11, pp. 1837-1847, 2005.
- [10] C. Z. Song, M. L. Niu, and G. S. Liu, "Some thoughts on strain research on the Qinling-Dabie orogenic belt," *Journal of Hefei University of Technology (Natural Science)*, vol. 28, no. 7, pp. 719-726, 2005.
- [11] C. Z. Song, G. W. Zhang, Y. S. Wang, J. H. Li, Z. C. Chen, and Z. C. Cai, "The constraints of strain partitioning and geochronology in luonan-luanchuan tectonic belts on qinling orogenic belt," *Science in China, Series D*, vol. 52, no. 3, pp. 300-312, 2009.

- [12] T. Wang, X. Z. Pei, X. X. Wang, N. G. Hu, W. P. Li, and G. W. Zhang, "Orogen-parallel westward oblique uplift of the Qinling basement complex in the core of the Qinling orogen (China): an example of oblique extrusion of deep-seated metamorphic rocks in a collisional orogen," *Journal of Geology*, vol. 113, no. 2, pp. 181–200, 2005.
- [13] T. Wang, X. X. Wang, W. Tian, C. L. Zhang, W. P. Li, and S. Li, "North Qinling Paleozoic granite associations and their variation in space and time: implications for orogenic processes in the orogens of Central China," *Science in China, Series D*, vol. 52, no. 9, pp. 1359–1384, 2009.
- [14] Z. Q. Xu, Y. L. Lu, Y. Q. Tang, and Z. T. Zhang, *Formation of the Composite Eastern Qinling Chains*, Environmental Science Press, Beijing, China, 1988.
- [15] J. F. Xu, Y. W. Han, and B. R. Zhang, "Geochemistry of the Mian-Lue ophiolites in the Qinling Mountains, Central China: constraints on the evolution of the Qinling orogenic belt and collision of the North and South China Cratons," *Journal of Asian Earth Sciences*, vol. 32, no. 5–6, pp. 336–347, 2008.
- [16] F. Wang, X. X. Lu, C. H. Lo et al., "Post-collisional, potassic monzonite-minette complex (Shahewan) in the Qinling Mountains (Central China): $^{40}\text{Ar}/^{39}\text{Ar}$ thermochronology, petrogenesis, and implications for the dynamic setting of the Qinling orogen," *Journal of Asian Earth Sciences*, vol. 31, no. 2, pp. 153–166, 2007.
- [17] X. Wang, T. Wang, B. M. Jahn, N. Hu, and W. Chen, "Tectonic significance of late Triassic post-collisional lamprophyre dykes from the Qinling Mountains (China)," *Geological Magazine*, vol. 144, no. 5, pp. 837–848, 2007.
- [18] X. Wang, T. Wang, I. Haapala, and J. Mao, "P-T conditions of crystallization and origin of plagioclase-mantled alkali feldspar megacrysts in the Mesozoic granitoids in the Qinling orogen (China)," *Lithos*, vol. 103, no. 3–4, pp. 289–308, 2008.
- [19] S. Lai, J. F. Qin, L. Chen, and R. Grapes, "Geochemistry of ophiolites from the Mian-Lue suture zone: implications for the tectonic evolution of the Qinling orogen, Central China," *International Geology Review*, vol. 50, no. 7, pp. 650–664, 2008.
- [20] Y. P. Dong, G. W. Zhang, F. Neubauer, X. Liu, J. Genser, and C. Hauzenberger, "Tectonic evolution of the Qinling orogen, China: review and synthesis," *Journal of Asian Earth Sciences*, vol. 41, no. 3, pp. 213–237, 2011.
- [21] Henan Provincial Bureau of Geology, 1 : 50000 Northern Xixia County, Regional Geological Survey Report of the People's Republic of China 1–159, 1973.
- [22] S. Y. Xiao, W. J. Zhang, Z. J. Song et al., *Metamorphic Stratum of the North Qinling*, Xi an Jiaotong University Press, 1988.
- [23] J. Liu, *Metamorphism of the Erlangping Group in the East Qinling [M.S. thesis]*, The Peking University, 1987.
- [24] E. P. Zhang et al., Ed., *Overview of Geological-Structural Features in the Qinling-Dabashan Region*, Geological Publishing House, Beijing, China, 1993.
- [25] F. Pei, Y. G. Zhang, and C. L. Liu, "Discovery and geological significance of the late Paleozoic spore fossils in North Qinling, Henan Province," *Regional Geology of China*, vol. 2, pp. 112–117, 1995.
- [26] G. H. Liu, S. G. Zhang, Z. D. You et al., *Major Metamorphic Groups and Their Metamorphic Evolution in the Qinling Orogenic Belt*, Geological Publishing House, Beijing, China, 1993.
- [27] D. L. Zhao, N. G. Hu, and S. Y. An, " $^{40}\text{Ar}/^{39}\text{Ar}$ Plateau age spectra of Erlangping Group, North Qinling and their geological implications," *Acta Mineralogica Sinica*, vol. 18, no. 1, pp. 101–104, 1998.
- [28] S. T. Suo, Z. Q. Zhong, and Y. H. Hu, "Tectonic boundary between Proterozoic and Paleozoic terrains in the Northern part of the Xixia and Neixiang, Henan Province," *Scientia Geologica Sinica*, vol. 1, pp. 12–21, 1990.
- [29] Z. Q. Zhong, Z. D. You, and S. T. Suo, "Petrological study on the ductile shear zones in the core of the Eastern Qinling orogenic belt, Western Henan," *Acta Geologica Sinica*, vol. 66, no. 2, pp. 121–130, 1990.
- [30] Y. Sun, X. X. Lu, S. Han, G. W. Zhang et al., "Composition and formation of Paleozoic Erlangping ophiolitic slab, North Qinling: evidence from geology and geochemistry," *Science in China*, pp. 49–55, 1996.
- [31] Y. L. Li, "Geological characteristics of tectonic boundary between Erlangping and Qinling Lithogenetic unit in the Northern Qinling Mountain," *Geology of Shannxi*, vol. 16, no. 2, pp. 9–16, 1998.
- [32] Y. L. Li, G. W. Zhang, and C. Z. Song, "Characteristics of Bidirectional subduction of Erlangping Backarc Basin," *Geological Journal of China Universities*, vol. 4, no. 3, pp. 286–293, 1998.
- [33] M. S. Wang, X. Q. Wu, F. Song et al., "The establishment of the main structural framework of the Maoji-Erlangping down-faulted zone in Henan and its significance," *Regional Geology of China*, vol. 18, no. 1, pp. 23–27, 1999.
- [34] G. W. Zhang, B. R. Zhang, X. C. Yuan et al., *Qinling Orogenic Belt and Continental Dynamics*, Science Press, Beijing, China, 2001.
- [35] L. D. Gao, Z. Q. Wang, and T. Wang, "New discovery of spores from the huoshenmiao formation of Erlangping Group, Xixia, Henan Province," *Geological Bulletin of China*, vol. 25, no. 11, pp. 1287–1294, 2006.
- [36] Y. P. Dong, G. W. Zhang, and B. Q. Zhu, "Proterozoic tectonics and evolutionary history of the North Qinling Terrane," *Acta Geoscientia Sinica*, vol. 24, no. 1, pp. 3–10, 2003.
- [37] Q. R. Yan, Z. Q. Wang, Z. Yan et al., "Timing of the transformation from seafloor spreading on the South margin of the North China block to subduction within the North Qinling orogenic belt," *Acta Geologica Sinica*, vol. 83, no. 11, pp. 1565–1583, 2009.
- [38] H. Y. Zhang, Z. Q. Wang, J. L. Liu et al., "The late Mesozoic extension-slipping-contraction of the Erlangping Group in the North Qinling tectonic belt, Central China," *Journal of Geomechanics*, vol. 15, no. 1, pp. 56–68, 2009.
- [39] N. S. Chen and Z. D. You, "An $^{40}\text{Ar}/^{39}\text{Ar}$ age spectrum of hornblende and its geological significances to Qinling Group in Shewei Area, Western Henan," *Acta Petrologica Sinica*, vol. 6, no. 4, pp. 54–58, 1990.
- [40] Z. Q. Zhang, D. Y. Liu, and G. M. Fu, *Isotopic Geochronology on Metamorphic Strata in the Northern Qinling Belt*, Geological Publishing House, Beijing, China, 1994.
- [41] Z. Q. Zhang, G. W. Zhang, D. Y. Liu et al., *Isotopic Geochronology and Geochemistry of Ophiolites, Granites and Clastic Sedimentary Rocks in the Qinling Orogenic Belt*, Geological Publishing House, Beijing, China, 2006.
- [42] G. Zhu, Y. Wang, G. Liu, M. Niu, C. Xie, and C. Li, " $^{40}\text{Ar}/^{39}\text{Ar}$ dating of strike-slip motion on the Tan-Lu fault zone, East China," *Journal of Structural Geology*, vol. 27, no. 8, pp. 1379–1398, 2005.
- [43] G. Zhu, D. Jiang, B. Zhang, and Y. Chen, "Destruction of the Eastern North China Craton in a backarc setting: evidence from crustal deformation kinematics," *Gondwana Research*, vol. 22, no. 1, pp. 86–103, 2012.
- [44] F. Y. Wu, J. Q. Lin, S. A. Wilde, X. Zhang, and J. H. Yang, "Nature and significance of the early cretaceous giant igneous

- event in Eastern China," *Earth and Planetary Science Letters*, vol. 233, no. 1-2, pp. 103–119, 2005.
- [45] M. G. Zhai, Q. C. Fan, H. F. Zhang, J. L. Sui, and J. A. Shao, "Lower crustal processes leading to Mesozoic lithospheric thinning beneath Eastern North China: underplating, replacement and delamination," *Lithos*, vol. 96, no. 1-2, pp. 36–54, 2007.
- [46] J. Deng, S. Su, Y. Niu et al., "A possible model for the lithospheric thinning of North China Craton: evidence from the Yanshanian (Jura-Cretaceous) magmatism and tectonism," *Lithos*, vol. 96, no. 1-2, pp. 22–35, 2007.
- [47] T. Wang, Y. Zheng, T. Li, and Y. Gao, "Mesozoic granitic magmatism in extensional tectonics near the Mongolian border in China and its implications for crustal growth," *Journal of Asian Earth Sciences*, vol. 23, no. 5, pp. 715–729, 2004.
- [48] J. Liu, G. A. Davis, L. Zhiyong, and F. Wu, "The Liaonan metamorphic core complex, Southeastern Liaoning Province, North China: a likely contributor to Cretaceous rotation of Eastern Liaoning, Korea and contiguous areas," *Tectonophysics*, vol. 407, no. 1-2, pp. 65–80, 2005.
- [49] J. Liu, H. Guan, M. Ji, and L. Hu, "Late Mesozoic metamorphic core complexes: new constraints on lithosphere thinning in North China," *Progress in Natural Science*, vol. 16, no. 6, pp. 633–638, 2006.
- [50] D. P. Yan, M. F. Zhou, H. L. Song, G. H. Wang, and M. Sun, "Mesozoic extensional structures of the Fangshan tectonic dome and their subsequent reworking during collisional accretion of the North China Block," *Journal of the Geological Society*, vol. 163, no. 1, pp. 127–142, 2006.
- [51] G. Xing, Q. Lu, R. Chen et al., "Study on the ending time of Late Mesozoic tectonic regime transition in south China—comparing to the Yanshan area in North China," *Acta Geologica Sinica*, vol. 82, no. 4, pp. 451–463, 2008.
- [52] W. Lin, P. Monié, M. Faure et al., "Cooling paths of the NE China crust during the Mesozoic extensional tectonics: example from the South-Liaodong peninsula metamorphic core complex," *Journal of Asian Earth Sciences*, vol. 42, no. 5, pp. 1048–1065, 2011.
- [53] H. Y. Zhang, Q. L. Hou, and D. Y. Cao, "Tectono-chronologic constraints on a Mesozoic slip and thrust belt in the Eastern Jiaodong Peninsula," *Science in China, Series D*, vol. 50, no. 1, pp. 25–32, 2007.
- [54] W. Sun, X. Ding, Y. H. Hu, and X. H. Li, "The golden transformation of the Cretaceous plate subduction in the West Pacific," *Earth and Planetary Science Letters*, vol. 262, no. 3-4, pp. 533–542, 2007.
- [55] Q. Hou, Q. Liu, J. Li, and H. Y. Zhang, "Late Mesozoic shear zones and its chronology in the Dabie Mountains, Central China," *Scientia Geologica Sinica*, vol. 42, no. 1, pp. 114–123, 2007.
- [56] Q. D. Xu, Z. Q. Zhong, and F. W. Yang, " $^{40}\text{Ar}/^{39}\text{Ar}$ dating of the Xiaolinling gold area in Henan Province," *Geological Review*, vol. 44, no. 3, pp. 323–327, 1998.
- [57] X. H. Chen, A. Yin, G. E. Gehrels et al., "Two phases of Mesozoic North-South extension in the Eastern Altyn Tagh range, Northern Tibetan Plateau," *Tectonics*, vol. 22, no. 5, pp. 8-1–8-22, 2003.
- [58] X. Y. Ma, "On analytical tectonics," *Earth Science—Journal of Wuhan College of Geology*, vol. 22, no. 3, pp. 1–9, 1983.
- [59] C. Passchier and R. Trouw, *Microtectonics*, Springer, Berlin, Germany, 2nd edition, 2005.
- [60] R. H. Vernon and G. L. Clarke, *Principles of Metamorphic Petrology*, Cambridge University Press, 2008.
- [61] R. A. J. Trouw, C. W. Passchier, and D. J. Wiersma, *Atlas of Mylonites- and Related Microstructures*, Springer, Berlin, Germany, 2010.
- [62] M. Stipp and K. Kunze, "Dynamic recrystallization near the brittle-plastic transition in naturally and experimentally deformed quartz aggregates," *Tectonophysics*, vol. 448, no. 1–4, pp. 77–97, 2008.
- [63] D. A. Wark and E. B. Watson, "TitanQ: a titanium-in-quartz geothermometer," *Contributions to Mineralogy and Petrology*, vol. 152, no. 6, pp. 743–754, 2006.
- [64] W. M. Behr and J. P. Platt, "A naturally constrained stress profile through the middle crust in an extensional terrane," *Earth and Planetary Science Letters*, vol. 303, no. 3-4, pp. 181–192, 2011.
- [65] E. A. J. Burke, "Raman microspectrometry of fluid inclusions," *Lithos*, vol. 55, no. 1–4, pp. 139–158, 2001.
- [66] V. Lüders, B. Plessen, and R. Primio, "Stable carbon isotopic ratios of CH_4 - CO_2 -bearing fluid inclusions in fracture-fill mineralization from the Lower Saxony Basin (Germany)—a tool for tracing gas sources and maturity," *Marine and Petroleum Geology*, vol. 30, no. 1, pp. 174–183, 2012.
- [67] M. Slobodnik, R. Melichar, V. Hurai, and R. J. Bakker, "Lithostratigraphic effect on Variscan fluid flow within the Prague synform, Barrandian: evidence based on C, O, Sr isotopes and fluid inclusions," *Marine and Petroleum Geology*. In press.
- [68] Z. G. Mu, "The laser microprobe $^{40}\text{Ar}/^{39}\text{Ar}$ dating method," *Earth Science Frontiers*, vol. 10, no. 2, pp. 301–307, 2003.
- [69] M. Beltrando, G. S. Lister, M. Forster, W. J. Dunlap, G. Fraser, and J. Hermann, "Dating microstructures by the $^{40}\text{Ar}/^{39}\text{Ar}$ step-heating technique: deformation-pressure-temperature-time history of the Penninic Units of the Western Alps," *Lithos*, vol. 113, no. 3-4, pp. 801–819, 2009.
- [70] E. H. Rutter and K. H. Brodie, "Rheology of the lower crust," in *Geology of the Lower Continental Crust*, D. Fountain, R. Arculus, and R. Kay, Eds., pp. 201–268, Elsevier, Amsterdam, The Netherlands, 1992.
- [71] G. Hirth, C. Teyssier, and J. W. Dunlap, "An evaluation of quartzite flow laws based on comparisons between experimentally and naturally deformed rocks," *International Journal of Earth Sciences*, vol. 90, no. 1, pp. 77–87, 2001.
- [72] H. Stünitz, J. D. Fitz Gerald, and J. Tullis, "Dislocation generation, slip systems, and dynamic recrystallization in experimentally deformed plagioclase single crystals," *Tectonophysics*, vol. 372, no. 3-4, pp. 215–233, 2003.
- [73] L. Mehl and G. Hirth, "Plagioclase preferred orientation in layered mylonites: evaluation of flow laws for the lower crust," *Journal of Geophysical Research B*, vol. 113, no. 5, Article ID B05202, 2008.
- [74] C. Sassier, P. H. Leloup, D. Rubatto, O. Galland, Y. Yue, and D. Lin, "Direct measurement of strain rates in ductile shear zones: a new method based on syntectonic dikes," *Journal of Geophysical Research B*, vol. 114, no. 1, Article ID B01406, 2009.
- [75] H. W. Zhou and N. S. Chen, "Metamorphism, deformation and metamorphic reactions of low-pressure metamorphic belt in East Qinling orogenic belt, Western Henan," *Earth Science—Journal of China University of Geosciences*, vol. 19, no. 1, pp. 9–18, 1994.

Research Article

The Mesozoic Tectonic Dynamics and Chronology in the Eastern North China Block

Quanlin Hou,¹ Qing Liu,¹ Hongyuan Zhang,² Xiaohui Zhang,³ and Jun Li³

¹ Graduate University of Chinese Academy of Sciences, Beijing 100049, China

² School of Earth Sciences and Resources, China University of Geosciences, Beijing 100083, China

³ Institute of Geology and Geophysics, Chinese Academy of Sciences, Beijing 100029, China

Correspondence should be addressed to Quanlin Hou, quhou@gucas.ac.cn

Received 12 January 2012; Revised 9 May 2012; Accepted 11 May 2012

Academic Editor: Yu-Dong Wu

Copyright © 2012 Quanlin Hou et al. This is an open access article distributed under the Creative Commons Attribution License, which permits unrestricted use, distribution, and reproduction in any medium, provided the original work is properly cited.

Mesozoic tectonic events in different areas of the eastern North China Block (NCB) show consistency in tectonic time and genesis. The Triassic collision between NCB and Yangtze results in the nearly S-N strong compression in the Dabie, Jiaodong, and west Shandong areas in Middle Triassic-Middle Jurassic. Compression in the Yanshan area in the north part of NCB was mainly affected by the collision between Mongolia Block and NCB, as well as Siberia Block and North China-Mongolia Block in Late Triassic-Late Jurassic. However, in the eastern NCB, compressive tectonic system in Early Mesozoic was inverted into extensional tectonic system in Late Mesozoic. The extension in Late Mesozoic at upper crust mainly exhibits as extensional detachment faults and metamorphic core complex (MCC). The deformation age of extensional detachment faults is peaking at 120–110 Ma in Yanshan area and at 130–110 Ma in the Dabie area. In the Jiaodong area eastern to the Tan-Lu faults, the compression thrust had been continuing to Late Mesozoic at least in upper crust related to the sinistral strike slipping of the Tan-Lu fault zone. The extensional detachments in the eastern NCB would be caused by strong crust-mantle action with upwelling mantle in Late Mesozoic.

1. Introduction

In recent years, Mesozoic tectonic regime inversion is becoming one of the focuses in the studies of tectonic evolution and geodynamics. The Mesozoic tectonic dynamics process in the eastern North China is one of the most typical examples. EW-trending structural frame was transformed to the NE-NNE-trending structural framework and a compressive tectonic system to extensional tectonic system during Mesozoic. This intracontinental geodynamic process has attracted sight of geologists from China and around the world. Several hypotheses, such as long-distance effect of Pacific Plate [1], comprehensive constraints of the adjacent blocks (including the subducted and extinct Kula Plate, [2]), adjustment of the stress after the deep subduction of the Dabie area [3], large-scale sinistral strike slip, mantle plume [4, 5], delamination of lithosphere, and/or continental root-plume tectonics, had been put forward during the last decade. These ideas, even though being of great benefit to the study on Mesozoic tectonic regime inversion, have neither given rise a complete

theoretical framework nor concluded a uniform tectonic dynamics process. It should be noticed that China continent stands on the junction of three plates including the Tethyan oceans, the paleo-Asian ocean, and the paleo-Pacific ocean. The relative movement among the three plates, especially the Pacific plate which subducted NW warding beneath China continent, strongly affects China continent in the Mesozoic era. Many other important tectonic events, such as the continental deep subduction along the Dabie mountains, the lithosphere thinning of the eastern China, and the rapid uplifting of crust in western China, took place during a relative short period, although slightly different. With respect to the study of inversion process of tectonic regime in the eastern North China Block (NCB), the correlation and effect of the adjacent tectonic blocks should be considered, especially long-distance effect of the paleo-Pacific in the east and paleo-Tethyan in the west, and mantle upwelling would be considered as a reasonable tectonic model [6, 7]. It is recognized that the Mesozoic tectonic dynamics and chronology is one key problem to understand the Mesozoic

TABLE 1: Mineral ^{40}Ar - ^{39}Ar data in the main shear zone of the eastern Dabie Orogenic Belt [11].

Shear zone	Mineral	Weighted mean plateau age (Ma)
Xiaotian-Mozitan shear zone	Biotite	124.17 ± 0.25
	Biotite	126.91 ± 0.30
Shuihou-Wuhe shear zone	Biotite	190.59 ± 0.42
Taihu-Mamiao shear zone	Hornblende	197.41 ± 0.46
	Biotite	189.42 ± 0.29
	Biotite	124.87 ± 0.21
Susong-Qingshuihe shear zone	White mica	194.01 ± 0.36
	Biotite	127.96 ± 0.30

tectonic regime inversion in the eastern NCB. Three areas, the Dabie area and the Jiaodong area at the south margin and the Yanshan tectonic belt at the north part of the eastern NCB, would be discussed here to recognize the Mesozoic tectonic dynamics process in the eastern NCB.

2. Mesozoic Tectonic Dynamics at the Dabie Area

The Dabie area, located between NCB and Yangtze block in Early Mesozoic, is at the south margin of the eastern NCB. It is a key region to understand the Mesozoic tectonic regime inversion from compression to extension in the eastern NCB.

2.1. Collisional Time Constraints during the Early Mesozoic. The time range could be indicated by three aspects as follows. (1) The ultrahigh-pressure metamorphic assemblages started inversion at about 220–240 Ma and cooled down to 300°C at 180 Ma (time of the ^{39}Ar - ^{40}Ar biotite clock start-up, [8, 9]). (2) Geomagnetism studies indicate that visual polar migration curve of Hehuai basin, located at the south margin of NCB, had not been consistent with that of the Yangtze block until 159 Ma [10], which indicated that the two blocks had jointed and the collision orogeny had completed by the time (159 Ma). (3) The sedimentation of the foreland molasse basin in the Badong-Echeng area in Hubei province began at Middle Triassic and finished in the Late Jurassic, which implies that the collisional orogeny developed from the Middle Triassic to the Late Jurassic. Therefore, the collisional orogeny of the Dabie area started at late stage of Early Triassic (~240 Ma) and ended at Middle Jurassic (~180 Ma).

$^{40}\text{Ar}/^{39}\text{Ar}$ dating of biotite and hornblende from the Shuihou-Wuhe shear zone and the Taihu-Mamiao shear zone, at the north and south sides of ultrahigh-pressure metamorphic zone in the Dabie area, respectively, was carried out (Table 1 after [11]). The results indicated that the first stage deformation occurred at about 190 Ma, probably reflecting the inversion and cooling of the ultrahigh-pressure metamorphic rocks in the postorogeny. It was suggested that, with the weakening of the orogenic activity and increasing of potential energy of gravity of the orogenic belt in the postorogeny, the principal compressional stress direction changed from horizontal to vertical, leading to the orogenic

laxity or collapse, and the rapid inversion of the ultrahigh-pressure metamorphic rocks; then the nearly completion of collision in the Dabie area is about 190 Ma. Perhaps this 190 Ma event extended to 160 Ma in the late Jurassic because of the subduction of the paleo-Pacific plate [12].

2.2. The Late Mesozoic Extensional Detachment. The Northern Dabie metamorphic complex was identified as the crystalline metamorphic core of the Late Mesozoic extensional tectonics, which divided the Dabie area into two extensional tectonic systems, the north extensional tectonic system and the south extensional tectonic system (Figures 1 and 2).

2.2.1. The North Extensional Tectonic System. The identification of extensional crenulation cleavage (C') in the north detachment zones indicated that it is a complete extensional tectonic system, extending NE or NNE along the Xiaotian-Mozitan faults where the principal extensional detachment zone was developed in the early Cretaceous (Figure 1). The shear strain (γ) in the central part of the north detachment zone is up to about 2.6 and gradually decreased outward. The measurements of rock finite strains in the detachment zone indicated that the shear displacement is at least 56 km.

2.2.2. South Extensional Tectonic System. The south extensional tectonic system is composed of, from north to south, the Shuihou-Wuhe shear zone, Taihu-Mamiao shear zone, and Susong-Qingshuihe shear zone, which could represent lower, middle, and upper detachment system, respectively, (Figure 1). Analysis of fabric and dislocation density of deformed quartz indicates that deformation temperature (>700°C, 650–700°C) and differential stress (92 Mpa, 70–84 Mpa) descended from north to south in the south extensional tectonic system. The shear displacement of the upper detachment zone is at least 12 km by measurements of deformed rock finite strains. The directions of the extensional detachment are SSW, SSE, and/or S. The Flinn parameters (K) of strain ellipsoids of the lower, middle and upper detachment systems are 0.01–0.1, 1, and >7 respectively, representing accordingly flattened strain ($K = 0.01$ –0.1), plane strain ($K \approx 1$), and extensional strain ($K > 7$) from north to south, which implies that the extensional detachment could be caused mainly by magma intrusions, consisting with the timing indicates.

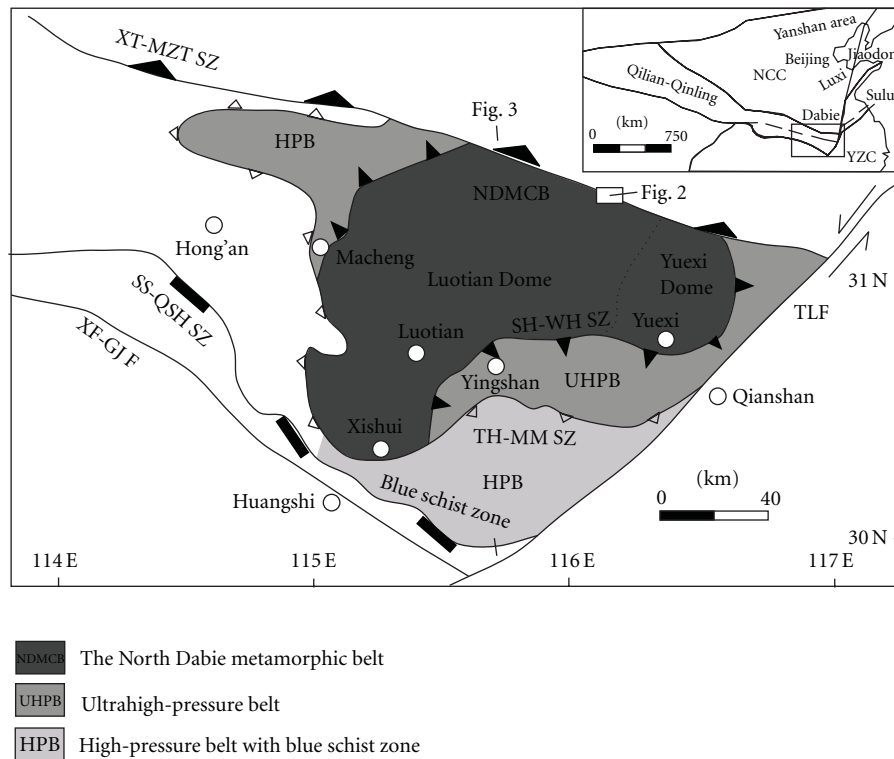


FIGURE 1: Sketch map of Late Mesozoic main shear zones in eastern Dabie Orogenic Belt, Central China (after [13]). NCP: Northern China Block; YZB: Yangzi Block; NHEB: North Huaiyang metamorphic belt; NDMCD: Northern Dabie metamorphic complex belt; UHPB: ultrahigh pressure metamorphic belt; HPB: high-pressure metamorphic belt; SH-WH SZ: Shuihou-Wuhe shear zone; TH-MM SZ: Taihu-Mamiao shear zone; SS-QSH SZ: Susong-Qingshuihe shear zone; XT-MZT SZ: Xiaotian-Mozitan shear zone; TLF: Tancheng-Lujiang fault (Tanlu Fault); XF-GJF: Xiangfan-Guangji fault.

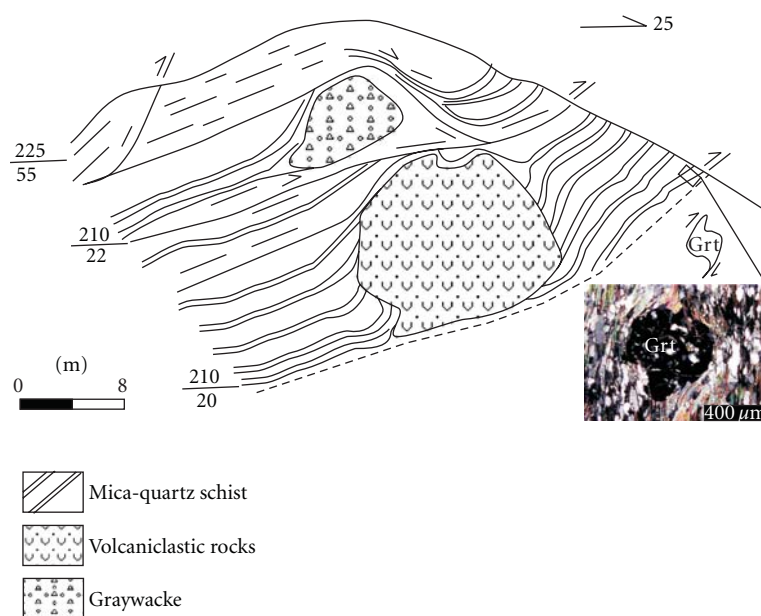


FIGURE 2: Late Jurassic volcaniclastic tectonite blocks were contained in mica-quartz schist (Pt_{2n}), north extensional detachment zone, implying the extension shearing after Late Jurassic. The microstructure picture of mica-quartz schist is shown in the right below the profile, which possibly indicates a dextral rotation of kinematics in the profile. The phenomenon is located near the Zhutang Village of Youdian Town in Jinzhai County of the Anhui Province.

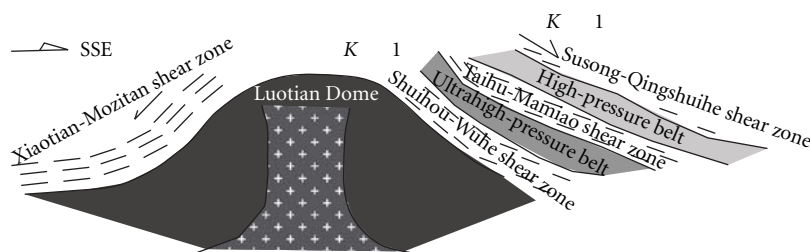


FIGURE 3: Extensional detachment model of Late Mesozoic, the Dabie Orogenic Belt.

2.3. The Chronology Constraints on the Extensional Detachment. In north extensional detachment zone, the shear zone developing in the Xinyang Group (Pt_{2n}) mica-quartz schist contains some allochthonous blocks from less than one meter to several meters in size of Late Jurassic volcanoclastic rocks and tuff. In addition, there are some field-scale harmonic recumbent folds in the Late Jurassic volcanoclastic rocks and the Late Proterozoic mica schist. Both Hong'an Group (Pt) and the Yanshanian granite (J₃-K₁) experienced extensional shear deformation together in the south extensional detachment system, which implies that the extensional detachment of both the south and north detachment systems took place after the Late Jurassic. The biotite and hornblende ⁴⁰Ar/³⁹Ar data from the north extensional tectonic system and in the Susong-Qingshuihe shear zone in the south detachment system reveal that the age of latter deformation is about 125 Ma (Table 1, after [11] (Figure 1)), which should represent the time of extensional detachment after orogeny. As a whole, the extensional deformation in the Dabie area mainly took place about 120 Ma ago.

2.4. Genesis of Extensional Detachment. At about 130–120 Ma, a little earlier than the detachment deformation age, numerous extensive granite and ultrabasic-basic plutons intruded into the Northern Dabie complex core. The ⁴⁰Ar-³⁹Ar and Rb-Sr isotopic analyses of rocks in the North Dabie also recorded the time at about 110–130 Ma. These chronology data imply that the magma intrusion played a major rule during the extensional detachment, which were supported by the finite strain measure analysis of rocks in the south extensional tectonic system (Figure 3). In addition, the ductile deformation of the plagioclase and pyroxene of pyroxenite and gabbros (115–130 Ma) in the Northern Dabie metamorphic complex (mainly refer to the Luotian Dome) implies that they once reached granulite facies during deformation and then uplift to the surface. Therefore, it is concluded that voluminous magmatic emplacement and delamination of lithosphere in Early Cretaceous induced the rapid uplift of the Northern Dabie as the center area of UHPM rocks and extensional detachment on both sides of the Northern Dabie complex core. The intense denudation results in the voluminous sediments in the Hefei basin. The high-pressure and ultrahigh-pressure eclogites probably emplaced during this process on the basis of our data (Figure 3).

Additionally, the distributions of the platinum group elements (PGEs) in the ultramafic and/or mafic rocks

(~120 Ma) in the Northern Dabie complex core show that their source regional upper mantle in Later Mesozoic enriched PGE (Pd ≈ 6.2 ppb in mantle). The original mantle before Mesozoic, however, depleted the PGE (Pd ≈ 2.3 ppb), according to the PGE distribution in Bixiling ultramafic rocks (older than 240 Ma) in the Northern Dabie complex core [14, 15]. The Later Mesozoic upper mantle with PGE enrichment in the Dabie area is supposed to be contaminated by about 8‰ Earth core materials, as the PGE contents in Earth core are much higher than in upper mantle [14, 15]. If thus, the enrichment mantle in the PGE must have been related to the Later Mesozoic extensional detachment in the Dabie area.

3. Mesozoic Tectonic Dynamics in the Jiaodong Area

The Jiaodong area, especially the eastern Jiaodong peninsula is located in the eastern terminal of the Dabie-Sulu ultrahigh pressure metamorphic belt, the eastern part of the south margin of the eastern NCB. As part of the collision orogenic belt between NCB and Yangtze block in Early Mesozoic, the eastern Jiaodong peninsula is significant in regional tectonic dynamics study in the eastern NCB.

The eastern Jiaodong peninsula can be divided into four lithotectonic units by four shear zones, the Shidao, Rongcheng, Mishan, and Mouping faults from SE to NW, respectively (Figure 4).

The Shidao shear zone is a broad ductile shear zone (>15 km in width) thrusting toward north and sinistral strike slipping in ENE-WSW direction. The total shear displacement is more than 90 km, in which the strike displacement is at least 19 km, the thrusting displacement >88 km, and the horizontal shrinkage >85 km, horizontal shrinkage ratio about 68% [18]. If Rongcheng, Mishan, and Mouping nappes were taken as an entirety, it turned about 25° clockwise (Figure 4), similar to the Korea peninsula which turned 30.5° clockwise [19].

The Rongcheng shear zone is a sinistral strike slipping and thrusting ductile shear zone dipping S or SSE in early stage (Figure 4). Different rocks, such as porphyritic granite (γ₅³, ~120 Ma), granitic gneiss, and hornblende schists (Pt₁) of the Weideshan rock bodies, overrode one another as thrusting sheets (Figure 5), indicating a strong thrusting and sinistral strike slipping during late Yanshanian epoch.

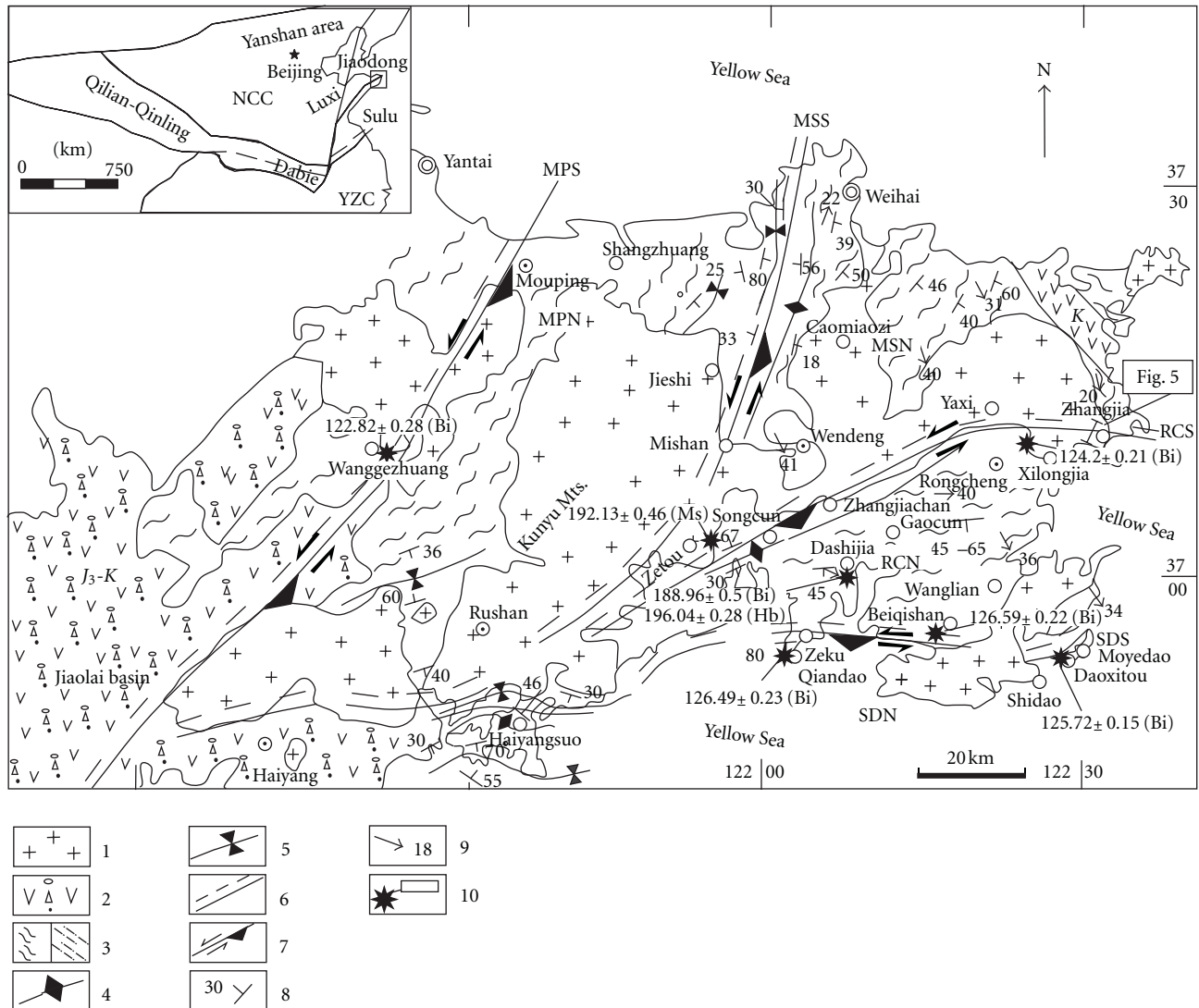


FIGURE 4: Geological map of the eastern Jiaodong peninsula (modified from [16, 17]). (Granite); (volcanic sedimentary rocks from Late Jurassic to Cretaceous); (gneiss rocks and mylonite zones); (syncline); (anticline); (brittle-ductile shear zones); (left lateral and reverse brittle shear sense); (layer occurrence); (lineation occurrence); (sample position and geochronological results). F₁, F₂, F₃, F₄: faults, namely, Shidao, Rongcheng, Mishan, and Mouping; I, II, III, IV: nappes, namely, Shidao, Rongcheng, Mishan, and Mouping.

However, it could not be excluded that Rongcheng shear zone would experience extensional strike-slip nature at late stage.

The Mishan shear zone is an almost upright sinistral strike slipping fault zone striking NNE, in which a tectono-clastic rock belt of wide was formed. Rocks have a notable change across the fault. A few meters width of mylonite bands was observed in the fault zone, indicating that it could be a ductile shear zone in the early stages, and then was reconstructed later by brittle fractures. Therefore, it is difficult to identify the attitude and nature of the zone. However, it holds somewhat that the later stage of the shear zone was generally in agreement with the brittle shear zones in the Eastern Jiaodong peninsula.

The Mouping shear zone is a compression sinistral strike-slip fault striking NE-SW in steep dip. The shear zone expressed as a brittle-ductile tectonite belt (20–30 km in width) and had extensional characteristics in late stage.

Mouping shear zone could be influenced by Tan-Lu faults, because similar tectonic behavior was proved in both the Mouping shear zone and the Tan-Lu fault zone, such as sinistral slip and long time of fault development.

The paleodifferential stress values of the Shidao, Rongcheng and Mouping shear zones are of 105 Ma, 99 Ma, and 85 MPa, respectively, showing a decrease tendency from south to north. The strain measurement and the quartz c-fabric analysis indicate that the deformation degree of those three shear zones decrease in order from south to north. The Flinn values (K) of the strain ellipsoid range between 0.6 and 0.75, implying flattening strain. Therefore, the thrusting in the Eastern Jiaodong peninsula should be from south to north in general.

$^{40}\text{Ar}/^{39}\text{Ar}$ chronological analyses on the biotite and hornblende from the Shidao, Rongcheng, and Mouping shear zones (Table 2, [20]) indicated two groups, ~190 Ma and

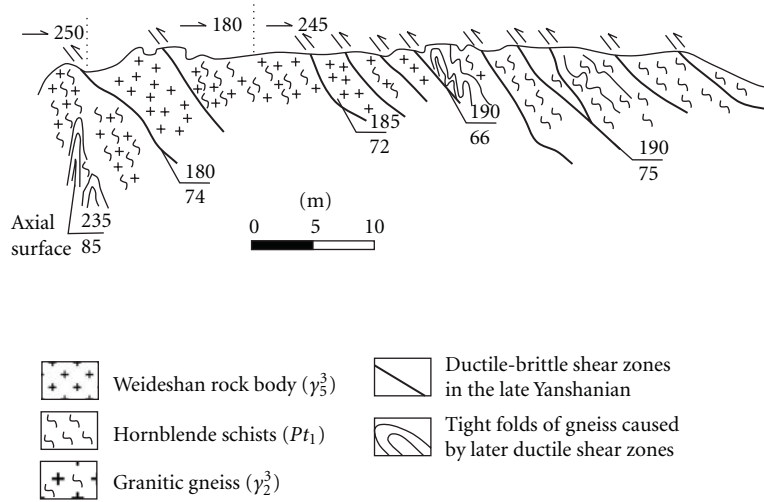


FIGURE 5: Structural outcrop sketch at Zhangjia, Rongcheng. At outcrop scale the porphyritic granite (γ_5^3), granitic gneiss, and hornblende schists (Pt_1) of the Weideshan rock body were found to be overriding together as the style of thrusting sheets.

TABLE 2: $^{40}\text{Ar}/^{39}\text{Ar}$ precise dating results of individual minerals in the eastern Jiaodong Peninsula [20].

Sample position and sample number	Lithology	Minerals selected	Serial number	$^{40}\text{Ar}/^{39}\text{Ar}$ plateau age, Ma	Tectonic setting of samples
Qiandao01120905	Granite gneiss	Biotite	R03020	126.49 ± 0.23	Shidao shear zone
Beiqishan01121002	Granite gneiss	Biotite	R03002	126.59 ± 0.22	Shidao shear zone
Daositou01121005	Granite gneiss	Biotite	R03026	125.72 ± 0.15	Shidao shear zone
Dashijia01120908B	Granite gneiss	Biotite	R03005	188.96 ± 0.50	Rongcheng nappe
Dashijia01120908H	Granite gneiss	Hornblende	R03019	196.04 ± 0.28	Rongcheng nappe
Zetou01120807	Granite mylonite	Muscovite	R03009	192.13 ± 0.46	Mishan nappe
Xilongjia01121101	Granite gneiss	Biotite	R03008	124.20 ± 0.21	Rongcheng shear zone
Wanggezhuang01121504	Quartzofeldspathic mylonite	Biotite	R03025	122.82 ± 0.28	Mouping shear zone

~120 Ma, amazingly similar to those of the Dabie area. The two groups might represent the ages of the reversion of ultra-high pressure metamorphic rocks during the postorogenic structural relaxation and the slip compressional deformation after the orogeny, respectively.

As well known, in the Early Cretaceous, almost the whole North China area was tectonically in an extensional or extruding setting. However, the large-scale sinistral strike-slipping of the Tan-Lu fault zone resulted in the sinistral strike-slipping compressional settings at least at the shallow part of the crust in the east side front of the Tan-Lu faults, to form the sinistral strike-slipping thrust nappes and the clockwise rotation of the blocks bounded by the shear zones. The subduction of the west Pacific plate toward NW and/or NNW resulted in the strike slipping and the northward movement at the east side of the Tan-Lu fault zone. Meanwhile, the deep part of the crust in the Jiaodong peninsula might be under the extensional tectonic background, according to the relative data of basins and volcanic rocks.

4. Mesozoic Tectonic Dynamics in the Yanshan Area

The Yanshan area, one famous intraplate orogen considered by some authors (e.g., [21, 22]), is located at the north part of the eastern NCB. The Yanshan area is the cradle of Chinese geologists. Since Wong [23] put forward “Yanshan Movement,” lots of attentions have been paid by geologists in the aspect of the Mesozoic strong tectonic deformation and severe magma activities. In recent years, the Mesozoic complex intraplate deformation has become one major focus of continental dynamics research in China.

The eastern segment of the Yanshan area is characterized with two ductile shear zones trending EW and NNE respectively, which controlled the tectonic framework of the northern North China. Field observations and structural analyses reveal that the EW trending ductile shear zones are mainly contributed to dextral compressional deformation that resulted from top-to-the-southeast oblique thrust

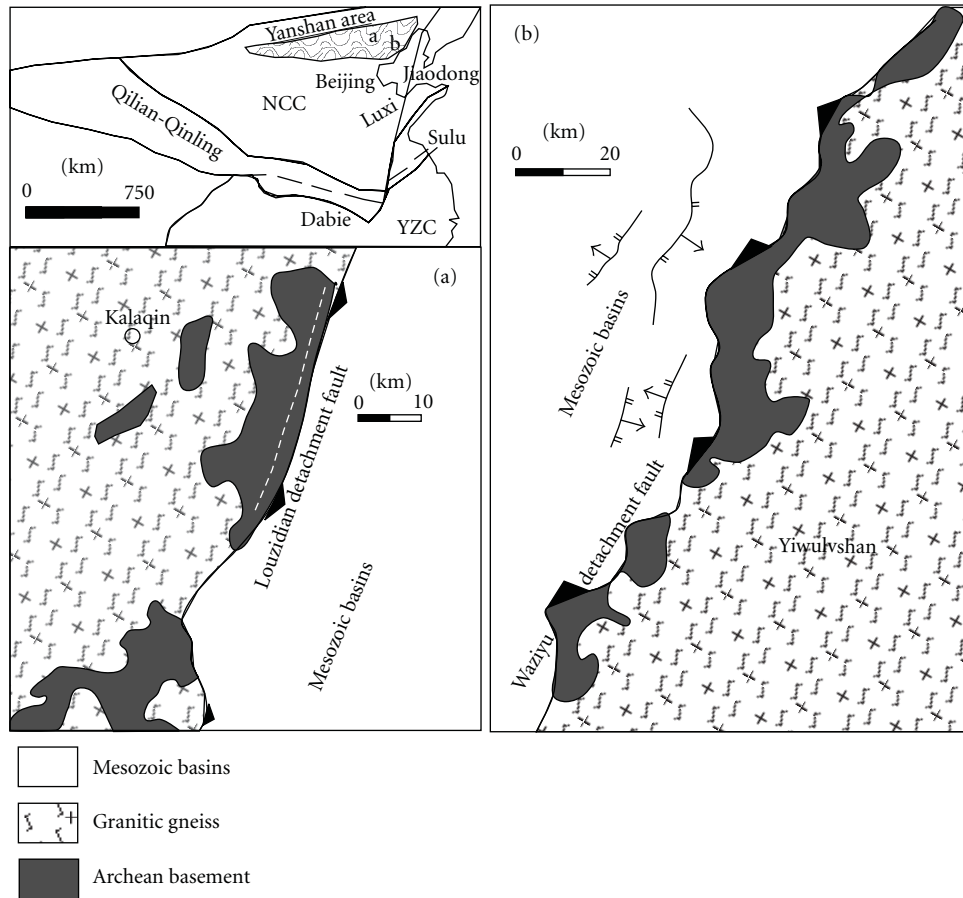


FIGURE 6: Geological map of the Eastern Yanshan Area. Simplified geological map showing major tectonic units of the Yanshan belt and its surrounding areas, with the locations of Kalaqin and Yiwulushan metamorphic core complexes indicated by a rectangle. (a) Sketch geological map of the Kalaqin metamorphic core complex (modified after [29]); (b) Sketch geological map of the Yiwulushan metamorphic core complex (adopted from [32]).

shearing, whereas the NNE trending ones are genetically related to sinistral strike slip and extensional faulting. The $^{40}\text{Ar}/^{39}\text{Ar}$ geochronology indicates that the top-to-the-southeast oblique thrusting event recorded by the EW-trending ductile shear zones mainly occurred in Late Triassic (Yanshanian, too) [24]. Recent studies have clarified a series of major Mesozoic contractional events in the Yanshan area [21, 25]. The Huairou thrust north of Beijing has overridden the Cambrian carbonates above the Middle Jurassic Tiaojishan formation (J_2) at Late Jurassic with a southern displacement direction. The Gubeikou-Pingquan fault features both south-vergent thrusting and dextral strike slipping with an age span from 148 to 132 Ma [21]. In summary, the activity period for contraction and thrusting at the Yanshan tectonic belt are mainly concentrated at Late Triassic and Late Jurassic.

Similar to most orogens, localized regions of large-magnitude extensional strain typified by metamorphic core complexes are also prominent geologic and physiographic features of the Yanshan tectonic belt. The examples include the Yunmengshan metamorphic core complex north of Beijing [26–28], the Kalaqin metamorphic core complex in the

Inner Mongolia [29–31], and the Yiwulushan metamorphic core complex in western Liaoning [31, 32].

As described by Han et al. [29] and Shao et al. [30], the Kalaqin metamorphic core complex is a major structural component of the Ma'anshan uplift with a length of about 100 km and a width of about 35 km (Figures 6(a) and 6(b)). The core of the uplift consists of Archean gneisses of epidote-amphibolite facies (>2.5 Ga), marbles and TTG series, Early Proterozoic schists and marbles of low green schist facies, Late Proterozoic Minganshan group slates, Cambrian carbonates, Early Permian-Middle Jurassic plutonic rocks, and Early Cretaceous granitic rocks. The eastern and western flanks of the uplift consist mainly of Jurassic-Cretaceous terrestrial volcanic and sedimentary strata. The Louzidian detachment fault, which consists of the Louzidian ductile shear zone and the related Louzidian normal fault, separates metamorphosed complexes in the footwall to the west from the unmetamorphosed Mesozoic and Cenozoic sedimentary covers in the hanging wall. Field observations and structural analyses reveal that the ductile shear zone was genetically related to sinistral strike slip and extensional

faulting. $^{40}\text{Ar}/^{39}\text{Ar}$ geochronology established an Early Cretaceous age for its formation [31].

As first reported by Ma et al. [33], geochronologically constrained by Zhang et al. [31] and further defined structurally by Darby et al. [32], the Yiwulüshan of western Liaoning displays many of the structural, metamorphic, and igneous features that characterize Cordilleran metamorphic core complexes. Situated along the eastern segment of the Yanshan area, the Yiwulüshan metamorphic core complex has an east-west dimension of 25 km and a north-south dimension of 60 km (Figure 6(c)). The core consists predominantly of Mesozoic granitoid plutons and their country rocks, which include migmatite, epidote-amphibolite facies paragneiss, and orthogneiss of the Archean crystalline basement. Plutons are granodioritic to granitic and grade outward into augen gneiss or migmatite. At structurally higher levels, it is the well-developed NNE-trending Waziyu ductile shear which, together with the related normal fault above it along the eastern margin of the Fuxin basin, separates the core of the dome from the hanging wall of the unmetamorphosed to low-grade metamorphosed Middle-Late Proterozoic Changcheng System and the Mesozoic sedimentary and volcanic rocks. Three synkinematic biotites from the Waziyu ductile shear zone give a $^{40}\text{Ar}/^{39}\text{Ar}$ plateau age span of 130–116 Ma and thus establish its main activity period as Early Cretaceous [31, 32]. Zircon U-Pb geochronology indicates that three representative batholiths (Lüshan, Jianlazishan, and Hengshan) at the core were mainly emplaced during Middle-to-Late Jurassic times, with ages of 164, 153, and 153 Ma, respectively [34]. Four other mineral samples from the core and the eastern flank give $^{40}\text{Ar}/^{39}\text{Ar}$ ages of 133 Ma (muscovite), 140 Ma (biotite), 156 Ma (K-feldspar), and 165 Ma (hornblende), respectively, (unpublished data), indicting the extensional exhumation of the metamorphic core complex range from east to west.

As a case with the Basin and Range Province of the Western United States, the isolated metamorphic core complexes within the Yanshan area, such as the Yunmengshan, Kalaqin, and Yiwulüshan metamorphic core complexes, represent the high-strain extension regions within a broad region of more distributed extensional deformation during Early Cretaceous [25–27, 30, 33, 35–38]. Their formation are contributes to gravitational collapse of an orogenically thickened crust that was facilitated by thermal weakening due to localized deep-seated plutonism and paleo-Pacific plate boundary reorganization [25, 31, 32].

5. Discussion and Conclusion

The statistics indicate that the main Mesozoic magmatic, metamorphic, and tectonic events on the Dabie, Luxi, Jiaodong, and Yanshan areas of the eastern NCB from south to north are consistent in time and genesis (Table 3, [39]). In the eastern NCB, the nearly S-N compression in Early Mesozoic dominated the formation of a series of thrusts trending almost E-W. In Cretaceous, the extension dominated the formation of a series of extensional detachment structures and metamorphic core complex. Many scholars had studied

the tectonic setting of the tectonic regime inversion in eastern NCB and gotten different opinions [7, 15, 40–43]. On the base of our studies and former researches, this paper discusses this issue briefly.

5.1. The Early Mesozoic Compression Setting. In the south of the NCB, the Mesozoic compressions occurred in Early-Middle Triassic-early Late Jurassic, such as the Dabie and Luxi areas, but, in the north, occurred a little later, such as the Yanshan area which experienced two periods: in the Late Triassic and the Late Jurassic.

The collision between the Yangtze block and the NCB began at Middle-Late Triassic, the Dabie-Sulu ultrahigh pressure metamorphic belt was formed at 242–224 Ma and cooled down to 300°C at 180 Ma [8, 9], which is approximately consistent with the early deformation age of ductile shear zone in Dabie-Sulu orogenic belt (Ar-Ar age of ~190 Ma, Tables 1 and 2, [11, 18]). Perhaps it was the geological record of orogenic relaxation at about 180–190 Ma, indicating the ending of collision orogenesis. The visual polar migration curve of NCB and Yangtze Block became consistency at 159 Ma [10]. In general, the collision between the NCB and the Yangtze Block might cause the nearly S-N strong compression thrusting in the southern NCB in Middle Triassic-Middle Jurassic (240 Ma–180 Ma) [20, 44].

The compressive shortening in the northern NCB was mainly affected by the collisions of the Mongolia block with the NCB and the Siberia block with the North China-Mongolia block. The collision time between the Mongolia block and the NCB was at about 250 Ma–200 Ma. This collision caused nearly S-N compression and formed a series of E-W striking thrust nappes of 250–200 Ma in Yanshan area, such as the thrust-nappes thrusting southward at 219 Ma in Yiwulüshan. The Mongolia-Okhotsk paleocean gradually closed eastward in Early-Middle Jurassic (190–170 Ma) and caused collision between the Siberia block and the North China-Mongolia block. The collision might keep on until Late Jurassic (160–150 Ma) and even later [42, 45–48], which formed the Late Jurassic thrust-nappes thrusting southward in the Yanshan tectonic belt, such as the thrust nappes of the Cambrian overriding the Tiaojishan formation (J_{2-3}) in the Huaibei town of the Huairou area and the Gubeikou-Pingquan thrust fault in northern Beijing. During the relaxation period of compression, however, episodic extensional stress fields resulted in a series of Jurassic volcanic rocks.

5.2. Late Mesozoic Extensional Tectonic Setting. In the Late Mesozoic, the tectonic regime was inverted into extensional setting in the NCB. The extensions in the shallow crust were mainly displayed by extensional detachment faults and metamorphic core complex. The deformation age of extensional detachment shear zones in Yanshan tectonic belt is 140–100 Ma with a peak period of 120–110 Ma, while in the Dabie and the Luxi area it is 130–110 Ma. The intrusion ages of the magmatic rocks in the metamorphic core complex mostly are 150–110 Ma, only a few reached 170–160 Ma, a little earlier than the detachment shear deformation on the

TABLE 3: Time-range index of main Mesozoic structure events in the eastern North China Block [39].

Structure belt	Dabie			West Shandong	Yanshan	
Rock type	(Ultra) mafic rocks	Granite/shear zone	Metamorphic rock (migmatite)	Intermediate-mafic rock	Intrusive	Shear zone
Isotopic age of compression (Ma)	220–240	190	230–240	230–250	165–180	~150 ~219
Isotopic age of extension (Ma)	120–130	~120	117–130	115–130	111–130	116–140
Structural index of compression	The oldest deposit in foreland molasse basin is Mid-Triassic and the youngest one is upper Jurassic			γ_5^3 undeformed	J_2 or J_3 (Tiaojishan group) deformed	
Structural index of extension	J_3, γ_5^3 deformed		J_3 or K_1 deformed	K_1 deformed		

whole. Though some areas such as Yanshan tectonic belt still show compression in shallow crust where thrust napping was developing, underplating and delamination had developed deeper.

It usually takes about tens to hundreds million years for deep underplating and delamination to exhibit extensional detachment structure in the shallow crust. Chronology and deformed rock strain data (such as the Dabie extensional detachment belt (Figure 3)) showed that magma intrusion directly caused extensional detachment. Some geologists related the extension to the NNW or NW subduction of the west Pacific plate into the Eurasia plate. Many evidences indicate that East-Asia circum-Pacific active continental margin began at Middle Jurassic (180 Ma), peaking at Late Jurassic-Early Cretaceous, equivalent to the B episode of the movement in the Yanshan area [42].

In Jurassic, the NCB was acted by three plates, such as the Yangtze, Siberian, and west Pacific plates, and with the orogenesis going on, the crust gradually thickened, potential energy difference increased, and the main compression stress gradually changed from horizontal to vertical. Especially with the thickening of the NCB crust, the lithosphere became unbalanced and the asthenosphere upwelled. Lithosphere underplating and delamination could cause lithosphere rebound; then partial melting, magma intrusion and volcanism occurred, which resulted in the uplift extension detachment of the crust. But whether the underplating and delamination in the eastern North China, beginning at Late Jurassic-Cretaceous, was related to the west Pacific plate subduction still needs to be further studied.

Some researchers suggested that the Late Mesozoic extensional tectonic setting in the eastern North China were mainly resulted from mantle branch structures [3–5, 49, 50]. This is a good way to interpret the Late Mesozoic thermal dome-extensional tectonic setting of the eastern North China. According to the study of the PGE distributions, it was suggested that the mantle was rich in PGE at 120 Ma, which is apparently different from the previous PGE-deplete mantle. Therefore, we speculate that the materials from the earth core was added to the Late Mesozoic mantle (at least 8%, [15]), which supported the opinion of mantle branch structure to some degree.

In the Jiaodong peninsula, however, the sinistral strike-slip compressions dominated in Late Mesozoic, forming a series of thrust-nappes thrusting northward, and the deformation age of ~120 Ma (Table 2, [20]). The sinistral strike slipping of Jiaodong and the Tan-Lu faults could be related to the NE-ward subduction of the west Pacific plate. Therefore, sinistral strike-slip-compression stress field was generated in the east front of the Tan-Lu Faults zone, resulting in the sinistral strike-slip thrust faults and the clockwise rotation (at about 25°) of the blocks bounded by the thrust faults in the Jiaodong peninsula, similar to the Korea peninsula. Then deep structures could not be consistent with shallow ones and deep underplating and delamination; even magma intrusion and volcanism could have happened, but they were not immediately displayed in the shallow. It also suggested that the Tan-Lu Faults zone could be an important tectonic boundary, which caused significant difference in Mesozoic tectonic setting on the both sides of the Tan-Lu Faults.

Acknowledgments

The authors would like to thank Professor Jiliang Li, Professor Wenjiao Xiao, Professor Mingguo Zhai, and Professor Zhihong Wang from Institute of Geology and Geophysics, Chinese Academy of Sciences, and Dr. Tianshan Gao from university of Science and Technology of China for their kind help in field work and discussion. This work has been supported by the following grants: the National Natural Science Foundation of China (Grants 41030422; 90714003).

References

- [1] S. Hu, Y. Zao, Z. Hu, J. Guo, and B. Xu, "Evolution and development of tectonics and magmatism at the active continental margin of east China (E 106°) during Mesozoic and Cenozoic," *Acta Petrologica Sinica*, vol. 10, no. 4, pp. 370–381, 1994 (Chinese).
- [2] J. S. Ren, B. G. Niu, and J. Zheng, "Tectonic frame and geodynamic evolution of eastern China," *Geological Research*, vol. 29, no. 30, pp. 43–55, 1997 (Chinese).
- [3] J. F. Deng, H. L. Zhao, and X. X. Mo, *Continental Roots-Plume Tectonics of China*, Beijing, China, Geological Publishing House, 1996.

- [4] J. Deng, S. Su, Y. Niu et al., "A possible model for the lithospheric thinning of North China Craton: evidence from the Yanshanian (Jura-Cretaceous) magmatism and tectonism," *Lithos*, vol. 96, no. 1-2, pp. 22-35, 2007.
- [5] S. V. Lysak, "Thermal history, geodynamics, and current thermal activity of lithosphere in China," *Russian Geology and Geophysics*, vol. 50, no. 9, pp. 815-825, 2009.
- [6] M. Zhai, J. Yang, and W. Liu, "The large-scale metallogenesis and large-scale cluster of gold-deposits in eastern Shandong, China," *Science in China D*, vol. 44, no. 8, pp. 758-768, 2001.
- [7] M. Zhai, R. Zhu, J. Liu et al., "Time range of Mesozoic tectonic regime inversion in eastern North China Block," *Science in China D*, vol. 47, no. 2, pp. 151-159, 2004.
- [8] B. R. Hacker, L. Ratschbacher, L. Webb, T. Ireland, D. Walker, and D. Shuwen, "U/Pb zircon ages constrain the architecture of the ultrahigh-pressure Qinling-Dabie Orogen, China," *Earth and Planetary Science Letters*, vol. 161, no. 1-4, pp. 215-230, 1998.
- [9] L. Ratschbacher, B. R. Hacker, A. Calvert et al., "Tectonics of the Qinling (Central China): tectonostratigraphy, geochronology, and deformation history," *Tectonophysics*, vol. 366, no. 1-2, pp. 1-53, 2003.
- [10] S. A. Gilder, P. H. Leloup, V. Courtillot et al., "Tectonic evolution of the Tancheng-Lujiang (Tan-Lu) fault via Middle Triassic to Early Cenozoic paleomagnetic data," *Journal of Geophysical Research B*, vol. 104, no. 7, pp. 15365-15390, 1999.
- [11] Q. Hou, Q. Liu, J. Li, and H. Zhang, "Late Mesozoic shear zones and its chronology in the Dabie Mountains, Central China," *Scientia Geologica Sinica*, vol. 42, no. 1, pp. 114-123, 2007.
- [12] S. W. Dong, J. M. Hu, S. Z. Li et al., "The Jurassic deformation in the Dabie Mountains and its tectonic significances," *Acta Petrologica Sinica*, vol. 21, no. 4, pp. 1189-1194, 2005.
- [13] S. Suo, Z. Zhong, and Z. You, "Extensional deformation of post ultrahigh-pressure metamorphism and exhumation process of ultrahigh-pressure metamorphic rocks in the Dabie massif, China," *Science in China D*, vol. 43, no. 3, pp. 225-236, 2000.
- [14] Q. Liu, *Study on the distribution of Platinum group elements in Dabie (ultra-) mafic rocks and Fuxin volcanic rocks [Ph.D. dissertation]*, Graduate University of the Chinese Academy of Sciences, Beijing, China, 2005.
- [15] Q. Liu, Q. L. Hou, X. H. Zhou, and L. W. Xie, "The distribution of platinum-group elements in gabbros from Zhujiapu, Dabie orogen," *Acta Petrologica Sinica*, vol. 21, no. 1, pp. 227-239, 2005.
- [16] M. Zhai, J. Guo, Q. Wang, K. Ye, B. Cong, and W. Liu, "Division of petrological-tectonic units in the Northern Sulu ultra high pressure zone: an example of thick-skin thrust of crystalline units," *Scientia Geologica Sinica*, vol. 35, no. 1, pp. 16-26, 2000 (Chinese).
- [17] M. Yang and G. Lü, *The Geology-Geochemistry of Gold Deposits of the Greenstone Belt in Jiaodong District, China*, Geological Publishing House, Beijing, China, 1996.
- [18] H. Y. Zhang, Q. L. Hou, and D. Y. Cao, "Study of thrust and nappe tectonics in the eastern Jiaodong Peninsula, China," *Science in China D*, vol. 50, no. 2, pp. 161-171, 2007.
- [19] X. X. Zhao, R. S. Coe, H. K. Chang et al., "Clockwise rotations recorded in Early Cretaceous rocks of South Korea: Implications for tectonic affinity between the Korea Peninsula and North China," *Geophysical Journal International*, vol. 139, no. 2, pp. 447-463, 1999.
- [20] H. Y. Zhang, Q. L. Hou, and D. Y. Cao, "Tectono-chronologic constraints on a Mesozoic slip and thrust belt in the eastern Jiaodong Peninsula," *Science in China D*, vol. 50, no. 1, pp. 25-32, 2007.
- [21] C. Zhang, G. Wu, D. Xu, G. Wang, and W. Sun, "Mesozoic tectonic framework and evolution in the central segment of the intraplate Yanshan orogenic belt," *Geological Bulletin of China*, vol. 23, no. 9-10, pp. 864-875, 2004 (Chinese).
- [22] J. Hu, X. Liu, Y. Zhao, G. Xu, J. Liu, and S. Zhang, "On Yanshan intraplate orogene: an example from Taiyanggou area, Lingyuan, Western Liaoning Province, Northeast China," *Earth Science Frontiers*, vol. 11, no. 3, pp. 255-271, 2004 (Chinese).
- [23] W. H. Wong, "Crustal movements and igneous activities in eastern China since Mesozoic time," *Bulletin of the Geological Society of China*, vol. 6, no. 1, pp. 9-37, 1927.
- [24] X. Zhang, T. Li, and Z. Pu, "⁴⁰Ar/³⁹Ar thermochronology of two ductile shear zones from Yiwulüshan, West Liaoning Region: age constraints on the Mesozoic tectonic events," *Chinese Science Bulletin*, vol. 47, no. 13, pp. 1113-1118, 2002.
- [25] G. A. Davis, Y. Zheng, C. Wang, B. J. Darby, C. Zhang, and G. E. Gehrels, "Mesozoic tectonic evolution of the Yanshan fold and thrust belt, with emphasis on Hebei and Liaoning provinces, northern China," in *Paleozoic and Mesozoic Tectonic Evolution of Central and Eastern Asia: From Continental Assembly to Intracontinental Deformation*, M. S. Hendrix and G. A. Davis, Eds., vol. 194 of *Geological Society of America Memoir*, pp. 171-197, 2001.
- [26] G. A. Davis, X. Qian, Y. Zheng et al., "The Huairou (Shuiyu) ductile shear zone, Yunmengshan Mts.," in *Proceedings of the 30th international Geological Congress Field Trip Guide*, Beijing Geological Publishing House, Beijing, China, 1996.
- [27] G. A. Davis, X. Qian, Y. Zheng et al., "Mesozoic deformation and plutonism in the Yunmengshan: a Chinese metamorphic core complex north of Beijing, China," in *The Tectonic Evolution of Asia*, A. Yin and T. M. Harrison, Eds., pp. 253-280, Cambridge University Press, Cambridge, UK, 1996.
- [28] G. A. Davis, Y. Zheng, C. Wang, B. J. Darby, C. Zhang, and G. E. Gehrels, "Geometry and geochronology of Yanshan belt tectonics," in *Proceedings of the 100th Anniversary Celebration of Peking University: Collected Works of International Symposium on Geological Science*, pp. 275-292, Department of Geology, Peking University, Beijing, China, 1998.
- [29] B. F. Han, Y. Zheng, J. Gan, and Z. Chang, "The Louzidian normal fault near Chifeng, inner Mongolia: master fault of a quasi-metamorphic core complex," *International Geology Review*, vol. 43, no. 3, pp. 254-264, 2001.
- [30] J. A. Shao, L. Q. Zhang, W. Jia, and P. Y. Wang, "Harkin metamorphic core complex in Inner Mongolia and its upwelling mechanism," *Acta Petrologica Sinica*, vol. 17, no. 2, pp. 283-290, 2001 (Chinese).
- [31] X. Zhang, H. Wang, and Y. Ma, "⁴⁰Ar/³⁹Ar age constraints on two NNE-trending ductile shear zones, Yanshan intraplate Orogen, North China Craton," *International Geology Review*, vol. 45, no. 10, pp. 936-947, 2003.
- [32] B. J. Darby, G. A. Davis, X. Zhang, F. Wu, S. Wild, and J. Yang, "The newly discovered Wuziyu metamorphic core complex, Yiwulü Shan, western Liaoning province, North China," *Earth Science Frontiers*, vol. 11, no. 3, pp. 145-155, 2004.
- [33] Y. Ma, S. Cui, G. Wu et al., "The structural feature of metamorphic core complex in Yiwulüshan mountains, western Liaoning," *Acta Geoscientia Sinica*, vol. 20, pp. 385-391, 1999 (Chinese).

- [34] X. H. Zhang, Q. Mao, H. F. Zhang, and S. A. Wilde, "A Jurassic peraluminous leucogranite from Yiwulüshan, western Liaoning, North China craton: age, origin and tectonic significance," *Geological Magazine*, vol. 145, no. 3, pp. 305–320, 2008.
- [35] G. A. Davis, B. J. Darby, Y. Zheng, and T. L. Spell, "geometric and temporal evolution of an extensional detachment fault, Hohhot metamorphic core complex, Inner Mongolia, China," *Geology*, vol. 30, pp. 1003–1006, 2002.
- [36] L. E. Webb, S. A. Graham, C. L. Johnson, G. Badarch, and M. S. Hendrix, "Occurrence, age, and implications of the Yagan-Onch Hayrhan metamorphic core complex, southern Mongolia," *Geology*, vol. 27, no. 2, pp. 143–146, 1999.
- [37] C. L. Johnson, L. E. Webb, S. A. Graham, M. S. Hendrix, and G. Badarch, "Sedimentary and structural records of Late Mesozoic high-strain extension and strain partitioning, east Gobi basin, Southern Mongolia," in *Paleozoic and Mesozoic Tectonic Evolution of Central and Eastern Asia: From Continental Assembly to Intracontinental Deformation*, M. S. Hendrix and G. A. Davis, Eds., vol. 194 of *Geological Society of America Memoir*, pp. 413–433, 2001.
- [38] J. Ren, K. Tamaki, S. Li, and Z. Junxia, "Late Mesozoic and Cenozoic rifting and its dynamic setting in Eastern China and adjacent areas," *Tectonophysics*, vol. 344, no. 3–4, pp. 175–205, 2002.
- [39] Q. L. Hou, Y. D. Wu, F. Y. Wu, M. G. Zhai, J. H. Guo, and Z. Li, "Possible tectonic manifestations of the Dabie-Sulu orogenic belt on the Korean Peninsula," *Geological Bulletin of China*, vol. 27, no. 10, pp. 1659–1666, 2008.
- [40] M. Zhai, R. Zhu, J. Liu et al., "Time range of Mesozoic tectonic regime inversion in eastern North China Block," *Science in China D*, vol. 33, no. 10, pp. 913–920, 2003.
- [41] Y. Zhao, Z. Yang, and X. Ma, "Geotectonic transition from Paleasian system and Paleotethyan system to Paleopacific active continental margin in eastern Asia," *Scientia Geologica Sinica*, vol. 29, no. 2, pp. 105–119, 1994.
- [42] Y. Zhao, G. Xu, S.-H. Zhang et al., "Yanshanian movement and conversion of tectonic regimes in East Asia," *Earth Sciences Frontiers*, vol. 11, no. 3, pp. 319–328, 2004.
- [43] Z. Yadong, G. A. Davis, W. Cong, B. J. Darby, and Z. Changhou, "Major Mesozoic tectonic events in the Yanshan belt and the plate tectonic setting," *Acta Geologica Sinica*, vol. 74, no. 4, pp. 289–302, 2000.
- [44] R. Y. Zhang, J. G. Liou, and W. G. Ernst, "The Dabie-Sulu continental collision zone: a comprehensive review," *Gondwana Research*, vol. 16, no. 1, pp. 1–26, 2009.
- [45] A. M. Ziegler, P. M. Ree, D. B. Rowley, A. Bekker, Q. Li, and M. Hulver, "Mesozoic assembly of Asia: constraints from fossil floras, Tectonics, and paleomagnetism," in *Tectonic Evolution of Asia*, T. M. A. Harrison, Ed., pp. 371–400, Cambridge University Press, Cambridge, UK, 1996.
- [46] A. Yin and S. Nie, "A Phanerozoic palinspastic reconstruction of China and its neighboring regions," in *Tectonic Evolution of Asia*, A. Yin and T. M. Harrison, Eds., pp. 442–485, Cambridge University Press, Cambridge, UK, 1996.
- [47] L. Zonenshain, M. Kuzmin, and L. Natapov, *Geology of USSR: A Plate Tectonic Synthesis*, vol. 21 of *Geodynamic Series*, American Geophysical Union, Washington, DC, USA, 1990.
- [48] Q. R. Meng, "What drove late Mesozoic extension of the northern China-Mongolia tract?" *Tectonophysics*, vol. 369, no. 3–4, pp. 155–174, 2003.
- [49] S. Niu, Z. Hou, and A. Sun, "The anti-gravity migration of metallogenic fluid from core and mantle," *Earth Science Frontiers*, vol. 8, no. 3, pp. 95–101, 2001.
- [50] J. Zheng, S. Y. O'Reilly, W. L. Griffin, F. Lu, M. Zhang, and N. J. Pearson, "Relict refractory mantle beneath the eastern North China block: significance for lithosphere evolution," *Lithos*, vol. 57, no. 1, pp. 43–66, 2001.

Research Article

Pan-African Paleostresses and Reactivation of the Eburnean Basement Complex in Southeast Ghana (West Africa)

Mahaman Sani Tairou,¹ Pascal Affaton,² Solomon Anum,³ and Thomas Jules Fleury²

¹ *Département de Géologie, Faculté des Sciences, Université de Lomé, BP 1515, Lomé, Togo*

² *Aix-Marseille Université, CNRS, IRD, CEREGE UMR34, 13545 Aix en Provence Cedex 04, France*

³ *Geological Survey Department, Koforidua Eastern Region, P.O. Box 672, Koforidua, Ghana*

Correspondence should be addressed to Mahaman Sani Tairou, msanitairou@yahoo.fr

Received 28 March 2012; Revised 18 May 2012; Accepted 25 May 2012

Academic Editor: Quan-Lin Hou

Copyright © 2012 Mahaman Sani Tairou et al. This is an open access article distributed under the Creative Commons Attribution License, which permits unrestricted use, distribution, and reproduction in any medium, provided the original work is properly cited.

This faulting tectonics analysis concerns the southernmost segment of the Dahomeyide Orogen and the West-African craton eastern margin in southeast Ghana. The analysis of strike-slip faults in the frontal units of the Dahomeyide Belt indicates that four distinct compressive events (NE-SW, ENE-WSW to E-W, ESE-WNW to SE-NW and SE-NW to SSE-NNW) originated the juxtaposition of the Pan-African Mobile Zone and the West-African craton. These paleostress systems define a clockwise rotation of the compressional axis during the structuring of the Dahomeyide Orogen (650–550 Ma). The SE-NW and SSE-NNW to N-S compressional axes in the cratonic domain and its cover (Volta Basin) suggest that the reactivation of the eastern edge of the West African craton is coeval with the last stages of the Pan-African tectogenesis in southeast Ghana. An extensional episode expressed as late normal faulting is also recorded in this study. This E-W to SE-NW extension, which is particular to the southernmost part of the Dahomeyide Belt, appears to be post-Pan-African. This extension probably contributed to the formation of a major Jurassic rifting zone that originated the Central Atlantic and the Benue Trough.

1. Introduction

Southeast Ghana is a geologically complex area (Figure 1). It includes three distinct structural domains [1–5] (1) the southeastern margin of the West African craton (WAC) consisting of Archean to Paleoproterozoic assemblages that underwent the Eburnean Orogeny (2000 ± 200 Ma); (2) the Neoproterozoic Volta Basin represented by its lower and middle megasequences (Bombouaka and Oti Supergroups); (3) the frontal structural units of the Pan-African Dahomeyide Orogenic Belt (600 ± 50 Ma).

The sedimentary sequence in the Volta Basin rests unconformably on the Eburnean basement complex. This basement and its cover constitute the western “Stable Zone” of our study area (with rock assemblages that did not undergo the Pan-African thermotectonic events); the eastern “Mobile Zone” is represented by the frontal part of the Pan-African Dahomeyide Orogenic Belt (Figures 1 and 2). This Mobile Zone overthrusts the Volta Basin in the North

and its Eburnean basement in the South. The Mobile Zone is described as a pile of west verging nappes involved in several folding phases [1, 6–10]. This juxtaposition of distinct lithostructural assemblages was resulted from the Pan-African tectogenesis. However, the characteristics of this tectogenesis are not yet well known, particularly in southeast Ghana.

At the scale of satellite images or aerial photographs and outcrops, this Pan-African tectogenesis is strongly expressed as a dense network of polyphase lineaments and fractures. The analytical study of these fractures will lead to the following: (1) characterization of the Pan-African paleostresses in the southernmost Dahomeyide segment, and (2) identification of the Pan-African markers on the southeastern margin of the Eburnean basement complex and its cover represented by the Volta Basin (i.e., on the Stable Zone). Following the work done on the Pan-African fracturing in southwest Niger [11] and northern Togo [10, 12, 13], the present tectonic analysis will lead to a better

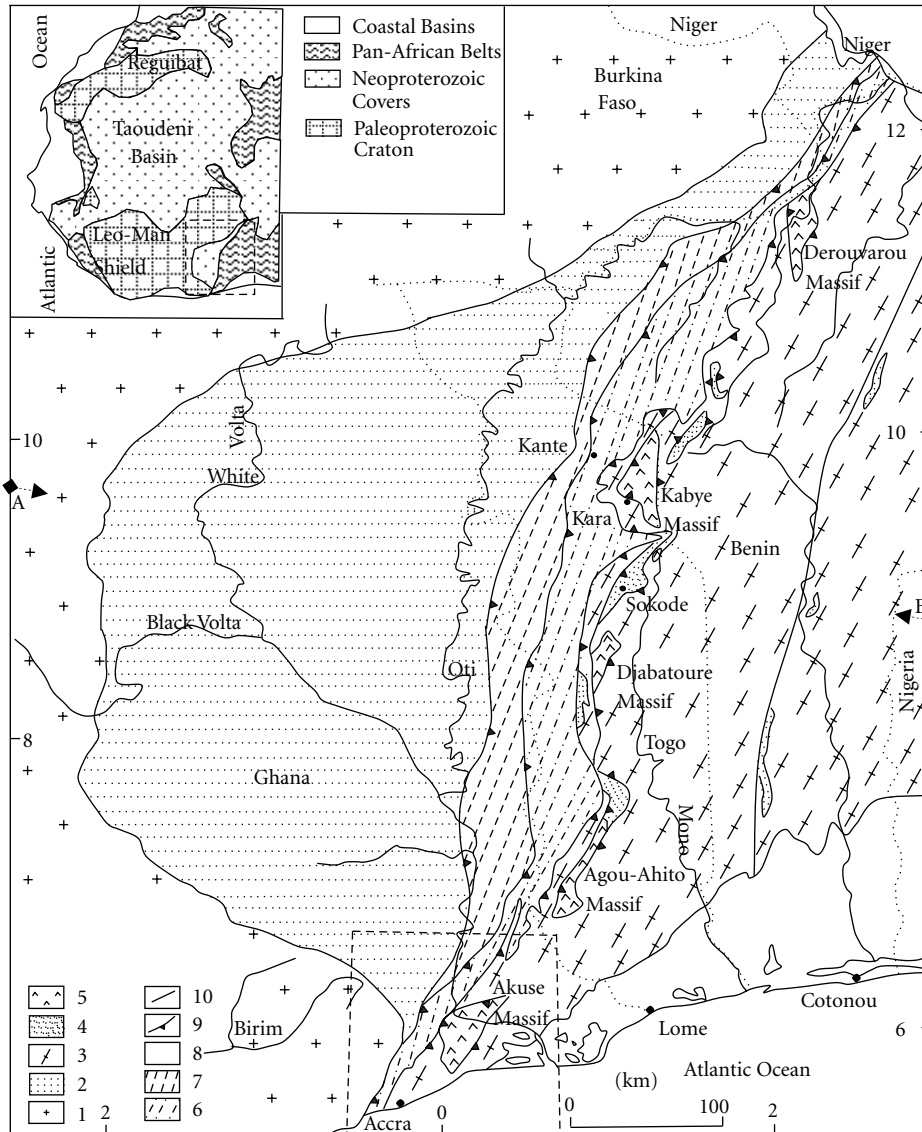


FIGURE 1: Schematic geological map with the “Stable Zone” (comprising the southeastern margin of the West african craton and its cover represented by the Volta Basin) and the Pan-African “Mobile Zone” (i.e., the frontal structural units of the Pan-African Dahomeyide belt): 1 = Eburnean basement complex (WAC); 2 = Neoproterozoic to Paleozoic cover (Volta Basin); 3 = internal and external gneiss-migmatite units; 4 = kyanite bearing micaceous quartzites; 5 = basic and ultrabasic massifs of the suture zone; 6 = Atacora or Akwapim structural unit; 7 = Buem structural unit; 8 = Meso-Cenozoic cover of the Gulf of Guinea Basin; 9 = thrust contact; 10 = Kandi fault mylonitic zone; A-B = schematic section line (Figure 2).

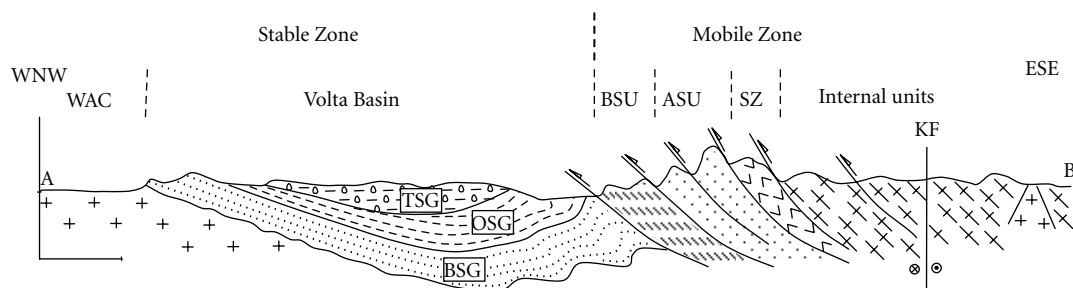


FIGURE 2: Schematic cross section (A-B, Figure 1) showing the relationships between the Stable Zone (i.e., the West african craton and the Volta Basin, with BSG = Bombouaka Supergroup, OSG = Oti Supergroup, TSG = Tamale Supergroup) and the Pan-African Mobile Zone (BSU = Buem structural unit; ASU = Atacora or Akwapim structural unit; SZ = suture zone; KF = Kandi fault).

understanding of the Pan-African paleostress orientations in the Dahomeyide Orogenic Belt.

2. Geological Setting

In the geological framework of this tectonic study, it is important to distinguish two different lithostructural domains as follows: the West-African Craton and its cover (Volta Basin) as the “Stable Zone” and the Pan-African domain made up of the frontal part of the Pan-African Dahomeyide Orogenic Belt as the “Mobile Zone” (Figures 1 and 2).

2.1. The Stable Zone. The Stable Zone corresponds to the southeastern margin of the Guinea [14] or Leo-Man Shield and its Neoproterozoic cover represented by the Volta Basin [1, 5, 9]. In southeast Ghana, the Stable Zone is mainly composed of Archean to Paleoproterozoic rocks involved in the Eburnean thermotectonic events and stabilized at the end of this orogeny (2000 ± 200 Ma). The Eburnean orogeny was not strongly rejuvenated during the Pan-African thermotectonic events (600 ± 50 Ma).

In Ghana, the West-African Craton is roughly equivalent of a gneiss-migmatite basement complex that includes multiple generations of granitic bodies. This complex contains supracrustal belts represented by volcanic, metavolcano-sedimentary or mainly metasedimentary formations defined as the Birimian and Tarkwaian units or groups [15]. In this basement complex, the first granite generations are orthogneissic and more or less migmatitic. These rocks are of granodiorite origin and Eburnean age (2200–2000 Ma; [16, 17]). Considering the recently recorded 2600 Ma ages [4, 14, 18], it is possible that these ancient granites are of Archean origin. The second generations are nonfoliated and crosscut young granites, sometimes very potassic in composition [2].

The supracrustal belts include a lower assemblage, the Birimian unit, and an upper assemblage, the Tarkwaian unit [2, 14, 15]. The lower assemblage includes the Lower Birimian unit, made up of metapelites associated with metamorphic rocks of various origins (greywackes, sandstones, arkoses, volcanic tuffs, siltites, volcanites, and pyroclastites); the Upper Birimian Unit is composed mainly of magmatic rocks (basic to intermediate lavas associated with pyroclastites, agglomerates, volcanic tuffs, and arkosic intercalations). According to Dampare et al. [19], the geochemical characteristics of the basaltic to andesitic metavolcanites indicate emplacement of these Birimian formations in an insular back-arc environment. The Birimian formations record three phases of deformation which, respectively, reflect the development of a NNE-SSW trending foliation, tight synforms and antiforms with NNE-SSW axes, and folding-induced cleavages crosscutting the earlier structures [14].

As regards the Tarkwaian formation, it is described essentially as a detrital assemblage unconformably on the Birimian unit [20]. It consists of polymictic conglomerates, gold-bearing conglomeratic quartzites, phyllites, and feldspathic sandstones. Very moderately folded and fractured by

cleavages, it corresponds to an early molasse of the Eburnean orogeny and exhibits a weak overprint of late Eburnean tectonic structures [15].

The sedimentary sequence of the Volta Basin lies unconformably on the southeastern margin of the West-African Craton (Figure 2). This basin appears as a semibasin (i.e., a half-basin), truncated to the East by the thrust front of the Dahomeyide Orogenic Belt [1, 9, 21]. Three megasequences are recognized. The lower megasequence or Bombouaka Supergroup (1000–600 Ma), represented in the boundary massifs, is made up of two sandy sequences with a mainly clayey-silty sequence sandwiched in between [1]. The middle megasequence or Oti Supergroup lies, with a *pro-parte* glacial unconformity, on the lower supergroup or directly on the Eburnean basement. It begins with a glaciogenic deposit (tillite or diamictite) that is overlain by carbonate and siliclastic formations. The assemblage of these three marker deposits (i.e., tillite, carbonate, siliclastic) is called the “Triad” and underlies a thick Vendian formation [4, 22, 23]. The Vendian formation is predominantly clayey and silty, with little intercalations of carbonates, siliclastics, sandstones, and tholeiitic volcanites [24]. The upper megasequence or Tamale Supergroup, with a possible lower Palaeozoic age, consists of conglomeratic formations with glaciogenic deposit. The Tamale Supergroup is a molasse derived from the uplift and consecutive rapid erosion of the adjacent Dahomeyide Orogeny [7, 25].

Structurally, the lower and middle megasequences show significant eastward thickening in the Volta Basin where they are folded and partially incorporated into the frontal units of the Pan-African Dahomeyide Orogenic Belt [8–10, 25]. According to Affaton [7], the associated structural and geophysical characteristics indicate a composite geodynamic evolution. Thus, the sedimentary sequence in the Volta Basin must be considered as the result of superposition of a passive margin type lower basin, corresponding to the Bombouaka and Oti Supergroups, and a foreland basin represented by the molassic formations of the Tamale Supergroup.

2.2. The Pan-African Mobile Zone. The Pan-African Dahomeyide Belt is located on the southeastern margin of the West-African Craton (Figures 1 and 2). It comprises different lithostructural units in the West (external structural units) or in the East (internal structural units), in relationship with the granulitic and eclogitic massifs representing the suture zone [1, 10]. The external structural units are composed of sediments and metasediments, representing the lateral equivalents of the lower and middle megasequences of the Volta Basin [7, 9, 26], and/or gneissic nappes corresponding to the Eburnean rocks that were highly reworked during the Pan-African orogeny [1, 18, 27–29].

The Buem structural unit corresponds to the outermost structural unit of the Dahomeyide Belt and has been directly overthrust onto the Volta Basin or the Eburnean basement complex (Figures 1 and 2). It consists of sedimentary or weakly metamorphosed sedimentary rocks (shales, quartzitic sandstones, hematitic rocks, mixtites, and sericite-schists) associated with volcanites and serpentinized peridotites

[24, 26]. Its eastern part is characterized by a typical and strong imprint of cataclasis expressed as a dense tangle of quartz veinlets [7, 10]. The Atacora or Akwapim structural unit is overthrust onto the Buem and described as a thick pile of nappes, essentially schistose in the West and quartzitic in the East [7, 8, 10]. It tectonically underlies the external nappes of the reworked basement complex (the Kara-Niamtougou or Mô Orthogneissic units, the Sokodé-Kéméni unit, the plutono-metamorphic Amlamé-Kpalimé and/or Ho unit) or the eclogitic/granulitic nappes of the suture zone [1, 29–31]. The suture zone is composed of highly metamorphosed rocks, showing a high gravitational gradient and strong crustal thickening [32–34]. The basic to ultrabasic massifs of this suture zone (Dérourvarou in northwest Benin; Kabye, Kpaza, Djabatouré-Anié, Agou-Ahito in Togo; and Akuse or Shai in southeast Ghana) are composed of granulites, locally eclogites, and carbonatites, associated with their retrograded equivalents, serpentinites, talcschists, and some metasedimentary rocks [1, 35–38].

The internal structural units are located to the East of the suture zone massifs, exposed as the western margin of the Benino-Nigerian metacraton [39]. They are made up of nappes of various gneisso-migmatitic complexes associated with quartzitic and minor amount of carbonated metasediments, intruded progressively by the Pan-African granites from the West [1, 40]. The majority of these rocks is considered as an Eburnean complex widely reworked during the Pan-African thermotectonic events (650–550 Ma; [18]).

Such a lithostructural assemblages in the Pan-African Dahomeyide Belt indicates a collision belt and defines an eastward increasing metamorphic gradient [1, 10]. The Pan-African tectogenesis is also characterized by progressive eastward superposition of five-phase deformation, considered as Dn, Dn+1, Dn+2, Dn+3, and Dn+4 [1, 13]. The Dn phase is coeval with the granularization resulted from the collision between the eastern margin of the West-African Craton and the Benino-Nigerian metacraton [41]. The tangential or nappe stacking phase (Dn+1 phase) corresponds to the formation of the main or regional foliation which is later involved in three postnappe (Dn+2 to Dn+4) folding phases associated with the final development stages of the Pan-African Dahomeyide Orogeny.

3. Lineament Analysis

The satellite image of the study area (Figure 3) clearly distinguishes two juxtaposed morphostructural domains (Figure 4(a)). A drastic contrast is revealed between the eastern Pan-African Mobile Zone and the western Stable Zone. The NNE-SSW Eburnean structural trends are well expressed within the Eburnean basement complex of this Stable Zone. On the contrary, the front of the Dahomeyide Belt clearly appears as a pile of west- or northwest-verging nappes. The regional submeridian foliation (Sn+1), is materialized by quartzitic bars, trending NE-SW. This foliation is refolded and cut by oblique kilometric lineaments which also follow NE-SW to ESE-WNW trends (Figure 4(c)). Within the craton and its cover (i.e., the Stable Zone), the network is

much more tangled. Indeed, the photofacies of the Eburnean basement complex and the Volta Basin Supergroups display lineaments trending differently in the SE-NW to SSW-NNE, NE-SW, and ESE-WNW directions (Figure 4(b)). In summary, the fracture networks of the Stable Zone and the Pan-African Mobile Zone are not superposable, even though their NE-SW and ENE-WSW lineaments seem comparable.

The relative complexity of the lineament network in the Stable Zone is interpreted to be due to the coexistence of Eburnean and Pan-African fractures. Such an hypothesis leads to an inference that, in response to the Pan-African tectogenesis, the Eburnean cratonic basement and its cover records Pan-African fractures and that the Eburnean fractures were reactivated.

The rectilinear character of all the lineaments observed in the study area indicates the presence of subvertical fracture planes. They are thus distinguishable from the thrust contacts that separate the nappes in the frontal part of the Dahomeyide Orogeny. Finally, the offset of quartzitic bands leads to consider some lineaments as true sinistral or dextral strike-slip faults (Figure 3).

4. Tectonic Analysis

4.1. Method. About 800 orientation measurements of striated planes were collected at fourteen faulted sites developing in different geological units in southeast Ghana (Figure 5). The studied outcrops are found in roadside sections or industrial quarries in competent rocks (granites, quartzites, micaceous quartzites, gneiss, dolomitic carbonates, and granulites) displaying one or several fracturing episodes. The abundance of striated planes has allowed considering only those with true and the best criteria indicating movement [42]. The majority of microfractures considered in this paper are recognized as conjugated strike-slip planes. Moreover, the Akwapim metasediments display striated slickensides, showing reverse (Peduase sites) or normal motion. The latter type may be resulted from the later motion due to the fact that the pitch is structurally higher than the strike-slip one. At the sites, the chronology of the different families of fractures was established based on crosscutting and superposition of incompatible striations [43]. Thus, planes with mineral recrystallization (amphibole, biotite, quartz, sericite, and calcite) clearly appear to be anterior to the “dry” or simply striated planes.

A manual stereographic examination has allowed completing the characterization of the striations. Computer processing of the data was done by using Angelier's [44] method version 2000 for the calculation of stress tensor (R4DT, INDVIR; [45]). With regard to the quality of the results, only planes with good interplanar spacing were considered. Table 1 summarizes the main paleostresses obtained from different faulted sites.

4.2. Results of Tectonic Analysis. The Mobile Zone sites were the first to be analyzed in order to reconstruct Pan-African paleostresses. The data collected in the Stable Zone (the Eburnean basement complex and the lower sandy cover,

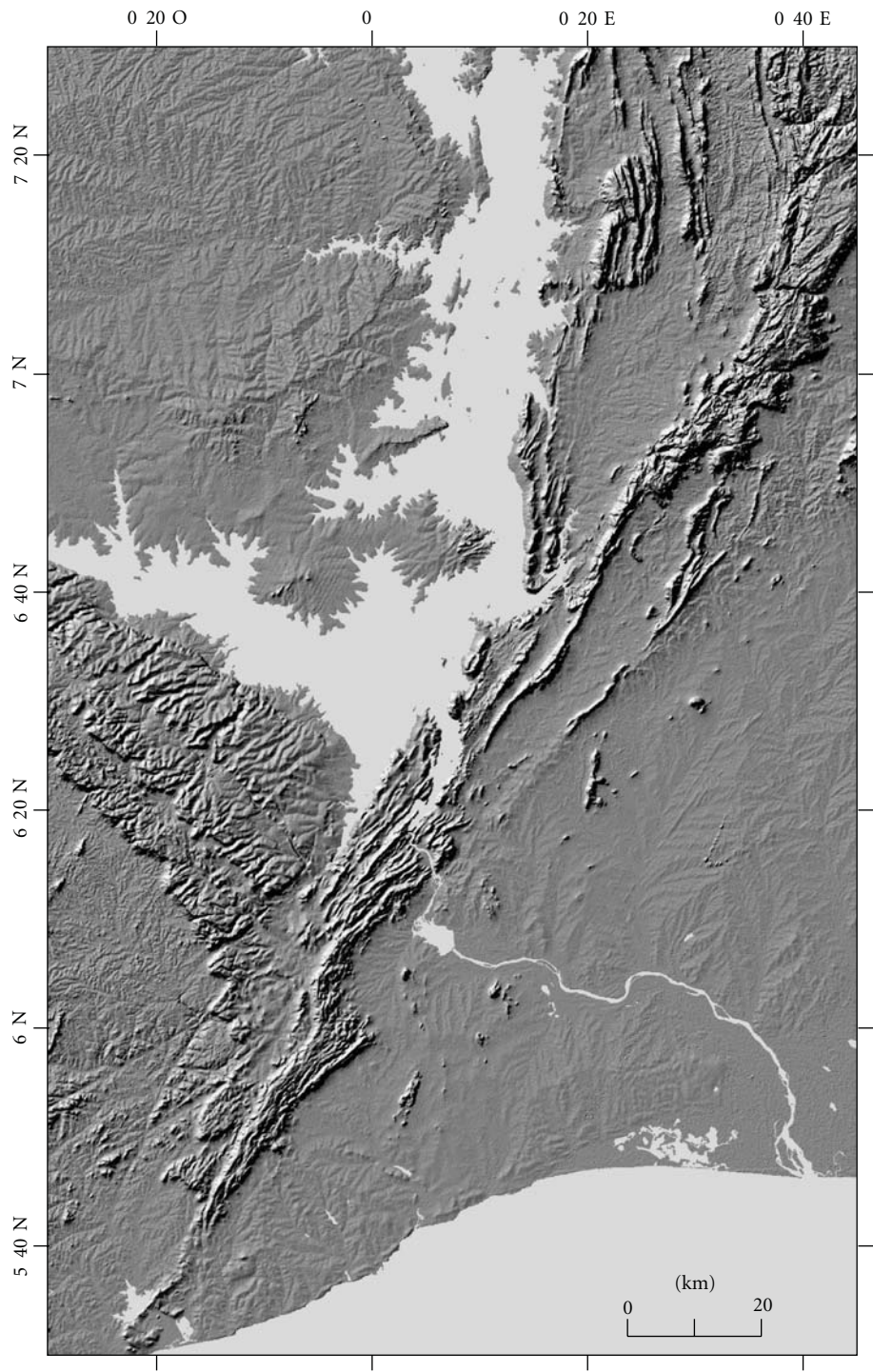


FIGURE 3: Satellite cover (MNT image) of southeast Ghana highlighting the juxtaposition of two highly contrasting morphostructural domains corresponding to the Pan-African Mobile Zone to the East and the Stable Zone (WAC and Volta Basin) to the West.

Figure 5) were then processed before comparing the results from the two zones.

4.2.1. *Pan-African Mobile Zone Sites.* Most of the sites in the Pan-African domain display a polyphase fracture network.

Some characteristics of such a fracture network are presented below.

Buem Structural Unit. The fracture in the Buem unit is well exposed in the Oterkpolu dolomitic carbonate quarry.

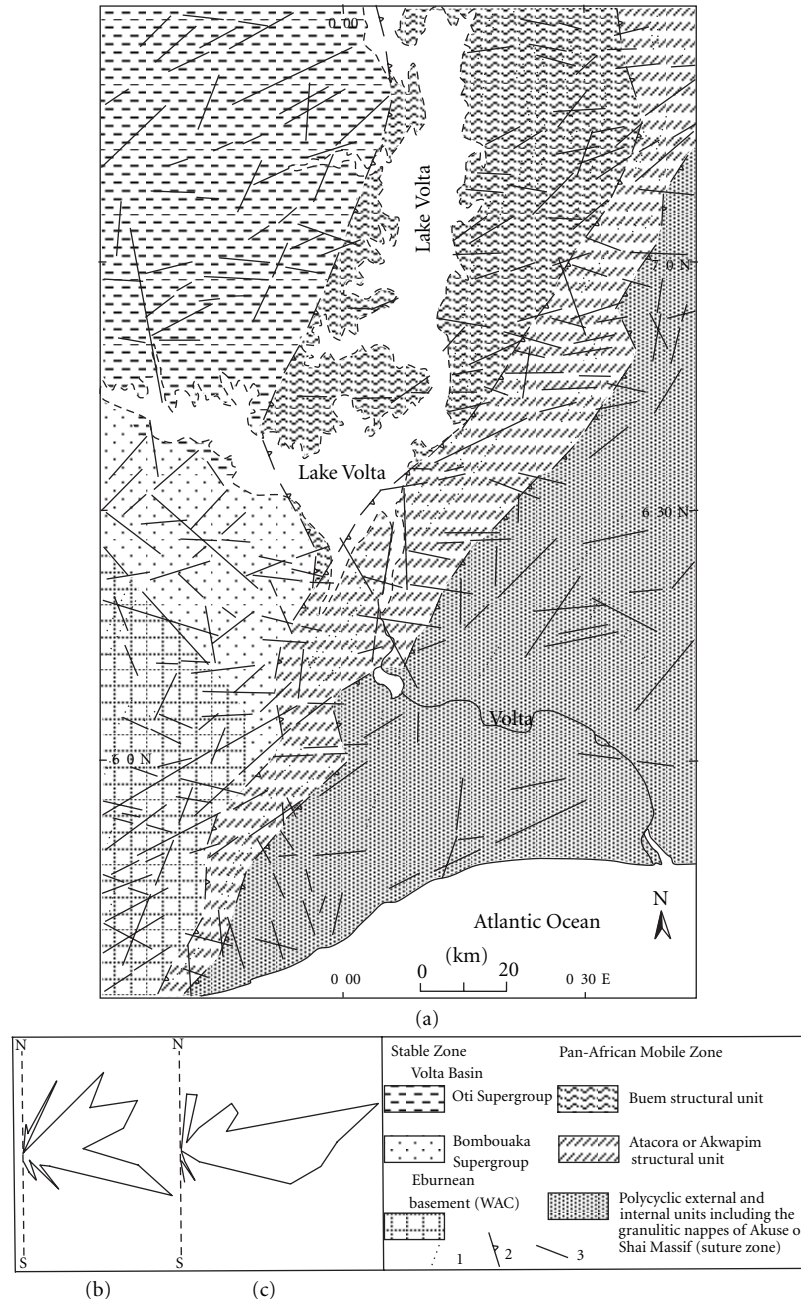


FIGURE 4: Lithostructural sketch highlighting the network of kilometric lineaments (a) and their distribution in the Stable Zone (b) and Mobile Zone (c): 1 = trace of Eburnean or Pan-African (Sn+1) foliation, 2 = major thrust contact, 3 = lineament.

The Bedded or banded bluish grey dolomitic carbonates show stratification planes that were strongly involved in decimetric (i.e., tens of centimeters) to metric (i.e., more than one meter) isoclinal folds (Figure 6(a)), generally overturned to the West with North-plunging submeridian axes (N175-20N). These Dn+1 folding structures are cut by two sets of conjugated strike-slip faults striking N90 to N110 (dextral) and N160 to N175 (sinistral), respectively. The result of analysis on this strike-slip system indicates a subhorizontal compressional N302-01 σ_1 axis (Figure 7(a); Table 1). A comparable compression is detected in the

quartzites at the eastern margin of the Buem structural unit (Twum site, Figure 5) despite minor fracturing in these rocks (Table 1). It is important to note the very discrete presence of reverse faults associated with strike-slip faults in the beds of the Oterkpolu dolomitic carbonate (Figure 6(b)). These planes, shallowly dipping to the East, indicate westward thrusting, recognized as late or post-Dn+1 folding that predates the strike-slip faulting.

Akwapim Structural Unit. Seven sites such as road cuts and artisanal quarries are chosen for paleostress analysis

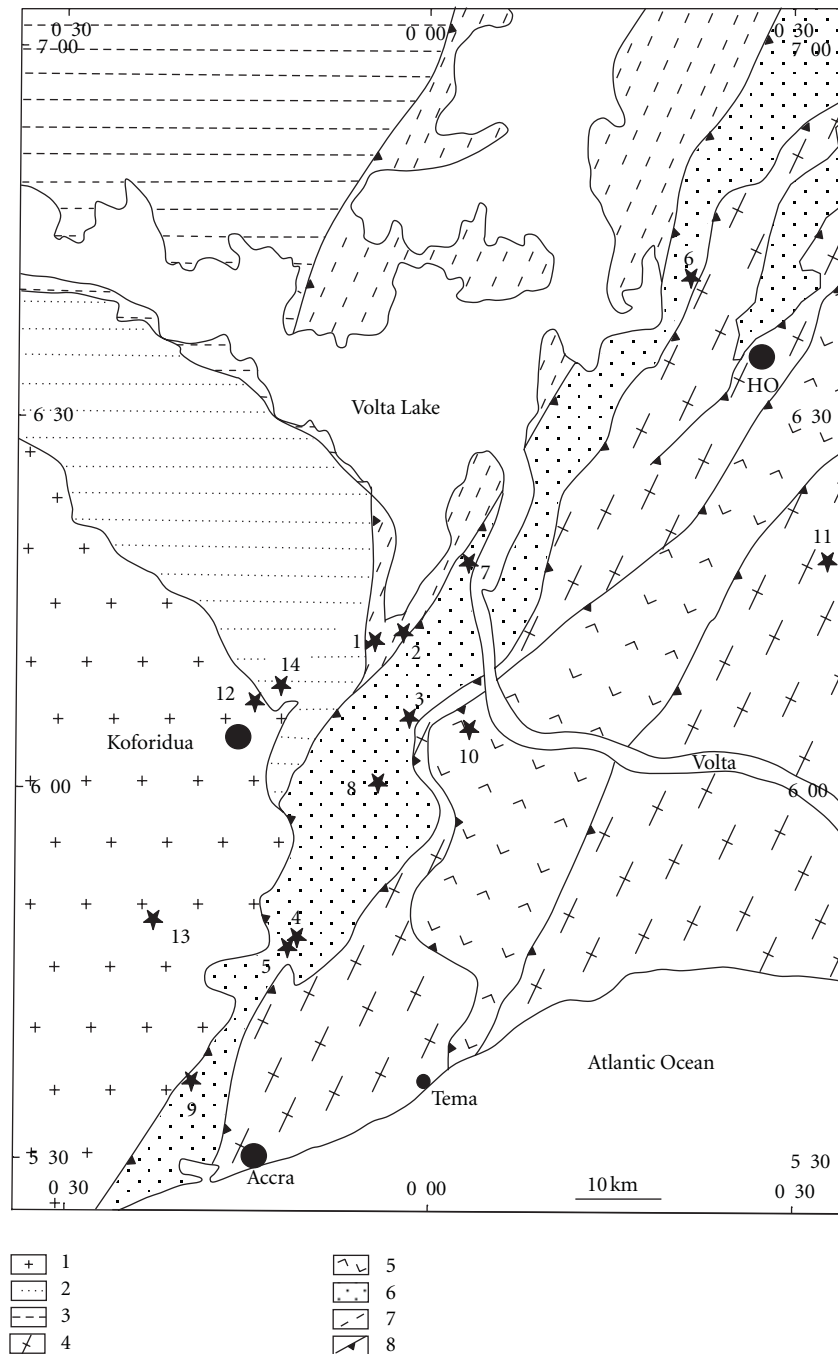


FIGURE 5: Location of the fourteen faulted sites (1 = Oterkpolu, 2 = Twum, 3 = Somanya, 4 = Peduase-N, 5 = Peduase-S, 6 = Bani-Kpeve, 7 = Akosombo, 8 = Adukrom, 9 = Ablikuma, 10 = Akuse, 11 = Ahunda, 12 = Aboabo, 13 = Nsawam, 14 = Nkurakan) in different geological units in southeast Ghana (1 = Eburnean basement, 2 = Bombouaka Supergroup, 3 = Oti Supergroup, 4 = external and internal polycyclic nappes, 5 = granitic nappes of the suture zone, 6 = Atacora or Akwapim structural unit, 7 = Buem structural unit, 8 = thrust contact).

(Figure 5). Numerous slickensides are well exposed in the shallow metasediments in this unit. At all these sites (Somanya, North Peduase, South Peduase, Bani-Kpeve, Adukrom, Akosombo, and Ablikuma), the kinematic criteria allow distinction of the following: (1) thrust planes, (2) several generations of strike-slip faults, and (3) normal fault planes.

Along the road section between Peduase and Ayimensa, many thrust planes are particularly well exposed. The identification of these planes as reverse faults allows the constitution of two northwest verging nappe piles. The analysis of these E-SE dipping reverse faults suggests that the nappe piles of the Akwapim Structural Unit (in Peduase

TABLE 1: Synthesis of the results of the processing of fracture planes studied at all faulted sites in southeast Ghana. The table summarizes, for each site, the geographic coordinates, the rock type (Rt) involved (DC = dolomitic carbonate, S-Q = sandstone or quartzite, MQ = micaceous quartzite, QS = quartzite and schist, G = granulite, OG = orthogneiss, MG = migmatitic gneiss, M-G = migmatite and granite), the number of planes (Np), plane type (Pt) analyzed (SSF = strike-slip faults, RF = reverse faults, and NF = normal faults), and trend and plunge of main paleostress axes (σ_1 , σ_2 , σ_3) obtained.

	Site	Coordinates		Rt	Np	Pt	σ_1	σ_2	σ_3
		Latitude	Longitude						
Pan-African Mobile Zone									
1	Oterkpolu	N06°11'37.7''	W00°04'42.9''	DC	24	SSF	302-01	37-73	212-17
2	Twum	N06°10'29.9''	W00°03'36.9''	S-Q	12	SSF	109-25	282-65	18-03
					33	SSF	37-13	166-69	303-16
					22	SSF	269-07	143-78	00-09
3	Somanya	N06°05'54.5''	W00°01'45.6''	Q	25	SSF	310-01	44-80	220-10
					9	NF	287-83	177-02	87-07
					36	RF	303-02	213-02	70-87
4	Peduase-N	N05°47'56.1''	W00°11'03.4''	QS	23	SSF	20-06	146-79	289-08
					23	SSF	260-03	161-73	350-17
5	Peduase-S	N05°47'28.8''	W00°11'33.1''	QS	31	SSF	141-02	31-84	231-06
					47	NF	259-72	52-16	144-08
					21	SSF	199-09	74-74	291-13
6	Bani-Kpeve	N06°40'78.6''	E00°21'14.0''	Q	28	SSF	158-04	53-75	249-15
					27	NF	262-81	13-03	104-08
7	Akosombo	N06°18'16.0''	E00°03'18.3''	QS	22	SSF	210-06	95-76	301-13
					15	NF	94-82	01-00	271-08
8	Adukrom	N06°00'40.6''	W00°03'59.4''	QS	32	SSF	149-03	48-76	239-14
9	Ablikuma	N05°37'03.9''	W00°17'39.3''	Q	13	SSF	202-01	301-83	111-06
					11	SSF	64-03	307-84	154-06
10	Akuse	N06°05'14.9''	W00°04'04.7''	G	9	SSF	186-21	356-69	94-03
					18	SSF	142-02	49-60	233-30
11	Ahunda	N06°18'29.9''	E00°32'39.7''	OG	14	SSF	174-02	288-86	84-04
Stable Zone									
12	Aboabo	N06°07'30.1''	W00°13'56.9''	MG	10	SSF	120-09	274-80	29-04
					18	SSF	173-02	290-86	83-04
13	Nsawam	N05°48'58.9''	W00°22'24.4''	M-G	30	SSF	340-07	234-66	73-23
14	Nkurakan	N06°08'06.0''	W00°12'10.4''	S-Q	24	SSF	02-14	137-70	269-13

sector) were emplaced during the maximum N302-02 σ_1 compression (Figure 7(b); Table 1).

The thrust contacts in the Peduase sector are cut by numerous strike-slip faults related to two or three conjugated sets in the Akwapim quartzites. The relatively old system includes sets of major planes with mineral recrystallization (quartz, sericite). These planes, with submeridian and NE-SW (N40 to N75) trends, are dextral and sinistral respectively (Figure 6(c)). These early strike-slip faults indicate a compression due to a major σ_1 subhorizontal paleostress trending N20 to N40 (Figure 7(c); Table 1). The trend of this principal paleostress appears to be confirmed at the Somanya site—N35 trending tension gashes (Figure 6(d)) that are deformed by subsequent Dn+2 folding.

Two families of dry fractures corresponding to conjugated planes are superimposed on the first strike-slip faults identified above. They are (1) NE-SW trending (N40 to N65) dextral and ESE-WSW trending (N105 to N125) sinistral,

and (2) ENE-WSW to ESE-WNW (N80 to N125) dextral and N140 to N165 or N350 to N10 sinistral (Figures 7(d) and 7(e)). The processing of the data relative to these last two systems of strike-slip faults suggest to relate the initial superposition of fractures to a subhorizontal σ_1 axis trending ENE-WSW to E-W (N260 to N270). The latest strike-slip faults rather appear to be due to systems of paleostresses whose major axes are NW-SE (N120) or NNW-SSE (N160). These axes are sometimes materialized by extensional joints (Figure 6(d)).

Finally, the Akosombo, Bani-Kpeve, Somanya, and Peduase sites display tectoglyphe bearing planes of characteristic normal faults (Figure 6(e)). This is the last generation of fractures that are generally found with submeridian to NE-SW trends as well as SE-NW to ESE-WNW trends (Figures 7(f) and 7(g)). They can be associated with late reactivations of normal faulting motion of the former strike-slip fault planes. These movements clearly postdate all the strike-slip

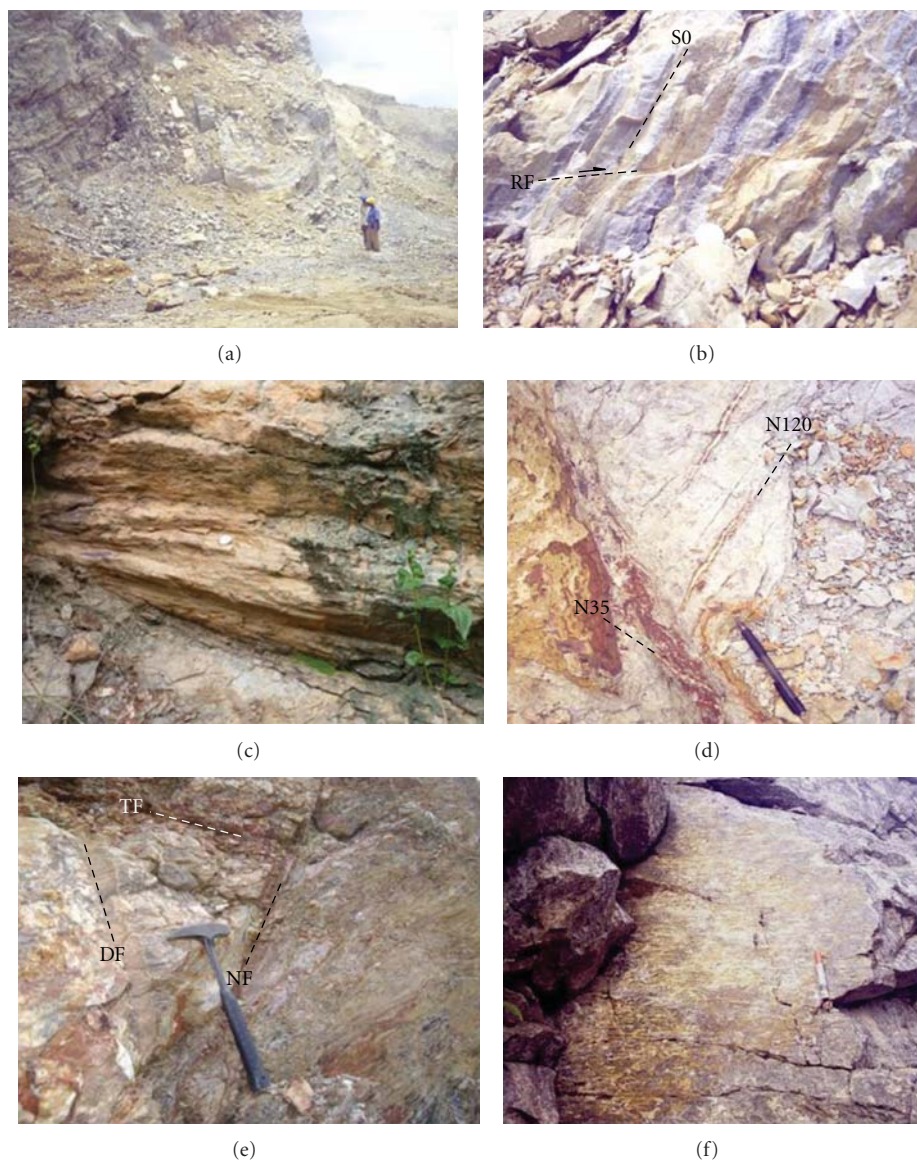


FIGURE 6: Structures of ductile and brittle deformations observed in southeast Ghana: (a) metric folds overturned to West and with submeridian axes in dolomitic carbonate of the Oterkpolu quarry; (b) N20-18E reverse fault plane in dolomitic carbonate of the Oterkpolu quarry (S0, N05-65E); (c) major N60-80NW sinistral strike-slip fault, with channel-like striation plunging at 15° NE (quartzite in a road section at Akosombo); (d) two generations of extension joints trending N35 and N120, inscribed on a Dn+2 decimetric fold (N60-20NE axis) and materializing the NE-SW and SE-NW σ_1 axes of major paleostresses of different ages (Somanya quarry); (e) late normal fault (Fn, N55-60SE) cutting a thrust plane (Fc) and a sinistral strike-slip fault (Fd, road section at Peduase-S site); (f) slickenside of a major sinistral strike-slip fault (N10-75W) with striations plunging at 12° to the South and superposed amphibolite and fibrous mineral lineation (Nsawam quarry).

faulting and seem to link to paleostresses indicating an E-W to SE-NW extension (Figures 7(f) and 7(g); Table 1).

Suture Zone and Internal Structural Units. The fracture data from the eastern sector (suture zone and internal structural units) were collected at an industrial granulite quarry in the Shai hills (Akuse site) and in the Hô augen gneiss (Ahunda site, Figure 5). Decimetric to metric bands of garnet-granulites are mainly cut by fractures with a strike-slip kinematics and the slickensides are carpeted with biotite.

These are N115 to N125 dextral and submeridian sinistral conjugated planes. These two families of major planes reflect a SE-NW (N142) compressional σ_1 axis. Moreover, N40 to N60 dextral and N160 to N175 sinistral minor fractures indicate a much later compression related to a maximum main paleostress σ_1 oriented N184-22 (Table 1).

At the Ahunda quarry, the SE-NW dextral and N20 to N40 sinistral conjugated strike-slip faults were identified with a primary N170 σ_1 trend (Figure 7(h); Table 1). In addition to these strike-slip faults, displacements were also

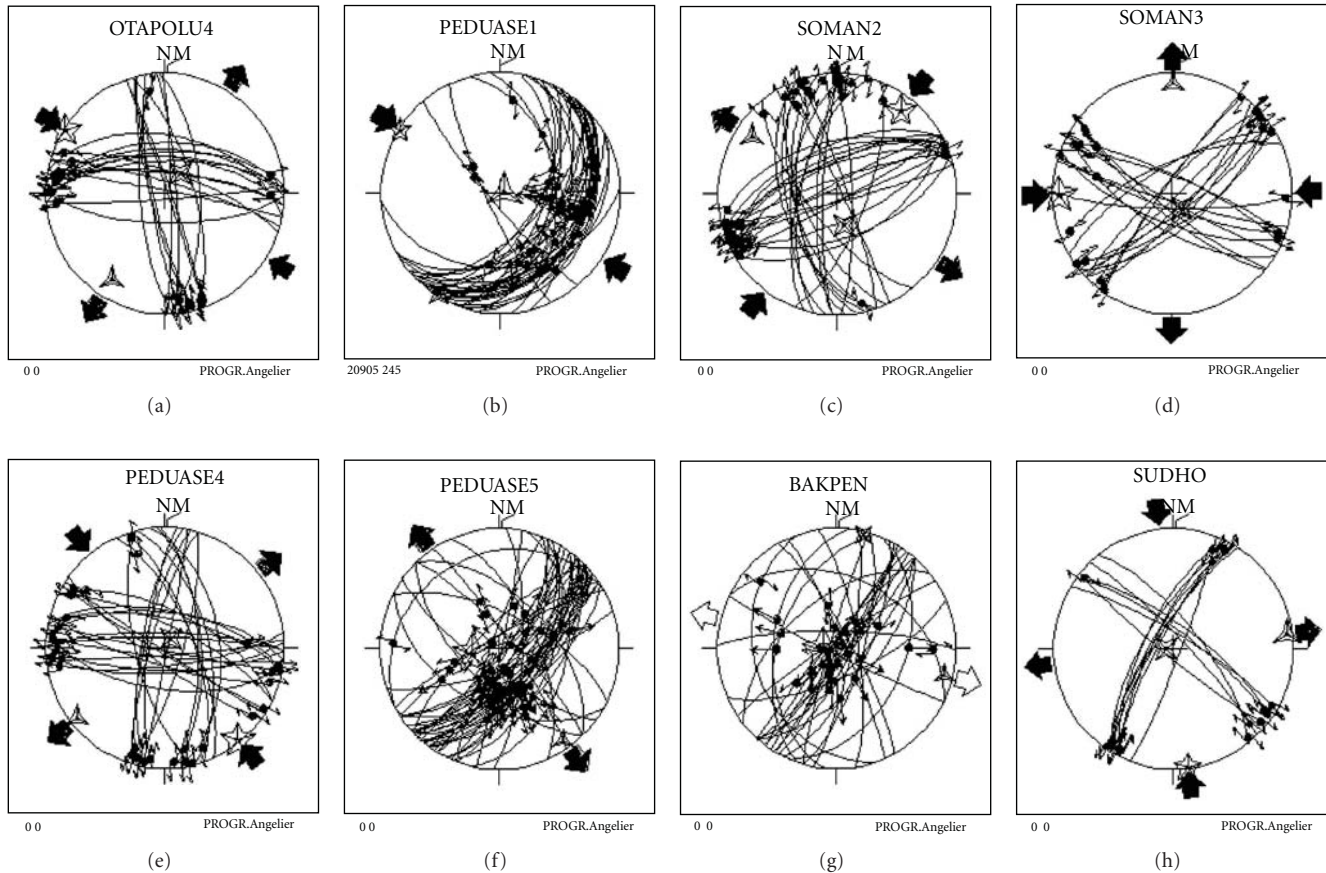


FIGURE 7: Stereograms obtained by processing striated fracture planes recorded in the Mobile Zone in southeast Ghana: (a), sets of strike-slip faults in dolomitic carbonates of the Oterkpolu quarry; (b), reverse faults or thrust planes in nappe pile of Peduase; (c), sets of primary strike-slip faults in quartzites at the Somanya quarry; (d) and (e), sets of secondary strike-slip faults in quartzites and schists (Somanya quarry and Peduase-N road section); (f) and (g), normal faults in quartzites and schists (Peduase-S and Bani-Kpeve road sections); (h) sets of strike-slip faults in augen gneiss at the Ahunda quarry. The stars represent poles of the σ_1 (star with 5 branches), σ_2 (star with 4 branches), and σ_3 (star with 3 branches) of paleostress axes.

identified on late N60 to N75 normal fault planes comparable to those due to an extensional movement in the quartzites of the Akwapim structural unit.

Pan-African Mobile Zone in Southeast Ghana. From the analysis of the striated planes in the Mobile Zone in southeast Ghana, three or four compressional axes and one late extensional axis can be identified (Figure 7). These axes resulted from the following: (1) thrust planes indicating reverse faults in the soles of nappes or thrust slices in the Peduase sector, (2) strike-slip faulting representing families of conjugated fractures attributed to distinct episodes, and (3) late normal faults. The first generation of strike-slip faults indicates a NE-SW compressional axis. Following this, the frontal units of the orogeny recorded two successive paleostress systems with primary E-W and SE-NW to SSE-NNW trending σ_1 axes. The number of fracturing episodes recorded by the Akwapim quartzitic facies appears greater than that in the other Pan-African units (Figure 7; Table 1), which could be explained by differences in the competence of the affected rocks.

The paleostresses deduced from the analysis of the fracture planes in the Buem dolomitic carbonates (Oterkpolu site) are comparable to those from the last episodes in the Akwapim structural unit. Similarly, the paleostress systems represented by the strike-slip faults identified in the eastern part (suture zone and internal structural units) are superposable on the paleostresses recorded in the Buem. The development of late strike-slip faults thus appears to be common in the Pan-African Mobile Zone.

The imprint of the E-W to SE-NW extensional episode suggests normal faulting. This post-Pan-African or very late tectonic episode is responsible for the reactivation of former fracture planes, leading to the superposition of high pitch striations that is incompatible with the primary movements.

4.2.2. Stable Zone Sites. Limited outcrops are discovered in the Stable Zone. Consequently only three faulted sites (Aboabo, Nsawam, and Nkurakan) were studied in the Eburnean basement complex and in the basal part of the lower megasequence of the Volta Basin (Figure 5). The fracture data collected at these sites therefore do not

comprehensively reflect the complexity of the lineament network identifiable at the satellite-image scale. However, the resulting data are still very useful and important.

Aboabo Sector. The Aboabo industrial quarry reveals migmatitic paragneisses with quartzo-feldspathic leucozones and dark centrimetric boudins. These facies of the Eburnean basement complex are also cut by two generations of aplitic or pegmatitic veins. More recent NE-SW centrimetric veins cut through the sinistral submeridian strike-slip faults. In the quarry, two fracture generations were identified. The older planes are generally covered with biotite or amphibole and quartz lineations. The latter ones are often associated with recrystallized fibres parallel to the subhorizontal lineation. The tectoglyphes indicate homogeneous strike-slip movements which appear to reflect late reactivations of older planes. The conjugated strike-slip faults are SE-NW trending (N120 to N155) dextral and NE-SW trending (N30 to N50) sinistral, indicating a compression with σ_1 axis orienting N172-02 (Figure 8(a); Table 1). The second slickenside generations are dry types and include two families of ENE-WSW trending (N70–N80) dextral and SSE-NNW trending (N160–N170) sinistral strike-slip faults. Analysis on these fracture planes led to discover a system of paleostress axes, with one main N120-02 σ_1 axis (Table 1).

Nsawam Sector. In the Nsawam quarry, dark gneisso-migmatitic facies of the Eburnean basement complex display numerous amphibolitic inclusions. They are associated with a complex of metric veins of leucogranites, aplites, and pegmatites. The assemblage is cut by the first generation type fractures as identified at the Aboabo site (Figure 6(f)). They are families of conjugated submeridian to NE-SW sinistral and ESE-WSW to SE-NW (N105 to N130) dextral strike-slip faults. The processing of the data indicates a compression with a main paleostress σ_1 orienting N340-07 (Figure 8(b), Table 1).

Volta Basin. Outcrops at the Nkurakan site are characterized by massive bands of quartzites or quartzitic sandstones with limited black shale intercalations. These facies belong to the Mpraeso Formation (lower part of Bombouaka or Kwahu Supergroup, [5]). Decimetric bands with SE dips (N50-35SE) are cut by strike-slip faults that are assembled around the ESE-WNW to SE-NW trending (N115 to N140) dextral and ENE-WSW to E-W trending (N75 to N95) sinistral. These strike-slip faults are resulted from a compression, with a main N-S and subhorizontal (N02-14) σ_1 axis (Figure 8(c), Table 1). This compressional axis is comparable to those derived from analysis of the fracture planes recorded in the facies of the Eburnean basement complex (at the Aboabo and Nsawam sites).

Stable Zone in Southeast Ghana. The Eburnean basement complex and the lower part of its cover display the imprints of two fracturing episodes due to compressions. The main episode is attributable to a system of paleostresses with a principal N-S to NNW-SSE trending σ_1 axis (Figure 8;

Table 1). On the slickensides of the principal strike-slip faults, recrystallized fibres or biotite orientations suggest that these paleostresses correspond to a late movement related to development of amphibole and quartz lineation (older late-Eburnean or pre-Pan-African movement associated with a much higher ambient temperature). The determined paleostress axes are superposable on the last Pan-African compression phases. The other episode is expressed as fracture planes indicating an ESE-WNW to SE-NW trending compressional axis (Aboabo site; Table 1). Finally, some tectoglyphe bearing planes of normal faults can be interpreted as markers of a late extensional episode identified at the Pan-African Mobile Zone sites.

5. Interpretation

In summary, the set of fractures observed in the frontal part of the Dahomeyide Belt in southeast Ghana are resulted from four Pan-African compressive phases followed by a very late or post-Pan-African extension probably of Devonian age [7].

The compressive episodes are materialized by west verging thrust planes and conjugated strike-slip faults. The latter allow determination of the main paleostress σ_1 axes, with successively NE-SW, ENE-WSW to E-W, and SE-NW to SSE-NNW trends. The order of involvement of the main paleostresses is defined based on the relative ages of the recorded strike-slip faults. The orientation of the different axes of the main paleostress σ_1 allows comparison with different Pan-African paleostresses recorded in northern Togo [13]. Comparing the Pan-African paleostresses determined in two segments of the Dahomeyide Belt (Table 2), the dense fracture network identified in the frontal part of the Mobile Zone in southeast Ghana should be produced from the superposition of four deformation phases (Dn+1 to Dn+4). As in northern Togo, the Pan-African compressional axis underwent a major clockwise rotation (of more than 140°) during the erection of the southern segment of the Dahomeyide Belt. Particularly noticing, the average NE-SW structural trend of this segment is not in agreement with the NE-SW compressive axis due to the Dn+1 deformation phase (tangential or nappe stacking phase). Indeed, the orientations of the thrust planes and the northwest verging nappes (Peduase nappe piles) rather reflect a primary N302-02 σ_1 paleostress axis (Figure 7(b)), which is superposable on the main paleostress of Dn+3 phase (Table 2). Far from supporting the results of [46], suggesting a NE-SW Dahomeyide nappe piling, this conclusion seems to contradict the suggestion that nappe stacking in northern Togo took place along an ENE-WSW axis [10, 13]. At a regional scale (Figures 3 and 4), it is striking that the southern segment of the Dahomeyide Belt is not in conformity with the submeridian appearance of the whole orogeny. This structural trend of the southernmost segment probably corresponds to a strong transposition related to the Dn+3 and Dn+4 Pan-African compressions. It is this transposition that justifies the present orientation of the main paleostress σ_1 which is related to the emplacement of the nappes in southeast Ghana.

In the cratonic domain and its cover (Stable Zone), only two compressional axes might be defined. They are

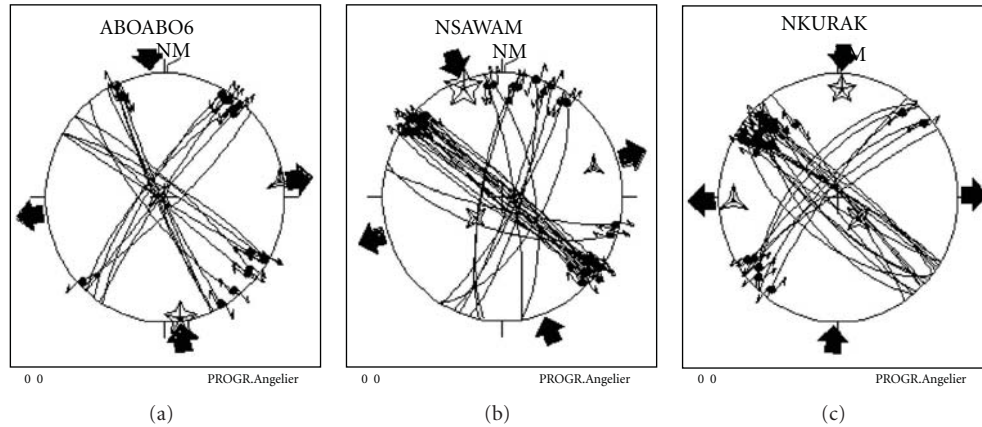


FIGURE 8: Stereograms obtained by processing striated planes recorded in the Eburnean basement complex and the basal part of the Volta Basin in southeast Ghana: (a), sets of strike-slip faults in migmatitic paragneisses of the Aboabo quarry; (b), sets of strike-slip faults in the Eburnean basement complex of the Nsawam quarry; (c), sets of strike-slip faults in quartzites at the Nkurakan quarry. The stars represent poles of the σ_1 (star with 5 branches), σ_2 (star with 4 branches), and σ_3 (star with 3 branches) paleostress axes.

TABLE 2: Correlation between the main Pan-African compressional axes in northern Togo and southeast Ghana.

Pan-African deformation phases	Compressional axis (σ_1) reconstructed in northern Togo (according to work by Affaton et al., [12]; Tairou, [10]; Tairou et al., [13])	Compressional axis (σ_1) reconstructed in southeast Ghana	
	Mobile Zone	Mobile Zone	Stable Zone
Dn+1	NE-SW to ENE-WSW (N40 to N80)	NNE-SSW to NE-SW (N20 to N40)	
Dn+2	ESE-WNW (N100 to N115)	ENE-WSW to E-W (N80 to N90)	
Dn+3	SE-NW (N120 to N130)	SE-NW (N120 to N130)	SE-NW (N120)
Dn+4	SE-NW to SSE-NNW (N140 to N150)	SE-NW to SSE-NNW (N140 to N175)	SSE-NNW to S-N (N340 to N02)

comparable to those related to the Dn+3 and Dn+4 Pan-African episodes (Table 2). The common expression of these last phases of deformation across each of the structural units of the Dahomeyide Belt implies that reactivation of the eastern margin of the West African craton itself was due to these episodes. Indeed, the frontal margin of the Dahomeyide Belt was overthrust onto this cratonic margin during the first Pan-African deformation (Dn+1 and Dn+2) and they together underwent the Dn+3 and Dn+4 episodes.

In short, the partial reactivation of the cratonic margin in southeast Ghana occurred during the major rotation peak of the Pan-African compressional axis. Two successive events materialize this reactivation as follows: (1) the development of ENE-WSW and SSE-NNW fractures indicating a main N120-02 σ_1 paleostress axis, typical of the SE-NW compression of the Dn+3 Pan-African phase; (2) the strike-slip reactivation of submeridian to NE-SW and E-W to SE-NW fracture planes associated with a primary compressive paleostress axis (N172-02 σ_1 and N02-14 σ_1 at Aboabo and Nsawam sites, resp.) that can be attributed to the final Pan-African Dn+4 compression. These late Pan-African reactivation planes belong to a fracture network known

in the whole West-African Craton, particularly in Burkina Faso [47]. They are associated with doleritic veins whose emplacement is related to late Eburnean to pre-Pan-African events and to the Central Atlantic prerifting [11].

In southeast Ghana, the late extensional movement is materialized by normal faults that are particularly well developed in the quartzites of the Akwapim structural unit. It is also responsible for normal faulting reactivations of strike-slip fault planes resulting from Pan-African compressional episodes. Popoff [48] correlated extension markers to the fracturing of an overstretching continent in response to the relaxation of the Pan-African orogenic stresses during the Middle Cambrian. Hitherto, such extension indicators were not reported in the northern and central segments of the Dahomeyide Belt [12, 13]. The development of such extensional markers in the southern segment suggests that they were resulted from a Paleozoic faulting tectonics which led to the Devonian deposits in Ghana (Accra, Sekondi, and Takoradi Basins) and at the base of the sedimentary sequence of the Keta and Togo coastal Basins [1, 9, 12, 49–52]. Therefore, this extension might be considered as a precursor event of the Jurassic rifting

that resulted in the opening of the Central Atlantic and the development of the Benue Trough in Nigeria.

6. Conclusion

The analysis of the dense fracture network in southeast Ghana has led to the reconstitution of the superposition of Pan-African to late- or post-Pan-African paleostresses recorded in the frontal margin of the Pan-African Dahomeyide Belt and the southeastern margin of the West-African Craton (WAC). Above a clear morphostructural contrast, the distribution of lineaments indicates a juxtaposition of two very different domains and suggests the coexistence of Eburnean and Pan-African fractures in the stable domain constituted by a part of the WAC (of Archean to Neoproterozoic age) and of its Neoproterozoic cover. In the lithostructural units of the Pan-African orogeny, the recorded fractures define four successive compressional axes oriented NE-SW, ENE-WSW, SE-NW, and SSE-NNW to S-N. These axes are comparable to those which are well known in the northern and central segments of the Dahomeyide Belt and correlated with four Pan-African tectogenesis phases (Dn+1 to Dn+4). As in northern Togo, the superposition of the paleostresses deduced from these deformation phases defines a major clockwise rotation (of more than 140°) of the compressional axis during the erection of the southern segment of the belt, while a rotation of 90 to 110° was expressed in the central segment of this orogen.

Despite the complexity of the lineament network characterizing the cratonic margin and its cover in southeast Ghana, the studied sites in this Stable Zone only present a few families of fractures and reworked strike-slip faults. An analysis of these structural elements has led to determine major paleostresses σ_1 axes which are superposable to those attributed to the Pan-African Dn+3 and Dn+4 compressive phases. These results suggest that the reactivation of Eburnean fractures is coeval with the last two phases of Pan-African tectogenesis.

In southeast Ghana, the peculiarity of brittle deformation is the recording of a post-Pan-African extensional phase. This late normal faulting corresponds to an E-W to SE-NW extension. It may be attributed to early (Cambrian to Devonian) episodes of the major Mesozoic fragmentation of the Western Gondwana. This fragmentation has resulted in the birth of the Central Atlantic and the Benue Trough in Jurassic.

References

- [1] P. Affaton, M. A. Rahaman, R. Trompette, and J. Sougy, "The dahomeyides orogen: tectonothermal evolution and relationships with the Volta basin," in *The West-African Orogen and Circum Atlantic Correlatives*, Dallmayer and Lécroché, Eds., pp. 107–122, ICGP, IUGS, UNESCO.
- [2] G. Rocci, G. Bronner, and M. Deschamps, "Crystalline basement of the West African craton," in *The West-African Orogen and Circum Atlantic Correlatives*, Dallmayer and Lécroché, Eds., pp. 31–61, ICGP, IUGS, UNESCO, 1991.
- [3] R. Trompette, "Neoproterozoic (600 Ma) aggregation of Western Gondwana: a tentative scenario," *Precambrian Research*, vol. 82, no. 1–2, pp. 101–112, 1997.
- [4] F. Kalsbeek, D. Frei, and P. Affaton, "Constraints on provenance, stratigraphic correlation and structural context of the Volta basin, Ghana, from detrital zircon geochronology: an Amazonian connection?" *Sedimentary Geology*, vol. 212, no. 1–4, pp. 86–95, 2008.
- [5] J. N. Carney, C. J. Jordan, C. W. Thomas, D. J. Condon, S. J. Kemp, and J. A. Duodo, "Lithostratigraphy, sedimentation and evolution of the Volta Basin in Ghana," *Precambrian Research*, vol. 183, no. 4, pp. 701–724, 2010.
- [6] P. Affaton, "Etude géologique et structurale du Nord-Ouest-Dahomey, du Nord-Togo et du Sud-Est de la Haute-Volta. Thèse de 3e Cycle," Trav. lab. Sci. Terre St Jérôme, Marseille. Fr., Sér. B., 10, 217p, 1975.
- [7] P. Affaton, "Le bassin des Volta (Afrique de l'Ouest): une marge passive d'âge Protérozoïque supérieur, tectonisée au Panafricain (600 ± 50 Ma)," Editions ORSTOM, Collection Etudes et Theses, Paris, 500p, 1990.
- [8] N. Simpara, *Etude géologique et structurale des unités externes de la chaîne panafricaine (600 Ma) des Dahomeyides dans la région de Bassar (Togo) [Ph.D. thesis]*, University of Aix-Marseille III, 1978.
- [9] P. Affaton, J. Sougy, and R. Trompette, "The tectono-stratigraphic relationships between the upper precambrian and lower paleozoic volta basin and the pan-african dahomeyide orogenic belt (West Africa)," *American Journal of Science*, vol. 280, no. 3, pp. 224–248, 1980.
- [10] M. S. Tairou, *La tectonique tangentielle panafricaine au Nord-Togo [Ph.D. thesis]*, Université de Lomé, 2006.
- [11] P. Affaton, P. Gaviglio, and A. Pharissat, "Réactivation du craton ouest-africain au panafricain : paléocontraintes déduites de la fracturation des grès néoprotérozoïques de Karey Gourou (Niger, Afrique de l'Ouest)," *Comptes Rendus de l'Académie des Sciences*, vol. 331, pp. 609–614, 2000.
- [12] P. Affaton, J. P. Gelard, and N. Simpara, "Paléocontraintes enregistrées par la fracturation dans l'unité structurale de l'Atacora (Chaîne Panafricaine des Dahomeyides, Togo)," *Comptes Rendus de l'Académie des Sciences*, vol. 312, pp. 763–768, 1991.
- [13] M. S. Tairou, P. Affaton, J.-P. Gélard, R. Aite, and B. E. Sabi, "Panafrican brittle deformation and palaeostress superposition in northern Togo (West Africa)," *Comptes Rendus—Geoscience*, vol. 339, no. 13, pp. 849–857, 2007.
- [14] L. Latouche and J. Fabre, "Le Précambrien du craton ouest-africain," in *Géologie du Sahara Occidental et Central. Protérozoïque Inférieur de la Dorsale de Guinée*, J. Fabre, Ed., vol. 108 of *Tervuren, African Geosciences*, pp. 15–72, Musée Royale de l'Afrique Centrale, Belgique, 2005.
- [15] B. Bessoles, "Géologie de l'Afrique," Le craton Ouest Africain. Mém. BRGM 88, 403p, 1977.
- [16] E. K. Agyei, J. E. J. M. Van Landewijk, R. L. Armstrong, J. E. Harakal, and K. L. Scott, "RbSr and KAr geochronometry of South Eastern Ghana," *Journal of African Earth Sciences*, vol. 6, no. 2, pp. 153–161, 1987.
- [17] W. Hirdes and D. W. Davis, "First U-Pb zircon age of extrusive volcanism in the Birimian Supergroup of Ghana/West Africa," *Journal of African Earth Sciences*, vol. 27, no. 2, pp. 291–294, 1998.
- [18] F. Kalsbeek, P. Affaton, B. Ekwueme, R. Frei, and K. Thrane, "Geochronology of granitoid and metasedimentary rocks from Togo and Benin, West Africa: comparisons with NE Brazil," *Precambrian Research*, pp. 218–233, 2012.

- [19] S. B. Dampare, T. Shibata, D. K. Asiedu, S. Osae, and B. Banoeng-Yakubo, "Geochemistry of Paleoproterozoic metavolcanic rocks from the southern Ashanti volcanic belt, Ghana: Petrogenetic and tectonic setting implications," *Precambrian Research*, vol. 162, no. 3-4, pp. 403-423, 2008.
- [20] N. R. Junner, *Geology of the Gold Coast and Western Togoland with Revised Geological Map*, Gold Coast Geological Survey Bulletin, 1940.
- [21] R. Trompette, "La chaîne panafricaine des Dahomeyides et le bassin des volta (bordure SE du craton Ouest-Africain)," *Mém. B.R.G.M.*, 92, pp. 9-62, 1980.
- [22] B. Amard and P. Affaton, "Découverte de *Chuarina circularis* (Acritarche) dans le bassin des Volta (Haute Volta et Bénin, Afrique de l'Ouest). Age protérozoïque terminal de la formation de la Pendjari et de la tillite sous-jacente," *Comptes Rendus—Académie des Sciences II*, vol. 299, no. 14, pp. 975-980, 1984.
- [23] B. Amard, "*Chuarina pendjariensis* n. sp., acritarche du bassin des Volta, Bénin et Burkina-Faso, Afrique de l'Ouest : un taxon nouveau du Cambrien inférieur," *Comptes Rendus—Académie des Sciences II*, vol. 324, no. 6, pp. 477-483, 1997.
- [24] P. Affaton, L. Aguirre, and R.-P. Menot, "Thermal and geodynamic setting of the Buem volcanic rocks near Tiélé, Northwest Bénin, West Africa," *Precambrian Research*, vol. 82, no. 3-4, pp. 191-209, 1997.
- [25] M. Deynoux, P. Affaton, R. Trompette, and M. Villeneuve, "Pan-African tectonic evolution and glacial events registered in Neoproterozoic to Cambrian cratonic and foreland basins of West Africa," *Journal of African Earth Sciences*, vol. 46, no. 5, pp. 397-426, 2006.
- [26] N. Simpara, J. Sougy, and R. Trompette, "Lithostratigraphie et structure du Buem unité externe de la chaîne panafricaine des Dahomeyides dans la région de Bassar (Togo)," *Journal of African Earth Sciences*, vol. 3, no. 4, pp. 479-486, 1985.
- [27] M. Caen-Vachette, K. J. M. Pinto, and M. Roques, "Plutons éburnéens et métamorphisme dans le socle cristallin de la chaîne panafricaine au Togo et au Bénin," *Revue de Géographie Physique et de Géologie Dynamique*, vol. 21, no. 5, p. 351, 1979.
- [28] K. Attoh, R. D. Dallmeyer, and P. Affaton, "Chronology of nappe assembly in the Pan-African Dahomeyide orogen, West Africa: evidence from $^{40}\text{Ar}/^{39}\text{Ar}$ mineral ages," *Precambrian Research*, vol. 82, no. 1-2, pp. 153-171, 1997.
- [29] Y. Agbossoumondé, R.-P. Menot, J.-L. Paquette, S. Guillot, S. Yéssoufou, and C. Perrache, "Petrological and geochronological constraints on the origin of the Palimé-Amlamé granitoids (South Togo, West Africa): a segment of the West African craton paleoproterozoic margin reactivated during the Pan-African collision," *Gondwana Research*, vol. 12, no. 4, pp. 476-488, 2007.
- [30] K. Attoh, "Dahomeyides in Southern Ghana: evidence for oceanic closure and crustal imbrication in a Pan—Africa," *Mern. C.I.F.E.G.* vol. 22, pp. 159-164, 1990.
- [31] M. S. Tairou, P. Affaton, B. E. Sabi, and K. F. Seddoh, "Tectonometamorphic evolution of the Mo and Kari-Niamtougou Orthogneiss Suites, Northern Togo," *Global Journal of Geological Sciences*, vol. 7, no. 2, pp. 93-100, 2009.
- [32] M. El-Hadj Tidjani, P. Affaton, P. Louis, and A. Socohou, "Gravity characteristics of the Pan-African Orogen in Ghana, Togo and Benin (West Africa)," *Journal of African Earth Sciences*, vol. 7, no. 24, pp. 241-258, 1997.
- [33] Y. Agbossoumondé, R.-P. Menot, and S. Guillot, "Metamorphic evolution of Neoproterozoic eclogites from south Togo (West Africa)," *Journal of African Earth Sciences*, vol. 33, no. 2, pp. 227-244, 2001.
- [34] K. Attoh and J. Morgan, "Geochemistry of high-pressure granulites from the Pan-African Dahomeyide orogen, West Africa: constraints on the origin and composition of the lower crust," *Journal of African Earth Sciences*, vol. 39, no. 3-5, pp. 201-208, 2004.
- [35] Y. Agbossoumondé, *Les complexes ultrabasiques de la chaîne panafricaine au Togo (Axe Agou—Atakpamé, Sud-Togo). Etude pétrographique, minéralogique et géochimique [Ph.D. thesis]*, Université Jean Monnet, St. Etienne, France, 1998.
- [36] R. P. Menot, Y. Agbossoumondé, S. Guillot, and G. Duclaux, "Pan-African subduction-collision event evidenced by high-P coronas in metanorites from the Agou massif (Southern Togo)," *Precambrian Research*, vol. 135, no. 1-2, pp. 1-21, 2004.
- [37] B. E. Sabi, *Etude pétrologique et structurale du Massif Kabyè, Nord-Togo [Ph.D. thesis]*, Université de Lomé, 2007.
- [38] K. Attoh and P. M. Nude, "Tectonic significance of carbonatites and ultrahigh-pressure rocks in the Pan-African Dahomeyide suture zone, southeastern Ghana," in *The Boundaries of the West African Craton*, N. Ennih, J.-P. Liégeois et al., Eds., vol. 297 of *Special Publications*, pp. 217-231, Geological Society, London, UK, 2008.
- [39] M. G. Abdelsalam, J.-P. Liégeois, and R. J. Stern, "The saharan metacraton," *Journal of African Earth Sciences*, vol. 34, no. 3-4, pp. 119-136, 2002.
- [40] M. Caen-Vachette, "Age pan-africain des granites de Sinendé, Save et Fita (Dahomey)," *Comptes Rendus de l'Académie des Sciences*, pp. 1793-1795, 1975.
- [41] P. Affaton, A. Kröner, and K. F. Seddoh, "Pan-African granulite formation in the Kabyè Massif of Northern Togo (West Africa): Pb-Pb zircon ages," *International Journal of Earth Sciences*, vol. 88, no. 4, pp. 778-790, 2000.
- [42] J. P. Petit, "Criteria for the sense of movement on fault surfaces in brittle rocks," *Journal of Structural Geology*, vol. 9, no. 5-6, pp. 597-608, 1987.
- [43] F. Bergerat, *Déformations cassantes et champs de contrainte tertiaires dans la plate-forme européenne [Ph.D. thesis]*, University Pierre and Marie Curie, Paris, France, 1985.
- [44] J. Angelier, "Tectonique cassante et néotectonique," *Annales de la Société Géologique de Belgique*, vol. 112, no. 2, pp. 283-307, 1990.
- [45] M. O. Aïte, *Analyse de la microfracturation et paléo-contraintes dans le Néocène post-nappes de Grande Kabylie (Algérie) [Ph.D. thesis]*, Université du Maine, 1994.
- [46] C. Castaing, C. Triboulet, J. L. Feybesse, and P. Chevremont, "Tectonometamorphic evolution of Ghana, Togo and Benin in the light of the Pan-African/Brasiliano orogeny," *Tectonophysics*, vol. 218, no. 4, pp. 323-342, 1993.
- [47] U. Wenmenga, M. Kecir, and P. Affaton, "Distribution des filons de dolérite d'après les interprétations géologiques de données aéromagnétiques et leur signification géodynamique (Burkina Faso, Craton ouest africain)," *Bulletin du Service Géologique National*, vol. 20, no. 2, pp. 254-261, 2009.
- [48] M. Popoff, "Du Gondwana à l'atlantique sud: les connexions du fossé de la Bénoué avec les bassins du Nord-Est brésilien jusqu'à l'ouverture du golfe de Guinée au crétacé inférieur," *Journal of African Earth Sciences*, vol. 7, no. 2, pp. 409-431, 1988.
- [49] M. K. Mensah, "On the question of the age of Sekondi Series Upper Devonian or Lower Carboniferous rocks of Ghana," *Ghana Journal of Science*, vol. 2, no. 33, pp. 134-139, 1973.
- [50] J. P. Sylvain, J. Collart, A. Aregba, and S. Godonou, "Notice explicative de la carte géologique 1/500.000 du Togo," *Mém. 6, D.G.M.G./B.N.R.M., Lomé—Togo*, 120p, 1986.

- [51] Y. D. Da Costa, *Biostratigraphie et paléogéographie du bassin sédimentaire côtier du Togo* [Ph.D. thesis], Université de Lomé, Togo, 2005.
- [52] A. A. Antobreh, J. I. Faleide, F. Tsikalas, and S. Planke, "Rift-shear architecture and tectonic development of the Ghana margin deduced from multichannel seismic reflection and potential field data," *Marine and Petroleum Geology*, vol. 26, no. 3, pp. 345–368, 2009.

Research Article

Different Origins of the Fractionation of Platinum-Group Elements in Raobazhai and Bixiling Mafic-Ultramafic Rocks from the Dabie Orogen, Central China

Qing Liu,¹ Quanlin Hou,¹ Liewen Xie,² Hui Li,³ Shanqin Ni,⁴ and Yudong Wu⁴

¹ Key Laboratory of Computational Geodynamics, Graduate University of Chinese Academy of Sciences, Chinese Academy of Sciences, 19 Yuquan Road, Beijing 100049, China

² State Key Laboratory of Lithospheric Evolution, Institute of Geology and Geophysics, Chinese Academy of Sciences, P.O. Box 9825, Beijing 10029, China

³ 416 Geological Prospecting Party, Bureau of Geology, Mineral Exploration and Development, Hunan Province, Zhuzhou 412007, China

⁴ Institute of Mineral Resources, Chinese Academy of Geological Sciences, 26 Baiwanzhuang Road, Beijing 100037, China

Correspondence should be addressed to Qing Liu, 790908619@qq.com

Received 13 January 2012; Accepted 11 May 2012

Academic Editor: Yi-Wen Ju

Copyright © 2012 Qing Liu et al. This is an open access article distributed under the Creative Commons Attribution License, which permits unrestricted use, distribution, and reproduction in any medium, provided the original work is properly cited.

Concentrations of the platinum group elements (PGEs), including Ir, Ru, Rh, Pt, and Pd, have been determined for both Raobazhai and Bixiling mafic-ultramafic rocks from the Dabie Orogen by fire assay method. Geochemical compositions suggest that the Raobazhai mafic-ultramafic rocks represent mantle residues after variable degrees of partial melting. They show consistent PGE patterns, in which the IPGEs (i.e., Ir and Ru) are strongly enriched over the PPGEs (i.e., Pt and Pd). Both REE and PGE data of the Raobazhai mafic-ultramafic rocks suggest that they have interacted with slab-derived melts during subduction and/or exhumation. The Bixiling ultramafic rocks were produced through fractional crystallization and cumulation from magmas, which led to the fractionated PGE patterns. During fractional crystallization, Pd is in nonsulfide phases, whereas both Ir and Ru must be compatible in some mantle phases. We suggest that the PGE budgets of the ultramafic rocks could be fractionated by interaction with slab-derived melts and fractional crystallization processes.

1. Introduction

The platinum group elements (PGEs), including Os, Ir, Ru, Rh, Pt, and Pd, are strongly siderophile and chalcophile elements. They have similar geochemical behaviors during magmatic processes. Traditionally, the PGEs are subdivided into two groups, the compatible IPGEs (Os, Ir, and Ru) and the incompatible PPGEs (Rh, Pd, and Pt) [1]. It has been suggested that the IPGEs are refractory and tend to be retained in the mantle peridotites during partial melting [2]. In contrast, the PPGEs are concentrated in the base metal sulphides (e.g., pentlandite, chalcopyrite), which are released to the melts along with the molten sulfide melts [2]. Because of their unique geochemical characteristics, the PGEs can be used to identify the magma sources and unravel the complex

petrogenetic processes, such as partial melting, melt percolation, and metasomatism in the mantle [1]. Mafic-ultramafic rocks have lower REE contents but higher PGE contents than other rocks, so the PGEs have advantages in studying their petrogenetic processes [1, 3–7].

In this study, we present the PGE data of both Raobazhai and Bixiling mafic-ultramafic rocks from Dabie Orogen, central China, to discuss their fractionation behaviours during magma evolution. The mechanisms of differentiation between these elements will be examined below, taking into account the geochemical affinities of the PGE and their partition in the mineral phases. The results also demonstrate that the PGEs can provide important information on the genesis of magmas.

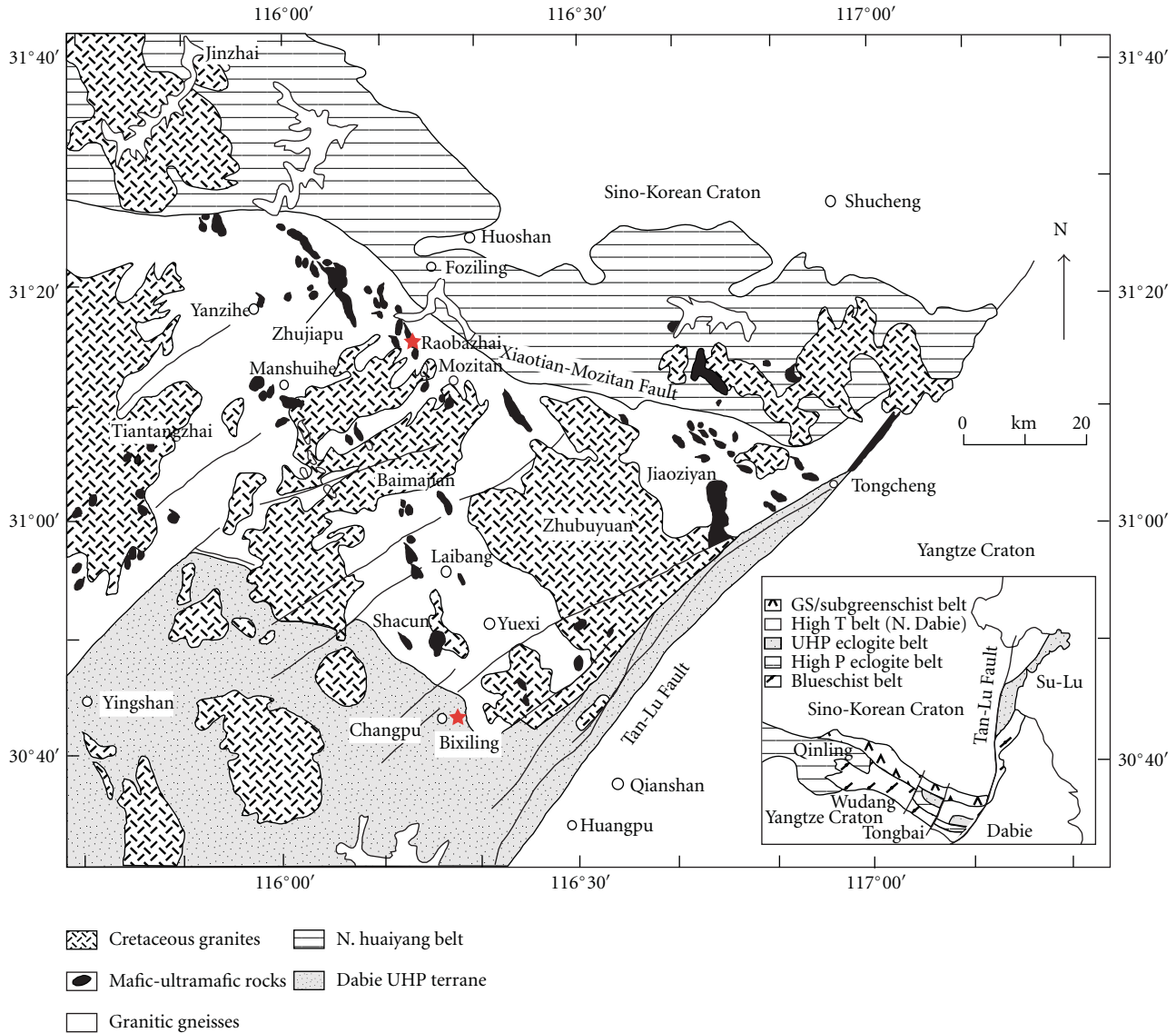


FIGURE 1: Simplified geological map of the Dabie Complex [8]. Sampling localities are roughly indicated by the names of Raobazhai and Bixiling.

2. Geological Background and Occurrence

The Dabie Orogen is the eastern segment of the Qinling-Dabie Orogen, which was formed by the continental collision between the Yangtze Craton and North China Craton (Figure 1). It has been subdivided, from north to south, into five main tectonic zones by several large-scale EW-trending faults [8, 10, 11].

The Raobazhai ultramafic massif is outcropped in the North Dabie high-temperature and ultra-high-pressure (HT/UHP) granulite-facies zone. It is located at ca 5 km south of the Xiaotian-Mozitan Fault (Figure 1), which is a major strike-slip fault along the eastern part of the Qinling-Tongbai-Dabie orogenic belt that might have witnessed the early evolutions of this orogenic belt [13]. Previous studies have suggested that the Raobazhai massif is a sheet-like peridotitic slice, which is in fault contact with the surrounding

amphibolite facies orthogneisses [14–16]. Migmatization can be locally observed in field. The long dimension of the massif is subparallel to the strike of the Xiaotian-Mozitan Fault and the regional foliation. The Raobazhai ultramafic body mainly consists of spinel harzburgites, with minor dunites and lherzolites [16]. They are all highly deformed and metamorphosed. Previous petrographic, geochemical, and thermobarometric studies have suggested that they represent a tectonic slice of the subcontinental lithospheric mantle [16–18]. Five representative samples have been selected in this study.

The Bixiling Complex is the largest (~1.5 km²) coesite-bearing mafic-ultramafic body in the Dabie Orogen, which occurs as a tectonic block that is enclosed within the foliated quartzofeldspathic gneisses in the eastern part of the Dabie UHP terrane (Figure 1). It consists predominantly of banded

eclogites and about 20 elongated lenses of garnet-bearing ultramafic rocks, for example, garnet peridotites, garnet pyroxenites, and wehrlites, which range from 50 to 300 m in length and from 5 to 50 m in width [19]. The contact between eclogite and ultramafic rocks is gradational. Field relationships and petrological evidence indicate a cumulate origin of the mafic-ultramafic rocks [19]. Therefore, the diverse rock types are considered, at least to a first approximation, as magmatically cogenetic [20]. The selected samples include three nattier blue eclogites (garnet, omphacite, kyanite, phengite, and rutile), two greenish black eclogites (garnet, omphacite, rutile, and quartz), and two garnet peridotites (olivine, orthopyroxene, clinopyroxene and garnet).

3. Materials and Methods

Samples were ground to 200 mesh powders using an agate mill. Whole-rock major elements were determined by X-ray fluorescence spectrometry (XRF) using a Phillips PW 2400 sequential XRF instrument at the Institute of Geology and Geophysics, Chinese Academy of Sciences (IGGCAS). The analytical precision is better than $\pm 2\%$ for major oxides. Bulk-rock rare earth elements (REE) were analyzed on the Plasma PQ2 inductively coupled plasma mass spectrometry (ICP-MS) at IGGCAS. Replicate analyses of a monitor sample suggest that the reproducibility for the REE analysis is better than 3.5%.

Whole-rock PGE contents were analyzed by fire assay (FA) method and measured on a Plasma PQ2 ICP-MS at IGGCAS. About 15 g sample powder, together with 20 g $\text{Na}_2\text{B}_4\text{O}_7$, 10 g Na_2CO_3 , 2 g Ni, 2 g S, and some SiO_2 , was fused in a fire-clay crucible at 1150°C for 2 hours. Then, the crucible was broken and a sulphide bead was recovered. The bead was dissolved in a Teflon beaker using 15 mL HCl. After the bead disintegrated into powder, 2 mL Te and 4 mL SnCl_2 were added into the solution. The solution was heated to become clear and then was filtered to collect the insoluble residue. The residue was cleaned and transferred into a Teflon beaker containing 2.5 mL aqua regia. Once the solution became clear, appropriate amounts of Re and Cd spike solutions were then added to the mixture, which was diluted with 50 mL H_2O for TJA Pro Excel inductively coupled plasma mass spectrometry (ICP-MS) determination. The detection limits, which are defined as average blank plus three standard deviations, for Ir, Ru, Rh, Pt and Pd were 0.002, 0.0086, 0.0048, 0.082, and 0.043 ppb, respectively. The PGE contents of most samples are higher than the detection limits, whereas both Ir and Ru contents of some samples are close to their detection limits. Replicate analyses of standard WPR-1 have respectively given values of 13.6 ppb Ir, 9.7 ppb Ru, 13.7 ppb Rh, 257 ppb Pt and 248 ppb Pd. The average element concentrations of replicate analyses of WPR-1 are within 10% of the certified value except Ir which is 13% lower.

4. Results

4.1. Raobazhai Mafic-Ultramafic Rocks. The major-, trace-elements and PGE concentration data of the Raobazhai

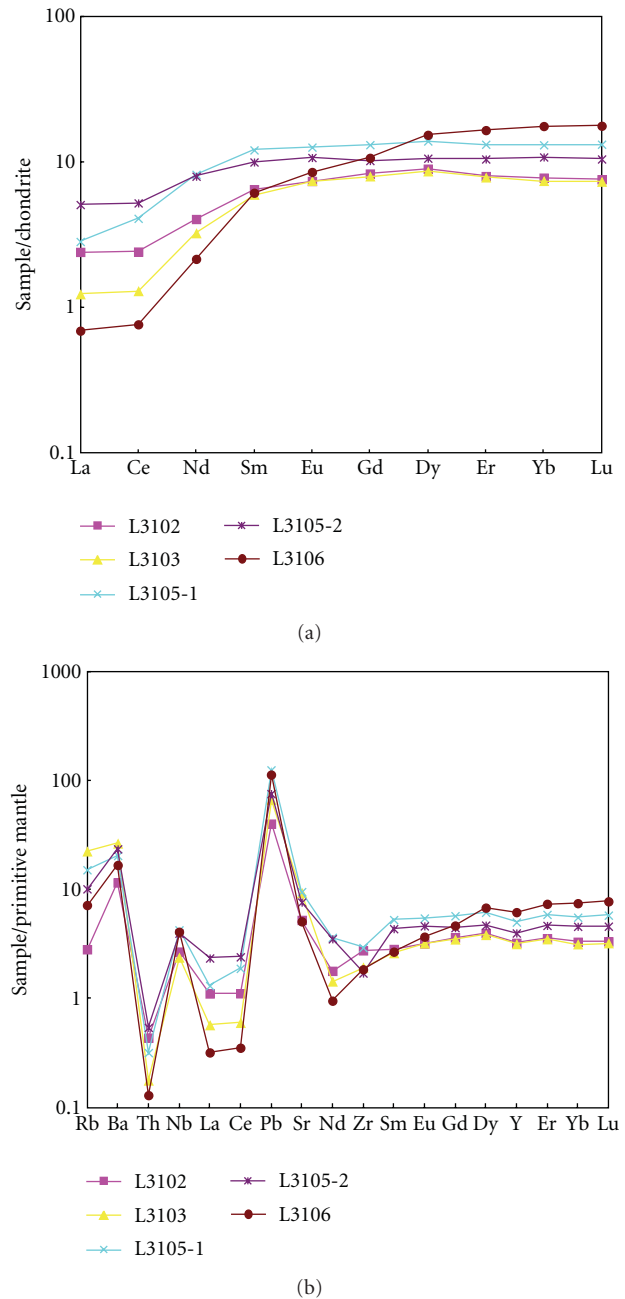


FIGURE 2: Chondrite-normalized REE patterns (a) and spider patterns (b) of Raobazhai mafic-ultramafic rocks (chondrite and primitive mantle values are from [9]).

mafic-ultramafic rocks are given in Table 1. The Raobazhai samples show consistent REE patterns (Figure 2(a)), that is, flat HREE patterns but variable depletion in LREE. Similar results have been reported in a previous study on the Raobazhai peridotites [9]. The REE are incompatible elements during partial melting of mantle peridotites; removal of basaltic components tend to decrease the REE contents of the mantle peridotites. In comparison, the LREE are more incompatible within mantle minerals than the HREE; therefore, the residual peridotites are depleted in LREE

TABLE 1: Major elements (wt%), trace elements (ppm), and PGE (ppb) concentration of Raobazhai and Bixiling mafic-ultramafic rocks.

Location	Raobazhai mafic-ultramafic rocks						Bixiling mafic-ultramafic rocks					
	L3102	L3103	L3105-1	L3105-2	L3106	L2906	L2907	L2912	L2908	L2909	L2910	L2911P
sample	L3102	L3103	L3105-1	L3105-2	L3106	L2906	L2907	L2912	L2908	L2909	L2910	L2911P
SiO ₂	46.81	47.99	46.23	45.64	44.72	50.65	50.66	46.88	42.96	42.97	42.11	38.42
TiO ₂	0.60	0.77	1.39	0.79	1.19	0.77	0.77	2.69	2.05	2.08	0.25	0.35
Al ₂ O ₃	13.94	11.94	13.33	14.11	15.02	16.64	16.09	13.95	13.57	13.84	8.85	6.61
Fe ₂ O ₃	12.99	11.21	12.35	12.87	14.82	9.31	9.34	18.83	20.89	20.63	14.3	15.91
MnO	11.00	11.53	10.45	10.83	9.46	0.15	0.15	0.24	0.14	0.14	0.2	0.2
MgO	0.23	0.18	0.20	0.21	0.28	7.47	7.76	5.49	7.08	7	24.65	28.71
CaO	11.72	12.20	12.04	11.48	11.50	11.92	12.01	9.26	12.02	11.99	5.33	3.07
Na ₂ O	2.11	2.11	2.13	2.28	1.82	2.1	2.21	2.37	1.23	1.22	0.21	0.31
K ₂ O	0.06	0.40	0.24	0.20	0.04	0.24	0.19	0.03	0.01	0.02	0.01	0.05
P ₂ O ₅	0.05	0.01	0.09	0.08	0.08	0.05	0.08	0.15	0.02	0.01	0.04	0.13
LOI	0.48	1.55	1.05	1.16	0.38	0.39	0.17				3.56	4.89
Total	99.99	99.90	99.49	99.64	99.32	99.7	99.42	99.24	99.39	99.48	99.51	98.66
Sc	42	44	49	46	56	40	39	50	55	57	15	11
V	257	326	347	272	318	225	232	389	911	918	99	102
Cr	1744	1258	1112	995	851	400	661	1			2673	7313
Co	45	46	55	56	46	41	42	45	93	82	118	146
Ni	185	224	223	240	99	72	79	6	12	10	802	1012
Cu	14	145	53	96	82	97	97	177	63	62	29	27
Zn	51	60	75	75	61	53	55	109	88	94	80	97
Ga	11	12	14	12	12	14	13	18	18	18	6	6
Rb	1.8	14.1	9.6	6.4	4.5	6.1	4.3	1.5	0.4	0.6	0.4	1.4
Sr	110	195	201	161	107	345	230	70	75	66	89	123
Y	15	14	23	18	28	10	10	19	7	7	5	5
Zr	31	22	33	19	21	7	10	17	11	12	11	13
Nb	1.9	1.7	3.0	2.8	2.9	0.5	0.5			0.1	0.3	0.6
Cs	0.6	0.5	0.6	1.0	0.9	0.4	0.3	0.1		0.1	0.3	0.2
Ba	81	184	143	164	117	87	74	27	11	17	14	36
La	0.8	0.4	0.9	1.6	0.2	3.1	2.1	3.2	0.3	0.3	1.7	4.6
Ce	2.0	1.1	3.3	4.3	0.6	7.1	3.8	10.2	0.8	0.8	4.3	8.6
Pr	0.4	0.3	0.8	0.8	0.2	1.2	0.6	1.7	0.2	0.2	0.8	1.2
Nd	2.4	1.9	4.9	4.8	1.3	5.8	2.7	9.2	1.4	1.4	3.6	5.5
Sm	1.26	1.15	2.34	1.93	1.19	1.54	0.91	2.55	0.93	0.98	0.95	1.23
Eu	0.54	0.54	0.91	0.78	0.62	0.66	0.46	1.09	0.43	0.45	0.32	0.37
Gd	2.16	2.07	3.41	2.65	2.77	1.76	1.42	3.34	1.24	1.28	0.9	1.15
Tb	0.43	0.41	0.66	0.52	0.65	0.32	0.29	0.59	0.22	0.24	0.15	0.17
Dy	2.9	2.8	4.5	3.5	5.0	2.1	2.1	3.9	1.5	1.6	1	1
Ho	0.6	0.6	0.9	0.7	1.1	0.4	0.4	0.8	0.3	0.3	0.2	0.2
Er	1.7	1.7	2.8	2.2	3.5	1.3	1.3	2.2	0.9	0.9	0.6	0.6
Tm	0.2	0.2	0.4	0.3	0.6	0.2	0.2	0.3	0.1	0.1	0.1	0.1
Yb	1.6	1.5	2.7	2.3	3.7	1.2	1.2	2.1	0.8	0.8	0.6	0.6
Lu	0.25	0.24	0.43	0.34	0.57	0.18	0.19	0.31	0.12	0.12	0.1	0.09
Hf	0.92	0.83	1.19	0.64	0.78	0.24	0.31	0.54	0.43	0.47	0.29	0.39

TABLE 1: Continued.

Location	Raobazhai mafic-ultramafic rocks					Nattier blue eclogite			Bixiling mafic-ultramafic rocks					Garnet peridotite	
Ta	0.209	0.08	0.14	0.17	0.147	0.031	0.029	0.002	0.001	0.003	0.021	0.037	0.086		
Pb	7.4	12.2	23.0	13.9	20.8	2.7	0.9	9.7	2	1.3	2.5	7.7	7.8		
Th	0.0	0.0	0.0	0.0	0.0	0.2	0.1	0.6	0.2	0.2	0.2	0.3	0.3		
U	0.02	0.01	0.05	0.06	0.02	0.06	0.04	0.17	0.08	0.08	0.05	0.1	0.1		
Ir	0.153	0.060	0.257	0.180	0.360	—	0.003	—	—	—	0.837	1.18	0.52		
Ru	0.487	0.297	0.367	0.520	0.513	0.003	—	0.007	—	0.03	0.723	1.76	1.357		
Rh	0.237	0.327	0.447	0.343	0.633	0.108	0.083	0.002	0.109	0.142	0.665	0.648	0.422		
Pt	3.86	8.77	9.71	7.65	14.33	0.34	0.20	0.08	0.16	0.29	12.00	3.40	3.75		
Pd	4.86	31.98	4.44	7.69	23.38	0.47	0.03	0.16	0.09	0.50	7.42	8.67	8.34		

(—): lower than the limits of detection.

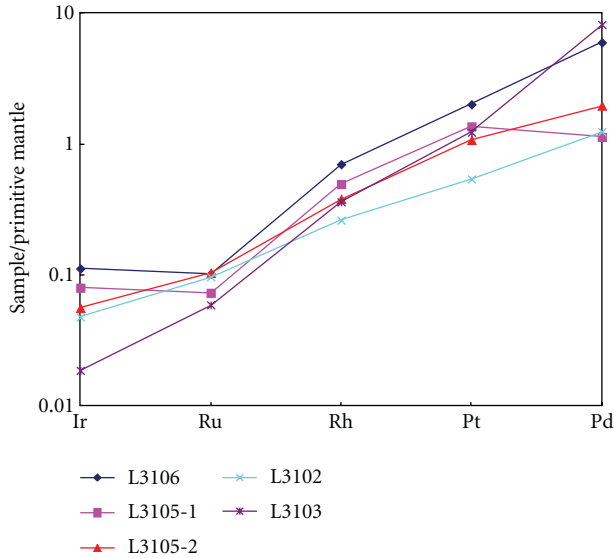


FIGURE 3: Primitive mantle-normalized PGE abundances for the Raobazhai mafic-ultramafic rocks (Normalizing values are after [1]).

relative to the HREE [21]. The Raobazhai peridotites are ubiquitously depleted in LREE, which suggest that they represent mantle residues after variable degrees of partial melting. In the (primitive mantle)-PM-normalized trace element diagram (Figure 2(b)), most Raobazhai samples show variable enrichment in LILE (e.g., Sr, Ba, and Rb). In particular, both Rb and Ba have concentrations ten times higher than those of the primitive mantle. The enrichment of LILE is an important feature of the Raobazhai mafic-ultramafic rocks. It has been suggested that enrichment of Rb and Ba in mantle peridotites could result from subduction-related metasomatism [21]. Zhi et al. [18] also concluded that the enrichment of LILE shown by the Raobazhai ultramafic rocks might be probably related to the slab-released fluids.

The total PGE contents of the Raobazhai mafic-ultramafic rocks range from 9.6 to 41.4 ppb, with an average of 24.4 ppb, which are higher than the estimated values of the primitive mantle (20.1 ppb) but similar to the Alpine-type orogenic peridotites, for example, Ronda (17.5–39.5 ppb) and the Beni Bousera (17.2–32.5 ppb) [22]. All Raobazhai mafic-ultramafic rocks display consistent and pronounced positive PGE patterns (Figure 3); they are strongly enriched in PPGEs (e.g., Pt and Pd) over IPGEs (e.g., Ir and Ru). Their Pd/Ir ratios vary from 17 to 65. Both Ir and Ru show good positive correlations with Ni, which suggest they behave as compatible elements during partial melting [23, 24]. In contrast, both Pt and Pd behave as incompatible elements. Therefore, the concentrations of Ir and Ru increase in the residual peridotites along with the melt extraction, whereas melts are enriched in both Pd and Pt relative to Ir and Ru. This suggests that the residual mantle peridotites should enrich in IPGEs over PPGEs, which is in contrast to the PGEs patterns shown by the Raobazhai mafic-ultramafic rocks. Therefore, the PGE budgets of the Raobazhai peridotites have been affected by processes other than partial melting.

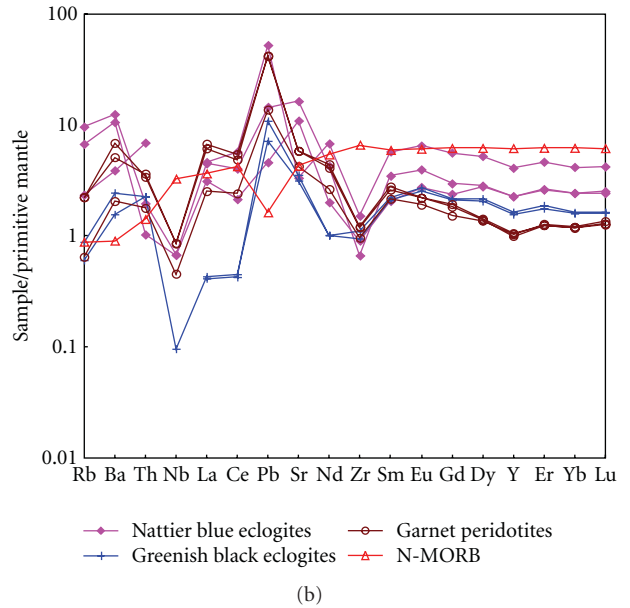
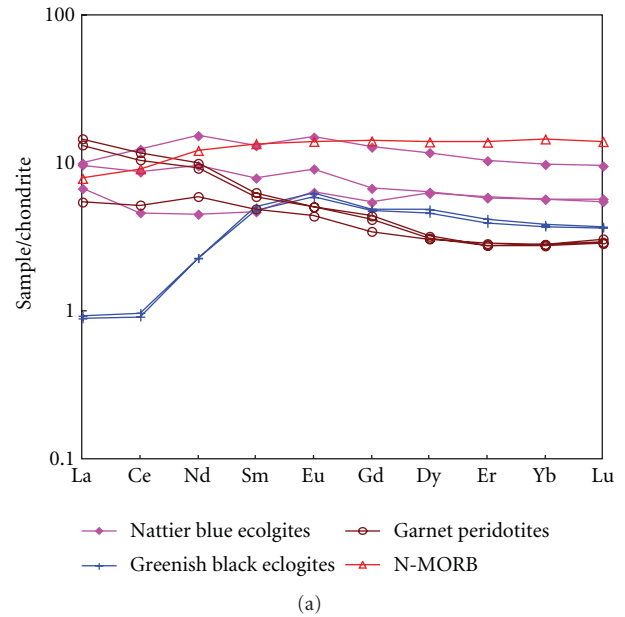


FIGURE 4: Chondrite-normalized REE patterns (a) and spider patterns (b) of Bixiling mafic-ultramafic rocks (Chondrite, Primitive mantle, and N-MORB values are from [9]).

4.2. Bixiling Eclogites and Peridotites. Both REE and PGE data for five eclogites and two garnet peridotites from Bixiling are given in Table 1, and their distribution patterns are shown in Figures 4 and 5. All eclogites show remarkable positive Eu anomalies, suggesting that they were originally transformed from rocks with cumulated plagioclase. Three nattier blue eclogites selected in this study have quiet similar REE patterns with variable enrichment in LREE (Figure 4(a)), which are consistent with results reported in a previous study [20]. Compared to the normal mid-ocean ridge basalts (N-MORB), the Bixiling nattierblue eclogites have relatively low HREE contents and are slightly enriched in LREE.

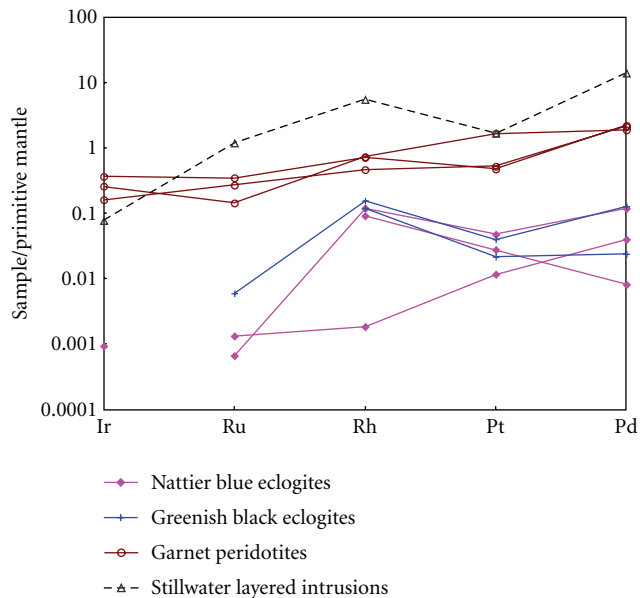


FIGURE 5: Primitive mantle-normalized PGE abundances for the Bixiling mafic-ultramafic rocks (Normalizing values are after [1]).

This suggests that they were not originally metamorphosed from N-MORB [20]. In contrast, the greenish black eclogites have lower REE contents and are strongly depleted in LREE (Figure 4(a)). This may be because the LREEs are incompatible in olivine, pyroxene, and garnet, but rich in liquid phase during the differentiation process, which make cumulation conglomerate facies that were formed by fractional crystallization have a relative depletion in LREE, and their HREE abundance also different from N-MORB. Compared to the eclogites, the garnet peridotites have lower HREE contents. They are variably enriched in LREE, which are also differed from both garnet peridotites entrained in kimberlites and Alpine-type orogenic peridotites [25]. The patterns suggest that these two garnet peridotites represent a more advanced crystal cumulation [20]. In the trace-element diagram (Figure 4(b)), both garnet peridotites and eclogites show pronounced negative Zr and Nb anomalies. Depletion of Zr has been suggested to be an indigenous feature of the upper mantle origin. The negative Nb anomaly is an important fingerprint of subduction-related magmas and continental crust. Based on Sr-Nd isotopes of the Bixiling eclogites and garnet peridotites, Chavagnac and Jahn [20] suggested that the Bixiling magmas were contaminated, probably by lower-crustal granulites that are depleted in LILE. The contamination did not significantly modify the Sr isotopes, but could result in lowering in ϵNd values and negative Nb anomaly as observed [20]. A previous study on oxygen isotopic compositions of silicate minerals in the Bixiling eclogites and garnet peridotites has suggested that the original magmas were derived from the upper mantle but probably contaminated by small amounts of crustal rocks during their differentiation processes [26].

The Bixiling mafic-ultramafic rocks display PGE patterns increasing from IPGEs to PPGEs (Figure 5), which

are different from that the mantle wedge xenoliths from Kamchatka [27] but very similar to the PGE patterns shown by the Stillwater layered intrusions [3]. The total PGE contents of garnet peridotites range from 14.39 ppb to 21.65 ppb. They have high Pd/Ir ratios up to 10 that are remarkably higher than that of the primitive mantle. It has been suggested that the typical mantle xenoliths and Alpine-type orogenic peridotites have flat PGE patterns, in which the PGEs are not fractionated [3]. Furthermore, partial melting would lead to depletion of PPGEs over IPGEs in the mantle residues, which should display flat to negative PGE patterns [3, 22, 28, 29]. Therefore, we suggest that the Bixiling garnet peridotites are refractory mantle residues after melt extraction but represent fractional crystallization products of mantle-derived melts, which is also supported by both trace-element and isotope compositions as discussed above.

The PGE patterns of both nattier blue eclogites and greenish black eclogites are distinguished from each other due to their very low contents of Ir and Ru, which are even lower than their detection limits. The Bixiling eclogites have low total contents of PGEs, which range from 0.25 ppb to 0.96 ppb. They display fractionated PGE patterns, which increase from IPGEs to PPGEs. This implies that they represent the late-stage products of magmatic differentiation. The PGE patterns of the Bixiling mafic-ultramafic rocks vary with the lithologies. The PGE content systematically decreases from the garnet peridotites to the eclogites, which show positive correlations with the MgO contents. Along with the magmatic differentiation, variations in PPGEs (i.e., Pt and Pd) are more limited than those observed for IPGEs (i.e., Ir and Ru). This suggests that the IPGEs are compatible during fractional crystallization and controlled by phases (e.g., metal alloys, chromite, olivine, or clinopyroxene) other than low-temperature sulphides [7].

5. Discussion

Although it has been suggested that the PGEs can be mobilized and fractionated by secondary post-magmatic events, such as hydrothermal alteration or weathering [30], it has been widely accepted that the PGEs are immobile under near-surface conditions. For example, Rehkämper et al. [31] suggested that the PGE budgets of abyssal peridotites have not been significantly disturbed by low-temperature alteration ($<150^{\circ}\text{C}$). Furthermore, it has also been suggested that the PGEs are immobile during serpentinization ($<600^{\circ}\text{C}$) processes, for which is commonly taken place under very reducing conditions [31, 32]. Büchl et al. [33] demonstrated that the PGEs are also significantly fractionated by hydrothermal fluids. Therefore, the fractionated PGE patterns observed in the Raobazhai peridotites cannot be ascribed to any secondary process; their PGE patterns reflect the magmatic processes occurred in the mantle, such as partial melting and melt percolation. The Raobazhai peridotites display enrichment in IPGEs over PPGEs, which is in stark contrast to the predicated PGE patterns of residual mantle peridotites. Hence, we believe that their PGE budgets have been affected by other processes than partial melting.

Recently, various studies have shown that the PGE budgets of mantle peridotites could be significantly disturbed by metasomatic processes, including melt/fluid infiltration and percolation [34–40]. Unlike hydrous fluids, slab-derived melts are capable of carrying HFSE (e.g., Zr, Hf, Nb and Ta) at some instances [41–43]. The mantle wedge could achieve such distinct geochemical signatures through extensive interaction with slab-derived melts [27]. It has also been suggested that slab-derived melts could fractionate the IPGEs from the PPGEs [27]. The positive relationship between Pt/Pd ratio and Hf concentration shown by the Raobazhai mafic-ultramafic rocks indicates that they have been metasomatized by slab-derived melts. Occurrence of hydrous mineral in Raobazhai mafic-ultramafic rocks also supports that they have been interacted with hydrous melts during subduction and/or exhumation [44]. Segregation of secondary sulfides from the volatile-rich melts into the mantle peridotites could increase their Pd abundances [34]. Enrichment of PPGEs over IPGEs in the Raobazhai peridotites could be interpreted by addition of secondary sulfides. In conclusion, both PGE and trace-elements data suggest that the Raobazhai mafic-ultramafic rocks have been metasomatized by slab-derived melts.

The partition coefficient of Cu between sulfide and silicate melts ($D^{\text{sulfide/silicate}}$) has been experimentally determined to be 900–1400, which is 3000–90000 for Pd [45]. The covariation between Cu and Pd is a useful indicator for sulphide fractionation. Because Cu is much less chalcophile than Pd, the Cu/Pd ratio should increase if sulphide is fractionated from a magma. In the Bixiling garnet peridotites and eclogites, The Cu/Pd ratio of the Bixiling garnet peridotites varies from 10^3 to 10^4 , whereas it ranges from 10^5 to 10^7 for the Bixiling eclogites. As shown in the Cu/Pd versus Pd diagram (Figure 6), the Cu/Pd ratios of the garnet peridotites are close to the mantle values, which suggests that they have not experienced sulphide segregation prior to their emplacement [12]. If sulfide segregation had occurred in the Bixiling garnet peridotites, then their Cu/Pd ratios should be greater than the normal mantle values because Pd is preferentially partitioning into sulfide liquid relative to Cu. The PGE patterns of the Bixiling eclogites are consistent with sulfide segregation from these samples. That is, the Cu/Pd ratio becomes elevated along with the increase of fractional crystallization.

Sulfide segregation is an inevitable process during fractional crystallization [7]. Fractional crystallization tend to decrease the FeO content in the residual magma, which might result in S saturation and thus formation of immiscible sulfide liquids [46]. The Bixiling garnet peridotites and eclogites were formed along with fractional crystallization, during which the S contents of the magmas became saturated to segregate sulfides. Removal of sulfides would lead to depletion of Pd in the residual magmas and increase in Cu/Pd ratio (Figure 6).

The Bixiling mafic-ultramafic rocks display a positive correlation between Ru and Pd, indicating that both elements are partitioning into the same kind of sulfides. The PGE data of the Bixiling mafic-ultramafic rocks suggest that

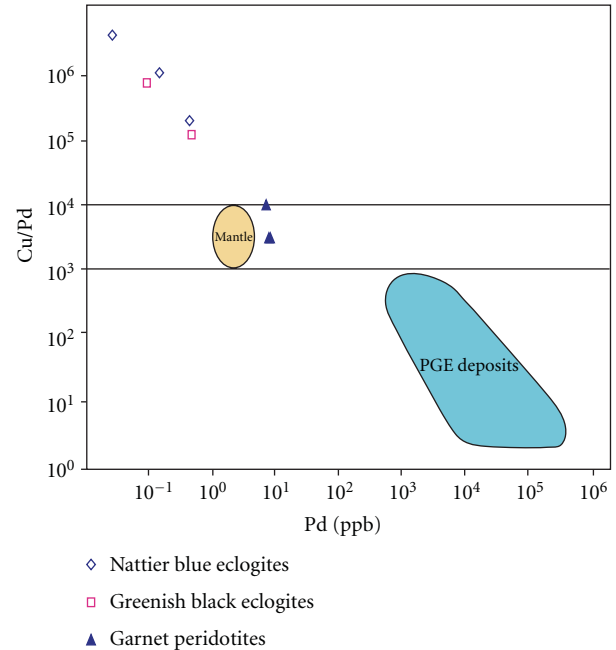


FIGURE 6: Plots of Cu/Pd ratios versus Pd for Bixiling mafic-ultramafic rocks (filled fields are after [12]).

the PGEs can be fractionated during magma differentiation. Both Ir and Ru are compatible in a nonsulfide phase, in which Pd is incompatible. Both petrological and geochemical studies have suggested that olivine [47, 48], spinel or chromite [49, 50], and refractory alloys [51, 52] are the most likely candidates [7]. However, modeling calculations have shown that neither olivine nor clinopyroxene can significantly fractionate the PGEs [7]. It has been suggested that the PGEs are not incorporated into the lattice of chromites but concentrated within tiny inclusions, such as sulfides or alloys. Therefore, chromites themselves are not able to fractionate the PGEs [52]. Keays [2] has suggested that both Ir and Os exist as Os-Ir alloys in the upper mantle. These tiny alloys can be physically segregated into the magmas during partial melting. They can be trapped within the crystallized silicate (e.g., olivine) and oxide (e.g., chromite) minerals, which results in the fractionation of the IPGEs from the PPGEs. Tredoux et al. [53] has also suggested that the PGEs and other nonlithophile elements could be aggregated together as clusters in silicate magmas. Theoretically, the IPGEs (i.e., Os and Ir) are more likely to form clusters than the PPGE (i.e., Rh and Pd) [53]. Therefore, we explain the enrichment of IPGEs rather than PPGEs in the Bixiling mafic-ultramafic rocks as entrainment of such clusters in these samples. The PGE alloys have been rarely reported in mantle peridotites, which could be due to their extremely small sizes. Microinclusions of Os, Ir, and Pt have been identified in Merensky sulfides, which support the occurrence of PGEs as polymetallic clusters in silicates [54]. However, future studies are still needed to investigate the PGE-rich phases in the mantle.

6. Conclusions

On the basis of the geochemical compositions of both Raobazhai and Bixiling mafic-ultramafic rocks, in particular PGE data, we can draw the following primary conclusions:

- (1) The Raobazhai mafic-ultramafic rocks show consistent PGE patterns, in which the PPGes (e.g., Pt and Pd) are strongly enriched over the IPGEs (e.g., Ir and Ru). Such patterns are in stark contrast to those displayed by refractory mantle residues after melt extraction, in which the IPGEs are enriched over the PPGes. This indicates that the PGE budgets of the Raobazhai mafic-ultramafic rocks have been affected by processes other than partial melting. Both REE and PGE data support that the Raobazhai mafic-ultramafic rocks have interacted with slab-derived melts during subduction and/or exhumation.
- (2) The Bixiling mafic-ultramafic rocks were formed through fractional crystallization and cumulation from magmas. The PGE patterns shown by the Bixiling mafic-ultramafic rocks were produced by the magmatic differentiation processes, during which fractional crystallization of silicate minerals and segregation of immiscible sulfide liquids are involved. The fractionated PGE patterns of the Bixiling mafic-ultramafic rocks reflect that Pd is incompatible in the nonsulfide phases, whereas both Ir and Ru are compatible in some mantle phases.

Acknowledgments

This research has been financially supported by the Nature Science Foundation of China (Grant no. 40702009; 41030422). The authors thank Tianshan Gao and Hongyuan Zhang for help in the field work, He Li and Xindi Jin for major and trace element analyses, and Caifen Nu and Hongliao He for their help in PGE analyses. Comments from two reviewers greatly improved the quality of this paper.

References

- [1] S. J. Barnes, R. Boyd, and A. Korneliussen, "The use of mantle normalization and metal ratios in discriminating between the effects of partial melting, crystal fractionation and sulphide segregation on platinum-group elements, gold, nickel and copper: examples from Norway," in *Proceedings of the Geo-Platinum Conference*, H. M. Prichard, J. W. Bowles, and P. Potts, Eds., pp. 113–143, Elsevier, Amsterdam, The Netherlands, 1988.
- [2] R. R. Keays, "The role of komatiitic and picritic magmatism and S-saturation in the formation of ore deposits," *Lithos*, vol. 34, no. 1–3, pp. 1–18, 1995.
- [3] S. J. Barnes, A. J. Naldrett, and M. P. Gorton, "The origin of the fractionation of platinum-group elements in terrestrial magmas," *Chemical Geology*, vol. 53, no. 3–4, pp. 303–323, 1985.
- [4] J. P. Lorand, "Abundance and distribution of CuFeNi sulfides, sulfur, copper and platinum-group elements in orogenic-type spinel ilmenite massifs of Ariège (Northeastern Pyrenees, France)," *Earth and Planetary Science Letters*, vol. 93, no. 1, pp. 50–64, 1989.
- [5] G. Garuti, C. Gorgoni, and G. P. Sighinolfi, "Sulfide mineralogy and chalcophile and siderophile element abundances in the Ivrea-Verbano mantle peridotites (Western Italian Alps)," *Earth and Planetary Science Letters*, vol. 70, no. 1, pp. 69–87, 1984.
- [6] G. Garuti, G. Fershtater, F. Bea, P. Montero, E. V. Pushkarev, and F. Zaccarini, "Platinum-group elements as petrological indicators in mafic-ultramafic complexes of the central and southern Urals: preliminary results," *Tectonophysics*, vol. 276, no. 1–4, pp. 181–194, 1997.
- [7] M. Rehkämper, A. N. Halliday, J. G. Fitton, D. C. Lee, M. Wieneke, and N. T. Arndt, "Ir, Ru, Pt, and Pd in basalts and komatiites: new constraints for the geochemical behavior of the platinum-group elements in the mantle," *Geochimica et Cosmochimica Acta*, vol. 63, no. 22, pp. 3915–3934, 1999.
- [8] B. M. Jahn, F. Wu, C. H. Lo, and C. H. Tsai, "Crust-mantle interaction induced by deep subduction of the continental crust: geochemical and Sr-Nd isotopic evidence from post-collisional mafic-ultramafic intrusions of the northern Dabie complex, central China," *Chemical Geology*, vol. 157, no. 1–2, pp. 119–146, 1999.
- [9] S. S. Sun and W. F. McDonough, "Chemical and isotopic systematics of oceanic basalts: implications for mantle composition and processes," *Magmatism in the Ocean Basins*, pp. 313–345, 1989.
- [10] B. R. Hacker, L. Ratschbacher, L. Webb et al., "Exhumation of ultrahigh-pressure continental crust in east central China: late Triassic-Early Jurassic tectonic unroofing," *Journal of Geophysical Research B*, vol. 105, no. 6, pp. 13339–13364, 2000.
- [11] J. Zheng, M. Sun, M. F. Zhou, and P. Robinson, "Trace elemental and PGE geochemical constraints of Mesozoic and Cenozoic peridotitic xenoliths on lithospheric evolution of the North China Craton," *Geochimica et Cosmochimica Acta*, vol. 69, no. 13, pp. 3401–3418, 2005.
- [12] S. J. Barnes and C. P. Picard, "The behaviour of platinum-group elements during partial melting, crystal fractionation, and sulphide segregation: an example from the Cape Smith Fold Belt, northern Quebec," *Geochimica et Cosmochimica Acta*, vol. 57, no. 1, pp. 79–87, 1993.
- [13] B. R. Hacker, L. Ratschbacher, L. Webb, T. Ireland, D. Walker, and D. Shuwen, "U/Pb zircon ages constrain the architecture of the ultrahigh-pressure Qinling-Dabie Orogen, China," *Earth and Planetary Science Letters*, vol. 161, no. 1–4, pp. 215–230, 1998.
- [14] X. Yang, "A cold ultramafic intrusive body in Dabieshan area, Anhui Province," *Bulletin of Nanjing Institute of Geology*, vol. 4, pp. 81–95, 1983.
- [15] S. Xu, L. Jiang, Y. Liu, and Y. Zhang, "Tectonic framework and evolution of the Dabie Mountains in Anhui, eastern China," *Acta Geologica Sinica*, vol. 5, pp. 221–238, 1992.
- [16] C. H. Tsai, J. C. Liou, and W. G. Ernst, "Petrological characterization and tectonic significance of retrogressed garnet peridotites, Raobazhai area, North Dabie Complex, east-central China," *Journal of Metamorphic Geology*, vol. 18, no. 2, pp. 181–192, 2000.
- [17] Q. Zhang, B. Ma, R. Liu et al., "A remnant of continental lithospheric mantle above subduction zone: geochemical constraints on ultramafic rock from Raobazhai area, Anhui province," *Science in China Series B*, vol. 38, no. 12, pp. 1522–1529, 1995.
- [18] X. C. Zhi, Y. B. Jin, Q. Meng, and T. S. Gao, "Trace element geochemistry of Raobazhai ultramafic complex, North Dabie

- Mountain," *Acta Petrologica Sinica*, vol. 20, no. 3, pp. 463–472, 2004.
- [19] R. Y. Zhang, J. G. Liou, and B. L. Cong, "Ultrahigh-pressure metamorphosed talc-, magnesite- and Ti-clinohumite-bearing mafic-ultramafic complex, Dabie mountains, east-central China," *Journal of Petrology*, vol. 36, no. 4, pp. 1011–1037, 1995.
 - [20] V. Chavagnac and B. M. Jahn, "Coexisting-bearing eclogites from the Bixiling Complex, Dabie Mountains, China: Sm-Nd ages, geochemical characteristics and tectonic implications," *Chemical Geology*, vol. 133, no. 1–4, pp. 29–51, 1996.
 - [21] H. Downes, "Formation and modification of the shallow sub-continental lithospheric mantle: a review of geochemical evidence from ultramafic xenolith suites and tectonically emplaced ultramafic massifs of Western and Central Europe," *Journal of Petrology*, vol. 42, no. 1, pp. 233–250, 2001.
 - [22] K. Gueddari, M. Piboule, and J. Amossé, "Differentiation of platinum-group elements (PGE) and of gold during partial melting of peridotites in the lherzolitic massifs of the Betico-Rifean range (Ronda and Beni Bousera)," *Chemical Geology*, vol. 134, no. 1–3, pp. 181–197, 1996.
 - [23] J. W. Morgan, "Ultramafic xenoliths: clue to the earth's late accretionary history," *Journal of Geophysical Research*, vol. 91, pp. 12375–12387, 1986.
 - [24] J. P. Lorand, L. Pattou, and M. Gros, "Fractionation of Platinum-group elements and gold in the upper mantle: a detailed study in Pyrenean orogenic lherzolites," *Journal of Petrology*, vol. 40, no. 6, pp. 957–981, 1999.
 - [25] W. F. McDonough and F. A. Frey, "Rare earth elements in upper mantle rocks," in *Geochemistry and Mineralogy of the Rare Earth Elements*, B. R. Lipin and G. A. McKay, Eds., vol. 21, pp. 99–145, Mineralogical Society of America, 1989.
 - [26] R. Y. Zhang, D. Rumble, J. G. Liou, and Q. C. Wang, "Low $\delta^{18}\text{O}$, ultrahigh-P garnet-bearing mafic and ultramafic rocks from Dabie Shan, China," *Chemical Geology*, vol. 150, no. 1–2, pp. 161–170, 1998.
 - [27] P. Kepezhinskis, M. J. Defant, and E. Widom, "Abundance and distribution of PGE and Au in the island-arc mantle: implications for sub-arc metasomatism," *Lithos*, vol. 60, no. 3–4, pp. 113–128, 2002.
 - [28] G. E. Brügmann, N. T. Arndt, A. W. Hofmann, and H. J. Tobschall, "Noble metal abundances in komatiite suites from Alexo, Ontario and Gorgona Island, Colombia," *Geochimica et Cosmochimica Acta*, vol. 51, no. 8, pp. 2159–2169, 1987.
 - [29] J. P. Lorand, R. R. Keays, and J. L. Bodinier, "Copper and noble metal enrichments across the lithosphere-asthenosphere boundary of mantle diapirs: evidence from the lanzo lherzolite massif," *Journal of Petrology*, vol. 34, no. 6, pp. 1111–1140, 1993.
 - [30] J. J. Standish, S. R. Hart, J. Blusztajn, H. J. B. Dick, and K. L. Lee, "Abyssal peridotite osmium isotopic composition for Cr-spinel, Geochem. Geophys. Geosyst. 2001GG000161, 2001.
 - [31] M. Rehkämper, A. N. Halliday, J. Alt, J. G. Fitton, J. Zipfel, and E. Takazawa, "Non-chondritic platinum-group element ratios in oceanic mantle lithosphere: petrogenetic signature of melt percolation?" *Earth and Planetary Science Letters*, vol. 172, no. 1–2, pp. 65–81, 1999.
 - [32] J. E. Snow and G. Schmidt, "Constraints on Earth accretion deduced from noble metals in the oceanic mantle," *Nature*, vol. 391, no. 6663, pp. 166–169, 1998.
 - [33] A. Büchl, G. Brügmann, V. G. Batanova, C. Münker, and A. W. Hofmann, "Melt percolation monitored by Os isotopes and HSE abundances: a case study from the mantle section of the Troodos Ophiolite," *Earth and Planetary Science Letters*, vol. 204, no. 3–4, pp. 385–402, 2002.
 - [34] J. P. Lorand, L. Reisberg, and R. M. Bedini, "Platinum-group elements and melt percolation processes in Sidamo spinel peridotite xenoliths, Ethiopia, East African Rift," *Chemical Geology*, vol. 196, no. 1–4, pp. 57–75, 2003.
 - [35] J. P. Lorand, G. Delpech, M. Grégoire, B. Moine, S. Y. O'Reilly, and J. Y. Cottin, "Platinum-group elements and the multistage metasomatic history of Kerguelen lithospheric mantle (South Indian Ocean)," *Chemical Geology*, vol. 208, no. 1–4, pp. 195–215, 2004.
 - [36] J. P. Lorand, A. Luguët, O. Alard, A. Bezons, and T. Meisel, "Abundance and distribution of platinum-group elements in orogenic lherzolites; a case study in a Fontete Rouge lherzolite (French Pyrénées)," *Chemical Geology*, vol. 248, no. 3–4, pp. 174–194, 2008.
 - [37] L. Reisberg, X. Zhi, J. P. Lorand, C. Wagner, Z. Peng, and C. Zimmermann, "Re-Os and S systematics of spinel peridotite xenoliths from east central China: evidence for contrasting effects of melt percolation," *Earth and Planetary Science Letters*, vol. 239, no. 3–4, pp. 286–308, 2005.
 - [38] H. Becker, M. F. Horan, R. J. Walker, S. Gao, J. P. Lorand, and R. L. Rudnick, "Highly siderophile element composition of the Earth's primitive upper mantle: constraints from new data on peridotite massifs and xenoliths," *Geochimica et Cosmochimica Acta*, vol. 70, no. 17, pp. 4528–4550, 2006.
 - [39] L. Ackerman, R. J. Walker, I. S. Puchtel, L. Pitcher, E. Jelinek, and L. Strnad, "Effects of melt percolation on highly siderophile elements and Os isotopes in subcontinental lithospheric mantle: a study of the upper mantle profile beneath Central Europe," *Geochimica et Cosmochimica Acta*, vol. 73, no. 8, pp. 2400–2414, 2009.
 - [40] Y. Xiao and H.-F. Zhang, "Effects of melt percolation on platinum group elements and Re-Os systematics of peridotites from the Tan-Lu fault zone, eastern North China Craton," *Journal of the Geological Society*, vol. 168, no. 5, pp. 1201–1214, 2011.
 - [41] M. J. Defant and M. S. Drummond, "Derivation of some modern arc magmas by melting of young subducted lithosphere," *Nature*, vol. 347, no. 6294, pp. 662–665, 1990.
 - [42] M. S. Drummond, M. J. Defant, and P. K. Kepezhinskis, "Petrogenesis of slab-derived trondhjemite-tonalite-dacite/adakite magmas," *Transactions of the Royal Society of Edinburgh, Earth Sciences*, vol. 87, no. 1–2, pp. 205–215, 1996.
 - [43] H. Martin, "Adakitic magmas: modern analogues of Archaean granitoids," *Lithos*, vol. 46, no. 3, pp. 411–429, 1999.
 - [44] L. Zheng, X. Zhi, and L. Reisberg, "Re-Os systematics of the Raobazhai peridotite massifs from the Dabie orogenic zone, eastern China," *Chemical Geology*, vol. 268, no. 1–2, pp. 1–14, 2009.
 - [45] S.-J. Barnes and W. D. Maier, "The fractionation of Ni, Cu, and the noble metals in silicate and sulphide liquids," in *Dynamic Processes in Magmatic Ore Deposits and Their Application in Mineral Exploration*, R. R. Keays, Ed., Short Course Notes 13, pp. 69–106, Geological Association Canada, 1999.
 - [46] W. Yi, A. N. Halliday, J. C. Alt et al., "Cadmium, indium, tin, tellurium, and sulfur in oceanic basalts: implications for chalcophile element fractionation in the Earth," *Journal of Geophysical Research B*, vol. 105, no. 8, pp. 18927–18948, 2000.
 - [47] G. E. Brügmann, N. T. Arndt, A. W. Hofmann, and H. J. Tobschall, "Noble metal abundances in komatiite suites from Alexo, Ontario and Gorgona Island, Colombia," *Geochimica et Cosmochimica Acta*, vol. 51, no. 8, pp. 2159–2169, 1987.

- [48] M. F. Zhou, "PGE distribution in 2.7-Ga layered komatiite flows from the Belingwe greenstone belt, Zimbabwe," *Chemical Geology*, vol. 118, no. 1–4, pp. 155–172, 1994.
- [49] I. O. Oshin and J. H. Crocket, "Noble metals in Thetford Mines ophiolites, Quebec, Canada—part I: distribution of gold, iridium, platinum, and palladium in the ultramafic and gabbroic rocks," *Economic Geology*, vol. 77, no. 6, pp. 1556–1570, 1982.
- [50] C. J. Capobianco, R. L. Hervig, and M. J. Drake, "Experiments on crystal/liquid partitioning of Ru, Rh and Pd for magnetite and hematite solid solutions crystallized from silicate melt," *Chemical Geology*, vol. 113, no. 1–2, pp. 23–43, 1994.
- [51] C. Ballhaus, "Is the upper mantle metal-saturated?" *Earth and Planetary Science Letters*, vol. 132, no. 1–4, pp. 75–86, 1995.
- [52] R. J. Walker, E. Hanski, J. Vuollo, and J. Liipo, "The Os isotopic composition of Proterozoic upper mantle: evidence for chondritic upper mantle from the Outokumpu ophiolite, Finland," *Earth and Planetary Science Letters*, vol. 141, no. 1–4, pp. 161–173, 1996.
- [53] M. Tredoux, N. M. Lindsay, G. Davies, and I. McDonald, "The fractionation of platinum-group elements in magmatic systems, with the suggestion of a novel causal mechanism," *South African Journal of Geology*, vol. 98, no. 2, pp. 157–167, 1995.
- [54] C. Ballhaus and P. Sylvester, "Spatial platinum-group-element distribution in magmatic sulfides: implications for the platinum group-element behavior during mantle melting," in *Proceedings of the 7th Annual V.M. Goldschmidt Conference*, pp. 15–16, 1997.

Research Article

FTIR and Raman Spectral Research on Metamorphism and Deformation of Coal

Xiaoshi Li,¹ Yiwen Ju,¹ Quanlin Hou,¹ Zhuo Li,² and Junjia Fan³

¹ Key Laboratory of Computational Geodynamics, College of Earth Science, Graduate University of Chinese Academy of Sciences, Beijing 100049, China

² State Key Laboratory of Petroleum Resource and Prospecting, China University of Petroleum, Beijing 102249, China

³ Key Lab of Basin Structure and Petroleum Accumulation, PetroChina Research Institute of Petroleum Exploration and Development, Beijing 100083, China

Correspondence should be addressed to Yiwen Ju, juyw03@163.com

Received 13 January 2012; Revised 17 April 2012; Accepted 17 April 2012

Academic Editor: Hongyuan Zhang

Copyright © 2012 Xiaoshi Li et al. This is an open access article distributed under the Creative Commons Attribution License, which permits unrestricted use, distribution, and reproduction in any medium, provided the original work is properly cited.

Under different metamorphic environments, coal will form different types of tectonically deformed coal (TDC) by tectonic stress and even the macromolecular structure can be changed. The structure and composition evolution of TDC have been investigated in details using Fourier transform infrared spectroscopy and Raman spectroscopy. The ductile deformation can generate strain energy via increase of dislocation in molecular structure of TDC, and it can exert an obvious influence on degradation and polycondensation. The brittle deformation can generate frictional heat energy and promote the metamorphism and degradation, but less effect on polycondensation. Furthermore, degradation affects the structural evolution of coal in lower metamorphic stage primarily, whereas polycondensation is the most important controlling factor in higher metamorphic stage. Tectonic deformation can produce secondary structural defects in macromolecular structure of TDC. Under the control of metamorphism and deformation, the small molecules which break and fall off from the macromolecular structure of TDC are replenished and embedded into the secondary structural defects preferentially and form aromatic rings by polycondensation. These processes improved the stability of macromolecular structure greatly. It is easier for ductile deformation to induce secondary structural defects than in brittle deformation.

1. Introduction

The study of macromolecular structure and complicated composition of coal is the most difficult and important topic in coal chemistry [1–4]. Effective analytical methods for coal structure and chemical composition research, such as Fourier transform infrared (FTIR) spectroscopy and Raman spectroscopy are, becoming more and more important for coal chemical researchers [5–15]. Previous studies discussed that with the upgrade of metamorphism, the aromatic structure of primary structure coal increased and expanded, whereas the side chain of aliphatic compound and functional group decreased. The hydrogen and oxygen deplete in coals; as a result, the condensation degree gradually improved. Aromatic structure is mainly composed of anthracite, and the condensation degree is further improved [2, 3, 5,

16, 17]. The coal basins in China experienced multiple tectonic movements and developed widely distribution of tectonically deformed coal (TDC) under the strong tectonic deformation environments [18]. Compared with primary structure coal, the evolution characteristics and ways of macromolecular structure of TDC are more complicated [8, 17–21]. The formation of lignite due to diagenesis could experience different degrees of metamorphism under various temperature-pressure conditions during geological history. If the coal seams are apparently affected by tectonic stress, they can produce deformation in certain degrees. For all the deformational coal seams, the process and mechanism of deformation (brittle deformation and ductile deformation) are actually different [17–21]. Many studies have been conducted in order to investigate the relationship between the group absorption frequency of FTIR and the

metamorphic grade of coals, as well as Raman spectral analysis on carbon materials [3–15, 19]; however, products about the studies of different deformation mechanisms and grades of TDC using FTIR and Raman spectrum analysis, and the analysis of evolution process and mechanisms in macromolecular structure of TDC, were rarely reported. Different deformation mechanisms will exert different influences on the macromolecular structure and composition of TDC [6, 7, 18, 19]. Based on the FTIR and Raman spectrum analysis of TDC samples from Huaibei coalfield, the evolution characteristics of macromolecular structure affected by the change of metamorphism and deformation grade are discussed. The aim of this paper is to explain the mechanism of tectonic deformational influence on the evolution of structural defects and chemical composition.

2. Samples and Experimental Methods

The TDC samples with different deformation and metamorphism ($0.7\% < R_{o,max} < 3.1\%$) were collected from Permo-Carboniferous coal bed in Huaibei coal field, which was strongly affected by the Mesozoic tectonic deformation. The coal seams were mainly distributed in graben, especially in syncline. The tectonic deformation altered the structure of coal seams remarkably and formed various types of TDC.

All samples are pretreated through demineralization and vitrinite centrifugation processes in order to better delineate the characteristics of the deformation and metamorphism of TDC samples. The demineralization process utilized HCl and HF to reduce the proportion of mineral matter in each sample ($<2\%$). The vitrinite centrifugation process used benzene and CCl_4 to increase the composition percentage of vitrinite to 80–90%. The group maceral and vitrinite reflectance ($R_{o,max}$) were tested as well.

The FTIR analysis on 32 samples and Raman analysis on 19 samples are conducted to further understand the evolution of macromolecular structure affected by deformation and metamorphism. It can be determined that the type of functional group and its change correlated with deformation and metamorphism in coal by analysis of absorption band, shown on infrared spectrum [7, 9]. The structural analysis and qualitative identification of molecular can be studied by Raman spectrum because the formation of Raman spectra is closely connected with the structure and the ordering degree of coal macromolecule [22]. FTIR was performed on Nicolet 750 microscopic infrared spectrometer in the Analytical Instrumentation Center in Peking University. The scan ranges from 4000 cm^{-1} to 650 cm^{-1} . Spectra were recorded by coadding 128 scans at a resolution of 8 cm^{-1} using an MCT/A detector and a KBr/Ge beam splitter. Raman was performed on Renishaw RM-1000 microscopic Raman spectrometer at the State Key Laboratory of Geological Processes and Mineral Resources in China University of Geosciences. The spectral resolution was 2.4 cm^{-1} , slit width was 2.5 cm^{-1} , and laser power on the sample surface was 0.8 mw; measurements were carried out using the 514.5 nm excitation wavelength with Ar^+ laser; acquisition time was 30 s. The spectra were measured under 25°C temperature.

3. Results and Analysis

Part of experiment results are listed in Table 1.

3.1. Parameter of FTIR Analysis. The types of functional group in TDC samples collected from Huaibei coal field are basically the same with other researchers [3, 7, 23]. But the peak positions and the changes of absorption peaks with the increase of metamorphic grade are different from others (Figure 1). The biggest difference between TDC and the primary structure coal showed on FTIR spectrum is reflected in the change of relative absorption strength but not the absorption frequency.

3.1.1. Evolution of Characteristic Frequency of Aromatic Structure. The characteristic frequency of aromatic structure includes the absorption strength of (1) 3049 cm^{-1} related to stretching vibration of CH in aromatic ring, (2) 1600 cm^{-1} related to vibration of C=C in aromatic ring, and (3) 749 cm^{-1} , 810 cm^{-1} , and 871 cm^{-1} related to the plane deformation vibration of CH in aromatic rings. With the increase of metamorphic grade, the absorption strength of 1600 cm^{-1} has little change in brittle deformational coal but decreases first and increases later in ductile deformational coal, and with the range from 0.994 to 1 (Figure 2(a)).

Generally, the change of absorption strength of 1600 cm^{-1} was not so obvious compared with the other frequencies. The absorption strength of 749 cm^{-1} , 810 cm^{-1} , and 871 cm^{-1} related to the plane deformation vibration of CH in aromatic ring is correlated with independent, two and more adjacent hydrogen atoms state, respectively. The strongest absorption strength of these frequencies is in the middle metamorphic grade and then in the higher and lower metamorphic grades it is the weakest (Figure 1). Figure 2(b) shows that this change is influenced by brittle and ductile deformation. The strongest absorption strength of 3049 cm^{-1} related to stretching vibration of CH in aromatic ring is also in the middle metamorphic grade and gradually decreases towards lower and higher metamorphic grades.

With the increase of deformational intensity (brittle and ductile deformation), the absorption strength of 1600 cm^{-1} increases at first and then decreases, which is inversed with the variation of absorption strength of 749 cm^{-1} (Figures 2(c) and 2(d)).

3.1.2. Evolution of Characteristic Frequency of Aliphatic Structure. The frequency of aliphatic structure includes absorption strength of (1) 2923 cm^{-1} and 2862 cm^{-1} related to the asymmetric stretching vibration of CH_2 and symmetrical stretching vibration of CH_3 , shown as shoulder absorption of 2923 cm^{-1} in aliphatic structure. These frequencies are the weakest in the middle metamorphic grade and increase in the lower and higher metamorphic grades and (2) 1442 cm^{-1} related to the asymmetric deformation vibration of CH_2 and CH_3 in alkane structure. With the increase of metamorphic grade, the change of absorption strength of 1442 cm^{-1} range from 0.8 to 0.99.

TABLE 1: Part of experiment results of TDC samples.

Series of deformation	Sample ID	$R_{o,max}/(\%)$	$R_{o,min}/(\%)$	$\Delta R_o/R_{o,max}$ ¹	FTIR					Raman ²	
					CH ₃ CH ₂		C=C	CH ₃ CH ₂	C-H	A_G	A_D
					2923	2826	1600	1442	749		
Brittle deformation coal	LHM06	0.98	0.83	0.15	0.557	0.326	0.991	0.815	0.317	113967	55594
	HZM03	1.93	1.67	0.13	0.344	0.220	0.994	0.822	0.348	515720	286732
	SK04	1.00	0.91	0.09	0.522	0.372	0.998	0.920	0.369	115158	58378
	HZM02	1.93	1.67	0.13	0.323	0.199	0.998	0.935	0.420	—	—
	LHM12	1.37	1.13	0.18	0.579	0.383	0.998	0.933	0.385	215980	131925
	STM02	1.41	1.12	0.21	0.647	0.403	0.994	0.806	0.380	272570	153720
	TYM04	0.95	0.8	0.16	0.504	0.354	1.000	0.895	0.176	137498	64296
	SK03	0.98	0.88	0.10	0.363	0.264	0.996	0.886	0.548	174251	78056
Ductile deformation coal	LHM04	1.40	1.18	0.16	0.657	0.414	0.988	0.893	0.450	394537	202143
	LHM09	1.39	1.12	0.19	0.599	0.406	0.996	0.951	0.362	—	—
	LLM04	0.83	0.60	0.28	0.547	0.378	0.999	0.918	0.282	324725	164211
	HZM10	2.62	2.02	0.23	0.671	0.406	0.996	0.913	0.301	461139	157064
	LHM02	1.38	1.08	0.22	0.582	0.38	0.998	0.946	0.385	—	—
	LHM03	1.58	1.18	0.25	0.555	0.351	0.988	0.840	0.406	420961	229994
	STM05	1.66	1.12	0.33	0.491	0.312	0.997	0.992	0.455	511926	306591
	XTM08	1.92	1.63	0.15	0.260	0.180	1.000	0.910	0.500	499840	260745

¹ $\Delta R_o = R_{o,max} - R_{o,min}$, ² The data of Raman was cited in [22].

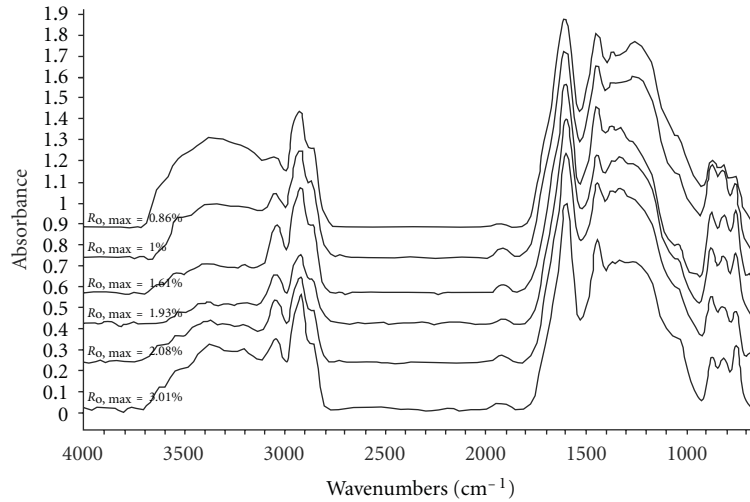


FIGURE 1: The infrared spectrum of TDC with different metamorphic stage.

With the increase of metamorphic grade, the absorption strength of aliphatic structure is much more complicated (Figures 2 and 3). The absorption strength of 2923 cm^{-1} increases first and then decreases in brittle and ductile deformational coal, but absorption strength change of 1442 cm^{-1} is not obvious. It is indicated that the aliphatic structure is gradually degraded with the increase of metamorphic grade in these two deformational mechanisms and this results in the decrease of aliphatic structure.

With the increase of deformational intensity, under the lower metamorphism grade, the absorption strength of 2923 cm^{-1} increases first and decreases later, which is

contrary to the absorption strength variation of 1442 cm^{-1} in brittle and ductile deformational coal (Figures 3(c) and 3(d)). Under the lower deformational intensity, the aliphatic functional groups, alkane branched chains, and a few aromatic rings break off at first, which promotes the metamorphism because of the brittle deformation. In the meantime, the dropped small molecules have not got enough time to form aromatic structure because of the rapid strain rate [19–22]. Part of dropped alkane branched chains are transformed into aliphatic functional groups, and others are turned to free macromolecules. Under the slow strain rate of ductile deformational coal [22], the dropped small

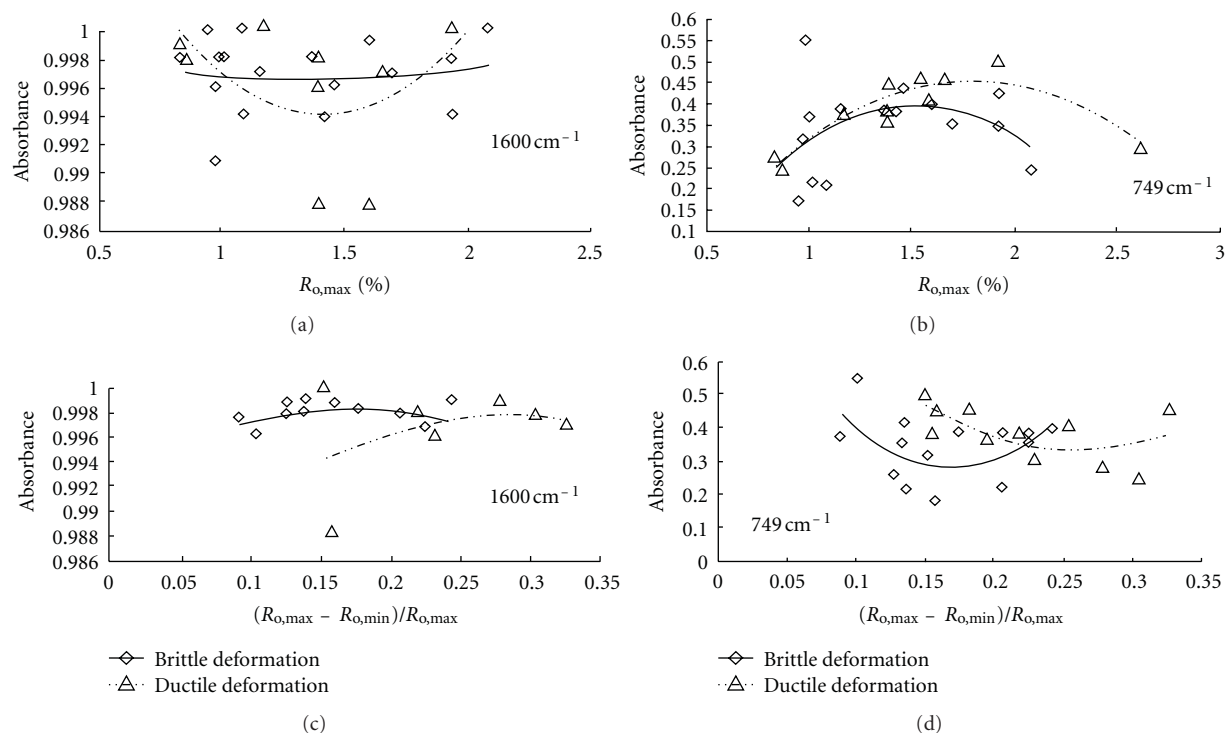


FIGURE 2: Relationship of aromatic absorbance peaks of TDC with different metamorphic and deformation stages. (a) and (b) relationship between aromatic absorbance peaks and metamorphic stages. (c) and (d) relationship between aromatic absorbance peaks and deformation stages.

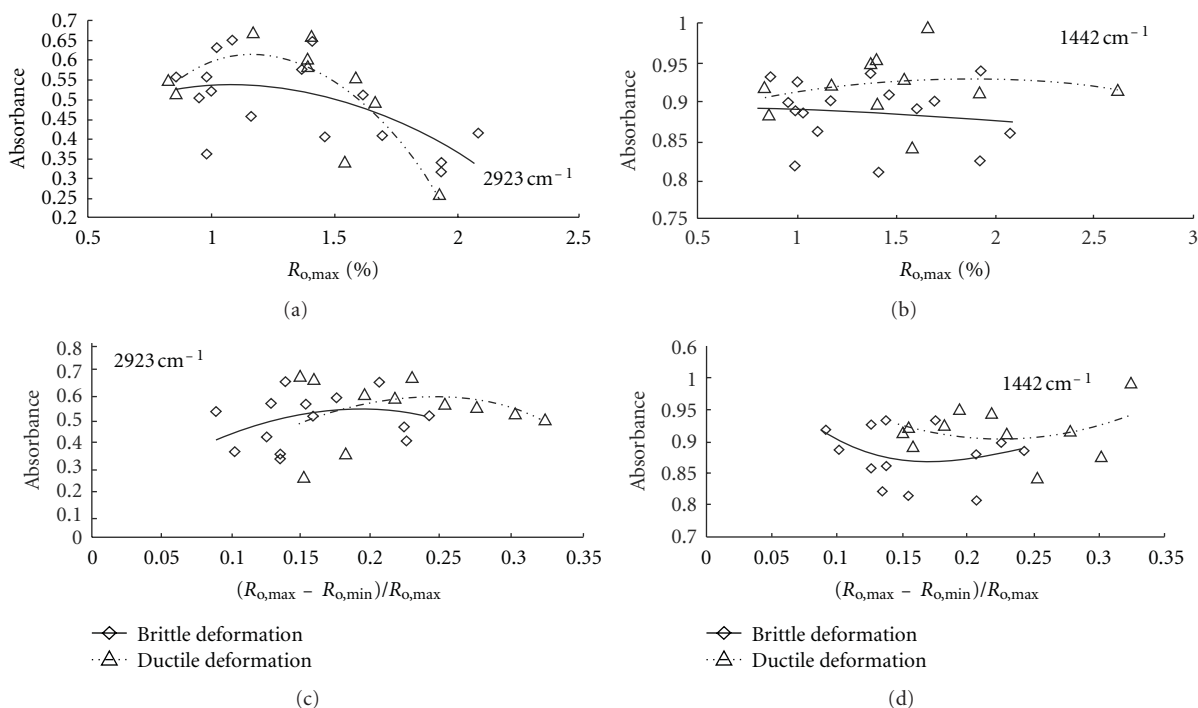


FIGURE 3: Relationship of aliphatic absorbance peaks of TDC with metamorphic and deformation stages. (a) and (b) relationship between aliphatic absorbance peaks and metamorphic stages. (c) and (d) relationship between aliphatic absorbance peaks and deformation stages.

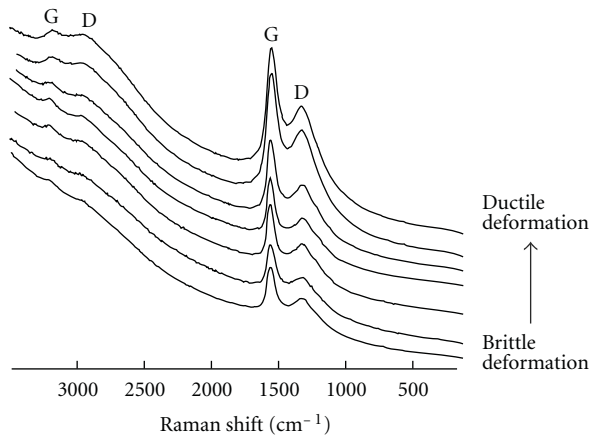


FIGURE 4: The Raman spectrum of TDC with different deformation mechanisms (from [22]).

molecules are combined to aromatic rings and increase the absorption strength of aromatic structure.

3.2. The Raman Spectral Analysis. Nakamizo studied the grinded graphite and graphitized coke applying Raman spectrum and found that the peak G in Raman spectrum is related to the deformation vibration of C=C on aromatic plane; the peak area of G (A_G) stands for the total number of aromatic rings [24, 25]. The grinding process could form structure defects. It is also suggested that secondary structural defects are produced by exogenic action like grinding process. Previous researchers suggested that the tectonic shear stress process and the grinding process were similar under the geological environment; both could generate secondary structural defects in coal graphite [26].

3.2.1. Evolution of the Peak Area of G (A_G). Two peaks (G and D) are observed in Raman spectrum in TDC samples from Huainan-HuaiBei coal field, which are in the range from 1590 cm^{-1} to 1600 cm^{-1} and the range from 1340 cm^{-1} to 1356 cm^{-1} , respectively (Figure 4).

Peak G in Raman spectrum is related to the deformational vibration of C=C on aromatic plane; A_G means peak area of G, the total number of aromatic rings [22, 26]. With the increase of metamorphic grade, for brittle deformational coal, the values of A_G increase but change gently like a convex curve in ductile deformational coal which is always higher than the values in brittle deformational coal (Figure 5(a)). It is indicated that the total number of aromatic rings increase in brittle deformational coal, but increase first and decrease later in ductile deformational coal when metamorphic grade increases. The FTIR data show that the change of total aromatic rings are relatively slight, but the absorption strength of every frequency band is changed which means that the undulatory property on the whole aromatic structure is caused by fracture, abscission, and cyclization of aliphatic structure in macromolecular structure of coal. With the increase of deformational intensity, the value of A_G increases in brittle deformational coal, but

first decreases and then increases in ductile deformational coal (Figure 5). The total number of aromatic rings formed in brittle deformational coal are relatively less than in ductile deformational coal. It is indicated that the ductile deformation played a more important role in the process of polycondensation in macromolecular structure of coal.

3.2.2. Evolution of the Peak Area of D (A_D). The Peak D is related to the lattice vibration of irregular hexagon in disordered sp^2 carbonaceous material connected with secondary structural defects between molecular structures [22, 25, 26]. A_D refers to peak area of D and reflects the change of secondary structural defects in the macromolecular structure and the degree of structure order. With the increase of metamorphic grade, the change of A_D is the same as A_G . The values of A_D increase in brittle deformational coal, but increase first and then decrease in ductile deformational coal (Figure 6(a)).

Previous research discussed that there were two types in D peak of Raman spectrum; the first one is induced by defects of primary structures (1370 cm^{-1}), and the other is induced by secondary structural defects (1360 cm^{-1}) which are also related to tectonic stress [26]. The peak D in Huaibei TDC samples is all distributed at 1360 cm^{-1} , indicating that the secondary structural defects generated by tectonic stress exist in TDC. With the increase of metamorphic grade, the secondary structural defects increase rapidly in brittle deformational coal, but increase prior to decrease in ductile deformational coal.

With the increase of deformational intensity, the value of A_D increases in brittle deformational coal, but decreases prior to increases in ductile deformational coal (Figure 6(b)). It is suggested that with the increase of deformational intensity, the secondary structural defects increase in brittle deformational coal, but decrease first and then increase in ductile deformational coal. However, the secondary structural defects in brittle deformational coal are always fewer than in ductile deformational coal. The increasing and accumulating of unit dislocation may transform the stress into strain energy in ductile deformational coal [19, 20, 22, 27], which is easier to generate the secondary structural defects in macromolecular structure of TDC.

4. Discussion

Compared with primary structure coal [2–7, 16, 17, 23, 25, 26], the difference of macromolecular structure shown by FTIR and Raman data of TDC is obvious with the increase of metamorphic grade. Ju et al. studied the different metamorphism-deformation environments and ultrastructure of various TDC using XRD and Nuclear magnetic resonance methods and observed the ultrastructure directly by High-resolution transmission electron microscope [28, 29]. The results reveal that the temperature and tectonic deformation could affect the metamorphism-deformation environment as shown by the change of the stacking of the basal structural units (BSU) layer L_c and the ratio of extension and stacking of the BSU layer L_a/L_c . Under the effect

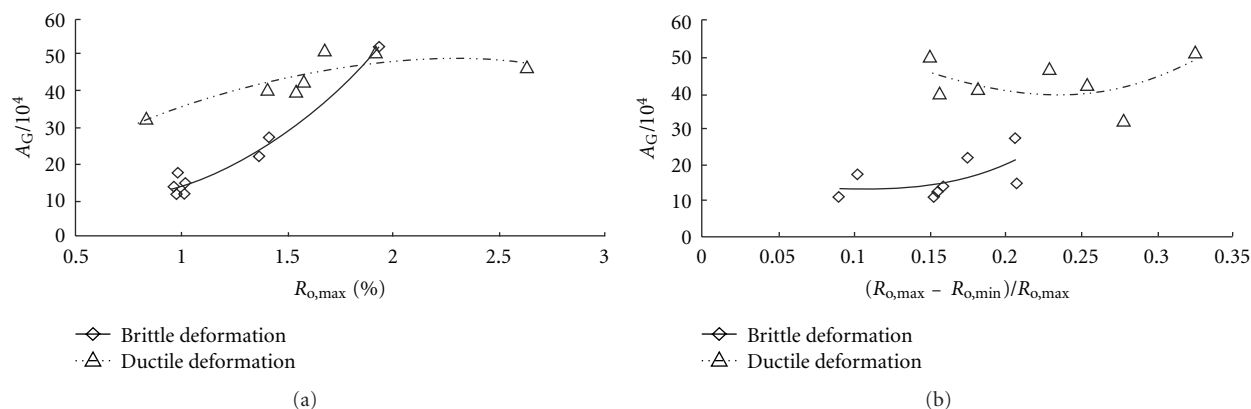


FIGURE 5: Relationship of A_G of TDC with their metamorphic and deformation stages: (a) relationship between A_G and metamorphic stages, (b) relationship between A_G and deformation stages.

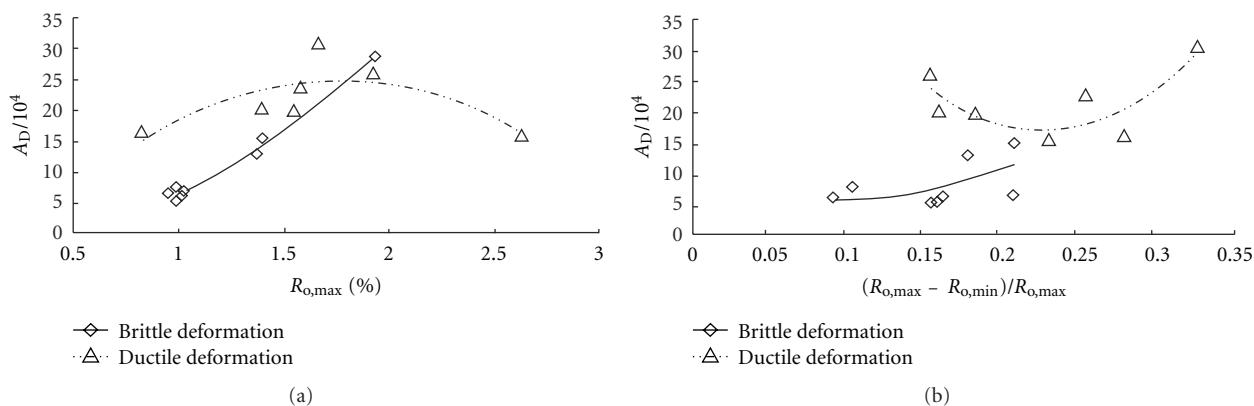


FIGURE 6: Relationship of A_D of TDC with their metamorphic and deformation stages: (a) relationship between A_D and metamorphic stages, (b) relationship between A_D and deformation stages.

of oriented stress, the orientation of the macromolecular structure becomes locally stronger, and the ordering degree of C-nets as well as the arrangement of the BSU is obviously enhanced. It is suggested that the temperature is not the only reason that results in carbonification process of coal, but also the tectonic deformation plays a very important role in this process [17, 28].

With the increase of metamorphic grade, the aliphatic structure and functional groups break off, and the aromatic structure is enriched in ductile deformational coal. However, for brittle deformational coal, the increase of aromatic structure is not obvious. It is indicated that the ductile deformation could produce apparent effect on degradation and polycondensation, and the increased metamorphic grade could promote the ductile deformation and the polycondensation process. The brittle deformation can only produce apparent effect on degradation and has little influence on polycondensation. The absorption strength of aromatic structure is developed as complementary to the aliphatic structure and aliphatic bands compared to the absorption peaks of aromatic and aliphatic structure. In lower metamorphic grade, there is much more aliphatic structures in TDC. Because of the fracture, abscission and cyclization of aliphatic

functional groups and alkane branched chains made the aromatic structure increase with the metamorphic grade rise.

With the increase of deformational intensity, the brittle deformation transforms the stress into frictional heat energy [19, 20, 22, 27], increases the kinetic energy, and promotes the degradation. The aliphatic functional groups and alkane branched chains break off first because of the high strain rate, and the residual of them will be transformed into aromatic structure so that the rangeability of aromatic structure in brittle deformation is relatively low. The ductile deformation transforms the stress into strain energy by increasing and accumulating of unit dislocation [19, 20, 22, 27], which promotes the polycondensation. In lower metamorphism stage with degradation as the main reaction, the aliphatic functional groups and alkane branched chains break off by ductile deformation. The dropped small molecules have enough time to form aromatic rings because of the slow strain rate, which results in more and more aromatic structure enrichment in ductile deformational coal.

Raman data show that the D peak of Raman spectrum is observed around 1360 cm^{-1} , indicating that secondary structural defects in TDC samples from Huaibei coal field are induced by tectonic deformation. In lower metamorphic

grade, the increase of the total number of aromatic rings and secondary structural defects are induced by brittle and ductile deformation, whereas by ductile deformation in higher metamorphic grade. This feature suggests that lower metamorphic grade is a benefit to brittle deformation, while the higher metamorphic grade can promote the ductile deformation. The FTIR spectrum shows that the ductile deformation can produce apparent effect on degradation and polycondensation, but brittle deformation exerts little influence on polycondensation. It is observed that degradation is the main reaction for macromolecular structure formation in lower metamorphic grade, instead of polycondensation in higher metamorphic grade. With the increase of deformational intensity, fewer secondary structural defects exist in brittle deformational coal than in ductile deformational coal, indicating that the ductile deformation can produce the secondary structural defects easier than brittle deformation.

To summarize, different deformational mechanisms change the chemical structure and produce the secondary structural defects, which are the main reason for various structure evolution of TDC compared with primary structure coals. Based on the XRD test about those TDC samples we studied early [29], with the increase of deformational intensity, the degradation is the main effect under brittle deformational coal. The brittle deformation can transform stress into frictional heat energy, increase the kinetic energy, and accelerate the movement of molecule (functional group) [19, 27, 29, 30]. The aliphatic functional groups and alkane branched chains break off by brittle deformation and promote the degradation as well, shown by decrease of L_c and L_a . With increasing deformation and accumulating thermal energy, the cyclization and aromatization of aliphatic functional groups increase and form aromatic rings and make the L_c and L_a increase. Meanwhile, for the ductile deformational coal, the aliphatic functional groups, alkane branched chains, and a fraction of aromatic rings break off by ductile deformational in the lower metamorphism stage shown by the decrease of L_c . The accumulating of unit dislocation may transform the stress into strain energy and the slow strain rate [19, 27, 29, 30]; parts of dropped small molecules have enough time to form aromatic rings and make L_a increase. In the higher-middle metamorphism stage, with the polycondensation as the main effect, this promotes more dropped small molecules to form aromatic rings and the polycondensation on the other side. With the increase of ductile deformation and accumulating of unit dislocation, the secondary structural defects are generated in this stage which can reduce the structural stability of TDC. The secondary structural defects make the aliphatic functional groups, alkane branched chains, and a fraction of aromatic rings break off selectively shown by decrease of L_a . With more secondary structural defects and small molecules dropped, these small molecules started to fill into secondary structural defects to stabilize the macromolecular structure. So the dropped small molecules splice and embed preferentially in secondary structural defects or residual aromatic structures and form aromatic rings to make the macromolecular structure of much stability.

5. Conclusions

- (1) With the increase of deformation and metamorphism, the change of FTIR and Raman spectrum shows different ways. The tectonic deformation made a very important role which affects the macromolecular structure of TDC. Different deformational mechanism induced different evolution process of macromolecular structure of TDC. The ductile deformation can produce apparent effect on degradation and polycondensation, but brittle deformation has little influence on polycondensation in lower metamorphic grade. In higher metamorphic grade, polycondensation is the main reaction in macromolecular structure of coal. It means that the degradation is the main effect under brittle deformation and the polycondensation under ductile deformation.
- (2) Tectonic deformation can produce the secondary structural defects in macromolecular structure of TDC. The increase of total number of aromatic rings and secondary structural defects is mainly caused by brittle deformation in lower metamorphic grade, but ductile deformation in higher metamorphic grade. Furthermore, the ductile deformation can produce the secondary structural defects easier than brittle deformation.
- (3) The existence of secondary structural defects reduces the stability of macromolecular structure in TDC. Brittle deformation promotes the degradation and makes the aliphatic functional groups and alkane branched chains break off selectively in lower metamorphic grade. With the increase of deformation and metamorphism, more secondary structural defects are produced and small molecules are dropped; the ductile deformation promotes the polycondensation, so the dropped small molecules splice and embed preferentially in secondary structural defects or residual aromatic structures and form aromatic rings to make the macromolecular structure of much stability.

Acknowledgments

This work is supported by the National Natural Science Foundation of China (Grants nos. 40772135, 40972131, and 41030422), the National Basic Research Program of China (Grants nos. 2009CB219601 and 2006CB202201), and the Strategic Priority Research Program of the Chinese Academy of Sciences (XDA05030100).

References

- [1] J. R. Levine and A. Davis, "The relationship of coal optical fabrics to alleghanian tectonic deformation in the central Appalachian fold-and-thrust belt," *Pennsylvania Geological Society of America Bulletin*, vol. 101, no. 10, pp. 1333–1347, 1989.
- [2] D. Y. Cao, S. R. Zhang, and D. Y. Ren, "The influence of structural deformation on coalification: a case study of

- carboniferous coal measures in the Northern foothills of the dabie orogenic belt," *Geological Review*, vol. 48, no. 3, pp. 313–317, 2002.
- [3] D. J. Zhang and X. F. Xian, "I.R. spectroscopy analysis of the groups in coal macromolecule," *Journal of Chongqing University*, vol. 13, no. 5, pp. 6–7, 1990.
 - [4] X. D. Zhu, Z. B. Zhu, and C. J. Han, "Quantitative determination of oxygen-containing functional groups in coal by FTIR spectroscopy," *Journal of Fuel Chemistry and Technology*, vol. 27, no. 4, pp. 335–339, 1999.
 - [5] J. Ibarra, E. Muñoz, and R. Moliner, "FTIR study of the evolution of coal structure during the coalification process," *Organic Geochemistry*, vol. 24, no. 6-7, pp. 725–735, 1996.
 - [6] Y. W. Ju, B. Jiang, G. L. Wang et al., *Tectonically Deformed Coals: Structure and Physical Properties of Reservoirs*, China University of Mining and Technology Press, Xuzhou, China, 2005.
 - [7] Y. W. Ju, B. Jiang, Q. L. Hou, and G. L. Wang, "FTIR spectroscopic study on the stress effect of compositions of macromolecular structure in tectonically deformed coals," *Spectroscopy and Spectral Analysis*, vol. 25, no. 8, pp. 1216–1220, 2005.
 - [8] J. Jehlička, O. Urban, and J. Pokorný, "Raman spectroscopy of carbon and solid bitumens in sedimentary and metamorphic rocks," *Spectrochimica Acta A*, vol. 59, no. 10, pp. 2341–2352, 2003.
 - [9] C. P. Marshall, E. J. Javaux, A. H. Knoll, and M. R. Walter, "Combined micro-Fourier transform infrared (FTIR) spectroscopy and micro-Raman spectroscopy of proterozoic acritarchs: a new approach to Palaeobiology," *Precambrian Research*, vol. 138, no. 3-4, pp. 208–224, 2005.
 - [10] S. Bernard, O. Beyssac, K. Benzerara, N. Findling, G. Tzvetkov, and G. E. Brown, "XANES, Raman and XRD study of anthracene-based cokes and saccharose-based chars submitted to high-temperature pyrolysis," *Carbon*, vol. 48, no. 9, pp. 2506–2516, 2010.
 - [11] A. Cuesta, P. Dhamelincourt, J. Laureyns, and J. M. D. Tascón, "Comparative performance of X-ray diffraction and Raman microprobe techniques for the study of carbon materials," *Journal of Materials Chemistry*, vol. 8, pp. 2875–2879, 1998.
 - [12] O. Beyssac, L. Bollinger, J. P. Avouac, and B. Goffé, "Thermal metamorphism in the lesser Himalaya of Nepal determined from Raman spectroscopy of carbonaceous material," *Earth and Planetary Science Letters*, vol. 225, no. 1-2, pp. 233–241, 2004.
 - [13] J. Jehlička, O. Urban, and J. Pokorný, "Raman spectroscopy of carbon and solid bitumens in sedimentary and metamorphic rocks," *Spectrochimica Acta A*, vol. 59, no. 10, pp. 2341–2352, 2003.
 - [14] J. Jehlička and C. Beny, "First and second order Raman spectra of natural highly carbonified organic compounds from metamorphic rocks," *Journal of Molecular Structure*, vol. 480-481, pp. 541–545, 1999.
 - [15] O. Urban, J. Jehlička, J. Pokorný, and J. N. Rouzaud, "Influence of laminar flow on preorientation of coal tar pitch structural units: Raman microspectroscopic study," *Spectrochimica Acta A*, vol. 59, no. 10, pp. 2331–2340, 2003.
 - [16] Y. Qin, *Micropetrology and Structural Evolution of High-Rank Coals in P. R. China*, China University of Mining and Technology Press, Xuzhou, China, 1994.
 - [17] Y. W. Ju and X. S. Li, "New research progress on the ultrastructure of tectonically deformed coals," *Progress in Natural Science*, vol. 19, no. 11, pp. 1455–1466, 2009.
 - [18] Y. W. Ju, B. Jiang, Q. L. Hou, and G. L. Wang, "The new structure-genetic classification system in tectonically deformed coals and its geological significance," *Journal of China Coal Society*, vol. 29, no. 5, pp. 513–517, 2004.
 - [19] Y. W. Ju, G. L. Wang, B. Jiang, and Q. Hou, "Microcosmic analysis of ductile shearing zones of coal seams of brittle deformation domain in superficial lithosphere," *Science in China D*, vol. 47, no. 5, pp. 393–404, 2004.
 - [20] Y. W. Ju, H. Lin, X. S. Li et al., "Tectonic deformation and dynamic metamorphism of coal," *Earth Science Frontiers*, vol. 16, no. 1, pp. 158–166, 2009.
 - [21] D. Y. Cao, X. M. Li, and S. R. Zhang, "Influence of tectonic stress on coalification: stress degradation mechanism and stress polycondensation mechanism," *Science in China D*, vol. 50, no. 1, pp. 43–54, 2007.
 - [22] H. Lin, Y. W. Ju, Q. L. Hou et al., "Raman spectra of tectonically deformed coals in brittle and ductile deformation mechanisms and its response to structural components," *Progress in Natural Science*, vol. 19, no. 10, pp. 1117–1125, 2009.
 - [23] D. J. Zhang and X. F. Xian, "The study of the macromolecular structure of coal by FTIR spectroscopy," *Spectroscopy and Spectral Analysis*, vol. 9, no. 3, pp. 17–19, 1989.
 - [24] M. Nakamizo, R. Kammereck, and P. L. Walker Jr., "Laser Raman studies on carbons," *Carbon*, vol. 12, no. 3, pp. 259–267, 1974.
 - [25] M. F. Li, F. G. Zeng, F. H. Qi, and B. L. Sun, "Raman spectroscopic characteristics of different rank coals and the relation with XRD structural parameters," *Spectroscopy and Spectral Analysis*, vol. 29, no. 9, pp. 2446–2449, 2009.
 - [26] Z. Zheng and X. H. Chen, "Raman spectra of coal-based graphite," *Science in China B*, vol. 38, no. 1, pp. 97–106, 1995.
 - [27] Q. L. Hou, J. L. Li, S. Sun et al., "Discovery and mechanism discussion of supergene micro-ductile shear zone," *Chinese Science Bulletin*, vol. 40, no. 10, pp. 824–827, 1995.
 - [28] Y. W. Ju, B. Jiang, Q. L. Hou, G. Wang, and S. Ni, "¹³C NMR spectra of tectonic coals and the effects of stress on structural components," *Science in China D*, vol. 5, no. 9, pp. 847–861, 2005.
 - [29] X. S. Li, Y. W. Ju, Q. L. Hou et al., "Structural response to deformation of the tectonically deformed coal macromolecular," *Acta Geologica Sinica (English Edition)*, In press, 2012.
 - [30] Q. L. Hou and D. L. Zhong, "The deformation and metamorphism in the wuliangshan ductile shear zone in Western Yunnan, China," in *Memoir of Lithospheric Tectonic Evolution Research*, pp. 24–29, Seismology Press, Beijing, China, 1st edition, 1993.

Research Article

Characterization of Coal Reservoirs in Two Major Coal Fields in Northern China: Implications for Coalbed Methane Development

Junjia Fan,^{1,2} Yiwen Ju,³ Quanlin Hou,³ Yudong Wu,⁴ and Xiaoshi Li³

¹ Research Institute of Petroleum Exploration & Development, PetroChina, Beijing 100083, China

² School of Earth and Space Science, Peking University, Beijing 100871, China

³ College of Earth Science, Graduate University of Chinese Academy of Sciences, Beijing 100049, China

⁴ MLR Key Laboratory of Metallogeny and Mineral Assessment, Institute of Mineral Resources, CAGS, Beijing 100037, China

Correspondence should be addressed to Yiwen Ju, juyw03@163.com

Received 12 March 2012; Accepted 2 May 2012

Academic Editor: Hongyuan Zhang

Copyright © 2012 Junjia Fan et al. This is an open access article distributed under the Creative Commons Attribution License, which permits unrestricted use, distribution, and reproduction in any medium, provided the original work is properly cited.

Based on the macroscopic and microscopic observation of coal structure, the vitrinite reflectance analysis, and the mercury injection testing of coal samples collected from Huaibei coalfield and Qinshui basin, the characterization of coal reservoir and its restriction on the development of coalbed methane are studied. The results indicate that coal reservoir in study area can be classified as five types according to the coal metamorphism and deformation degrees, and they are respectively high grade metamorphic and medium deformational to strongly deformational coal (I), high grade metamorphic and comparatively weakly deformational coal (II), medium grade metamorphic and comparatively strongly deformational coal (III), medium grade metamorphic and comparatively weakly deformational coal (IV), and low grade metamorphic and strongly deformational coal (V). Furthermore, the type II and type IV coal reservoirs are favorable for the development of the coalbed methane because of the well absorptive capability and good permeability. Thus, southern part of Qinshui basin and south-central of Huaibei coal field are potential areas for coalbed methane exploration and development.

1. Introduction

Coal is not only a kind of mineral fuel but also the reservoir of coalbed methane (CBM). CBM as an unconventional natural gas has gained much attention from researchers around the world. The exploration and development of CBM in America has commercialized over 20 years, and CBM production has industrialized in Australia and Canada in recent years. Based on the successful exploration and development of CBM in USA, the relevant progresses on CBM exploration and development have been summarized during recent years [1–4]. However, because of distinct difference in geological background and coal reservoir characterization, CBM exploration and development in China had not developed successfully as America.

Coal is a kind of porous medium, and its pore structure not only affects gas content but also restricts permeability and recovery of coalbed methane. Currently, scholars have

studied pore structure of coals and metamorphic deformational environment by using vitrinite reflectance testing, electronic scanning observation, mercury intrusion testing, low-temperature nitrogen adsorption experiment, nuclear magnetic resonance testing, and CT technology, and they have obtained better understanding on pore structure of coal reservoir, coalbed methane accumulation and recovery [2, 5, 6]. However, few scholars combined metamorphism with deformation of coal to discuss pore structure and its restriction on CBM development. In fact, the metamorphism and deformation of coal are affecting coal reservoir property at the same time. Because deformation to some degree can lead to metamorphism, and metamorphism process often accompanied deformation of different degree. Metamorphism and deformation of coal are synthetic processes; they are closely related and mutually interacted. When metamorphism and deformation are allocated reasonably, gas content and permeability of coal reservoir can reach best

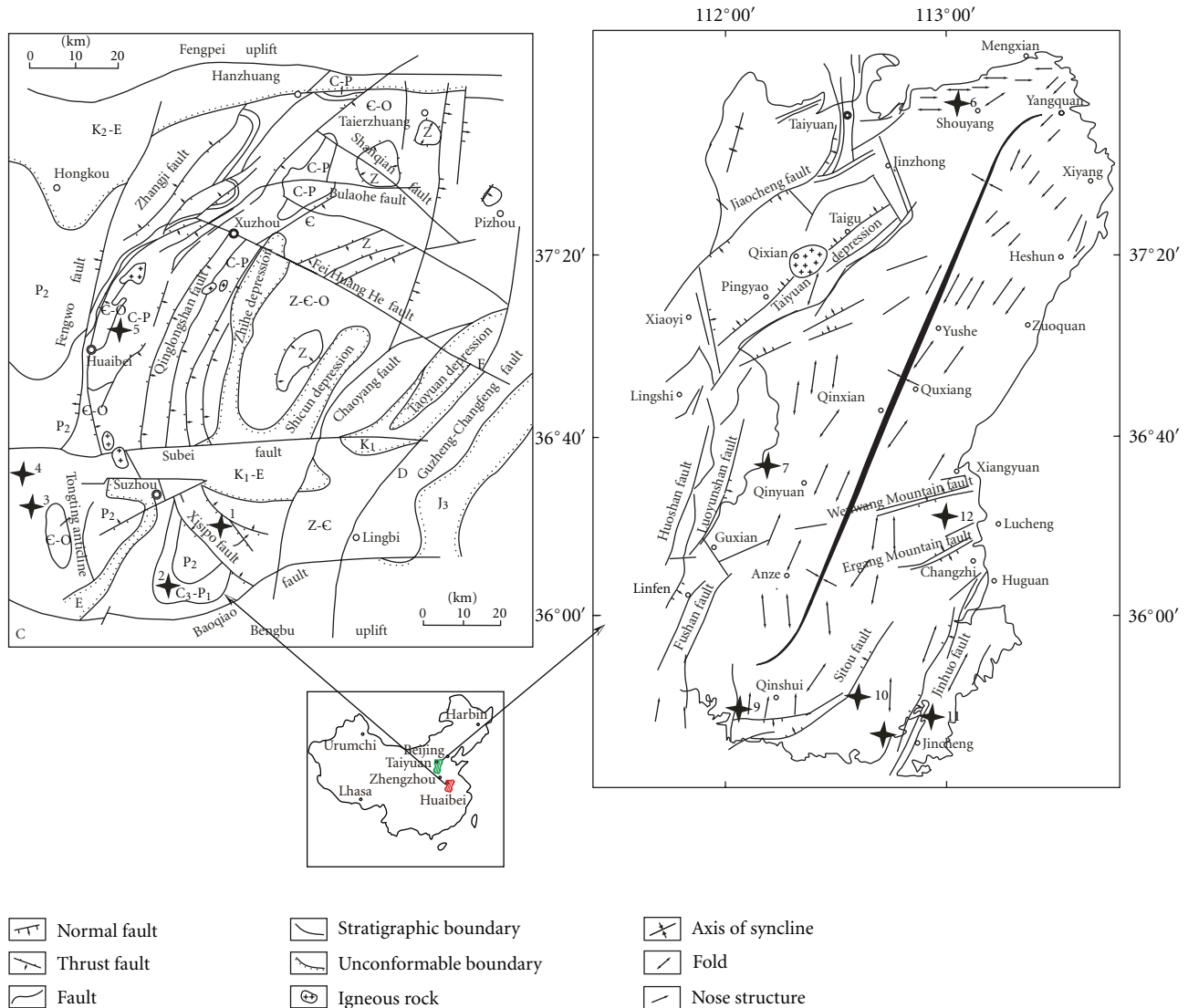


FIGURE 1: Regional geology sketch of Huaibei coalfield and Qinshui basin, and sampling localities (modified from [7–10]) (1) Luling Coalmine; (2) Qinan Coalmine; (3) Linhuan Coalmine; (4) Haizi Coalmine; (5) Shitai Coalmine; (6) Huangdangou; (7) Qinxin Coalmine; (8) Zhangcun Coalmine; (9) Laomufeng Coalmine; (10) Sihe Coalmine; (11) Chengzhuang Coalmine; (12) Wangtaipu Coalmine.

performance and become the favorable coalbed gas reservoir. Better understanding of metamorphism and deformation of coal can get the proper information of coal reservoir, which is of great importance for coalbed methane development. This paper studies metamorphic and deformational characteristics of coal samples collected from Huaibei Coalfield and Qinshui basin and analyzes the pore structures of different coal samples and their restrictions to coalbed methane recovery.

2. Geological Setting

Huaibei coalfield and Qinshui basin are typical coal-bearing and coalbed methane-bearing areas in North China. The Huaibei coalfield is located in the northern Anhui province at the southeastern margin of the North China plate sandwiched between W-E direction developed Fengpei uplift and

Bengbu uplift (Figure 1). The Huaibei coalfield is controlled by two groups of faults, one in the EW direction and formed before Carboniferous-Permian and the other in the NNE-NE direction and formed after the coal measure depositional age. The EW-direction faults mainly include the Banqiao fault and Subei fault. The NNE-NE direction faults mainly involve the Zhangji fault, Qinglongshan fault, and Chaoyang fault. These regional faults are located in the southern, northern, eastern, and western parts, respectively. The Xuzhou-Suzhou thrust fault system is another important structure system, which is located in the northeastern area. The coal seams of this area mainly occurred in the folds, especially in synclines. These folds also can be divided into two groups, one group in the NW direction and another in the NNE-NE direction. The NW-striking folds are including the Luling syncline and Tongting anticline, and the NNE-NE striking folds are including the Shuixiao syncline, Zahe syncline, Sunan

syncline, Sunan anticline, Nanping syncline, Wayang syncline, and Huaigu anticline (Figure 1). The Huaibei coalfield has experienced multistage strong tectonic movements and much magmatic activities since the coal depositional age. It is considered that the most important magmatism happened in Yanshanian and the coalfield was greatly altered during this time. There are distinct differences in magmatic activities among its subareas. The magmatism in the north of the Subei fault is stronger than that in the southern part, and the magmatic rocks change gradually from basic rocks in the east, to intermediate rocks in the central area, and to acid rock in the west.

Qinshui basin, which lies in the eastern part of North China, is a synclinorium striking NE-SW direction along Yushe-Qinxian-Qinshui. To the West, the basin edge is defined by Lüliang Mountain, while the eastern part of the basin is bounded by Taihang Mountain which is uplifting area experienced folding-break uplifting since Mesozoic. The area of Qinshui basin is $3.2 \times 104 \text{ km}^2$ (about 300 km in length and 150 km in width). Compared to surrounding area, tectonics of the Qinshui basin is comparatively weak. The deformation degree weakened from its edge to the inner basin, and in the rim, more thrust faults were developed, which indicates horizontal extrusion. Secondary structures are developed in different area of the basin.

On the whole, tectonic deformation in Huaibei coalfield is comparatively strong, magma hydrothermalism is active, and deformation and metamorphism of coal in this area are intense [11]. Therefore, different coals which indicate the combined effects of tectonism and thermodynamic action are developed. While the Qinshui basin is situated in the transitional area of regional tectonism and deep magma thermology action, where coal reservoir experienced moderate tectonic deformation and distinct magma-thermal action, the metamorphic degree of coal reservoir is strong and the deformational degree is comparatively weak. Consequently, research on the coal samples in these areas is of great significance.

3. Samples and Analytical Methods

This research investigates the metamorphism, deformation, and the pore structure systems of coal samples selected from the Huaibei Coalfield and the Qinshui basin by using macro-microscopic observation, vitrinite reflectance (R_o) measurements, mercury intrusion capillary pressure (MICP) testing, and porosimetry. Furthermore, based on tectonically structural coal (TDC) genetic classification [12], systematic classification of coal samples in study area is proposed.

R_o measurements (oil immersion) are conducted in Material and Physical Laboratory of the China University of Geoscience (Beijing). Firstly, representative coal samples were polished to coal section and observed by using of oil-immersion objective of MPV-3 microphotometer, and then over 50 points are counted for each sample and calculated the even value as the R_o value. Mercury intrusion capillary pressure (MICP) testing was carried out in the Key Laboratory of Natural Gas Development of the Langfang Branch Research Institute, PetroChina. Fresh coal samples were chosen and

conducted by MICP test using autopore 9410 porosimeter, its working pressure is 0.0035 MPa–206.843 MPa, resolution is 0.1 mm^3 , the volume of powder dilatometer is 5.167 cm^3 , and low limit of pore diameter is 7.2 nm.

4. Results

4.1. Metamorphic Characterization of Coal Samples. Metamorphism of coal is a key factor which influences the generation, occurrence, enrichment, and recovery of CBM, and has attracted much attention by scholars for long time [1, 13–15]. Furthermore, deformation of coal also affects porosity of coal and permeability of CBM which restrict effective recovery of CBM; therefore, metamorphism and deformation characterization and their relationship have been the key issue by scholars in recent years [16, 17]. In order to distinguish effect of metamorphism of coal on CBM and its relationship to CBM enrichment and permeability, researchers classified coal into high-rank, medium-rank, and low-rank coal reservoir according to its metamorphic degree [18–20]. Results of R_o measurements show that the R_o values in study area varies from 0.78% to 4.66%. The R_o values of coal samples from the Qinshui basin are comparatively high, and the even value is over 1.5%, while R_o values of coal samples from the Huaibei Coalfield range from 0.8% to 3.0% which indicates coals here have a wide metamorphic range. Based on the previous study [2, 12] according to the metamorphism degree, coals in study area are further divided into high-rank coal ($R_o > 2.0\%$), medium-rank coal ($R_o = 1.3\%–1.9\%$) and low-rank coal ($R_o = 0.5\%–1.2\%$).

4.2. Deformational Characterization of Coal Samples. Macroscopic observation of representative coal samples shows that the difference of deformation degree is distinct in different areas. It is observed that cataclastic structure coal, mortar structure coal, granulitic structure coal, schistose structure coal, scale structure coal, wrinkle structure coal, and mylonitic structure coal are developed in study area (see Figure 2).

In Huaibei Coalfield, the major coal seams of Haizi Coalmine, Linhuan Coalmine, Luling Coalmine and Qinan Coalmine are no. 8 and no. 9 coal seam of the Lower Shihezi formation of middle Permian and no. 10 coal seams of Shanxi formation of Permian, while the major coal seams in Shitai Coalmine are no. 3 coal seams of Upper Shihezi Formation of Middle Permian. In Qinshui basin, the major coal seams are no. 3 coal seams of Shanxi Formation of lower Permian. Borehole observation of coal seams in coal mines and R_o testing of representative samples show that the metamorphic features among different coal samples are obvious. Highly metamorphic and strongly deformational coal seams are featured by wrinkle structure, scaling structure, matrix oriented arranged, and S-C structural fabric; highly metamorphic and comparatively weakly deformational coals are characterized by tension fractures and tension-shear fractures; medium-grade metamorphic and comparatively strongly deformational coals show scaling structure, flowing structure, and S-C structural fabric; tension fracture, shear fracture, and tension-shear fracture are developed

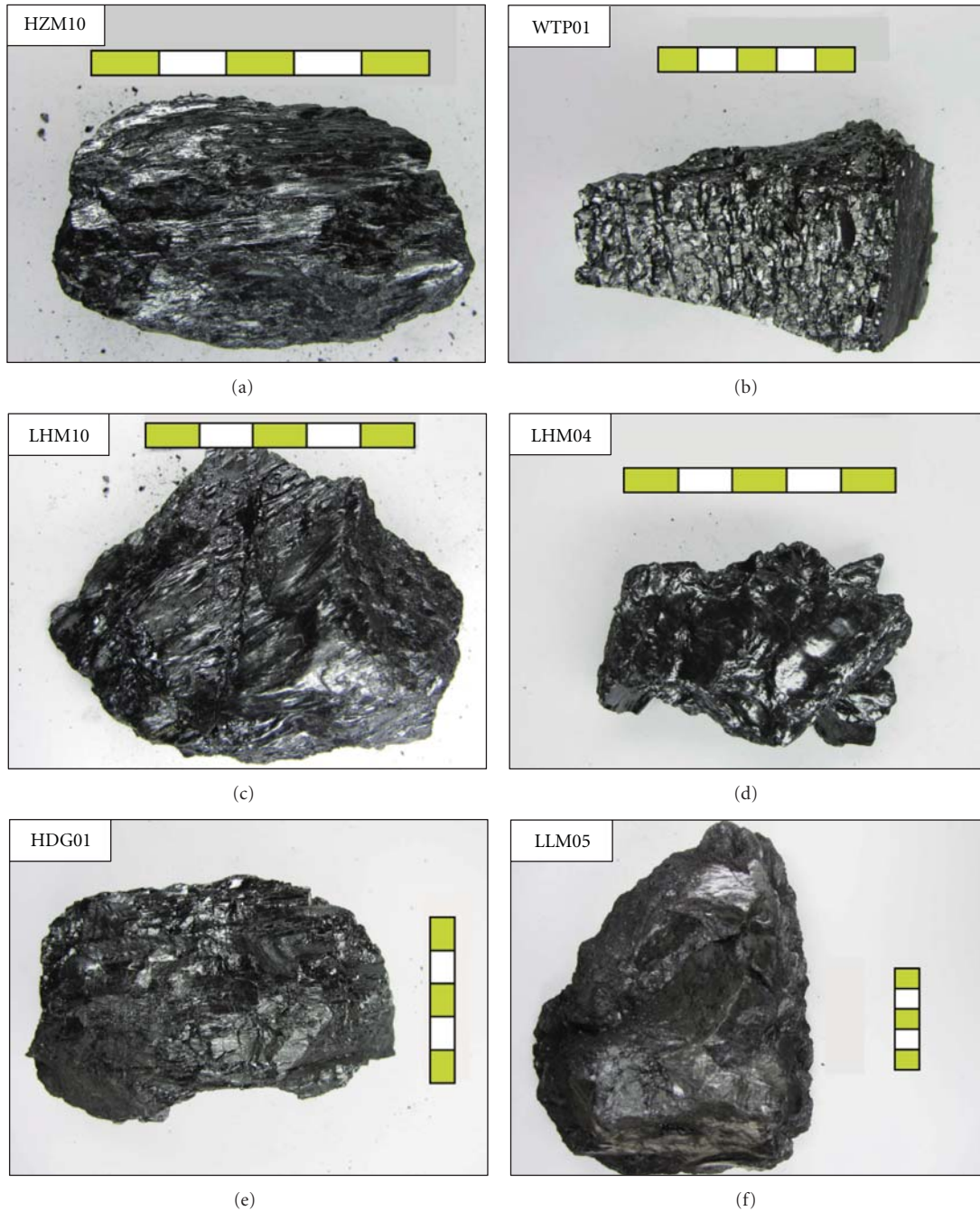


FIGURE 2: Photos of different metamorphic and deformational coals.

in medium-grade metamorphic and comparatively weakly deformational coal reservoirs; low-grade metamorphic and strongly deformational coal reservoir are featured by obvious wrinkle structure, flowing structure, and oriented arranged matrix (see details in Table 1).

In Huaibei coalfield, deformation of coal reservoirs is strong, and wrinkle structure coal and mylonitic structure coal are formed universally, while in Qinshui basin, the whole deformation degree for coal reservoir is comparatively weak and cataclastic structure coal and mortar structure coal are formed. According to deformational degree, coal

samples are divided into strongly deformational coal, comparatively strongly deformational coal, and comparatively weakly deformational coal (see details in Table 1).

4.3. Pore Structure of Coal Samples. Pores of coal samples are further classified as macropores (diameter > 1000 nm), mesopores (diameter > 100 nm), transitional pores (diameter $= 10\text{--}100$ nm), and micropores (diameter < 10 nm) according to the pore classification proposed by the Former Soviet Union scholars [21]. Gas in macropores and mesopores of coal reservoir existed as laminar flow and

TABLE 1: Macro-micro characteristics and different metamorphic-deformational types of coal samples.

Sample	Location	Strata	Coal seams	$R_o/\%$	Metamorphism	Deformation	Coal type	Characterization	Type
HZM08	Haizi(HC)	Lower Shihezi	8	2.62	High	Comparatively strong-strong	WSC	Wrinkle structure, soft coal body	I
HZM10	Haizi(HC)	Lower Shihezi	8	2.62			WSC	Directionally arranged matrix	
LHM05	Linhuang(HC)	Lower Shihezi	9	3.01			SSC	Scaling structure, matrix rotated	
HZ07*	Haizi(HC)	Lower Shihezi	8	2.81			MSC	Wrinkle structure, flowing structure	
LMF01	Laomufeng(QB)	Shanxi	3	2.82			CSC		
WTP01	Wangtaipu(QB)	Shanxi	3	4.66	Comparatively weak-weak		MS	Tension fractures, shear fracture	II
SH02	Sihe(QB)	Shanxi	3	2.93			MS	tension-shear fractures developed	
CZ01	Chengzhuang(QB)	Shanxi	3	3.18			GSC		
LHM10	Linhuang(HC)	Lower Shihezi	9	1.39	Medium	Comparatively strong	SSC	Scaling structure Soft coal body	III
LHM04	Linhuang(HC)	Lower Shihezi	9	1.40			WSC	Wrinkle structure, obvious flowing structures-C structural fabric	
STM03	Shitai(H)	Lower Shihezi	3	1.50			WSC		
LHM09	Linhuang(HC)	Lower Shihezi	9	1.39			WSC		
QX01	Qinxin(QB)	Lower Shihezi	3	1.72			CSC		
HDG01	Huangdangou(QB)	Lower Shihezi	3	1.85	Comparatively weak		MC	Cleats developed, tension fracture, shear fracture, tension-shear fracture	IV
HZM02	Haizi(HC)	Shanxi	10	1.93			MC		
ZC01	Zhangcun(QB)	Shanxi	3	1.72			SC	Fracture developed	
LLM05	Luling(HC)	Lower Shihezi	8	0.86	Low	Strong	MSC	Wrinkle structure, flowing structure, directionally arranged matrix	V
QN09*	Qinan(HC)	Shanxi	10	0.81			MSC		
QN15*	Qinan(HC)	Shanxi	10	0.98			MSC		

CSC: cataclastic structure coal, MC: mortar structure coal, GSC: granulitic structure coal, SC: schistose structure coal, SSC: scaling structure coal, WSC: wrinkle structure coal, MSC: mylonitic structural coal. Location with "HC" represents a coal mine in Huaibei Coalfield, location with "QB" represents a coal mine in Qinshui Basin.

TABLE 2: Analytical results for different metamorphic deformational coal samples by mercury-injecting testing.

No.	Sample	Type	Mercury ejection efficiency/%	Porosity/%	Pore distribution and content		
					<10 ² nm/%	10 ² –10 ³ nm/%	>10 ³ nm/%
1	HZM08	I	38.3	9.2	76.9	14.0	9.1
2	HZM10		53.9	6.9	82.8	10.2	7.0
3	LHM05		51.6	3.0	80.0	11.7	8.3
4	HZ07*		—	10.2	94.9	5.1	0
5	LMF01	II	68.7	2.7	78.8	7.7	13.5
6	WTP01		58.0	7.2	90.0	3.5	6.5
7	SH02		70.0	2.5	70.5	5.9	23.6
8	CZ01		75.0	1.9	94.2	2.6	3.2
9	LHM10	III	59.0	2.2	69.9	11.9	18.2
10	LHM04		44.8	2.7	72.0	11.5	16.5
11	STM03		52.4	2.2	55.8	2.7	30.5
12	LHM09		29.9	4.9	60.5	15.5	34.0
13	QX01	IV	66.5	2.7	76.3	10.2	13.5
14	HDG01		48.9	4.6	77.7	6.5	15.8
15	HZM02		49.8	2.5	69.0	13.0	18.0
16	ZC01		49.9	7.1	63.6	9.6	26.8
17	LLM05	V	32.6	9.0	45.6	30.7	23.7
18	QN09*		—	4.0	40	51.9	8.1
19	QN15*		—	3.8	54	39.4	6.6

Note: data with * after Ju [1].

steady-flow form, while gas in micropores of coal reservoir existed as diffusive and adsorbed form. Therefore, pores with diameters larger than 100 nm are favorable for permeability improvement, while pores with diameters less than 100 nm are advantageous to CBM adsorption; we named this kind of pores as adsorption pore. Transitional pores and micropores provide main accumulation space for CBM, and macropores mainly affect the desorption and recovery of CBM. See the results of mercury injection testing in Table 2.

5. Discussion

Metamorphism and deformation are closely related to the evolution of coal reservoir; different metamorphism of coal may cause different deformation, while the deformation of coal to some extent can bring about metamorphism. Previous research indicates that pore structure, gas adsorption, and permeability varied with coal metamorphism. In addition, coal reservoir property and CBM content changed with coal deformation [9, 15, 22].

Based on coal borehole and macro-microscopic observation of representative coal samples, coal reservoirs in study area are divided into five types (see Table 1): high-grade metamorphic and medium deformational to strongly deformational coal (I), high-grade metamorphic and comparatively weakly deformational coal (II), medium-grade metamorphic and comparatively strongly deformational coal (III), medium-grade metamorphic and comparatively weakly deformational coal (IV), and low-grade metamorphic and strongly deformational coal (V). Results indicate that

porosity and pore structure coal vary with coal metamorphism and deformation.

5.1. Pore Structure Characterization of Different Metamorphic and Deformational Coal Reservoirs. Pore structure, pore distribution of different diameters, and pore connectivity are illustrated by using porosimetry and mercury injection testing (see Figure 3). Porosity of coal samples varies from 1.9% to 10.2% which shows distinct change in different metamorphic and deformational coal reservoirs. The median porosity is between 4.5% and 5%. For the Type I coal reservoir the mean porosity is 7.3%, the mean porosity of type II coal reservoir is 3.6%, mean porosity of type III coal reservoir is 3.0%, mean porosity type IV coal reservoir is 4.3%, and mean porosity of type V coal reservoir is 5.6%. Previous research proposed that porosity increased with R_o value when R_o varied from 0.88% to 4.6% [15, 23]; however, this regulation in our study is not obvious, especially for low-grade metamorphism and strong deformational coal reservoirs which have comparatively high porosity. This can be explained by strongly deformation of coal which changed the pore structures of coal reservoir. For coal reservoir, the porosity of about 7% is favorable for CBM accumulation and development [24]. Nevertheless, porosity of coal in the study area is low; this is inherent shortage for high-rank coal. Therefore, as far as porosity of coal is concerned, type I and type V coal reservoirs are advantageous for CBM development, type II and type IV coal reservoirs are moderate, and type III reservoir is not favorable.

The results of mercury injection testing of representative coal samples show that pore structure changed distinctly

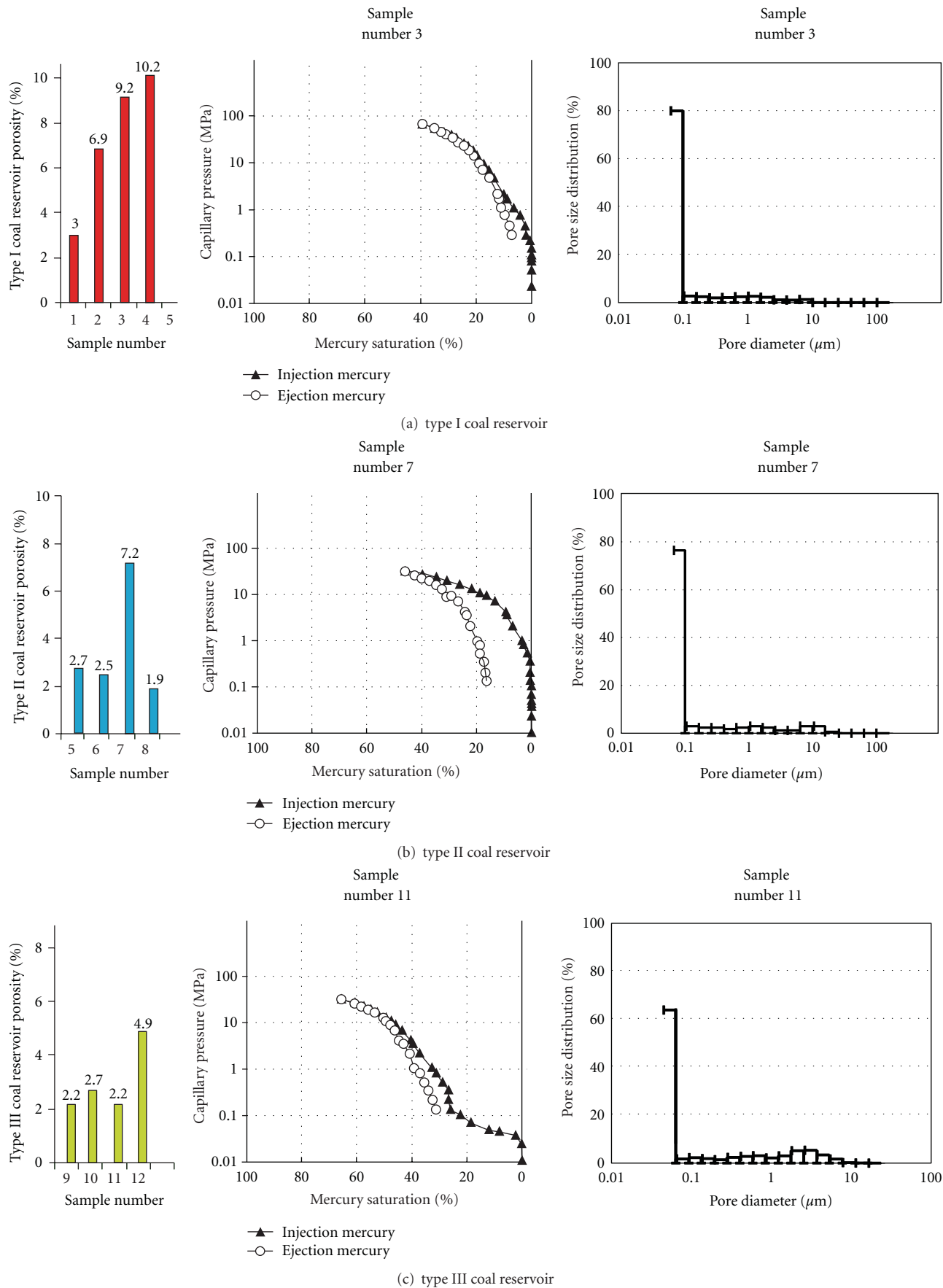


FIGURE 3: Continued.

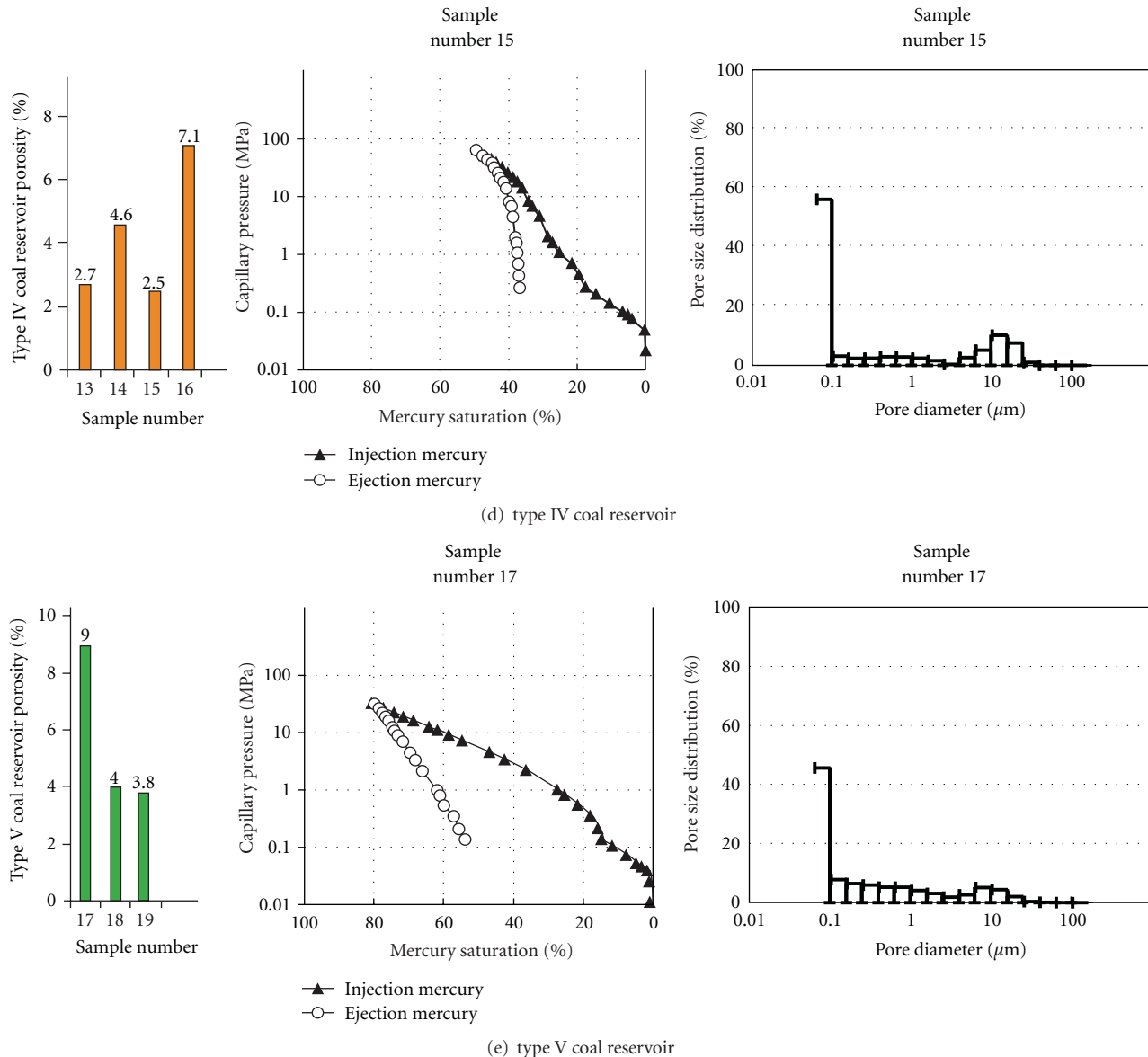


FIGURE 3: Porosity and mercury injection curves of different metamorphic-deformational coals in study area.

with the variation of metamorphism and deformation. The ejection efficiency of coal samples varies from 29.9% to 75%, and the mean mercury ejection efficiency of type I coal reservoir is 47.9%, mean mercury ejection efficiency of type II coal reservoir is 67.9%, the type III is 46.5%, that of type IV is 53.8%, and that of the last type is 32.6%. Generally, the higher the ejection efficiency, the better the pore connectivity. It is indicated that type II and type IV reservoirs, which have connected pore system and better gas permeability, have better pore connectivity. For high-grade metamorphic coal, micropores are major pores and macropores and mesopores are less. Thus, gas permeability of this type of coal reservoir is generally low. Type I reservoir is characterized by worse pore connectivity and low permeability. While pore connectivity of type II reservoir is better, it has favorable permeability which is resulted from existence of a great deal of fracture

generated with deformation of coal reservoir. The mercury ejection efficiency of type III coal reservoir is low, and pore connectivity is worse which may result from strong metamorphism of coal. Mercury ejection efficiency of type IV reservoir is higher, which is contributed by a number of cleats in coal and superimposed fractures generated by deformation. Type V reservoir's pore connectivity is worse which mainly resulted from strong deformation.

On the whole, for type I coal reservoir, the pore content with diameter less than 100 nm accounts for 80% and the mercury injection curves and ejection curves show that the pore connectivity is poor. Type II coal reservoir has lower percentage of pore with diameter less than 100 nm, but the pore connectivity is better. Type III coal reservoir, although the percentage of pore with diameter is high (>100 nm), the pore connectivity is not so good. For type IV coal reservoir,

percentage of the pore diameter is higher (>1000 nm) and the pore connectivity is becoming favorable. The last type coal reservoir, with the percent of pore diameter primarily between 100 and 1000 nm, is greater than other types, but the pore connectivity is poor.

5.2. Pore Structure and Fracture and Their Restrictions to CBM Recovery. Gas content, permeability, strata pressure, and burial depth are significant parameters for prediction of coalbed methane recovery. However, the metamorphism and deformation of coal and their restrictions on CBM recovery have not gained considerable attention [14]. In general, gas content and permeability are various in different types and brittle deformation can improve gas adsorption content [15]. Nevertheless, strongly deformation will affect the CBM permeability. On the coal metamorphism aspect, gas content increases with metamorphism, which is favorable for CBM accumulation; however, macropore content decreases with the increase of metamorphism, which is disadvantageous for CBM seepage. Exploration and development of CBM proved that CBM recovery is affected by numerous factors. Qinshui basin is located in transitional zone affected by tectonism and deep magma activity. Deformation of coal reservoirs in Qinshui basin is weak, and metamorphics of coal reservoirs are high. Tectonic deformation is strong in Huaibei Coalfield, and magma thermal activity is active; thus, different metamorphic coal reservoirs developed, and their flowing structure, wrinkle structure, is universal.

Affected by tectonism and magma activity, pore structure of different types of coal reservoir is varying. Type I coal reservoir is dominated by adsorption pore, which indicates that this kind of coal has better gas adsorptive capacity. Its ejection mercury curve shows worse pore connectivity, and the permeability is low, which is disadvantageous for CBM desorption. Metamorphic grade of type II reservoir is high, its dominating pores are micropores, and coal reservoir experienced some extent deformation generated numerous fractures; therefore, reservoirs have large gas accumulation space and better permeability, which contribute to CBM development. Gas adsorptive capacity of type III coal reservoir is favorable; however, strong deformation results in decrease of pore connectivity which is unfavorable for CBM seepage. For type IV coal reservoir, numerous cleats in coal and superimposed tectonic fractures contribute to permeability improvement. For type V coal reservoir, although its dominating pores are micropores, the pore connectivity is worse; this is unfavorable for CBM desorption.

In summary, type II coal reservoir has strong gas adsorptive capacity and superimposed some extent structural deformation which generated numerous fractures, and its pore connectivity becomes well, so CBM recovery is good. Type IV coal reservoir has a great deal of cleats, better pore connectivity, and strong gas adsorption capacity; thus, CBM recovery in this kind of reservoir is favorable.

6. Conclusion

Based on coal mine investigation of two major coalfields in northern China, combined with macro-microscopic

observation and laboratory testing and analysis of representative samples, some conclusions can be drawn as follows.

(I) Coal reservoir in study area can be classified into five types according to the coal metamorphism and deformation degrees, which, respectively, are high-grade metamorphic and medium deformational to strongly deformational coal (I), high-grade metamorphic and comparatively weakly deformational coal (II), medium-grade metamorphic and comparatively strongly deformational coal (III), medium-grade metamorphic and comparatively weakly deformational coal (IV), and low-grade metamorphic and strongly deformational coal (V).

(II) Pore structure of different metamorphic and deformation coal reservoirs featured by the following characterization: for type I reservoir and type II reservoir, their major pore are micropores; however, type I coal reservoir has poor pore connectivity, and type II coal reservoir has favorable pore connectivity; type III coal reservoir has less micropores compared to type I and type II pore reservoir, and its pore connectivity is worse; therefore, it is not favorable reservoir for CBM development. Type IV coal reservoir has higher micropore content and numerous cleats, and its pore connectivity is better; therefore, it is advantageous for CBM seepage. Type V coal reservoir has lower micropore contents and comparative mesopore content, but pore connectivity is worse, so it is unfavorable for CBM permeability.

(III) The reservoirs characterized by moderate metamorphism with weak deformation and superimposed tectonic fractures also have strong adsorptive capacity and favorable permeability which are advantageous for the development of CBM.

Acknowledgments

This work is supported by the National Basic Research Program of China (also called 973 Program) (Grant nos. 2009CB219601), the National Natural Science Foundation of China (Grant nos. 40972131, 41030422, 40772135), National Science and Technology Major Project of China (Grant nos. 2011ZX05060005; 2011ZX05039-004; 2009ZX05039-003), and the Strategic Priority Research Program of the Chinese Academy of Sciences (XDA05030100). The authors sincerely thank two anonymous reviewers for their kind comments and useful suggestions.

References

- [1] Y. W. Ju, B. Jiang, G. L. Wang et al., *Tectonic Coals: Structures and Physical Properties of Reservoirs*, China University of Mining and Technology, Xuzhou, China, 2005.
- [2] H. Zhang, X. Y. Li, Q. Hao et al., *Study on Scan Electron Microscope of China Coal*, Geological Publishing House, Beijing, China, 2003.
- [3] Y. Ju, B. Jiang, Q. Hou, and G. Wang, "Relationship between nano-scale deformation of coal structure and metamorphic-deformed environments," *Chinese Science Bulletin*, vol. 50, no. 16, pp. 1784–1795, 2005.
- [4] W. Sun, C. Shi, J. Zhao, and L. Zhao, "Application of X-CT scanned image technique in the research of micro-pore texture

- and percolation mechanism in ultra-permeable oil field—taking an example from Chang 82 formation in the Xifeng oil field,” *Acta Geologica Sinica*, vol. 80, no. 5, pp. 775–779, 2006.
- [5] Y. Ju, B. Jiang, Q. Hou, Y. Tan, G. Wang, and W. Xiao, “Behavior and mechanism of the adsorption/desorption of tectonically deformed coals,” *Chinese Science Bulletin*, vol. 54, no. 1, pp. 88–94, 2009.
 - [6] J. C. Quick and D. E. Tabet, “Suppressed vitrinite reflectance in the Ferron coalbed gas fairway, central Utah: possible influence of overpressure,” *International Journal of Coal Geology*, vol. 56, no. 1–2, pp. 49–67, 2003.
 - [7] S. F. Han, *Geological Condition and Prediction of Coal Accumulation in Huainan and Huaibei Coalfields*, Geological Publishing House, Beijing, China, 1990.
 - [8] G. L. Wang, D. Y. Cao, and B. Jiang, *The Thrust and Nappe Tectonics and Gravitational Sliding Structure in Southern North China*, China University of Mining and Technology, Xuzhou, China, 1992.
 - [9] Y. Ju, B. Jiang, Q. Hou, G. Wang, and A. Fang, “Structural evolution of nano-scale pores of tectonic coals in southern North China and its mechanism,” *Acta Geologica Sinica*, vol. 79, no. 2, pp. 269–285, 2005.
 - [10] G. L. Wang, Y. W. Ju, M. L. Zheng et al., *Tectonics of Energy Resource Basins in the Northern China*, China University of Mining and Technology, Xuzhou, China, 2007.
 - [11] Y. W. Ju, J. J. Fan, J. Q. Tan et al., “Basin-mountain evolution, lithosphere transformation and their relationship with coalbed methane accumulation in North China,” *Coal Geology of China*, vol. 21, no. 3, pp. 1–5, 2009 (Chinese).
 - [12] Y. W. Ju, B. Jiang, Q. L. Hou, and G. L. Wang, “New structure-genetic classification system in tectonically deformed coals and its geological significance,” *Journal of the China Coal Society*, vol. 29, no. 5, pp. 513–517, 2004.
 - [13] R. M. Bustin and C. R. Clarkson, “Geological controls on coalbed methane reservoir capacity and gas content,” *International Journal of Coal Geology*, vol. 38, no. 1–2, pp. 3–26, 1998.
 - [14] P. H. Zhang, “Key parameters of coal reservoir related to coalbed methane recovery of China,” *Natural Gas Geoscience*, vol. 18, no. 6, pp. 880–884, 2007 (Chinese).
 - [15] C. S. Zhu, “The relationship between coal porosity and coal rank,” *Coal Geology & Exploration*, no. 5, pp. 29–33, 1986 (Chinese).
 - [16] H. Li and Y. Ogawa, “Pore structure of sheared coals and related coalbed methane,” *Environmental Geology*, vol. 40, no. 11–12, pp. 1455–1461, 2001.
 - [17] J. Q. Shi, S. Durucan, and I. C. Sinka, “Key parameters controlling coalbed methane cavity well performance,” *International Journal of Coal Geology*, vol. 49, no. 1, pp. 19–31, 2002.
 - [18] C. Laxminarayana and P. J. Crosdale, “Role of coal type and rank on methane sorption characteristics of Bowen Basin, Australia coals,” *International Journal of Coal Geology*, vol. 40, no. 4, pp. 309–325, 1999.
 - [19] C. R. Clarkson and R. M. Bustin, “Effect of pore structure and gas pressure upon the transport properties of coal: a laboratory and modeling study. 1. Isotherms and pore volume distributions,” *Fuel*, vol. 78, no. 11, pp. 1333–1344, 1999.
 - [20] L. R. Radovic, V. C. Menon, C. A. Leon et al., “On the porous structure of coals: evidence for an interconnected but constricted micropore system and implications for coalbed methane recovery,” *Adsorption*, vol. 3, no. 3, pp. 221–232, 1997.
 - [21] B. B. Hodot, *Coal and Gas Outbursts*, China Publishing House of Industry, Beijing, China, 1966, Translated by S. Z. Song, Y. A. Wang.
 - [22] X. Su, L. Zhang, and X. Lin, “Influence of coal rank on coal adsorption capacity,” *Natural Gas Industry*, vol. 25, no. 1, pp. 19–21, 2005 (Chinese).
 - [23] Q. L. Zhang, Q. Zhang, H. Zhang et al., “Adsorption characteristics of different rank coals in different area, China,” *Coal Geology & Exploration*, vol. 2, no. z1, pp. 68–72, 2004 (Chinese).
 - [24] Y. B. Yao and D. M. Liu, “Developing features of fissure system in Henan coal reserves seams and research on mining of coal bed methane,” *Coal Science and Technology*, vol. 4, no. 3, pp. 64–68, 2006.

Research Article

Total Scanning Fluorescence Characteristics of Coals and Implication to Coal Rank Evaluation

Junjia Fan,^{1,2} Keyu Liu,¹ Yiwen Ju,³ Shaobo Liu,¹ and Lili Gui¹

¹ Research Institute of Petroleum Exploration & Development, PetroChina, Beijing 100083, China

² The School of Earth and Space Science, Peking University, Beijing 100871, China

³ College of Earth Science, Graduate University of Chinese Academy of Sciences, Chinese Academy of Sciences, Beijing 100049, China

Correspondence should be addressed to Yiwen Ju, juyw03@163.com

Received 15 March 2012; Accepted 22 April 2012

Academic Editor: Yu-Dong Wu

Copyright © 2012 Junjia Fan et al. This is an open access article distributed under the Creative Commons Attribution License, which permits unrestricted use, distribution, and reproduction in any medium, provided the original work is properly cited.

Total Scanning Fluorescence (TSF), as a kind of new fluorescence technique, has great significance and wide application in identifying hydrocarbon inclusions of reservoirs, hydrocarbon migration pathways and palaeo-current oil-water interfaces. Total scanning fluorescence (TSF) is characterized by high efficiency, requiring low sample amount and high accuracy. Vitrinite reflectance (R_o) is one of significant parameters for determining coal ranks, it cannot only reflect coalification features, but also provide a favorable indicator for coal ranks. In order to establish a relationship between vitrinite reflectance (R_o) and the characteristic parameters derived from total scanning fluorescence (TSF), fourteen coal samples (coal powder without separating macerals) collected from Qinshui basin and Huaibei coalfield are tested by TSF technique and vitrinite reflectance (oil immersion), respectively. It shows that TSF parameters are related to vitrinite reflectance value, although TSF parameters and fluorescence intensity of coals differ in Qinshui basin and Huaibei coalfield. Research indicates that more factors should be taken into consideration for coal sample TSF testing in the future so as to obtain an empirical formula relationship between R_o and TSF parameters.

1. Introduction to Total Scanning Fluorescence (TSF) Technique

Fluorescence spectroscopy is a technique that has had wide application in characterizing hydrocarbon mixtures. Ultraviolet (UV) fluorescence is inherently more selective for aromatic compounds than conventional absorption measurements and at least an order of magnitude more sensitive. Fluorescence methods are particularly useful for the detection and measurement of organic compounds containing one or more aromatic functional groups. Since all oils contain a significant amount of aromatic compounds, with one to four (or more) aromatic rings and their alkylated analogues, oils exhibit distinctive fluorescence “fingerprints.” These “fingerprints,” used in conjunction with other analyses, can provide significant information for typing oils, shale extracts, and sea bottom sediment extracts [1]. Fluorescence analysis technique is significant in identifying hydrocarbon inclusion,

hydrocarbon migration pathway, and palaeocurrent water-oil interface [2–4]. It includes three items, quantitative grain fluorescence (QGF), quantitative grain fluorescence-extract (QGF-E), and total scanning fluorescence (TSF). TSF technique is used in this study. TSF which developed from 1980s, was used to test aromatic hydrocarbon and concentration. This method of obtaining three-dimensional fluorescence data is scanning emission spectra continuously at different excitation wavelength, then plotting fluorescence “fingerprints” in the form of Ex-Em contour or Ex-Em-IF contour using Surfer software.

Conventional fluorescence analyses are traditionally used fixed emission/excitation wavelengths or fluorescence emission spectra (at a fixed excitation wavelength) to characterize aromatic mixtures qualitatively and quantitatively. Fixed wavelength and synchronous scanning fluorescence suffer from nonselectivity and are generally ineffective in structural elucidation of mixtures. Despite the ability to select both the

TABLE 1: Laboratory procedure to clean coal for TSF analysis.

Disaggregation	Sample core of cuttings, crushed to powder, dry-sieved to obtain grains with a 1000 to 63 μm size distribution
DCM (dichloromethane)	10-minute ultrasound bath in 20 mL HPLC grade DCM
DCM (dichloromethane)	1-week digestion at room temperature in DCM

TABLE 2: Characteristic parameters derived from TSF experiment.

Sample number	Region	Coal types	R_o (%)	TSF Max	Max Ex (nm)	Max Em (nm)	$R1$	$R2$
(1)	Qinshui basin	Cataclastic structure coal	2.42	706675	308	438	3.1	2.8
(2)	Huaibei coalfield	Mylonitic structural coal	0.86	4577	260	420	5.8	7.5
(3)	Huaibei coalfield	Wrinkle structure coal	1.38	371668	258	363	1.0	1.4
(4)	Huaibei coalfield	Wrinkle structure coal	1.5	18969	314	459	3.1	3.7
(5)	Qinshui basin	Cataclastic structure coal	2.82	11106	302	432	2.7	2.0
(6)	Huaibei coalfield	Cataclastic structure coal	3.01	49325	258	458	5.9	7.0
(7)	Qinshui basin	Mortar structure coal	4.66	681	234	344	1.5	1.3
(8)	Qinshui basin	Cataclastic structure coal	2.93	451	244	409	1.4	1.4
(9)	Qinshui basin	Mortar structure coal	1.69	38229	308	458	2.9	3.1
(10)	Huaibei coalfield	Wrinkle structure coal	2.62	43472	254	369	2.8	3.2
(11)	Qinshui basin	Cataclastic structure coal	1.72	40830	314	469	2.6	2.7
(12)	Huaibei coalfield	Wrinkle structure coal	1.39	9886	258	458	4.9	5.7
(13)	Huaibei coalfield	Scaling structure coal	3.01	1256963	258	423	4.6	5.5
(14)	Huaibei coalfield	Wrinkle structure coal	1.4	563584	258	433	3.7	4.3

excitation and emission wavelengths, conventional fluorescence methods have limited applicability and are difficult to interpret because spectra of complex mixtures cannot be satisfactorily resolved. In an attempt to overcome these problems, a methodology for total scanning fluorescence was developed. A three-dimensional, contour and tabular presentation of the data is possible. Compared with the traditional fluorescence technique, total scanning fluorescence system has several advantages over simpler scanning methods: (1) the acquisition of multiple fluorescence spectra is faster; (2) the amount of fluorescence data per sample is greatly increased; (3) the stored data can be extensively manipulated by computer; (4) individual excitation spectrum can be retrieved from the total fluorescence spectrum and analyzed for the intensity and wavelength of maximum excitation and/or emission fluorescence [5, 6].

Vitrinite reflectance is one of the significant parameters for determine coal ranks. It cannot only reflect coalification degree, but also provide a favorable indicator for coal ranks and oil maturity around the world. It is obvious that R_o is an important part for coal rocks analysis, reservoir evaluation, and hydrocarbon system research. Early in 1960s, Former soviet and America have established national standard for R_o testing, and International Standard Organization published R_o testing standard (draft) in 1980s. So far, there have been at least ten kinds of methods for testing vitrinite reflectance [7]. Most of vitrinite reflectance testing need to microscopic observation and statistics, so the results are always depending on the experiments operators' experiences. With the development of technique, the testing procedures are greatly simplified, and testing time is shortened obviously. However, some subjective factors of testing procedure are inevitable.

This paper analyses the fluorescence characteristics of coal samples and manages to apply TSF technique into coal ranks testing in order to explore a fast, effective, and accurate method to evaluate coal ranks.

2. Samples and Experiments Procedures

Coal samples were collected from coal-bearing region of north China, Qinshui basin and Huaibei coalfield. From the perspective of structural geology, Qinshui basin is situated in the transitional area of regional tectonism and deep thermology action, where coal reservoir experienced moderately tectonic deformation and distinct magma-thermal action, thus the metamorphic degree of coal reservoir is strong and the deformational degree is comparatively weak [8–10]. The tectonic deformation in Huaibei coalfield is comparatively strong, and magma hydrothermalism is active; deformation and metamorphism of coal in this area is strong. Based on the understanding on regional geology, fourteen coal samples are collected.

R_o measurements (oil immersion) and TSF testing are conducted in the key laboratory of basin structure and hydrocarbon accumulation, CNPC. R_o measurements (oil-immersion) are conducted according to following procedures. Firstly, representative coal samples were polished to coal section, and observed by using of oil-immersion objective of DETA V4000 microphotometer, and then over 50 points are counted for each sample, and calculated the even value as the R_o value.

Total scanning fluorescence testing is conducted by Varian Cary-Eclipse of the key laboratory of basin structure and hydrocarbon accumulation, CNPC. Varian Cary-Eclipse

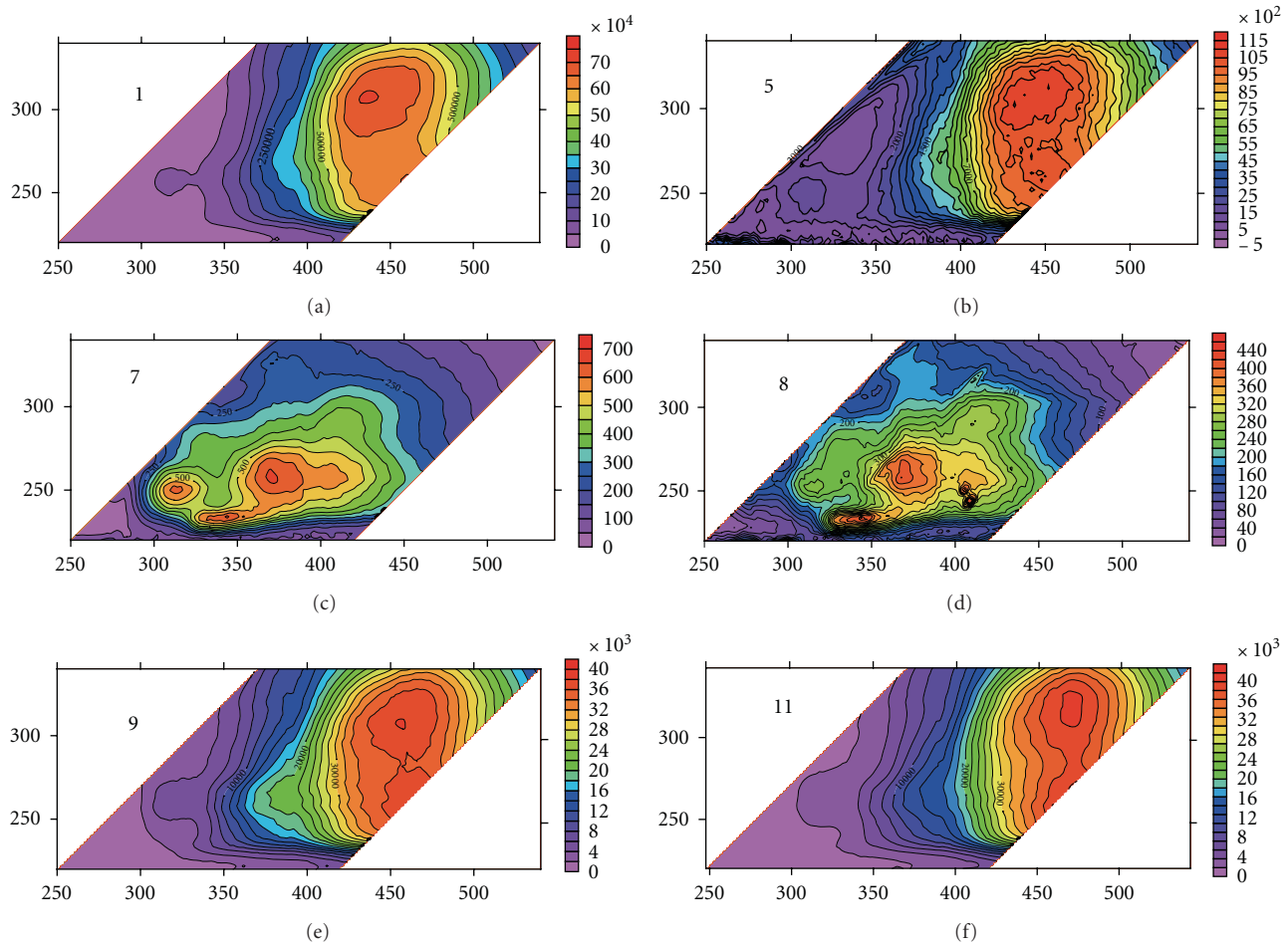


FIGURE 1: TSF hydrocarbon fingerprint map of coal samples in Qinshui basin.

is composed of spectrophotometer, special sample platform, color filter, data collector and QGF, QGF-E, TSF software package. The first step is coal sample crushing, then putting the crushed coal into agate mortar, grinding coal sample into uniform coal powder, then weighing 0.1 g by high-precision electronic balance; put the coal powder into 50 mL beaker, and pour into 10 mL dichloromethane; put the beaker into supersonic bath for 10 minutes; extracting the liquid into a glass bottle and tightly capped, put it in room temperature for a week so as to subside suspended matter of coal powders (see Table 1). Then, set up the experimental parameters, excitation wavelength range is 200–340 nm, and offset is 30 nm. Based on the experimental results, the TSF Max, Max Em, R1 and R2 can be calculated (see Table 2). The excitation and emission monochromators are simultaneously varied with the excitation wavelength offset 30 nm lower than the emission wavelength in synchronous methods.

3. Results and Discussions

The results of vitrinite reflectance testing and TSF analysis are summarized (see Table 1). R_o of coal samples covers a large scope, varying from 0.86–4.66(%). And TSF parameters

are obtained by analysis software, TSF Max is the maximum fluorescence intensity which can reflect the components of different coals; Max Ex represents the maximum excitation (Ex) wavelength; Max Em represents the maximum emission (Em) wavelength; the R1 parameter is a ratio between TSF emission intensity at 360 nm and 320 nm at an excitation wavelength of 270 nm, R2 parameter are the an ratio between TSF emission intensity at 360 nm and 320 nm at a excitation wavelength of 270 nm, R1 and R2 are closely related to the API and maturity. Fingerprints can be obtained by using surfer software (see Figures 1 and 2). The coal samples are characterized by different deformational degrees, they are cataclastic structure coal, mortar structure coal, wrinkle structure coal, scaling structure coal, and mylonitic structural coal, respectively [11, 12].

On the whole, the TSF parameters of coal samples are relevant to vitrinite reflectance values. TSF results show that TSF R1 increases with the decreasing of R_o (this trend is contrary to the variation trend of oil with R_o value from 0.55–2%) (see Figure 3). Ex wavelength of coal samples from Qinshui basin is increasing with TSF parameter R1 distinctly; Ex wavelength of coal samples in Huaibei coalfield is similar; however, the trend is not as distinct as the

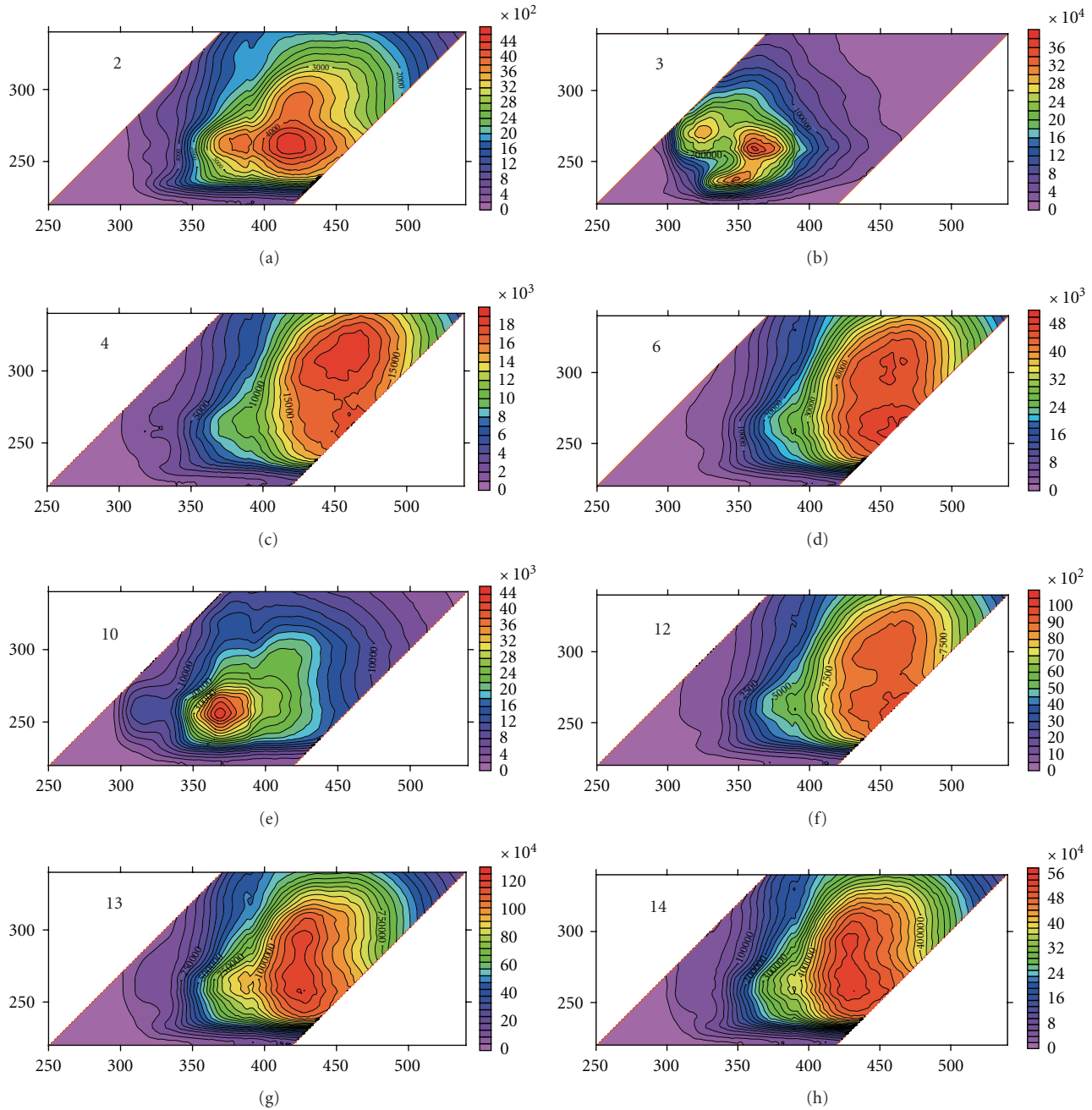


FIGURE 2: TSF hydrocarbon fingerprint map of coal samples in Huaibei coalfield.

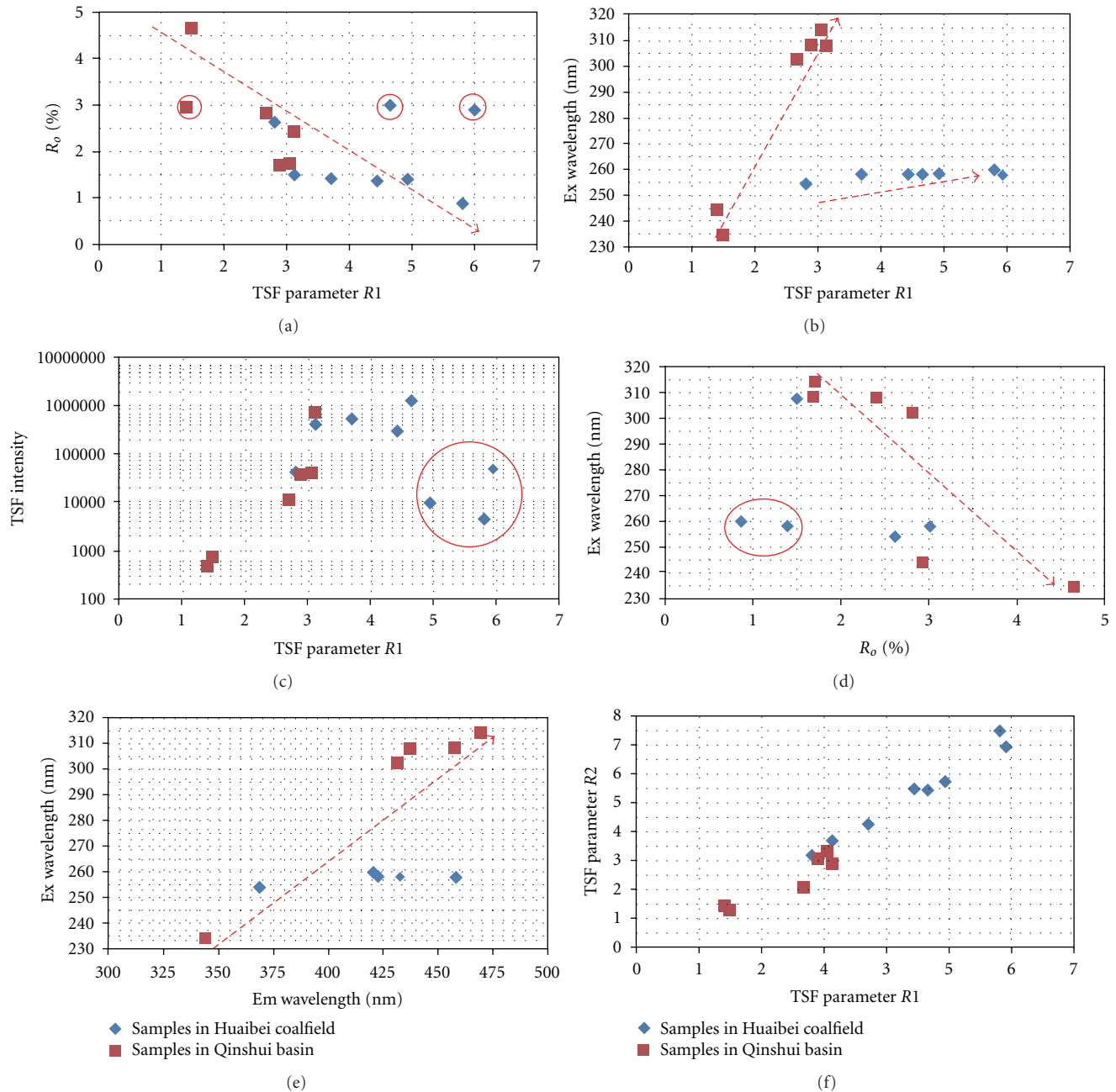
one in Qinshui basin. This indicates that the difference of geological background of coal samples should be taken into consideration when discussing the relationship between vitrinite reflectance and TSF parameter R_1 .

Furthermore, fluorescence intensity of coal samples increases with TSF parameter R_1 (there are three anomalous samples from Huaibei coalfield). Ex wavelength decreases with the increasing of R_o (two samples from Huaibei coalfield are anomalous). Ex wavelength and Em wavelength of coal samples show good correlation, Ex wavelength of coal samples increases with Em wavelength coal samples. Overall, TSF parameters R_1 and R_2 also have favorable correlation,

TSF parameter R_1 increases with TSF parameter R_2 . These anomalous samples may be relevant to the macerals content of coal sample because the coal samples did not separate the vitrinite, inertinite, and exinite. And the deformation characteristics may be other influencing factor; therefore, samples for TSF testing should be collected based on the similar geological background.

4. Conclusions

Research shows that fluorescence characteristics parameters of coals are related to R_o values of coals in the study area.

FIGURE 3: The relationship between R_0 and TSF parameters.

Vitrinite reflectance value of coal samples increases with TSF R1 of coal samples in Qinshui basin, while the relationship between vitrinite reflectance of coal samples and TSF R1 in Huaibei coalfield is not clear; fluorescence intensity of coals increases with coal ranks, and excitation wavelength increases with TSF R1.

In summary, TSF technique can reflect the coal maturity at some extent. TSF parameters and vitrinite reflectance have a good correlation, and fluorescence intensity of coals is a significant parameter. TSF technique may provide a fast, effective method to determine coal ranks; however, more different type coal samples should be conducted by TSF

experiments, meanwhile more factors such as macerals and geological background of coal samples should be considered before the experiments so as to establish empirical formulas between TSF parameters and vitrinite reflectance value of coals.

Acknowledgments

This work is supported by the National Natural Science Foundation of China (Grant nos. 40772135, 40972131 and 41030422), the National Basic Research Program of China (Grant nos. 2009CB219601 and 2006CB202201), and the

Strategic Priority Research Program of the Chinese Academy of Sciences (XDA05030100).

References

- [1] J. M. Brooks, M. C. Kennicutt, L. A. Barnard et al., "Applications of total scanning fluorescence to exploration geochemistry," *Offshore Technology Paper*, vol. OTC-4624, pp. 393–400, 1983.
- [2] S. W. Li, L. F. Liu, L. Chao et al., "Application of quantitative grain fluorescence technique in study of silurian palaeo oil pools distribution in the center tarim basin," *Journal of Jilin University*, vol. 36, no. 05, pp. 813–819, 2006.
- [3] K. Liu, P. Eadington, and D. Coghlan, "Fluorescence evidence of polar hydrocarbon interaction on mineral surfaces and implications to alteration of reservoir wettability," *Journal of Petroleum Science and Engineering*, vol. 39, no. 3-4, pp. 275–285, 2003.
- [4] K. Liu and P. Eadington, "A new method for identifying secondary oil migration pathways," *Journal of Geochemical Exploration*, vol. 78, pp. 389–394, 2003.
- [5] K. Liu, X. Pang, Z. Jiang, and P. Eadington, "Quantitative estimate of residual or palaeo-oil column height," *Journal of Geochemical Exploration*, vol. 89, no. 1–3, pp. 239–242, 2006.
- [6] K. Liu and P. Eadington, "Quantitative fluorescence techniques for detecting residual oils and reconstructing hydrocarbon charge history," *Organic Geochemistry*, vol. 36, no. 7, pp. 1023–1036, 2005.
- [7] P. S. He, "Summerizing the reflectance and determining methods of vitrinite," *Mineral and Rocks*, vol. 8, no. 1, pp. 87–97, 1988.
- [8] Y. W. Ju, J. J. Fan, J. Q. Tan et al., "Basin-mountain evolution, lithosphere transformation and their relationship with coalbed methane accumulation in North China," *Coal Geology of China*, vol. 21, no. 3, pp. 1–5, 2009.
- [9] S. F. Han, *Geological Condition and Prediction of Coal Accumulation in Huainan and Huaibei Coalfields*, Geological Publishing House, 1990.
- [10] G. L. Wang, Y. W. Ju, M. L. Zheng et al., *Tectonics of Energy Resource Basins in the Northern China*, China University of Mining and Technology, Xuzhou, China, 2005.
- [11] Y. W. Ju, B. Jiang, Q. L. Hou, and G. L. Wang, "New structure-genetic classification system in tectonically deformed coals and its geological significance," *Journal of the China Coal Society*, vol. 29, no. 5, pp. 513–517, 2004.
- [12] X. S. Li, Y. W. Ju, Q. L. Hou, and H. Lin, "Spectrum research on metamorphic and deformation of tectonically deformed coals," *Spectroscopy and Spectral Analysis*, vol. 31, no. 8, pp. 2176–2182, 2011.